

Study and characterisation of different metal alloys processed through Laser Powder Bed Fusion


ScuDo
Scuola di Dottorato ~ Doctoral School
WHAT YOU ARE, TAKES YOU FAR

Doctoral Dissertation
Doctoral Program in Materials Engineering (30th Cycle)

# Study and characterisation of different metal alloys processed through Laser Powder Bed Fusion

## PhD thesis

By

## Francesco Trevisan

**Supervisors:**
Dott. Diego Manfredi, Supervisor
Prof. Paolo Fino, Tutor

**Doctoral Examination Committee:**
Prof. Federica Bondioli, Referee, University of Parma
Dr.-Ing. Karl-Heinz Lang, Referee, Karlsruhe Institute of Technology

Politecnico di Torino
2018

# Declaration

I hereby declare that, the contents and organization of this dissertation constitute my own original work and does not compromise in any way the rights of third parties, including those relating to the security of personal data.

Francesco Trevisan

2018

* This dissertation is presented in partial fulfillment of the requirements for **Ph.D. degree** in the Graduate School of Politecnico di Torino (ScuDo).

*Alla mia amata Trieste*

# Acknowledgment

I am grateful to the Italian Institute of Technology, Centre For Sustainable Future Technologies (CSFT@PoliTo), for my PhD scholarship and to Politecnico di Torino, Department of Applied Science and Technology (DISAT), for the third level PhD courses. Moreover, I would like to thank the Monash Centre for Additive Manufacturing (MCAM) at Monash University and the Institut für Angewandte Materialien (IAM) at Karlsruhe Institute of Technology (KIT) for the scientific collaboration carried out during this thesis.

I would like to express my deep gratitude to Dr. Diego Manfredi for his constant work as supervisor and mentor during the three years of PhD, Dr. Flaviana Calignano for her expertise and training in the use of the EOSINT M270 machine and for helping to write scientific papers, Dr. Massimo Lorusso for its support in the characterisation and testing of the material investigated.

Acknowledgements for their contributions go to: Prof. Paolo Fino as tutor of my PhD studies, Prof. Mariangela Lombardi and Prof. Matteo Pavese for their scientific support. Moreover, I would like to thank all the technical staff in Politecnico for their time and assistance.

My deep gratitude goes also to Prof. Xinhua Wu and all the researchers and technicians at MCAM for their collaboration and support during the period I spent at their research centre. Furthermore, I would like to thank Prof. Martin Heilmaier and Dr. Karl-Heinz Lang for the opportunity to carry the fatigue tests and analyses on Ti-6Al-4V titanium alloy at KIT laboratories.

Finally I would like to thank all the persons who stayed closed to me during the PhD, particularly: my mother and father for their daily encouragement, love and support, my brothers Alessandro and Roberto together with their families, my colleagues Cat, Simone and Bea in IIT for the coffee breaks, lunches, discussions and laughs had together, Luisa for constantly and strongly helping me supporting every single day of PhD, my flatmates of Casa Zingari Ciccio and Totò who went along with me in the last three years and became my friends, my old friends from Triest University Marco, Barze, Paru, Spina (finally you are cited in the acknowledgements of one of my theses my dear Riccardo!), from high school Sara,

Jack, Cusci, Degra, Vale, Prez, Tommaso, Silvia, and Sterpo, for our never-ending friendship started long time ago.

Finally, I would like to thank my loved native city Trieste which I deeply miss from the bottom of my heart.

# Abstract

Additive Manufacturing (AM) techniques inspired a substantial revolution in the way of concept and produce metal components for industry. Among all the available AM processes, Laser Powder Bed Fusion (LPBF) inspired a noticeable series of investments, studies and standardisation routes since the great interested it acquired in several industrial sectors. In the past years numerous researchers demonstrated how this process produces metal components with innovative and unprecedented microstructures and mechanical properties, disclosing new horizons in the scientific and industrial research.

This thesis took under investigation the study and characterisation of three different metal alloys, A357 aluminium alloy, Ti-6Al-4V titanium alloy and pure copper, respectively, all processed by LPBF. Furthermore, the investigation of different post-processing heat treatments was took under study. The processed samples, as well the metal powders used, were characterised by microscopic and macroscopic analyses.

The study on A357 aluminium alloy processed by LPBF investigated the process parameters necessary to build full dense components for industrial applications. By correctly combining hatching distance and scanning speed it was possible to fabricate completely dense specimens keeping a good productivity rate. Moreover, the effects of different heat treatments on specimens microstructure and mechanical properties were studied. Particularly, a stress relieving and a subsequent T6 precipitation hardening treatment were performed on the full dense LPBF parts, investigating the effects of different temperatures and durations in the case of T6 treatment. Longer solution treatments enabled to obtain higher hardness values and to reduce the time required to reach peak hardening conditions during ageing. While stress relieving strongly softened the material, a maximum hardness comparable to as-built parts conditions was obtained after subsequent 8 h solution treatment, water quenching and 3 h ageing treatment. Stress reliving treatment slightly modified the as-built microstructure by favouring the diffusion of Si but did not removed the melt pool structures present, furthermore it noticeably increased the elongation at break to detriment of tensile strength. Further T6 treatment modified the tensile properties to values comparable with the as-built conditions eliminating melt pools anisotropic features.

The study on Ti-6Al-4V titanium alloy investigated the microstructural, tensile and fatigue properties of the LPBF fabricated parts, produced with two different gas atomised powders. The two powders contained two level of oxygen inside the chemical composition, a low and a high amount, in order to simulate the LPBF processing of Ti-6Al-4V ELI and Ti-6Al-4V grade 5, respectively. Two different building orientations, vertical and horizontal, were chosen for the specimens fabrication and moreover three different testing conditions were considered: after stress relieving, after stress relieving plus heat treatment and after stress relieving plus Hot Isostatic Pressing (HIP). Processing a subsequent heat treatment after stress relieving reduced tensile strength and increased ductility by coarsening $\alpha + \beta$ lamellar structure while $\beta$ columnar grains faded. HIP post-processing closed the major part of porosities and defects and enabled to greatly increase both ductility and fatigue resistance. Pores and defects were detected as the most influencing factors upon the fatigue properties, rather than building orientation and oxygen content, which mostly influenced tensile strength. Only stress relieved and HIPped samples resisted more than the chosen endurance limit of $10^7$ cycles at high applied strength than the other specimens.

The study carried out on pure copper investigated the feasibility of processing such material with LPBF using a commercial machine equipped with an infrared 200 W fibre laser. The specimens fabricated did not exceed the 83 % of density due to the low absorptivity of copper to infrared radiation, but Diffuse Reflectance Spectroscopy (DRS) analysis demonstrated how modifying the laser radiation from infrared wavelengths to the green ones, the powder bed absorption raised. As-built samples did not present oxides traces inside the microstructure and were constituted by $\alpha$-Cu phase. The microstructure was constituted by both equiassic and elongated grains depending on the heat fluxes generated inside the material in the horizontal and vertical cross sections.

# Contents

# List of Figures

# List of Tables

# Chapter 1

# Introduction

In the past thirty years a new manufacturing approach have been growing and developing in modern industry. This new method begins from a computer aided design (CAD) model and layer by layer fabricates net-shape components: all the processes adopting this manufacturing philosophy are labelled as Additive Manufacturing (AM) technologies.

The current official definition of AM is:

"*a process of joining materials to make objects from 3D model data, usually layer upon layer, as opposed to subtractive manufacturing methodologies.*" [1]

AM technologies have the potential of revolutionizing the way of perceiving the manufacturing of products and since many years, specific journals are referring to these processes as the vanguards of a new manufacturing era, called “third industrial revolution” [2]. AM sector is still growing to maturity and shows great promises for manufacturing future components with sophisticated geometries in new industrial supply chain. From aerospace to biomedical, from automotive to jewellery, the marketing opportunities for AM have been constantly growing and increasing their revenues.

In the next chapters, an overall description of actual AM scenario is presented. From the origins of first 3D printers to the present AM applications in industries, describing and contextualizing the different principal AM processes. Particularly, a great interest is given to Laser Powder Bed Fusion (LPBF) process, assigning a deeper presentation of the material science and engineering aspects related to this processes.

# 1.1 Additive Manufacturing

## 1.1.1 Standard manufacturing technique

AM process chain involves a number of standard operations, beginning from the realization of the virtual CAD model of the product and finishing in the part physical realization. In Figure 1 the AM production route is schematically represented. Different AM processes involve different software and hardware systems but above all the basic approach is kept the same.

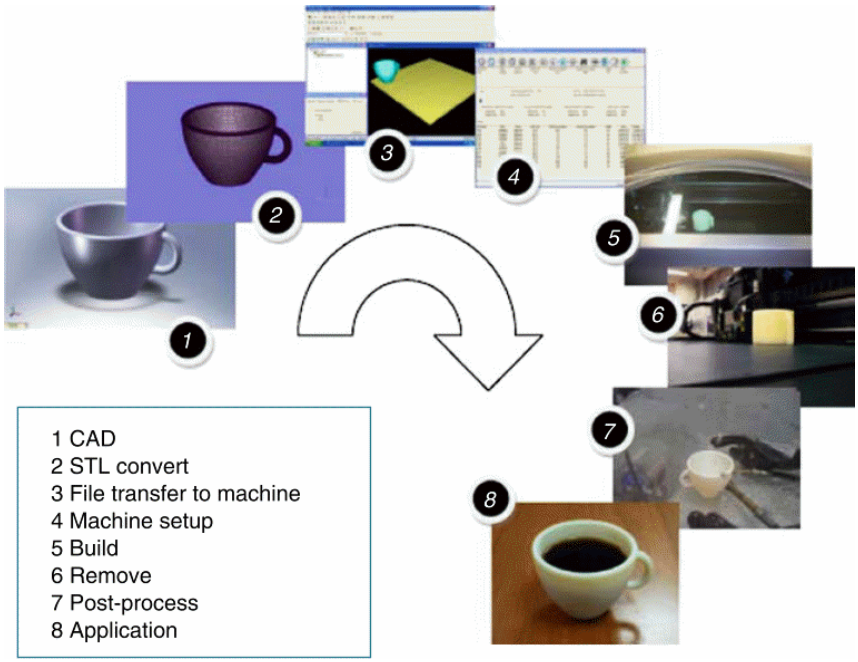


**Figure 1.** General AM production route from CAD to final part [3].

Firstly a CAD model is generated in order to reproduce the desired part geometry. The design can be obtain by almost any professional CAD solid modeling software, or, by reverse engineering techniques. Reverse engineering permits to model and export a precise geometric virtual representation of a object to CAM/CAM systems. The physical object can be digitized by computer tomography (CT), magnetic resonance imagining (MRI) or laser scanning [4]. Reverse engineering is significantly adopted in medical applications, such as prosthesis implantation, where prosthesis design has to fit the patient body shape with high geometrical accuracy [5]. The CAD model represents the 3D model of the part and must be converted in a .stl file to be fabricate. This file format is the de facto standard interface for AM systems and takes its name from the term

stereolithography (SL) [1]. The .stl converted file consists in a surface model constituted by triangular facets which approximate the shape of the CAD 3D model. Once completed, the .stl file is sent to the AM system software and the setting of the production can be concluded. Before launching the manufacturing process, firstly the position and the orientation of the part and secondly the process parameters used during the AM process must be checked and optimized. Indeed not all the geometries are free to be fabricated by AM and furthermore each material requires specific parameters settings in order to be correctly manufactured. The remaining operations of AM route (building, removal and post-processing) are closely dependent on the specific AM system chosen [3].

### 1.1.2 History of metal AM

The origins of AM technologies took place in the early 80s, when Charles Hull invented the first form of Three Dimension (3D) Printing, called stereolithography: a vat photopolymerisation process which starts from photocurable polymers in their liquid form and adopts one or more laser to selectively reticulate and consolidate the material in the final shape of the part [1]. It was the first time that a CAD file was put in communication with a machine to fabricate computer modelled parts. In this process only surface files were important and they were named as .stl files (referring to SL process): each virtual slice of the model was then transformed into a real polymeric one. Commercially speaking, the first application of 3D printing appeared in 1986 when Hull created "3D Systems", the first company specialised in the developing and production of 3D machines [6]. 3D systems is still representing one of the most industrialized 3D printing company in the world, producing an approximate revenue of $ 654 million in 2014 [7]. At the same time 3D Systems was optimizing and patenting SL, Carl Deckard and Dr. Joe Beaman, an undergraduate student and an assistant professor, respectively, at University of Texas (Austin, USA), started working on a new technology known as selective laser sintering (SLS). SLS can be described as a laser powder bed process which selectively melts powdered materials layer by layer, adopting specific lasers in an enclosed chamber [1]. In 1989 Deckard and Beaman commercialised the first SLS machines (Mod A and Mod B) able to 3D print polymeric materials [6].

On the other side, further development had been necessary to observe the birth of the first AM machines able to process metals and ceramic materials. The first step in the metal AM had been carried out by German EOS company, founded in 1989 by Dr. Hans J. Langer and Dr. Hans Steinbichler [8]. In the early 90s, they showed their first prototype of a direct metal laser sintering (DMLS) machine and

in 1995 they launched on the market the first DMLS system [9]. The technology was very similar to the SLS one, but it can also sinter metallic powders. Since 1997 EOS invested lot of energies and resources in developing their systems, making DMLS one of the most popular AM processes in metal manufacturing. Moreover, metal laser sintering systems have been widely developed and commercialised all over the world, enriching the market possibilities and the products range. Almost during the same years, at Sandia National Laboratories in Alburquerque (New Mexico, USA), a new typology of AM process defined as Laser Engineering Net Shaping (LENS®) was developed [10]. Differently from DMLS, where a powder bed is fused by a laser beam, LENS technique selectively deposits powders under a high power laser, melting and consolidating the material upon a substrate. The part is built layer by layer deposition, having the head and the base substrate systems able to move in the space. The first commercialisation of the process has been carried out by Optomec, Inc in the 1997 and until now more than 20 LENS® systems have been developed and commercialised [11]. Year 1997 represented also the dawn of another very famous AM company, the Swedish Arcam AB, worldwide known for their patented technology, named Electron Beam Melting (EBM). Developed together with Chalmers University of Technology, this powder bed technology adopts an electron beam to selectively melt the metal powder bed. The first commercialised machine appeared in the 2002 and since that year Arcam's business strategy has been focused on the orthopaedics and aerospace markets [12]. Apart from lasers and electron based technologies, in the early 90s, Binder Jetting (BJ) process was developed at Massachusetts Institute of Technology (MIT) [13]. Differently from the other AM processes, it selectively deposit a liquid organic bonding agent on a powder bed, joining the metal particles together. Layer by layer, the part containing both binder and metal powder (called "green" part) is produced and later treated at high temperature in two consequent steps, de-binding and sintering. Actually, BJ technology is commercialised by ExOne company, officially founded in the 2005 as a spin-off of Extrude Hone Corp [13]. The last group of AM processes industrially adopted to fabricate metallic component, is named Sheet Lamination. This particular family of processes involves the stacking and joining of 2D metal slices to produce a 3D component. Joining can be obtained both with adhesion (e.g. gluing) or metallurgical bonding (e.g. brazing or diffusion bonding) [14]. The newest and most studied process of Sheet Lamination technology is the Ultrasonic Additive Manufacturing (UAM), developed and commercialised by Fabrisonic since 2011 [15]. Figure 2 schematically illustrates the timeline of AM technologies developments and significant events related to them [14].

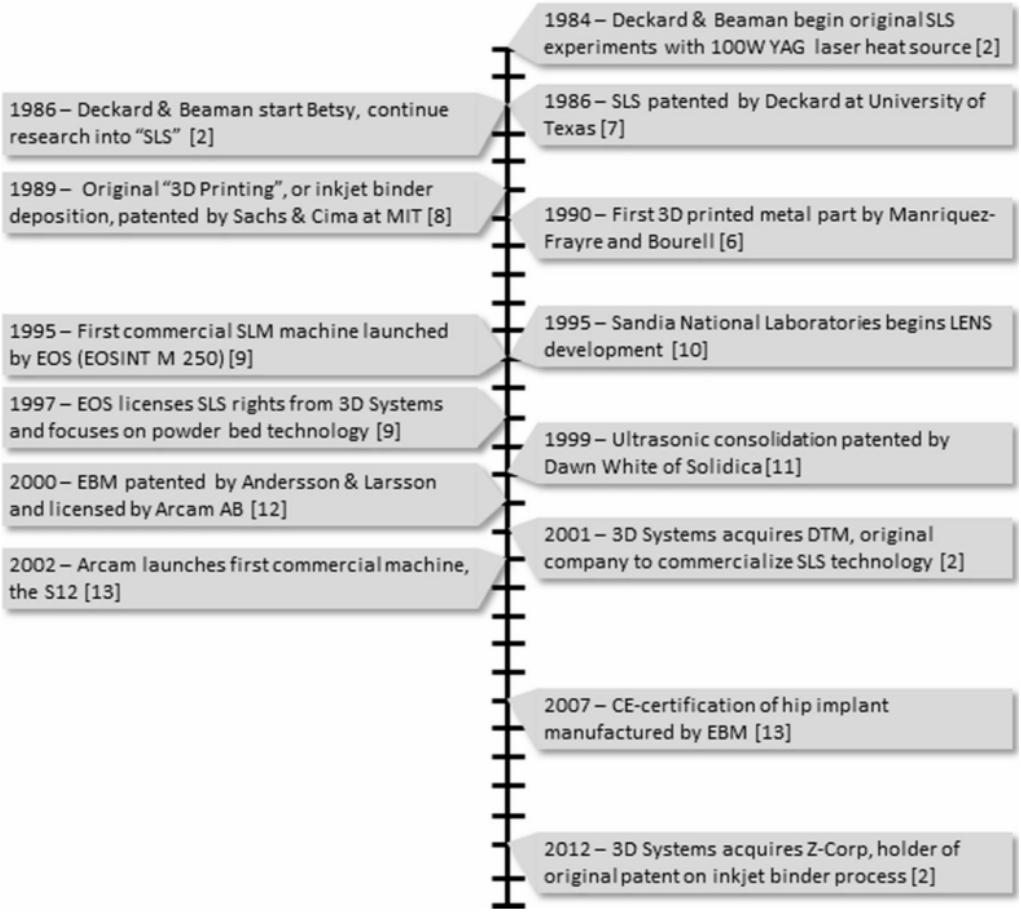


**Figure 2.** Timeline of significant events in metal AM development [14].

### 1.1.3 Applications overview

In the last years AM technologies encountered high interest from several industry markets such as the aerospace, the automotive, and the medical ones. Some of the principal advantages which motivated the wide adoption of AM technologies are:

- Material and energy waste reduction. Differently from conventional subtractive techniques such as machining or tooling AM can efficiently process near-net shape parts.

- Design revolution. AM process are able to customize the product without additional costs and reproduce complex architectures with internal channels and free-form enclosed

or lattice structures, revolutionizing the component design to lighter models.

- New supply chain. AM process can work directly close to the customer (distributed manufacture), reducing the transportation, packaging and warehousing costs (e.g. offshore facilities).

In aerospace industry, metal AM processes have been used for fabricating structural parts, turbine blade, fuel injection nozzles [16–19], accounting 12.3% of the global amount of AM applications [20]. Indeed the adoption of AM in aircraft provides abundant energy cost reductions, due to the lower amount of expensive materials required for manufacturing and particularly to the fuel savings from lighter weight components. Furthermore, AM opens the possibility to manufacture high performance materials such as Ti-6Al-4V or nickel super-alloys limiting the difficulties related to the machining or tooling of such alloys [20,21]. As an example, the bionic partition for Airbus A320 aircraft produced by DMLS is shown in Figure 3 [22]. The innovative structure is not only stronger but also 25 kg lighter than previous models. One of the most publicized aerospace component produced by AM is the LEAP engine fuel nozzle produced by GE Aviation (Figure 4). This component has been fabricated with an intricate new design for internal cooling channels and a reduced weight (more than 25 % weight loss). In this case, instead of producing and then assembling 18 single parts as occurs in traditional manufacturing, the AM part required one single operation to be fabricated [19,20]. The innovative nozzle has also been certified for the implantation on civil aircrafts, and by 2020 a mass production of more than 100,000 parts is expected [20,23].

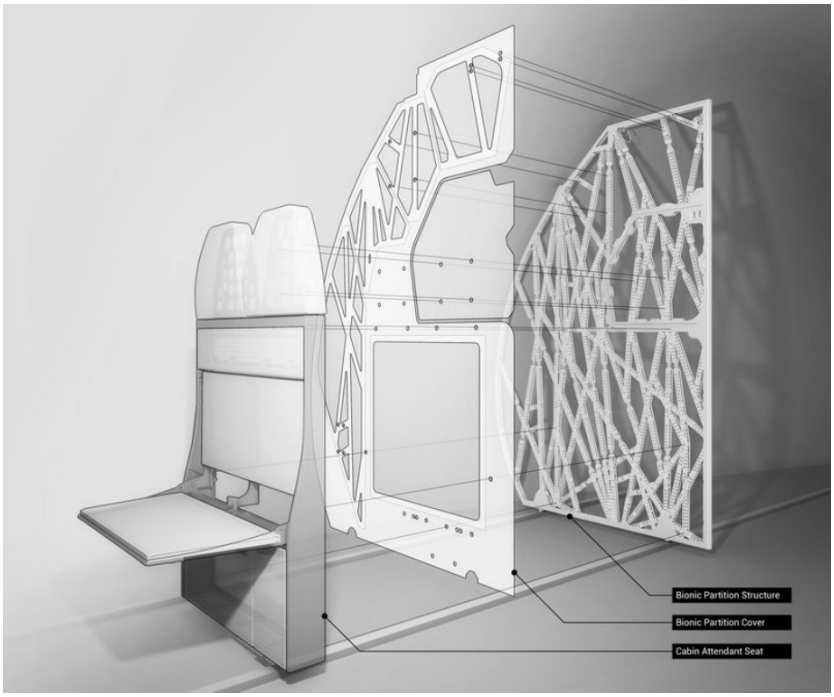


**Figure 3.** Bionic partition for Airbus A320 aircraft produced by DMLS (*with the Courtesy of www.3ders.org [17]*).

**Figure 4.** LEAP engine fuel nozzle produced by GE aviation (*with the Courtesy of GE reports [24]*).

For space engineering, an example of AM application is the fabrication of NASA rocket injector for J-2X engine of the next Space Launch System: AM

process considerably accelerated the production time, requiring weeks rather than months, compared to traditional manufacturing [20]. No material joints have been necessary to produce the part, implying higher mechanical properties and a superior safety and less costs compared to traditional manufactured version.

In the automotive industry, AM processes find their place for the prototypes production of cylinder heads, brake rotors, rear axles for Lamborghini in a cost effective way [25]. Furthermore, AM processes require significantly less operations in the mould fabrication, minimizing the processing costs and lead time, attracting further interest by automotive industries [26]. Indeed, Audi company recently signed a development partnership with EOS company, in order to innovate the tool manufacturing processing [27].

Definitively, the medical field is another considerably developed and profitable market for AM applications. Freedom of design, new lattice structures for higher mechanical properties [28–40], better prosthesis biocompatibility [41–44] and particularly patient personalised prosthesis, all motivated the rapid and significant growth of AM technologies in the biomedical sector [7,45]. The AM feasibility of producing patient customized implants, reproducing patient tissues, organs and bones with extremely high precision, is totally changing several medical sectors, from dentistry to surgery (Figure 5) [46–50]. Indeed, AM is able to replicate the interior architectures of bones, muscles, nerves and vasculature structures using compatible materials. In this way, the body healing is accelerated, the surgical interventions appear less invasive and risky and implant rejection is considerably reduced [47].

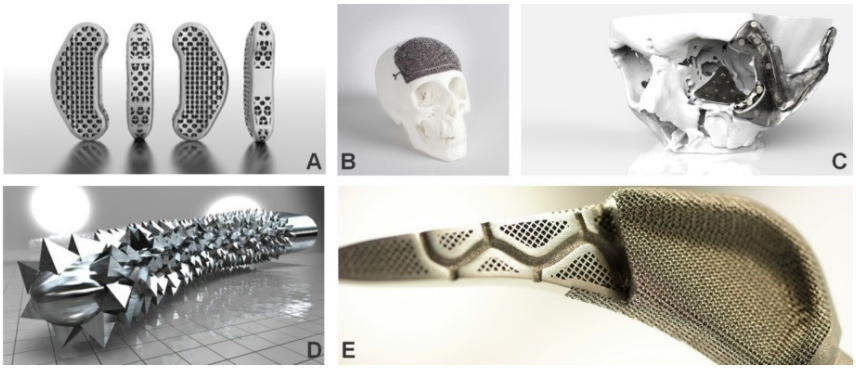


**Figure 5.** Examples of biomedical devices realized by AM methods [45]. A) Spinal fusion implant (*with the courtesy of EOS [51]*). B) Cranial implant (*with the courtesy of EOS [51]*). C) Skull implant (*with the courtesy of Renishaw [52]*). D) Bone rasp (*with the courtesy of Autodesk Within [53]*). E) Orthopaedic implant (*with the courtesy of Concept [54]*).

As in the case of aero-space industry, the tooling operations reduction and the less amount of wasted materials represent other two advantages that highly influenced the spread of AM process in medical devices industries, making the production cheaper and faster [9]. Compared with the traditional manufacturing route, the fabrication through EBM of a hip stem prosthesis had a cost 35 % lower [55]. Already in 2015 more than 100,000 acetabular implants were produced by AM processes and over half of them implanted in to patients [7]. Furthermore, the possibility to process functionally graded materials, with enhanced biocompatible properties compared to traditional ones [56–59], and particularly new graded structures such as controlled-porosity scaffolds, open new horizons to further innovative devices [9,60–62].

Together with the aerospace, automotive and medical applications, also other several industrial markets have been opening to AM processes adoption: promising investments have been carried on by armament, furniture, jewellery, sports, toys, textiles, food industry [25]. Furthermore, tools and mould producers are adopting AM technologies in their manufacturing routes: indeed, future perspectives about AM future are highly seeing these technologies working together with the traditional manufacturing processes, joining the advantages of both together. The AM industry revenues grew by 17,4 % in 2016, and even more (25,9 %) in 2015, representing a total market of $ 6.063 billion [63]. Considering that to reach the first billion AM industry took almost 20 years and assuming the high growth observed in the last 5 years, the overall market is expected to exceed $ 21 billion by 2020 [7].

### 1.1.4 AM standards

All metal AM processes share the same manufacturing “layer by layer” approach, but consistently differ for the form feedstock (wire, sheet or powder), the energy source (laser, electron beam) and several other factors, such as the process atmosphere, process temperature or post-processing operations. In the past years, the lack of AM processes categories represented a crucial issue in the AM industry, making the educational and standards-development challenging. As a consequence, grouping AM single processes made easier the knowledge transferring and also the standards drawing up. The standardisation need has been the first interest for the manufacturing market, particularly for the biomedical and aerospace companies which firstly applied AM processes in their manufacturing routes [64]. Indeed the standards regarding traditional manufacturing processes or materials are not always suitable for AM: material anisotropy depending on the building strategy adopted, final surface finishing and even the amount of recycled powder are all influencing

factors of AM fabricated parts and are not considered in previous standards related to traditional techniques [64]. Upcoming standardisation is globally driven by customers' requirements and possible future market opportunities. The high priority is given to process and equipment, qualification and standardisation, AM modelling and simulation topics [64].

One of the first standards published for AM processes is the ASTM F2792 (2012) [1], which provides the current AM processes organization in seven categories, four of them regarding metal systems:

- Sheet Lamination
- Binder Jetting
- Direct Energy Deposition (DED)
- Powder Bed Fusion (PBF).

In addition to ASTM F2792 (2012) [1], other standards regarding AM processes have been realized since now: Table 1 summarises the list of existing ASTM standards focused on metal AM.

**Table 1.** ASTM standards on AM processes and materials.

| Standard Number | Name | Description |
|---|---|---|
| **ISO/ASTM 52921:2013 (E)** [65] | Standard Terminology for Additive Manufacturing— Coordinate Systems and Test Methodologies | This terminology includes terms, definitions of terms, descriptions of terms, nomenclature, and acronyms associated with coordinate systems and testing methodologies for additive manufacturing (AM) technologies in an effort to standardize terminology used by AM users, producers, researchers, educators, press/media, and others, particularly when reporting results from testing of parts made on AM systems |
| **ISO/ASTM 52900:2015** [66] | Standard Terminology for Additive Manufacturing– General Principles– Terminology | This International Standard establishes and defines terms used in additive manufacturing (AM) technology, which applies the additive shaping principle and thereby builds physical 3D geometries by successive addition of material |
| **ASTM F3122–14** [67] | Standard Guide for Evaluating Mechanical Properties of Metal Materials Made via Additive Manufacturing Processes | This standard serves as a guide to existing standards or variations of existing standards that may be applicable to determine specific mechanical properties of materials made with an additive manufacturing process |

| | | |
|---|---|---|
| **ISO/ASTM 52915:2016** [68] | Standard Specification for Additive Manufacturing File Format (AMF) Version 1.2 | This International Standard provides the specification for the Additive Manufacturing File Format (AMF), an interchange format to address the current and future needs of additive manufacturing technology |
| **ISO/ASTM 52901:2016** [69] | Standard Guide for Additive Manufacturing – General Principles – Requirements for Purchased AM Parts | This document defines and specifies requirements for purchased parts made by additive manufacturing. It gives guidelines for the elements to be exchanged between the customer and the part provider at the time of the order, including the customer order information, part definition data, feedstock requirements, final part characteristics and properties, inspection requirements, and part acceptance methods |
| **ISO/ASTM 52910:2017** [70] | Standard Guidelines for Design for Additive Manufacturing | This document gives guidelines and best practices for using additive manufacturing (AM) in product design. It is applicable during the design of all types of products, devices, systems, components, or parts that are fabricated by any type of AM system |
| **ASTM F3049-14** [71] | Standard Guide for Characterizing Properties of Metal Powders Used for Additive Manufacturing Processes | This guide introduces the reader to techniques for metal powder characterization that may be useful for powder-based additive manufacturing processes including binder jetting, directed energy deposition, and powder bed fusion |

| | | |
|---|---|---|
| **ASTM F2924-14** [72] | Additive Manufacturing Titanium-6 Aluminium-4 Vanadium with Powder Bed Fusion | This specification covers additively manufactured titanium-6aluminium-4vanadium (Ti-6Al-4V) components using full-melt powder bed fusion such as electron beam melting and laser melting |
| **ASTM F3001-14** [73] | Additive Manufacturing Titanium-6 Aluminium-4 Vanadium ELI (Extra Low Interstitial) with Powder Bed Fusion | This specification covers additively manufactured titanium-6aluminium-4vanadium with extra low interstitials (Ti-6Al-4V ELI) components using full-melt powder bed fusion such as electron beam melting and laser melting |
| **ASTM F2971-13** [74] | Standard Practice for Reporting Data for Test Specimens Prepared by Additive Manufacturing | This practice describes a standard procedure for reporting results by testing or evaluation of specimens produced by additive manufacturing (AM) |
| **ASTM F3056-14** [75] | Standard Specification for Additive Manufacturing Nickel Alloy (UNS N06625) with Powder Bed Fusion | This specification covers additively manufactured UNS N06625 components using full-melt powder bed fusion such as electron beam melting and laser melting |

| | | |
|---|---|---|
| **ASTM F3055-14a** [76] | Standard Specification for Additive Manufacturing Nickel Alloy (UNS N07718) with Powder Bed Fusion | This specification covers additively manufactured UNS N07718 components using full-melt powder bed fusion such as electron beam melting and laser melting |
| **ASTM F3184-16** [77] | Standard Specification for Additive Manufacturing Stainless Steel Alloy (UNS S31603) with Powder Bed Fusion | This specification covers additive manufacturing of UNS S31603 components by means of laser and electron beam-based full melt powder bed fusion processes |
| **ASTM F3187-16** [78] | Standard Guide for Directed Energy Deposition of Metals | Directed Energy Deposition (DED) is used for repair, rapid prototyping and low volume part fabrication. This specification is intended to serve as a guide for defining the technology application space and limits, DED system set-up considerations, machine operation, process documentation, work practices, and available system and process monitoring technologies |

## 1.2 Metal Additive Processes

### 1.2.1 Sheet Lamination

This particular family of processes involves the stacking and joining of 2D metal slices to produce a 3D component. A considerable number of processes are based on sheet lamination and mostly differ on the material used and on the technique adopted to join and cut the metallic sheets. The metal slices can be cut to their final shape before the adhesion step (Form-then-Bond approach) or can be machined after the joining (Bond-then-Form approach) [3]. In Figure 6 the Form-then-Bond approach is exposed: the metal slices are cut by an automatic system following the CAD model and then joined together reproducing the final shape of the component. Differently from the Bond-then-Form approach, the amount of removed material is considerably low but some limitations to design the parts and to automate the process for complex geometries exist.

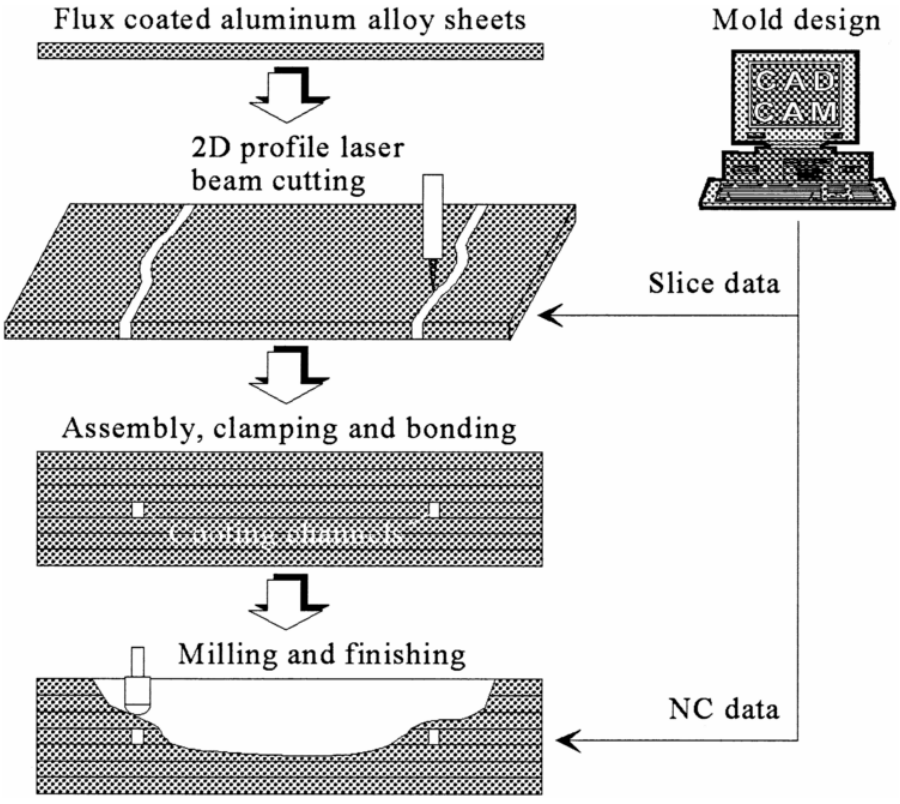


**Figure 6.** Schematic representation of sheet lamination Form-then-Bond approach [79].

The joining mechanism can be achieved by metallurgical bonding, obtained by brazing [79], diffusion bonding [80], laser [81], resistance welding [82] or ultrasonic consolidation [14]. The Ultrasonic Additive Manufacturing (UAM), also known as Ultrasonic Consolidation (UC) is one of the most studied and used sheet lamination processes [3,14,83–85]. Developed in 2003 by Dawn White [86], this process joins metal foils together by ultrasonic metal welding (USW) and removes the excess of material by an integrated Computer Numerical Control (CNC) machining system. A schematic illustration of the process is exposed in Figure 7a, while in Figure 7b an image of the first commercial UAM platform (Alpha UAM) is reported.

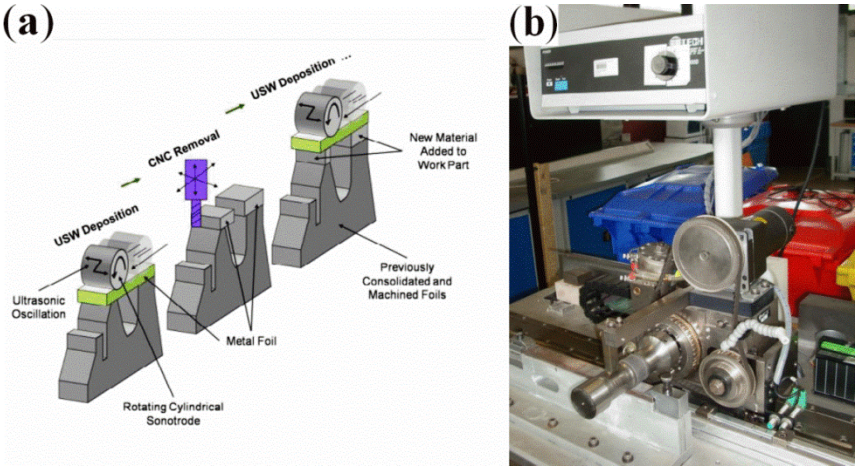


**Figure 7.** Ultrasonic Additive Manufacturing (UAM) technology: (a) schematic illustration of the process and (b) first commercial platform (Alpha UAM) [87]

In UAM the component is fabricated on a flat building platform, connected to a heater source (maximum 200 °C). Starting from the bottom of the part, several metals sheets are joined by ultrasonic bonding and then trimmed by CNC milling [87]. During the process the CNC milling tool shapes the slice contour of one level (usually 4 layers) according to the component final geometry [3]. The ultrasonic bonding is provided by a rotating sonotrode which applies a normal force directly along the thin metal foil (generally 100 ÷ 150 μm thick) and oscillates transversally to the motion direction (at constant 20 kHz frequency). Several mechanisms provide material bonding between metal foils, such as mechanical interlocking, plastic deformation of interface asperities and diffusion bonding. Once the metal foil is deposited another foil is deposited adjacent to it: the process is repeated until, layer by layer, the part is completed [3].

UAM can be assumed as an hybrid AM process which involves both additive and subtracting technologies, as machining or laser processing [87]. The first advantages of this hybrid nature are the surface finishing and dimensional accuracy that can be obtained thanks to CNC milling system. Indeed, compared to other AM processes, UAM fabricated parts do not possess any stair-stepping defects and any layer thickness dependence. However, UAM process is not able to produce complex overhanging structures because no support material necessary to sustain such complex architectures can be deposited. Another advantage is the low temperature conditions UAM process works with. Indeed, even if in the contact regions between single metal foils the temperature raises considerably (50 % of material melting temperature [14]), the overall temperature of the entire part remains around room temperature. As a consequence, differently from what happens in powder bed fusion components, the amount of residual stresses, deformations and shrinkages are negligible in UAM fabricated parts, avoiding post-processing heat treatments and enhancing the mechanical properties of the final products. Furthermore, sheet lamination is able to manufacture composites parts by alternating foils of dissimilar materials [88–91]. In fact, metal composites can be manufactured in two distinct ways. The first one is stacking metal foils of two metal difficult to joint (e.g. aluminium and copper) while the second way is to insert fibers between single layers (e.g. TiNi fibers between Al foils), improving the mechanical and physical properties of the part.

For the metal sheet lamination process, the principal provider of UAM systems and products is Fabrisonic company [15]. The machines of SonicLayer serie are able to process aluminium, copper, steel and stainless steel and combination of dissimilar metals, with a maximum building volume of 1800 x 1800 x 900 mm. Accademic research is also very attracted to UAM developing, and several research centres are active in this field as Loughborough University, Univeristy of Louisville, Oak Ridge National Laboratory, the Ohio State University, Clemson Unviersity and Edison Welding Institute (EWI) [87].

### 1.2.2 Binder jetting

Basically, binder jetting (BJ) is an AM process in which powdered material is joined together by a liquid agent selectively deposited layer by layer. It is commonly used for sand casting applications, but in the last years it has also been improved in order to process metals and ceramics too [92]. In Figure 8, a schematic representation of BJ process is illustrated.

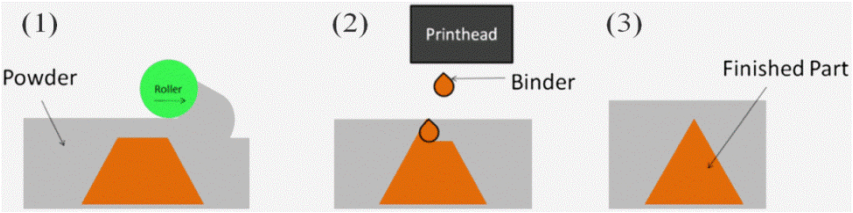


**Figure 8.** Schematic representation of binder jetting process [93].

The BJ process generally consists in several subsequent steps: printing, curing, de-powdering, sintering (in some cases followed by infiltration), annealing and finishing. The first printing process begins with the deposition of a thin layer of powder: a levelling roller moves the powders from the feed bed upon the print bed, depositing one layer of constant thickness. Subsequently the liquid binder is selectively spread by the inject print head upon the powder bed. The chemical composition of the binder varies depending on the material, as in the case of metallic powder when aqueous binder can be used [94]. Once binder spreading operation is concluded, the print bed moves under an electrical infrared heater to dry the binder. Then the print bed lowers down of one layer thickness height and at this point the levelling roller deposits another layer of powder, starting again the process from the first step. When the last layer of the final product is processed, a fragile binder-metal composite (also named "green part") is obtained. The operator removes it from the printing system and transfers to an oven for the curing procedure: such operation, which takes between 6 and 12 hours, implies an increase in the strength of the green part before the beginning of the sintering process [14]. Subsequently, the green part is de-powdered and later sintered, in order to completely remove the organic phase and reduce the porosities inside the material. In the case of metals powders, such as steel ones, sintering is carried out at high temperature (~ 1100 °C) for 24 ÷ 36 hours, generally leaving 40 % porosity inside the part [14]. In such cases, after sintering low melting alloys (e.g. bronzes [14,95]) are infiltrated inside the part to obtain full dense components.

The properties of final parts fabricated by BJ, such as the dimensional accuracy or the surface quality, are influenced by several variables and parameters that can be grouped in: design factors (e.g. strut thickness in lattice structures), powders properties (e.g. particle shape and dimension, flowability), binder properties (e.g. viscosity and volatility) and process parameters (e.g. layer thickness, printing saturation, heater power ratio, curing temperature and time). Furthermore, also the post-processing sintering treatment conditions can highly influence final part properties [96].

As described by Chen et al. [96] the printing saturation (S) is defined as the ratio between the volume occupied by the binder ($V_{binder}$) and the air space ($V_{air}$):

$$S = \frac{V_{binder}}{V_{air}} = \frac{V_{binder}}{(1 - PR) \cdot V_{solid}}$$

Where PR is the Packing Rate and refers to the fraction of volume of powder in a given volume of powder and air. S factor indicates the quantity of binder deposited during the printing operations. The amount of binder strongly determines the green part stability during BJ. Indeed, in the case of low quantities of binder the powder cannot firmly join together and the green part risks to collapse during the process. On the opposite, excessive quantities of binder considerably reduce surface finishing and part geometry accuracy, and require longer drying time and more consumption of energy. The drying time is another fundamental process parameter to consider for BJ because also related to binder drying and surface finishing features. In addition, it is possible to consider also the heater power ratio factor, that describes the heater power consumption during the process and regulates the binder drying during the process. High power ratio values lead to higher shrinkages and higher consumption of electricity while low values are not able to dry enough the binder damaging the green part stability during the process [96].

BJ is a low thermal process which does not requires high energy sources, such as lasers or electron beam systems, and furthermore can process both metal [92,93,95–98] and ceramic systems [99,100]. As a consequence, the associated costs are extremely low, considered the absence of protective atmosphere or vacuum conditions during the process: these advantages of BJ make this technology highly competitive on the market. Actually, ExOne is the major producer of BJ systems and products, offering a vast choice of industrial printers and materials: both ceramic and metals powders are available on the market, such as 316L and 17-4 stainless steel, 625 and 718 Inconel alloys, cobalt-chrome, tungsten carbide, zircon and several others [101].

### 1.2.3 Direct energy deposition

Several technologies are classified as Direct Energy Deposition (DED) systems and all are based on melting and deposit of metallic materials adopting a focused thermal energy. DED technologies can be distinguish depending on the heat source used (laser beam, electron beam or arc-plasma), material feedstock form (powder or wire) and working atmospheres (inert or vacuum) [78]. Moreover since 2013

several hybrid systems coupling DED with CNC milling have been released, joining together the additive and subtracting manufacturing approaches [7]. DED processes have been used to repair, remanufacturing, cladding and manufacture components for different industrial sectors, like the aerospace and biomedical ones. Compared to the other AM processes, DED possess the unique possibility to fabricate compositionally graded materials depositing metals and ceramics layers with different compositions and creating in this way functionally graded structures [102–106].

#### 1.2.3.1 Laser based DED systems

The most popular DED system adopts powdered feedstock and laser heat source to process metals and ceramics because of the higher precision achievable on the final products: in Figure 9 powder-feed laser-based DED process and equipment are illustrated. A high energy laser beam is delivered in the centre of the noodle and focused upon the working plane by a system of lenses. Coaxially with the nozzle, the powder and the protective gas are delivered on the workpiece. The lenses and the entire nozzle move along the z-axis direction, obtaining equal deposition at different heights, instead the working plane is able to move horizontally in x and y directions, forming the desired cross-sectional geometry of the product.

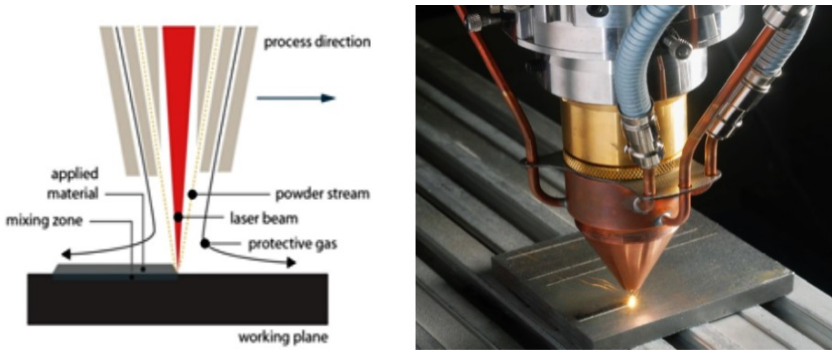


**Figure 9.** Powder-feed laser based Direct Energy Deposition process and equipment [45,107].

Powder-feed laser-based DED is commercialised under four major versions of the technology: Laser Engineered Net Shaping (LENS™), Direct Metal Deposition (DMD), and Directed Light Fabrication (DLF). LENS™ and DLF, commercialised by Optomec and Precision Optical Manufacturing respectively, differ from DMD for the working atmosphere conditions and for in-built feedback control system [102,108]. In DMD process the inert gas, which prevents melt oxidation and favours

the motion of powders, is flown coaxially with the nozzle instead in LENS™ and DLF the entire process is carried out inside a glove box. Finally, the in-built feedback control system, present only in the DMD machines, collects in-line informations regarding the process (melt pool stability; melt pool shape and dimensions) and allows to adjust the input process parameters and keep the dimensional accuracy and material integrity during the deposition [109].

DED process parameters able to determine the good quality of deposited materials are the powder feed rate, laser power, layer thickness and deposition speed. These factors directly influence amount of melt material, melt pool dimensions, cooling rates and thermal gradients and surface roughness [102,110–112]. Furthermore, material-laser interaction must be also be considered indeed the material absorptance determines the amount of energy absorbed during the laser manufacturing [102]. In DED machines laser systems vary between Nd:YAG and $CO_2$ lasers with laser wavelengths between ~ 1 and ~ 10 μm: consequently the related absorptance of the powders varies on the basis of wavelength used, varying the melting behaviour of the material during DED process [113]. In the case of low absorptance higher laser power is required in order to avoid partial melting and defects formation inside the deposited material [10,102,114]. Similar issues can be also observed in LPBF processes and represent central point in the material development for laser-based AM technologies [114–116].

Generally, in DED process the powder-feedstock approach works with an average layer thickness between 20 and 100 μm, achieving final roughness values between 9 and 16 μm and dimensional accuracy of ± 0.05 mm [117]. Moreover, functional graded components can be fabricated varying the material feedstock [56–58,103–105,118]. Balla et al. [57] realised Ti-$TiO_2$ graded structures for orthopedically applications, fabricating the first 10 layers in pure Ti and the subsequent ones at different $TiO_2$ concentrations (50, 90 and 100 %). A negative aspect of powder-feed DED systems is the slow deposition rate (~ 10 g/min) [117] which considerably limits their applications in medium-large parts production.

Laser-based DED systems with higher productivity are the wire-feed systems, also known as Wire Laser Additive Manufacturing (WLAM). The WLAM equipment is mainly constituted by a laser, an automatic wire-feed system, CNC systems and some auxiliary mechanisms for the shielding atmosphere or workpiece heating: Figure 10 shows a representation of the process.

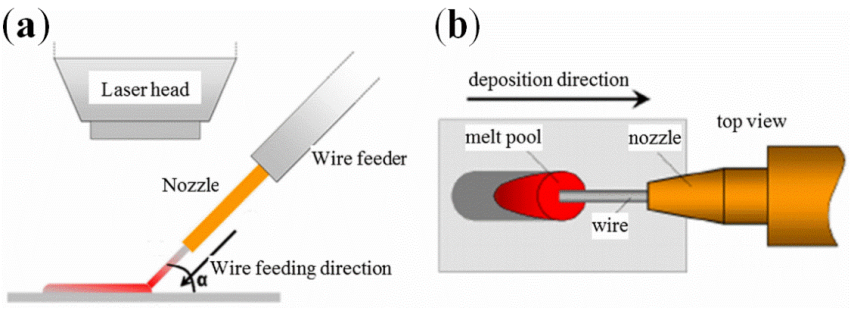


**Figure 10.** Schematic representation of WLAM process: side-view (a) and top-view (b) imagines of the wire-feed technology [117].

During the process, the laser fuses the substrate creating a melt pool where the automatic system feeds the metallic wire: the metal melts, solidifies and creates a metallurgical bond with the substrate. The coordinate motion of the laser and wire-feed systems permits to create a continuous laser track while the substrate movement in the horizontal plane allows to obtain the desired section of the final part [117]. During WLAM process, the part quality is highly influenced by the wire feed orientation (Figure 10), the wire feed rate, welding speed and dimension of the deposit: all these parameters are strongly related to the laser power value used [117].

Compared to powder-feed systems, WLAM process has a 100 % material capture efficiency, indeed the quantity of deposited material is exactly the amount of wire fed. Such effort reduces the amount of wasted material and energy in the process. Moreover, the deposition rate is considerably high, reaching 330 g/min in the case of stainless steel parts [117]. However, WLAM possesses limitations in producing complex, large and/or fully dense components [102]. Indeed, for complex geometries high accuracy and low porosity levels are difficult to achieve without any surface treatment, such as CNC machining. As a consequence the choice between adopting a powder-feed or wire-feed DED process depends on the parts geometry to be obtained [3]. An innovative approach based on join together powder and wire laser-based DED systems has been adopted and descripted by Syed et al. [119]. In their study they described how adopting both wire and powder feed during laser deposition process enhanced the deposition efficiency and reduced the surface roughness. The system developed was based on WLAM equipment with the addition of a self-made nozzle, used to feed the metal powder (316 L stainless steel) directly above the melting pool [119].

### 1.2.3.2 Electron Beam Freeform Fabrication

Developed by NASA, Electron Beam Freeform Fabrication ($EBF^3$) technology is able to process several metals and alloys and is generally employed to produce complex, near-net-shape components. The process is analogous to the WLAM one (Figure 11) a part from the use of high vacuum conditions ($10^{-4}$ bar or less). A focused electron beam creates a melt pool in the substrate where the wire feedstock is deposited. The use of an electron beam enables to effectively process a wide range of conductive materials such as steel and Ti alloys, including also aluminium and copper alloys which are difficult to process with laser systems due to the low absorptance [120]. Moreover, compared to laser-based AM systems, $EBF^3$ possess higher power efficiency (> 90 %), high coupling efficiency and reduced chemical contamination thanks to the vacuum processing conditions. Commonly, complex part are manufactured adopting thin metal wires, reaching high precision, while larger components are fabricated at high deposition rates using larger diameter wires (Figure 12). $EBF^3$ deposition rates can vary between 2 and 10 g/m, depending on the material and on the final product. Furthermore, recent upgraded $EBF^3$ systems are able to produce compositionally graded materials thank to dual wire feeder systems [102,121].

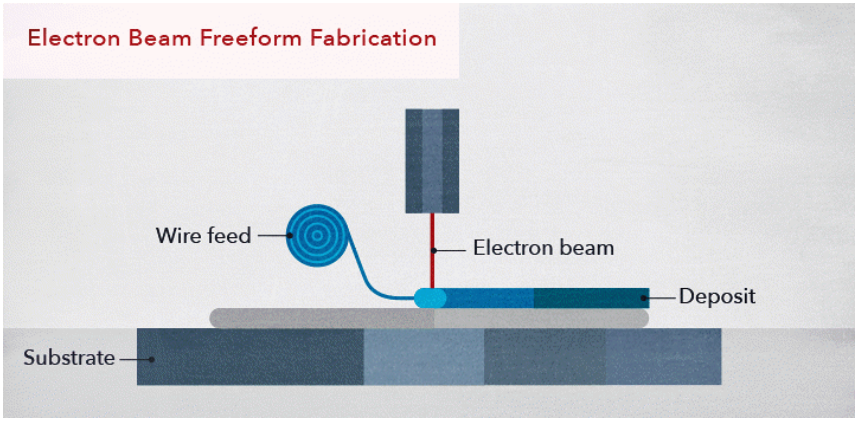


**Figure 11.** Schematic illustration of the Electron Beam Freeform Fabrication ($EBF^3$) process (*with the Courtesy of cerasis.com* [122]).

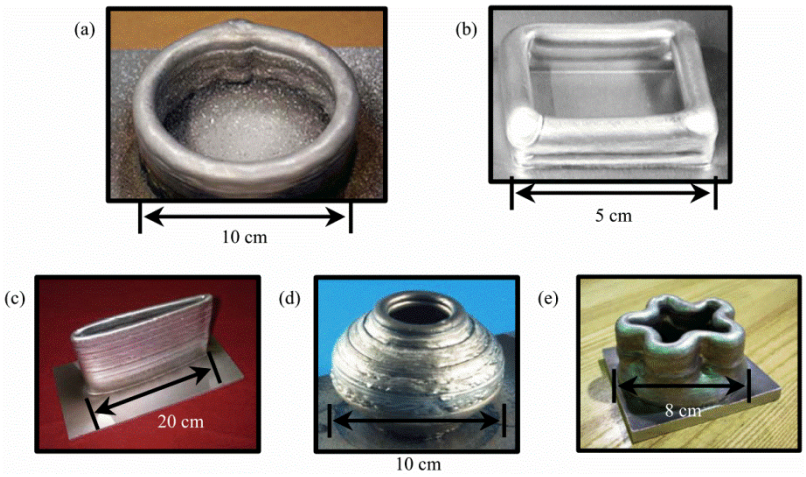


**Figure 12.** Aluminium components produced by EBF[3] with different process parameters: (a) high deposition rate, (b) different wire feed angle, (c) complex curvature, (d) overhanging structures and (e) different deposition strategies [121].

### 1.2.3.3 Wire and arc additive manufacturing

Wire And Arc Additive Manufacturing (WAAM) processes adopt an inert gas welding technique to fabricate near-net-shape metal components [117]. Developed by Rolls Royce, WAAM technology is mainly constituted by a robotic controller which coordinates the motion and welding process; industrially a laser profiler is also integrated in order to control the bead profile during welding [117].

The arc-based WAAM technology can employ either a Gas Metal Arc Welding (GMAW) or a Gas Tungsten Arc Welding (GTAW) or either a Plasma Arc Welding (PAW) systems, as resumed in Figure 13. While GMAW is based on an electric arc welding formed between a consumable wire electrode and the substrate, GTAW and PAW employ non-consumable electrodes to create the arc. In these last two technologies the wire feed angle varies, modifying the product surface quality and bead profile, increasing the difficulties related to the process standardisation. Instead, in the case of GMAW the wire feed is perpendicular to the workpiece and coaxial with the nozzle, simplifying the welding mechanism [117].

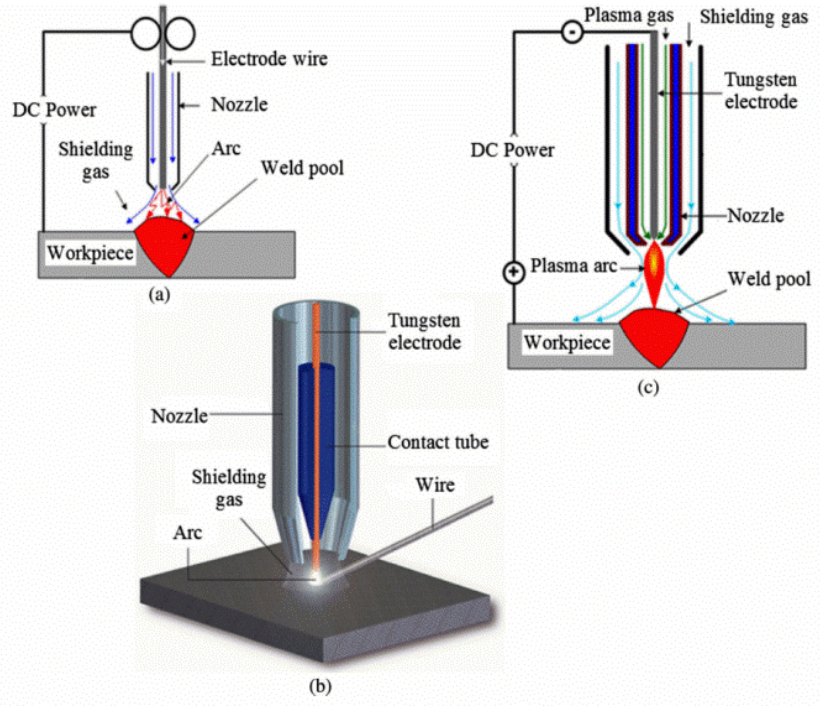


**Figure 13.** Schematic representation of the (a) GMAW, (b) GTAW and (c) PAW systems [117].

The majority of weldable alloys has been processed by WAAM, such as Ti alloys, steels and nickel alloys [102,124,125]. Thanks to high deposition rates (between 50 and 130 g/min), high material usage efficiency, lower costs and higher safety, WAAM has rapidly become competitive with laser and electron based deposition processes. However, WAAM commercial systems are still not widely spread in the manufacturing market, due to the presence of technical challenges: for example the high energy source used creates an excessive amount of residual stresses and distortions inside the final parts [126,127].

#### 1.2.3.4 Hybrid DED systems

Low geometrical accuracy in the final parts produced by DED systems remains a big limitation of these technologies. Such effort mainly depends on the splitting into slices of the part model and it is closely dependent on the chosen process. To overtake such issue, new hybrid systems have been proposed, joining together the benefits of both additive and subtracting technologies [128,129]. At the Indian Institute of Technology, Bombay, the first Hybrid-Layered Manufacturing (HLM) process has been developed: the hybrid process integrates a WAAM system and a

CNC milling process and has been employed to fabricate tools and dies as reported in Figure 14 [129].

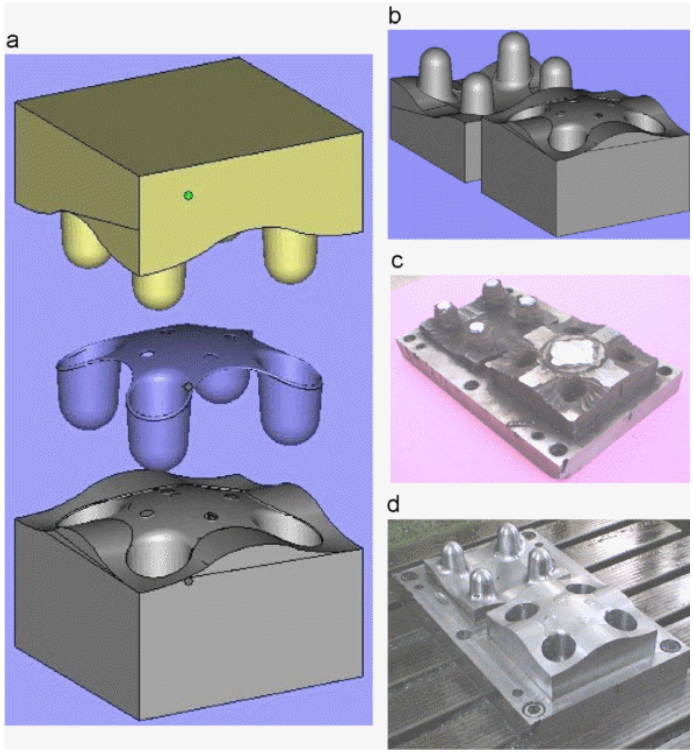


**Figure 14.** Injection molding dies created by HLM during the different phases of the process [128].

During the process, the GMAW system deposits the material and additively produces the final geometry of the product. The welding bead presents irregularities, elevated roughness and oxide layers: the integrated CNC milling mills the surface of the deposited layer providing a good weld surface quality. The process continues alternating deposition and milling steps until the final near-net-shape product has been fabricated [128,129]. Karunakaran et al. [130] compared the realisation of egg-template adopting an HLM process and a traditional CNC milling one: the case-study showed that the hybrid system allowed to reduce costs up to ~ 22 % and reduce production time up to ~ 38 %. These achievements were possible thanks to the time savings from elimination of roughing operations, machine programming and setting, and particularly to material saving [130,131].

## 1.2.4 Powder Bed Fusion Processes

Powder bed fusion (PBF) processes selectively melt metal powder adopting a focused energy source. These technologies represent the major part of the metal AM market owing to their application in several fields, particularly the aerospace and biomedical ones. The different PBF technologies principally differ for the energy source used to melt the powder; according to this, they are mainly divided in Laser Powder Bed Fusion (LPBF) and electron beam melting (EBM) processes [14,132].

### 1.2.4.1 Electron Beam Melting

Electron beam melting (EBM) process, developed and patented by Arcam AB Swedish company (recently acquired by General Electrics [133]), utilizes electron beam energy to melt metal powder bed: the hardware system is simplified in Figure 15. The electron beam is generated by the electron-gun (60 kV), sited in the upper part of the machine, and focused on the powder bed by an electromagnetic lenses system. Firstly, the electron beam preheats the powder bed to 80 % of melting temperature ($T_M$), adopting high scan rates (~ $10^4$ mm/s) and high beam current (~30 mA). Subsequently, the scan rate and current are lowered to $10^2$ mm/s and 5 – 10 mA, respectively, fully melting the metal powders according to the CAD model of the component. Once the scanning is completed, the building platform lowers down of one layer thickness: generally EBM works adopting layer thickness between 50 and 200 μm, depending on the material. Two hoppers provide the metal powder which is deposited by a rake upon the building platform: once the deposition step is completed, the process is repeated from the beginning. The powder is generally constituted by spherical particles, with an average size between 45 and 105 μm, obtained by gas atomisation. Like any electron beam system, EBM process works under vacuum conditions (about $1 \times 10^{-5}$ mbar), moreover during the electron scanning of the powder bed a partial pressure of He ($2 \times 10^{-3}$ mbar) is flown inside the process chamber avoiding any material chemical contamination. For such reasons EBM is suited for processing materials with a high affinity to oxygen such as titanium alloys.

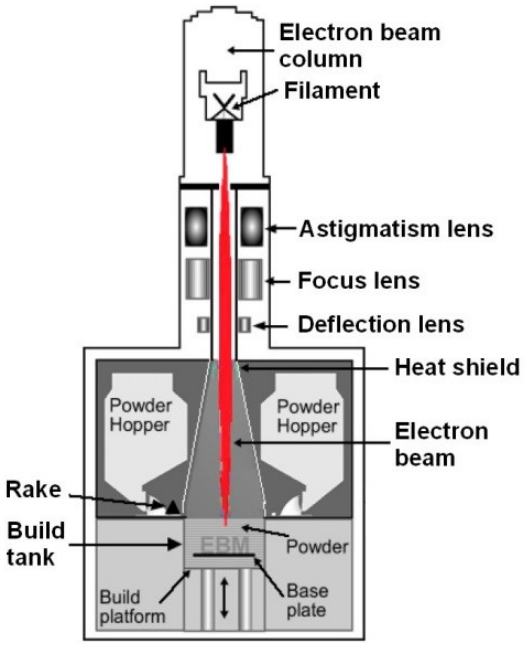


**Figure 15.** Schematic representation of EBM process [45].

Differently from other metal AM processes, EBM preheats the powder bed to high temperatures (e.g. ~ 750 °C for Ti alloys [134] or 400 °C for pure Cu [135]) in order to slightly sinter the metal powders and increase the electrical conductivity of the powder bed avoiding process instabilities [136]. Latter effects are the reduction of residual stresses inside the manufactured parts and the modification of microstructures. Indeed in EBM parts the amount of residual stresses is considerably lower and final microstructures appear coarsen compared to LPBF or DED parts. This is due to the lower thermal gradients and cooling rates that characterize EBM process; this effort reduces parts distortions and avoids post-processing annealing treatment of the part [137]. The main process parameters, principally related to the electron beam melting, define the amount of energy delivered and the strategy adopted to melt the powder bed: beam power, scanning velocity, distance between lines, scanning strategy, focus offset. In EBM melting is generated by the absorption of the electron beam by the powder bed: the kinetic energy of incident electrons is transferred to the powder particles, transformed into heat inducing the creation of melt pool [138]. When powders absorb electron kinetic energy they also gain increasingly negative charge with accidental detrimental effects such as “smoke” and beam diffusion ones [3]. In order to avoid high concentration of negative charges in the powder bed the scan strategies must be adjusted correctly: furthermore only conductive powders, like metal ones, can be

used with EBM. This is one major limitation of electron beam melting when it is compared to laser-based technologies [3].

EBM is characterised by elevated scanning speed (up to 8000 m/s [139]) and high layer thickness allowing elevated productivity rates compared to LPBF processes. Furthermore, vacuum operating conditions reduce the chemical contamination of the component in contrast with low oxygen content atmosphere used in LPBF. Together with the lower residual stresses amount, these advantages made EBM highly competitive in the AM market, even if the surface quality of the parts results inferior to LPBF one. Indeed, due to higher layer thickness values and bigger particles size used in EBM, final roughness varies between 25 and 35 μm, almost three times the LPBF one (~ 11 μm) [136]. Higher roughness values can reduce the fatigue resistance of the components, limiting the number of industrial applications, and may require post-processing surface modifications. Although, at the same time, studies carried on interactions between human body and prosthesis made by EBM demonstrated that cells adhesion upon such rough surfaces is highly favoured [140–142]. As a consequence, EBM has been largely adopted in the biomedical field, in particular in the orthopaedic market [143]: acetabular cups, knee, maxillofacial plates, hip, jaw replacements, etc. produced by EBM have been already certified since 2007 and approved for in-body applications since 2010 (United States Food and Drug Administration (FDA)) [144]. Since 2014, more than 40.000 acetabular cups have been produced and insert inside patients body [145] thanks to the EBM ability to produce cellular structures, with high regulation of pore size, strut diameter and cell geometry: some examples are shown in Figure 16.

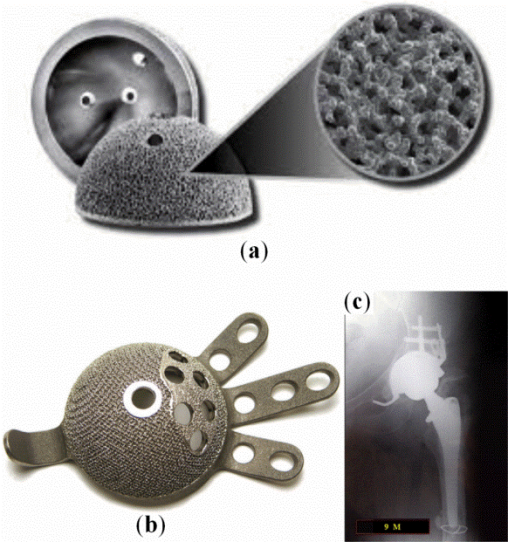


**Figure 16.** Examples of acetabular cups made by EBM process. (a) Ti-6Al-4V implant with surface roughness designed for better osseintegration (*Courtesy of Arcam* [146]). Orthopaedic applications of Trabecular Titanium$^{TM}$: (b) external trabecular structure with optimised surface cell structures, (c) radiological outcome of the acetabular cup after implantation [142].

Together with biomedical applications, EBM parts were particularly interesting for their exploitation in the aerospace field for reduced costs related to the "buy-to-fly" ratio (how many kg of material are purchased to produce 1 kg of final part) [147] and the possibility to fabricate parts in gamma-TiAl alloys [148–152]. In their case study, Dehoff et al. [147] described how adopting EBM process reduced the processing cost of a Ti-6Al-4V BALD bracket of about 50 % compared to traditional manufacturing: choosing EBM process permitted to reduce the buy-to-fly ratio from 33:1 to 1:1 thanks to ~100 % material efficiency of the AM process. Since its foundation, Arcam AB has commercialised over than seven commercial types of EBM machines and more than 150 systems have been installed all over the world [145].

#### 1.2.4.2 Laser Powder Bed Fusion

Laser Powder Bed Fusion (LPBF), or Laser Beam Melting (LBM), utilises a focused laser beam to selectively melt a layer of metal powder and to create three-dimensional parts. Generally the laser system is based on an Yb fiber laser, with power values up to 1 kW. The LPBF process begins with the deposition of a layer of powder over the building platform by a powder spreading system (widely named as recoater blade): the process is able to deposit a controlled amount of powder with

layer thickness variable between 20 and 60 μm. As soon as the powder has been spread, the laser system directs the focused beam on the powder bed, selectively melting the material, according to the CAD model of the part. Once the layer has been processed, the building platform lowers of one layer thickness and the process restarts from the deposition step. Layer by layer the part is fabricated and ready for the post-processing operations, which commonly involve the removal of the support structures and the heat treating of the parts. A schematic representation of the LPBF process is shown in Figure 17: a detailed description of the instrument, the parameters and physical phenomena involved in the process is given in the following chapter.

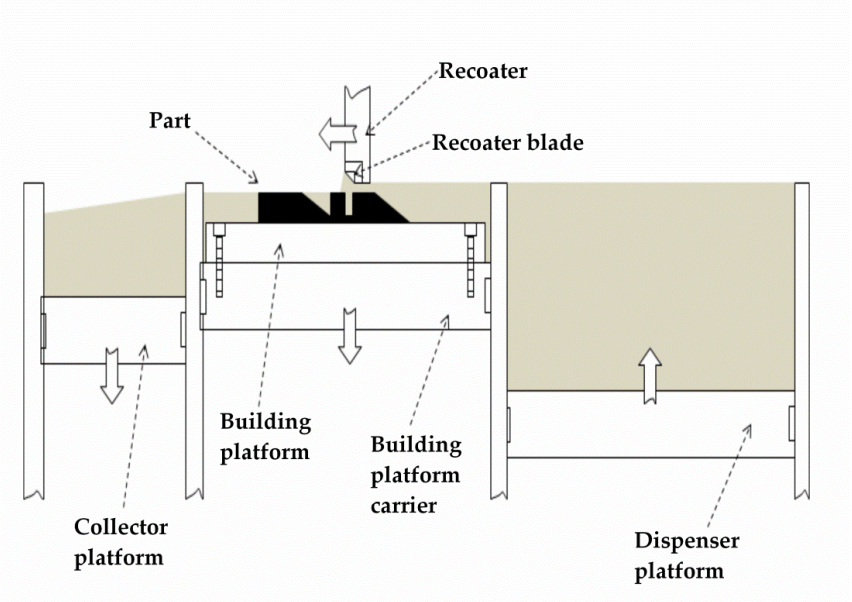


**Figure 17.** Schematic representation of LPBF process [153].

Nowadays several commercial systems are based on LPBF technology and mainly differ on the hardware systems involved, such as the laser system used or the dimensions of the machine. In Table 2 the principal LPBF systems available on the market are schematically listed: it must be noted that depending on the company the LPBF process is called with a different name. In order to avoid incomprehension in this thesis the process is referred as Laser Powder Bed Fusion, as stated in the ASTM standard F2792-12a [1].

**Table 2.** Main LPBF machines and producers available on the market nowadays

| Company | Process | Machine | Lasers | Building volume |
|---|---|---|---|---|
| **EOS GmbH** [154] | Direct Metal Laser Sintering (DMLS) | EOS M 100 | Yb fiber laser; 200 W | Ø 100x95 mm |
| | | EOS M280 | Yb-fiber laser, 200 or 400 W | 250x250x325 mm |
| | | EOS M290 | Yb fiber laser; 400 W | 250x250x325 mm |
| | | EOS M400 | Yb-fiber laser; 1 kW | 400x400x400 mm |
| **Concept Laser GmbH** [155] | LaserCUSING® | Mlab cusing | Fiber laser 100 W | 90x90x80 mm |
| | | Mlab cusing 200R | Fiber laser 200 W | 100x100x100 mm |
| | | M1 cusing | Fiber laser 200 or 400 W | 250x250x250 mm |
| | | M2 cusing / M2 cusing multilaser | Fiber laser 200 or 400 W / Multilaser version with two fiber laser 200 W | 250x250x280 mm |
| | | X Line 2000R | Two fiber laser 1 kW | 800x400x500 mm |
| **Renishaw** [156] | Laser Powder Bed Fusion (LPBF) | RenAM 500M | Yb fiber laser 500 W | 250×250×350 mm |
| | | AM 400 | Optical system 400 W | 250x250x300 mm |
| | | AM 250 | 200 or 400 W | 250x250x365 mm |

| | | | | |
|---|---|---|---|---|
| **Realizer** [157] | Selecting laser melting (SLM) | SLM 50 | Fiber laser 20 or 120 W | Ø 70x40 mm |
| | | SLM 125 | Fiber laser 100 or 400 W | 125x125x200 mm |
| | | SLM 300i | Fiber laser 400 or 1000 W | 300x300x300 mm |
| **Sisma Industry** [158] | Laser metal fusion (LMF) | mysint100 | Fiber laser 200W | Ø 100x100 mm |
| | | mysint300 | Fiber laser 500W | Ø 300x400 mm |
| **SLM Solutions GmbH** [159] | Selecting laser melting (SLM) | SLM 125 | IPG fiber laser 400 W | 125x125x125 mm |
| | | SLM 280 2.0 | Single configuration: IPG fiber laser 400 or 700 W<br>Twin configuration: two IPG fiber laser 400 or 700 W<br>Dual configuration: one IPG fiber laser 700 W and one IPG fiber laser 1000 W | 280x280x365 mm |
| | | SLM 500 | Twin configuration: two IPG fiber laser 400 or 700 W<br>Quad configuration: four IPG fiber laser 400 or 700 W | 500x280x365 mm |
| **Trumpf** [160] | Laser metal fusion (LMF) | TruPrint 1000 | Fiber laser 200 W | Ø 100x100 mm |
| | | TruPrint 3000 | Fiber laser 500 W | Ø 300x400 mm |

| | | | | |
|---|---|---|---|---|
| **3D Systems** [161] | Direct Metal Printing (DMP) | ProX DMP 100 | Fiber laser 50 W | 100x100x100 mm |
| | | ProX DMP 200 | Fiber laser 300 W | 140x140x125 mm |
| | | ProX DMP 300 | Fiber laser 500 W | 250x250x330 mm |
| | | ProX DMP 320 | Fiber laser 500 W | 275x275x420 mm |

LPBF process has been consistently used for aerospace and biomedical applications as already presented in chapter 1.1.3. From the specific point of view of LPBF process, the market situation is observing a considerable and constant grew in the machine sales all over the world. GE Aviation company has invested almost $3.5 billion setting new productions plants equipped with EOS M-280 printers in order to reach the production rate of 100,000 fuel nozzles by 2020 [162]. Moreover, in 2017 GE company acquired Concept Laser GmbH, expanding the headquartes, growing its employee base and support teams, in order to accelerate the evolution of LPBF process [163]: similarly DMG Mori company acquired the majority share in Realizer GmbH in February 2017 [164]. Another example can be the one of SLM Solutions Group AG which showed an increase in the machine sales of 85 % in the first half of 2016, attesting a total revenue of €33.5 million [165].

# Chapter 2

# Laser Powder Bed Fusion Process

Laser Powder Bed Fusion process (LPBF), also known as Selective Laser Melting (SLM) or Direct Metal Laser Sintering (DMLS), represents a complex and innovative manufacturing technique in the fabrication of metal components for industry. From a material engineering point of view, the studies on process and materials properties are crucial aims in the technology development. Indeed, the great industrial investment in LPBF motivates the interest in material properties and process optimisation in order to consolidate and expand the industrial LPBF adoption.

In the present chapter the principal process parameters and raw materials properties are presented and described, together with the main physical and metallurgical phenomena of LPBF process. Finally, microstructural and mechanical properties and effects of post-processing operations are described.

## 2.1 LPBF influent factors

The LPBF involves a great number of factors and variables able to influence the properties of the final parts. These factors can be grouped in the two main categories, related to powder properties and process parameters, as reported in Table 3 [153].

**Table 3.** Laser Powder Bed Fusion (LPBF) variables [153].

| Powder Properties | Process Parameters | |
|---|---|---|
| Particle shape | Laser power | Layer thickness |
| Particle size and distribution | Scanning speed | Scanning strategy |
| Chemical composition | Hatching distance | Building orientation |
| Thermal conductivity | Protective atmosphere | Gas flow |
| Melting temperature | Laser beam diameter | Bed temperature |
| Absorptivity/reflectivity | Laser type | - |

## 2.1.1 Powder Properties

Powder bed fusion processes such as Electron Beam Melting (EBM) or LPBF can be classified as powder metallurgy processes like sintering, Hot Isostatic Pressing (HIP) or Metal Injection Molding (MIM) ones. As a consequence, the final properties of the fabricated parts, such as density, surface roughness and chemical composition, strictly depend on the quality of the adopted powder. Determining the properties of the used feedstock is a necessary requirement: improved confidence in powder selection allows to produce reproducible components with known and predictable properties, as described in the ASTM standard F3049-14 [71].

### 2.1.1.1 Principal powder production methods

Among the many methods developed in powder metallurgy for the production of powder, AM processes generally adopt metallic powder produced by water, gas and plasma atomisation [166].

Atomisation processes are based on the disintegration of melt metal into small droplets which rapidly solidify by the use of high pressured gas or water: the main differences between these processes depends on the atomisation medium and on the physical state of the feedstock material as schematically represented in Figure 18.

The choice of the specific atomisation medium depends on the material to be processed. Air and water atomisation are commonly chosen for the production of steel powders, assuring high production rates and low costs although the powders contains a large amount of oxides derived by oxygen presence in the atomisation medium. On the other hand, inert gas atomisation is generally adopted for the

production of high-purity powders of special steels, like, stainless steels, and of super-alloys, aluminium alloys, titanium alloys. Indeed using a high purity inert gas such as $N_2$ or Ar can help in reducing the amount of oxygen inside the powders to values of 100 ppm [167]. Both gas and water atomisation processes start with melting the feedstock alloy which is free to fall inside the atomisation chamber through a nozzle. Together with the molten metal the atomisation medium is symmetrically introduced around the steam of liquid metal causing the atomisation and solidification phenomena (Figure 18a,b) [166].

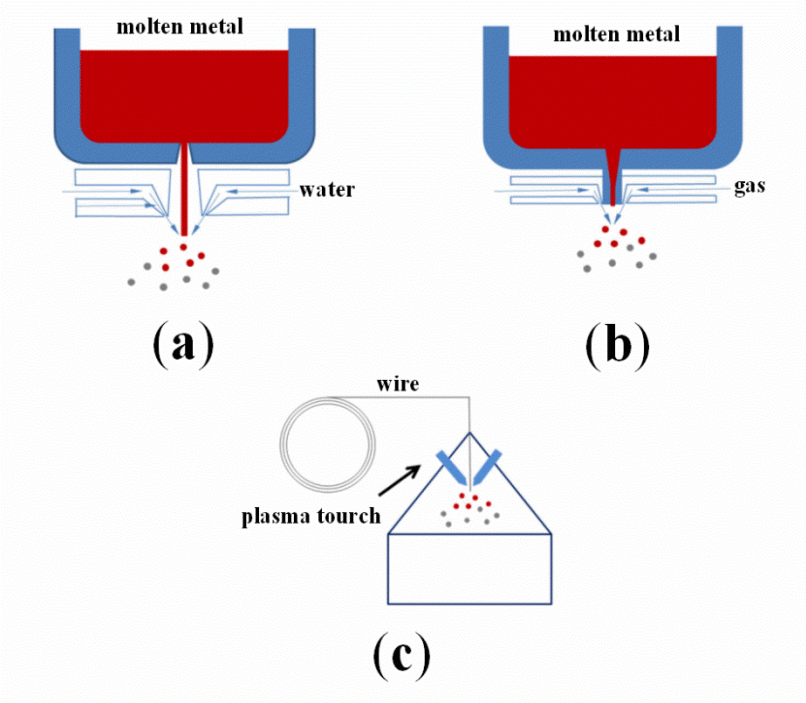


**Figure 18.** Schematic representation of principal powder atomisation processes: (a) water atomisation, (b) gas atomisation and (c) plasma atomisation [168].

Differently from gas and water atomisation methods, plasma atomisation utilises plasma torch to produce a high velocity jet of extremely hot ionized inert gas to melt and rapidly solidify the material. Furthermore, instead of molten feedstock alloy, in plasma atomisation a pre-alloyed wire is fed inside the atomisation process chamber. Adopting such strategy permits to produce high-purity material since the liquid metal does not contact any solid surface before solidification, strongly reducing the contamination risks [168].

#### 2.1.1.2 Particle shape

During LPBF the powders must be able to flown easily upon the building platform, covering the entire processing area homogeneously. Indeed, to prevent formation of defects inside the parts, the layer of powder must be continuous and must possess constant thickness upon the building platform: areas with lower or higher amount of metallic particles could be sites of excessive or insufficient melting and could favour the creation of pores or cracks or even delamination effects [166]. At the same time, the powder bed must possess the highest stacking density (also known as “packing density” or “tap density”) avoiding the presence of voids which could promote the formations of defects inside the final part.

The shape of the particles directly influences the movement and the stacking of the powder in the powder bed. Commonly spherical powders are preferred among irregular shaped particles due to their higher stacking density and flowability. Flowability describes the ability of a powder to flow freely in a regular and a constant way [169]. Apart from stacking density and particles shape, flowability depends also on particle size, granulometric distribution, oxides and moisture presence [169–171]. So, a powder with good flowability can be moved without assistance, while granular materials with low flowability (such flakes, dendritic or irregular shaped particles) require the employment of mechanical devices such as vibrators or agitators.

An example of metallic powders for LPBF process are illustrated in Figure 19a,b. Gas and plasma atomised powders are generally preferred to water atomized ones due the very good sphericity and higher chemical composition purity. Gas atomized powders represent the bigger section of the market since the higher number of producers and lower costs compared to plasma atomized powders. On the opposite, water atomisation process enables to produce metal powders in a more productive and cheap way, but the particles possess irregular shapes (Figure 19c). The lower packing density and flowability of irregular shaped powders have prevented their adoption in the powder bed processes.

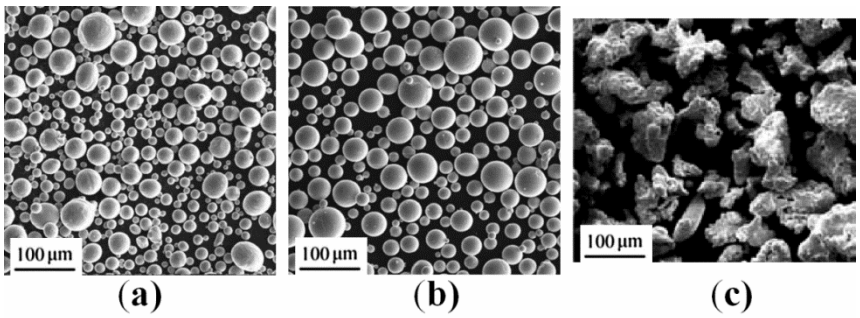


**Figure 19.** Examples of metallic powders produced by different atomisation methods: (a) and (b) Ti-6Al-4V powders made by gas atomisation and plasma atomisation methods, respectively [168]; (c) H13 tool steel particles made by water atomisation technique [172].

#### 2.1.1.3 Particle size and distribution

Particles size and particle size distribution represent two fundamental properties for the selection of metallic powders for LPBF due to their great influence on flowability and stacking density of the powder bed and even on mechanical properties of the final components [166,173–175]. Furthermore, the mean size of gas atomised powder depends also on the layer thickness adopted during LPBF process, and consequently on the production rate. The most common value adopted for the layer thickness is 30 µm: as a consequence gas atomised powders for LPBF machines usually possess a mean size comprised between 15 and 45 µm. Commonly the powder bed must possess a certain amount of fine particles to fill the voids between the larger ones. In this way it is possible to increase the stacking density and optimise other materials properties such as surface quality and mechanical strength [173].

Due to the higher surface area, smaller particles can be easily melted by the laser beam, improving the melting behaviour of the powder bed and increasing the densification of the parts. At the same time, the finer is the particle size, the lower appears to be the flowability [175]: larger surface areas increase the amount of adhesive interparticular forces, which negatively affect the motion of the metal particles and consequently the flowability of the entire powder bed [166]. On the opposite side, the larger particles possess less interparticular interactions, leading to higher flowability, and are beneficial for higher breaking elongations, as demonstrated by Spierings et al. [173]. The graphs in Figure 20a,b report some examples of powder size distribution curves. Generally, particle distribution is described by the three diameter values $D_{10}$, $D_{50}$ and $D_{90}$, respectively, which

indicate the diameter corresponding to the 10, 50 and 90 % of the total particles population. These values can be easily obtained from the investigation of a granulometry curve, as the one shown in Figure 20c.

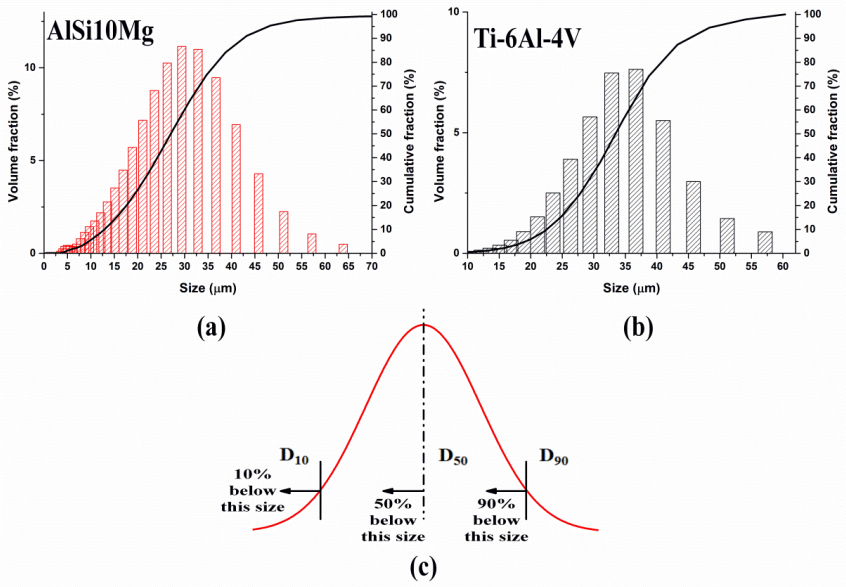


**Figure 20.** Examples of particles size distribution: volume and cumulative fractions of AlSi10Mg alloy (a) and Ti-6Al-4V alloy (b) gas atomised metal powders (from the author's own unpublished work); (c) scheme of a granulometry curve and $D_{10}$, $D_{50}$, $D_{90}$ diameters (*Courtesy of Horiba.com*).

Many industrial methods can be adopted to monitor the powder size distribution such as the sieving technique, laser light diffraction, gravitational sedimentation, optical and electron microscopy followed by image analysis [166,175–177]. Sieving consists in shaking the powder through a stacked series of sieves with decreasing mesh sizes. Gravitation sedimentation uses X-ray absorption or light scattering to determine the particle concentration at different heights within a monitored container of liquid at different times. Microscopy-based techniques use optical light microscopes, scanning electron microscopes (SEM) to visually discern size information. Laser light diffraction involves deconvolving and inverting the summation of the scattered light pattern produced by each sampled particle. This last technique has been particularly adopted in LPBF studies and researches [178–180].

Generally the flowability of powder has been investigated by standardised methods based on the Hall [181] and Curvey [182] funnels, but such techniques have turned out not to be applicable in the case of metal powders for LPBF process

[180]. Recently, an innovative method has been developed to characterise and compare the powder flowability, the Revolution Powder Analyzer (RPA) [45]. This technique allows to measure the flowability and packing behaviour by determining the avalanche behaviour of the powder: for further description of this method refer to specified literature [180,183].

#### 2.1.1.4 Chemical composition

Because of their high surface area, micrometric metal powders are strongly susceptible to intense oxidation phenomena. Gas atomisation uses inert gases such as argon or nitrogen to cool the melt metal and obtain spherical powders avoiding oxygen contaminations. In the case of aluminium and titanium alloys the high affinity of the metal with oxygen greatly increases the risks of oxidation and even explosion during atomisation. As a consequence the process atmosphere must be frequently check and monitored and a considerable amount of Ar is consumed. For these reasons the cost related to Al and Ti gas atomized powders can reach ten times the values of the cast ingot or three-four times the value of steel gas atomised powders. Thus in this last case the atomisation medium employed is nitrogen gas and the relative costs are much lower than argon. Once produced metal powders are usually stored in inert gas filled bags or vacuum containers in order to prevent any further oxidation or humidity contamination. Indeed it has been established that the presence of oxide layers and moisture in the powder bed greatly affect the flowability and defects generation in the final piece [175].

Oxide layers are commonly present upon particle surface, particularly in the case of Al or Ti alloys due to their high affinity with oxygen. These could be considered as thin ceramic layers that alter the absorption of radiation during LPBF and modify the melting behaviour of the melt pool during the process. Moreover, oxygen can be transferred inside the alloy and alter the phase composition of the metal system, as in the case of titanium alloys [184–188]. The oxide layers are generally disrupted by the laser beam, thanks to the high laser power, but in some cases the ceramic materials are incorporated inside the melt pool: this feature leads to the creation of inner defects inside the metal part which highly influence the mechanical and fatigue properties [189,190].

Moisture and humidity favour the formation of hydrogen bonds upon the particle surface, creating chemical interactions between single particles and reducing sliding motion and flowability. Furthermore, as demonstrated by Weingarten et al. [191], hydrogen presence upon particles surface could leads to

the creation of gas entrapped porosities inside the final components, especially for Al or Ti based alloys. This type of porosity can be avoided modifying the melting behaviour of the melt pool during LPBF, favouring the degasification of the melt, or by pre-drying the powders. Li et al. [192] performed a drying treatment on Al-12Si powders at 100 °C for 1 h and compared the densification behaviour during LPBF with the same powder not-treated. Adopting X-ray Photoelectron Spectroscopy (XPS) analysis, the presence of Al metal and carbonated hydroxide ($Al–O–CH_xO$) was detected in the case of the not dried powders. Drying treatment removes the moisture ($H_2O$) from particles surface and promotes the decrease of $Al–O–CH_xO$ amount and the increase of Al one. From density analysis it appeared that the densification increased considerably (>99 % dense parts) using dried powders instead of as-received ones. Thus by removing moisture presence the formation of Al oxides and hydroxides during LPBF was prevented and final parts porosity was reduced, demonstrating the effectiveness of powder pre-drying treatment [193,194].

## 2.1.2 LPBF Process Parameters

In a simply description LPBF process involves the absorption of a laser beam energy by the metal powder causing the melting of the material. LPBF machines include several parameters, proper of the laser source and of the building chamber, which singularly and in a combined way affect the melting behaviour and the final quality of the fabricated part. The effects of the process parameters on the densification and material final properties are described in Chapter 3 Chapter 4 while in this section a brief description of the single parameters involved is given.

### 2.1.2.1 Laser type and laser power

Typically LPBF machines use fiber laser based on Nd:YAG or Yb:YAG systems, with laser power up to 1 kW, as listed in Table 2. In the previous versions of the industrial machines, a $CO_2$ laser system was commonly employed instead. The difference between these laser equipment depends on the laser wavelength produced, almost 1 μm for the fiber lasers and 10 μm for the $CO_2$ ones, respectively [195]. Varying the laser wavelength modifies the absorptivity of the powder bed and consequently the amount of energy delivered for melting [114,195]. Aluminium or copper absorptivities to YAG lasers are considerably low compared to titanium or steels, which possess values comprised between 40 and 47 % [196]. In fact, in the aluminium case absorptivity reaches almost 9 % [190,196]. Copper powder bed presents a mean absorptivity of 0.59 % when irradiated by 1 μm

wavelength laser beam. For laser beams with higher wavelength than 1 μm, the absorptivity is even lower: at 10 μm, the mean absorptance of copper powder is just 0.26 % [114,197]. On the other way, when laser wavelength is reduced to smaller values, copper absorptance considerably increases: at 0.5 μm wavelength, it reaches values close to 40 % [198]. Considering the low absorptivity of some materials full densification can be achieved providing higher power values: varying the laser power has direct effects on the melting behaviour and strongly interacts with the scanning speed and hatching distance parameters. Older machines were equipped with laser system between 100 and 200 W while nowadays the machine producers are providing facilities with laser power of 400 W and either up to 1 kW (Table 2): in such way the productivity of LPBF has been improved and more alloy systems have been able to be processed.

#### 2.1.2.2 Scanning speed

Scanning speed parameter describes the laser scan velocity at which the laser spot moves over the powder bed. Scanning speed values can vary between 50 and 5000 mm/s, depending on the LPBF equipment adopted. Obviously this parameter influences the time of exposition of the powder bed to the laser beam and consequently the melting behaviour. Too high scanning speed values can limit the amount of absorbed energy and deal to an incomplete melting of the material, while on the opposite low velocities can provoke melt pool instability [199,200]. The incomplete melting of the material causes the formation of keyhole pores inside the final parts (Figure 21a) while melt pool instabilities favour the gas entrapment within the melt pool and the creation of metallurgical pores (Figure 21b) [196,201].

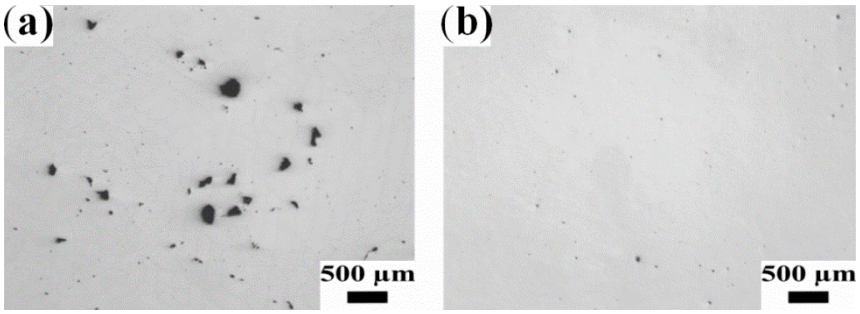


**Figure 21.** Examples of LPBF parts porosity: (a) keyhole porosities and (b) metallurgical pores [201].

Scanning speed effects on melting behaviour are generally considered together with laser power, as described later. However, laser scan velocity is obviously related to productivity: ignoring other process parameters variation (such as

hatching distance), doubling the scanning speed will approximately halve the build time of the powder layer.

#### 2.1.2.3 Laser beam diameter

Laser beam diameter, or spot size, defines the surface area directly subjected to the laser beam: in YAG laser systems its' value is typically around 100 μm but can vary between 70 and 150 μm. The spot size is strongly related to the minimum resolution achievable during LPBF process, such as the minimum wall thickness [3]. Indeed, in conjunction with laser power, scanning speed and hatching distance, it defines the melt pool size. Typically LPBF laser beam intensity possesses a Gaussian distribution so the exposed area that effectively melts is primarily at the centre of the laser beam [202,203]: the beam intensity decreases radially getting away from the centre, so it is important to define the correct dimension of the laser spot and the curing zone [204].

Increasing the laser power will increase the energy density of the outer region of the laser beam, allowing to scan a wider area of the powder bed, but at the same time will enlarge the energy intensity at the centre of the melt track: this high energy density at the centre can provoke melt instability and evaporation phenomena [202]. Furthermore the difference between the laser spot area and the effective scanned surface creates a dimensional error in the geometry accuracy at the part contour (Figure 22). Thus the position of the laser beam is commonly corrected and shifted by half of the width of the contour to the inside, making the part contour corresponding exactly to the CAD model: such variation is called beam offset and varies depending on the used machine, the chosen material and the adopted laser system [204–206].

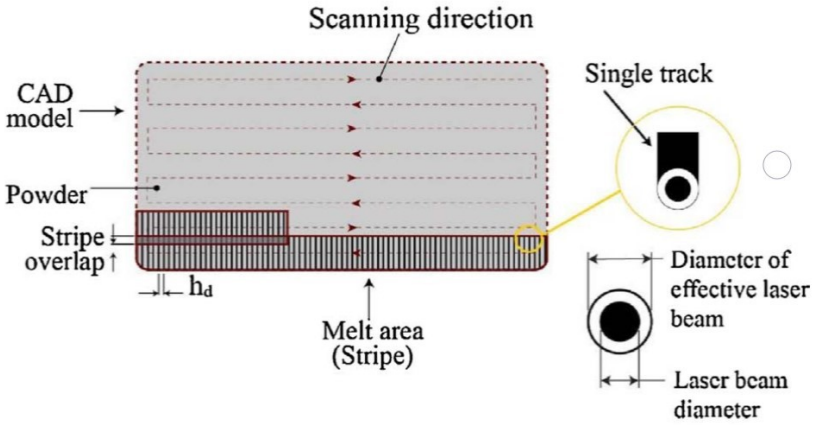

**Figure 22.** Schematic representation of effective laser beam diameter and laser hatching scheme: $h_d$ represents the distance between two consecutive hatch lines, also known as "hatching distance" [206].

#### 2.1.2.4 Hatching distance

The distance between two consecutive scan lines is defined as hatching distance (Figure 22): commonly it is set at about a quarter at the diameter of the laser beam. This parameter regulates the melting of the powder bed and particularly the overlapping between the scanned areas. Indeed to improve the densification of the materials the cured zone of the laser track (caused by the Gaussian distribution of the laser beam) are overlapped: the grade of overlapping depends on the energy provided (laser power, scanning speed, radius beam etc.) and on the material processed. For these reasons hatching distance represents a focal parameter to be optimized for production: Figure 23 shows the effects of different hatching distance values on the materials processing [207]. Furthermore it regulates the productivity rate of LPBF process. High hatching distance values provide less time to scan the powder layer while narrow hatching distances deal to an higher number of laser scans.

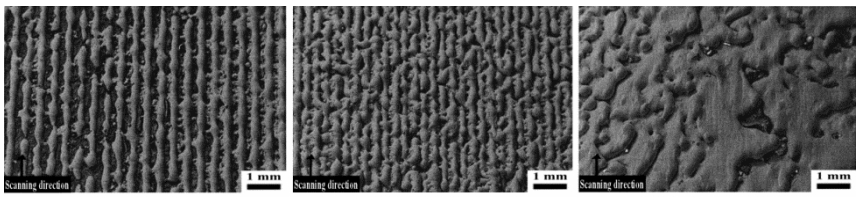


**Figure 23.** Effects on material processing adopting decreasing hatching distance values: (a) 0.4 mm, (b) 0.3 mm and (c) 0.1 mm [207].

#### 2.1.2.5 Layer thickness

This parameter represents the thickness of the single slice of the CAD model and of the layer of powder deposited on the building platform. It directly affects the build time, surface finish and the consolidation behaviour of the material: an increase in layer thickness deals to a higher production speed and a lower surface finish. Regarding the consolidation behaviour, excessive layer thickness values can determine defects generation between consecutive layers and delamination. Indeed, with too large amount of powder to process, the energy provided by the laser could not be enough to melt the entire layer, leaving un-melted particles entrapped in the material, pores and cracks. Decreasing the layer thickness favours the densification,

thanks also to the remelting of previous layers, and moreover means lower shrinkage increasing the dimensional accuracy and surface smoothness. On the opposite the productivity rate decreases considerably, requiring more times and layers to fabricate the final component.

The choice of layer thickness does not only depend on the material processed but also on the geometry of the final product. For instance, with curved objects, the "staircase effect" happens: this error is related to the difference between the rectangular nature of the powder layer and the digital geometry of the curved surface (Figure 24). In order to minimise such effect, which alters the accuracy of the final part, thinner layer and smaller particles should be adopted.

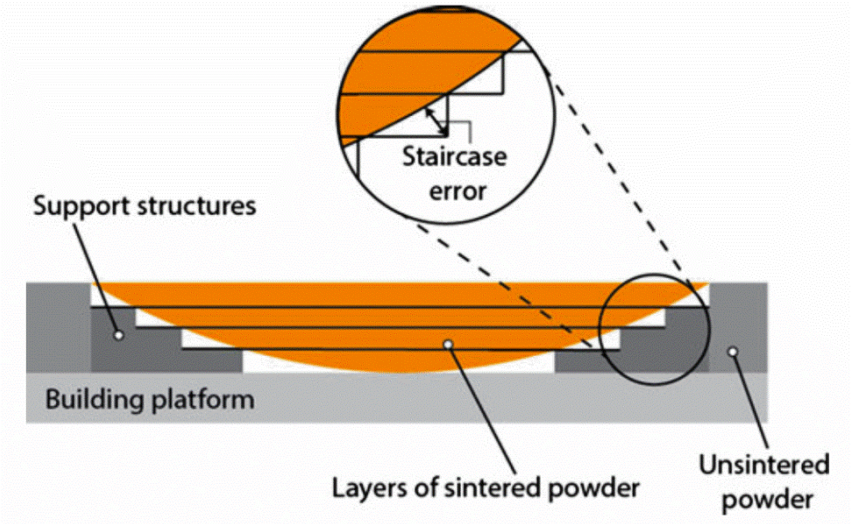


**Figure 24.** LPBF process and staircase effect error [208].

### 2.1.2.6 Energy density

As previously described, in the LPBF process, a laser beam focused onto the powder bed transfers heat energy and melts the material. In an attempt to define the correct quantity of energy to be transferred to powder bed, Simchi et al. [193] investigated the combinations of parameters which directly control the energy input during LPBF. Considering the materials properties as constant, the energy input transferred to the material is related to the laser irradiation-material interaction period and consequently to the number and duration of laser exposures. The process parameters that directly affect the energy input are: laser power (P), scanning speed (v), scan line spacing or hatching distance (h), and layer thickness (t). In order to

investigate the synergic effect of these parameters the energy density factor ψ [109] was defined according to

$$\psi = \frac{P}{v\ x\ h\ x\ t} \qquad \left[\frac{W}{J^3}\right]$$

Several authors adopted this equation to investigate the effects of different energy densities on LPBF parts [209–211]. For instance, Meier et al. [211] studied the processing of 316 L stainless steel powders selecting numerous combination of process parameters. From the results they established that the higher density and the lower surface roughness for those specimens built with energy density between 40 and 90 J/mm$^3$. Instead in the case of specimens fabricated with higher energy density values, melt pool instabilities and balling phenomena were detected. Balling can be described as the sphereodisation of the liquid melt pool during laser-material interaction [212,213], interrupting the melt layer where is not indicated by CAD.

On the other hand, considering that many commercial LPBF systems maintain the layer thickness values fixed, other authors [196,205,214] did not take into account for the process parameter optimisation, applying a surface energy density approach. Olakanmi et al. [215], for example, investigated the processing map for Al, Al-Mg, and Al-Si powders studying the correlation between powder bed behaviour and energy input delivered during LPBF. To do this, laser power varied between 20 and 240 W, scanning speed between 20 and 250 mm/s while hatching distance was kept fixed at 0.1 mm. From the results, the densification behaviour map was described to be composed by four regions, summarized as follows:

- "No marking" region. At lower energy densities than 3.2 J/mm$^2$ metal particles did not appear to be continuously connected.

- "Partial marking" region. Between 3.3 and 10 J/mm$^2$ the material was characterised by an agglomerate network of densified material containing a considerable quantity of small, open and deep porosities. The incomplete melting can be related to the low amount of energy input which was not able to produce enough liquid phase to fill the voids between particles and to close porosities.

- "Good consolidation" region. Dense material was obtained using energy densities between 12 and 30 J/mm$^2$, reaching density values from 60 to 80 %. Higher energy densities increased powder bed temperature and melt

pool stability. Melt material presented lower viscosity facilitating porosities infiltration and enhancing densification.

- "Excessive balling" region. Balling phenomenon occurred due to the excess of energy input. Energy densities above 30 J/mm$^2$ promoted the formation of excessive liquid phase and the instability of melt pool, which generated balling.

Other several studies on LPBF did not considered hatching distance in the energy density calculation and investigated the processing map in terms of linear energy density [203,213,216–219]. Yadroitsev et al. [203] investigated the combined effects of laser power and scanning speed on melting behaviour of single laser tracks for 316 L stainless steel, tool steel H13, copper alloy CuNi10, and superalloy Inconel 625. The starting assumption was that fabricated parts properties were mainly dependent on each single laser track and each single layer. From the results appeared that for each material the stability zone of the processing map was characterised by continuous track while the instability zone appeared for low scanning speeds. The range of the optimal scanning speed is larger for higher laser power, and it narrows for high thermal conductivity materials.

#### 2.1.2.7 Scanning strategy

Scanning strategy represents the geometrical pattern of the laser tracks during LPBF: in Figure 25 some examples of the possible scanning strategies are resumed [220]. The first image, Figure 25a, describes an "island strategy" where the entire scanning domain is partitioned into several areas with a fixed size. Inside each island the laser beam scans the powder bed following the set laser parameters such as laser power, scanning speed and hatching distance, rotating the laser track direction respect to the previous layer. Differently from the "island strategy", the entire scanning domain can be processed adopting continuous line scanning: the direction of the laser tracks can be maintained fixed between each powder layer (Figure 25b,c) or can vary following a certain angle (Figure 25d-f). Adopting a certain scanning strategy produces different thermal gradients and temperature fields [139] and consequently influences also material densification, microstructure and residual stresses inside the material [196,221–223]. Indeed a correct overlapping between consequent laser tracks consents to remelt the consolidated material, reducing inner porosity, improving intra layer adhesion, increasing material temperature and so reducing thermal residual stresses. The rotated scanning strategies allow to reduce the amount of porosity and residual stresses

inside final parts compared to unidirectional scanning strategies, due to the better laser tracks overlapping between consequent layers [139,224,225].

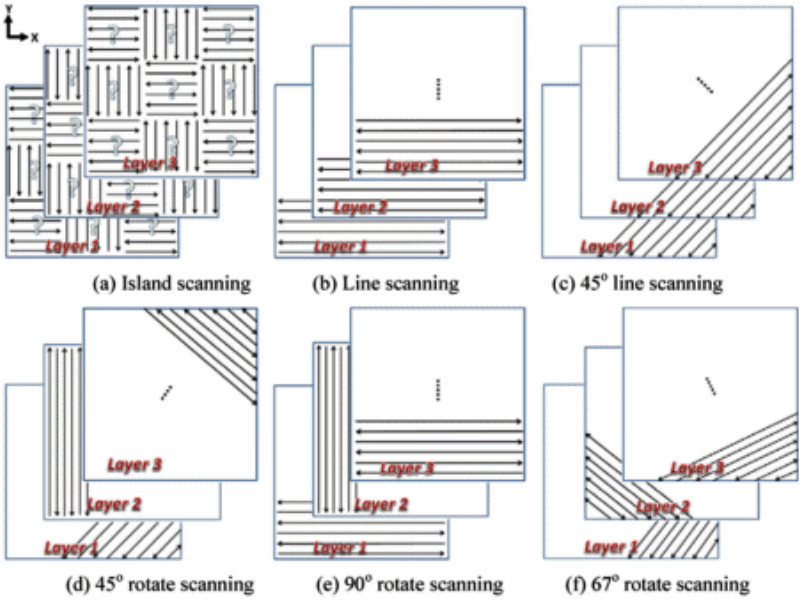


**Figure 25.** Examples of scanning strategies in LPBF technology [220].

Also the final mechanical properties of the LPBF parts vary according to the scanning strategy adopted. Guan et al. [226] investigated the influence of the hatch angle, which corresponds to the rotation angle between consequent layers, among the tensile properties of 304 stainless steel parts made by LPBF. Varying the hatching angle over 90°, 105°, 120°, 135° and 150° it was found that the best yield and ultimate tensile strengths were measured for specimens build adopting 105° hatching angle, due to the reduction of residual stresses and anisotropy. Cheng et al. [220] explored a 3D sequentially-coupled finite element (FE) model to study the thermomechanical responses in the LPBF process, simulating part temperature, residual stresses and deformation evolution applying different scanning strategies. It was observed that the best processing conditions were obtained with 45° line scanning strategy. Indeed the accumulation and amount of residual stresses were considerably lower compared to other scanning strategies investigated. Similarly, Lu et al. [227] studied the island size effect on the residual stress of Inconel 718 components processed by LPBF. From the results appeared that a 5 × 5 $mm^2$ island size allowed to reduce the amount of residual stresses compared to 7 × 7 $mm^2$ or 3 × 3 $mm^2$ island sizes. Such effort was related to the different heat accumulation provoked by varying the island size. Thus it was believed that the different island

dimension can affect the thermal distribution in the powder bed, influencing the heating and cooling rates in the material. It was established that increasing the island size induced prolonged heating of the powder bed and less effective energy transfer from the laser source to the metal particles. Instead smaller islands, with shorter scanning vectors, produced larger temperature gradients due to the higher residue heat of the previous scan pass. Su et al. [223] analysed the effects of three different types of track overlapping regimes (intra-layer, inter-layer and mixed overlapping regimes) on relative density and processing efficiency of 316L parts fabricated by LPBF (Figure 26). The highest density was measured with inter-layer overlapping regime (Figure 26b) which was obtained adopting track space lower than 0.2 mm.

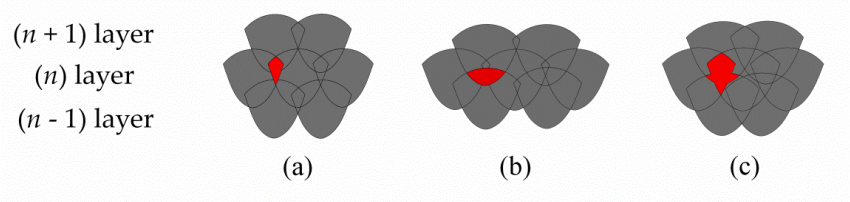


**Figure 26.** Three types of overlapping regimes under inter-layer stagger scanning strategy: (a) intra-layer; (b) inter-layer; and (c) mixed overlapping regime [153].

#### 2.1.2.8 Building orientation

The building orientation of the parts during the LPBF process highly influences the microstructure, hardness values and mechanical properties of the final parts. The orientation of the component, exposed in Figure 27, affects the microstructural evolution of the part and creates anisotropy and defects inside the material [209,210,228,229] and even influences the surface roughness [230]. Yadroitsev et al. [229] investigated the relation between tensile properties of LPBF Inconel 625 specimens and building orientation. The vertical specimens showed a lower elastic modulus than the horizontal ones probably due to a higher number of defects, generated by a higher amount of residual stresses, as also observed in other researches [231].

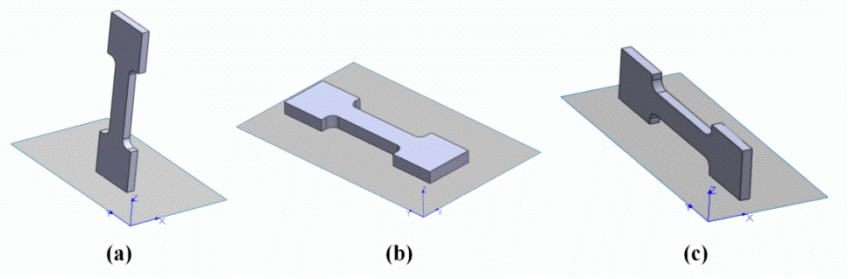


**Figure 27.** Examples of building orientations in LPBF technology: main direction parallel to the *xz*-plane (a), to the *xy*-plane (b) to the *zx*-plane (c). The z axis distinguishes the building direction, while the x and y axes recognize the building platform plane [153].

Although, the anisotropic response of the material during tensile loading can be related to the microstructural anisotropy caused by the local heat flow which is can be controlled by means of the scanning strategy [228]. Chlebus et al. [232] investigated the tensile properties and fracture behaviour of Inconel 718 LPBF specimens built with different orientation. The different orientation of columnar grains, which depends on the building orientation adopted during the process, affected the mechanical response of the specimens in relation to the direction of loading: in particular vertical specimens showed the lowest tensile strength compared to other specimens. Shifeng et al. [233] investigated the correlation between melt pool boundaries (MPBs) and tensile properties of 316L stainless steel LPBF parts, fabricated with different building orientations. Two different MPB types were determined in the as-built microstructure (Figure 28): layer-layer" MPBs and "track-track" MPBs, generated by multi-layer and multi-track melt pool overlapping during LPBF, respectively. From tensile tests appeared that horizontal specimens, built parallel to *xy* plane (Figure 27b), possessed higher tensile strength and lower ductility compared to vertical samples build z axis (Figure 27a).

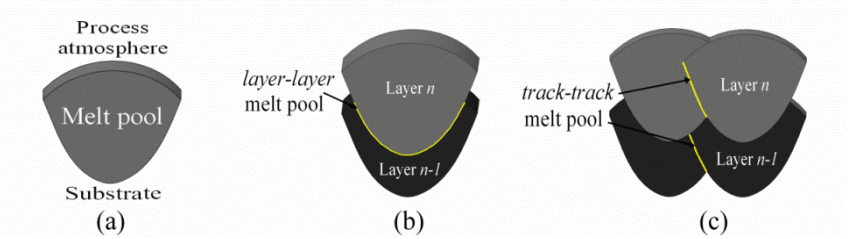


**Figure 28.** Representative scheme of different types of molten pool boundaries (MPBs): (a) single MPB; (b) "layer-layer" MPB; and (c) "track-track" MPB [153].

The higher ductility could be explained by the fact that vertical samples possess a larger number of slipping surfaces compared to horizontal specimens. Indeed,

when vertically fabricated samples were tested, slipping occurred along both layer-layer" and "track-track" MPB surfaces, while in the case of horizontally built specimens, it only occurred along the "track-track" surfaces (Figure 28).

#### 2.1.2.9 Protective atmosphere

The process atmosphere during LPBF is another factor which closely influences the amount and type of defects inside the material and consequently the mechanical properties of the parts [189,194,234–237]. Fine metal powders are very susceptible to oxidation due to their high surface area, and even low amount of $O_2$ can favour the creation of oxide layers on particles surfaces. Such oxide layers alter the melt pool stability during LPBF promoting balling phenomena [189]. Wang et al. [234] studied the influence of three different inert atmospheres, adopting high purity argon (Ar), nitrogen ($N_2$), and helium (He), on porosity and mechanical properties of Al-Si12 alloy LPBF parts. From the results appeared that adopting Ar or $N_2$ gases did not have appreciable effects on the material densification, while in the case of He a slight difference was measured: high porosity regions, composed of 50 μm diameter pores, were detected in isolated areas of the fabricated samples. The sizes of such areas did not influenced the density analysis but did influence the specimens ductility. Comparable results were obtained by Zhang et al. [238], who studied how these three different protective atmospheres and hydrogen ($H_2$), which acts as a deoxidizer gas, mixed in different modes, influenced densification of 316L parts. From density measurements appeared that neither Ar or $N_2$ affected porosity formation when used in pure form, while on the other hand the He or $H_2$ addiction increased the pores amount by more than 10 %. The explanation of such results was related to the different plasma conditions created adopting different gasses. Indeed modifying the gas in the process chamber alters the plasma location with respect to the melt pool: in the case of He or $H_2$ plasma is located at higher position compared to Ar and $N_2$ gases because of the specific low gravity and different ionization energies. Once the plasma plume is far from the melted material the energy transfer from the laser beam can be obstructed, generating defects inside LPBF components. In addition Ferrar et al. [236] studied the effect of inert gas flow on the repeatability of the LPBF parts and demonstrated how this factor directly affects densification behaviour and compression resistance of porous components. The gas flow promoted the removal of condensate material generated during laser scanning reducing the energy absorption from the laser source and consequently increasing defects formation. Masmoudi et al. [239] formulated a model to investigate the interaction between powder bed, laser beam and process atmosphere during LPBF:

in such way it was possible to study the influence of argon gas pressure on melt pool behaviour during the process. From the results emerged that reducing the overall pressure from 995 to 1 mbar, the solid laser track appeared less continuous leaving signs of slight re-melting of the solid surface. In the case of 100 mbar atmosphere the quantity of evaporated material was much higher than in the case of less rarefied atmospheres. Furthermore the vapour created expanded significantly in the process chamber differently from high pressure conditions. Indeed the adoption of inert gas, such as argon, allows to reduce oxidation and to constrain evaporated material on the melt pool.

#### 2.1.2.10 Platform temperature

Generally building platforms of LPBF machines are equipped with electric resistances able to heat the metallic substrate up to 200 °C and more. Several studies demonstrated that heating the building platform has an important effect on the microstructural evolution and mechanical properties of the LPBF parts [201,240–243]. Buchbinder et al [242] demonstrated that platform preheating implies a significant coarsening of dendrites in AlSi10Mg parts. Temperature above 200 °C slows down the solidification rate resulting in less fine microstructures, consequently affecting the final micro-hardness of the parts.

Moreover it was evinced that increasing the platform temperature enables to reduce the amount of residual stresses and distortions in the as-fabricated parts [243,244]. Zaeh et al. [244] showed very limited final distortions of the pieces realized adopting 200 °C platform temperature compared to the 100 and 20 °C cases (Figure 29): both metallurgical transformations in the material and reduced plastification effects were indicated as possible explanations of the effect.

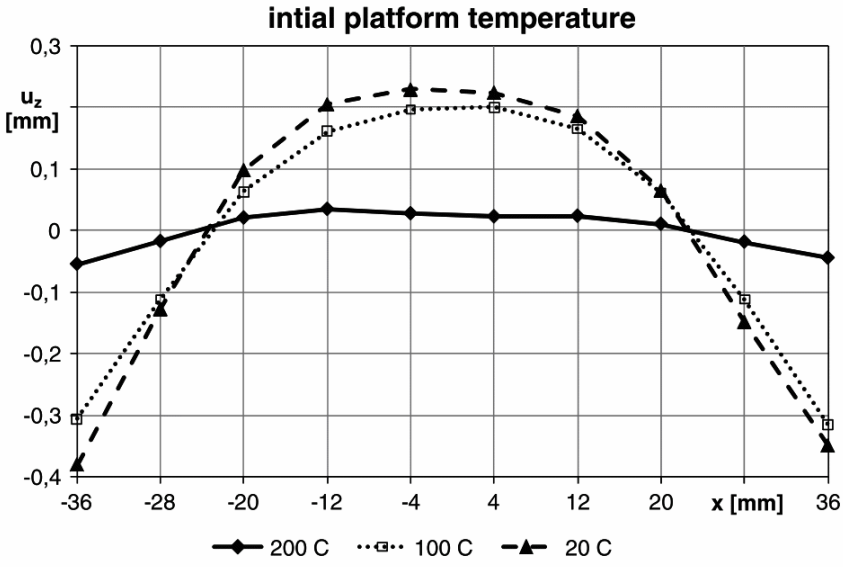


**Figure 29.** Parts distortion as a function of the initial building platform temperature [244].

## 2.2 Materials for LPBF

Since the beginning of metal additive manufacturing, steels, aluminium alloys, titanium alloys, cobalt-chrome alloys and nickel super alloys have been the principal materials processed by LPBF. For industrial reasons, end users and producers in the aerospace, aeronautic and biomedical sectors highly encouraged the development of LPBF processing of these materials. Furthermore, the processing acknowledge of these alloys, since that time processed by traditional manufacturing techniques, was well affirmed and consolidated. Indeed some of the most frequently studied Al alloys for LPBF are based on the binary system Al-Si, which also represent almost 80 % of the aluminium alloys used in casting process. The alloys based on such system possess high fluidity, high weldability, good corrosion resistance and low thermal expansion coefficient and for these reasons they are good candidates for LPBF process.

In the last few years, universities and industries have been investing a considerable effort and amount of money in the LPBF materials and process improvement, particularly in the development of new alloys for industrial applications. Table 4 lists the main metal alloys studied for LPBF up to nowadays. The next goal for the LPBF future is represented by the development of specific

alloys based on the laser melting process in order to fully achieve the best performing materials adapt for LPBF.

**Table 4.** Main materials processed by LPBF in the last years.

| Metal alloy | Example | Reference |
|---|---|---|
| **Steels** | stainless steel 316L | [238,245] |
| | stainless steel 304L | [226,231] |
| | maraging steel | [246,247] |
| **Titanium** | Pure Titanium Grade 2 | [218,248,249] |
| | Ti-6Al-4V Grade 5 | [250–252] |
| | Ti-6Al-4V Grade 23 | [253–255] |
| | Ti-6Al-7Nb | [256–258] |
| | Ti–24Nb–4Zr–8Sn | [259] |
| **Nickel superalloys** | Inconel 718 | [260–262] |
| | Inconel 625 | [263,264] |
| | Hastelloy X | [265] |
| **Copper** | Pure copper | [115] |
| | Copper alloys | [116,266–270] |
| **Precious metals** | Gold | [271] |
| **Aluminium alloys** | Pure aluminium | [189] |
| | Al-Cu (2139) | [272] |
| | AlSi10Mg | [153,189,273] |
| | AlSi12 and AlSi12Mg | [189,190,274] |
| | Al-Mg-Si (A6061) | [190,275] |
| | AlSi7Mg | [201,240,276,277] |

## 2.3 LPBF systems adopted

Within this thesis two LPBF systems manufactured by EOS GmbH, Germany were adopted to produce metal samples: an EOSINT M270 Dual mode machine for the studies on A357 and pure copper powders and an EOSINT M280 for the investigations on Ti-6Al-4V alloy. Both the machines shared the same manufacturing approach and differed for the laser system adopted and for the dimensions of the internal chamber (Table 2).

The EOSINT M270 Dual Mode LPBF machine (Figure 30) was equipped with a 200 W Yb fiber laser beam, while the internal building chamber dimensions are 250 mm x 250 mm x 215 mm. Instead EOSINT M280 possessed a 400 W Yb fiber laser and a bigger internal chamber (250 mm x 250 mm x 325 mm).


**Figure 30.** Example of EOSINT M270 machine adopted in this thesis [278].

The 3D CAD model of the samples were created adopting Solidworks software, then sliced and further processed adopting Materialise's Magics software. Finally the sliced specimens were imported in the process computer of EOS machine. The process computer controls the machine and allow the interaction with the operator. The laser system, incorporated in the upper part of the machine, irradiates the laser beam against a system of mirrors and lenses which deflects and focuses it upon the building platform. The building chamber mounted exactly below

the lenses system accommodates the building platform, the heater system and a system of screws which enable the platform vertical movement. The heater system, placed below the building platform, allows to increase the building platform temperature from 35 °C up to 150 °C. As shown in Figure 17 on the right side of the building platform chamber the dispenser chamber is collocated and contains the metal powder to be processed, while on the other side the collector chamber is installed. The dispenser system moving from right to left transports the necessary metal powder on the building platform and the powder in excess in the collector chamber. The entire process is carried on under Ar gas flow in order to reduce the amount of oxygen inside the chamber: as a consequence excessive oxidation and fire risks are avoided. Although a system of $O_2$ sensors monitors the chamber atmosphere during the process. The LPBF process can not be started if the $O_2$ level excesses 0.1 % while during the process the $O_2$ concentration can vary between 0.01 and 0.12 %. In order to avoid excessive waste of Ar, a recirculating filter system is connected to the machine: such system extracts the gas from the process chamber, filters it and then supplied back inside the machine.

# Chapter 3

# LPBF of Al-Si-Mg alloys

## 3.1 State of the art

Al alloys received considerably attention from numerous industrial fields, such as automotive [279], defence, aerospace etc., thanks to the outstanding high strength to density ratio [280], adequate hardenability [199], good corrosion resistance [280,281] and excellent weldability [199] and castability [282]. These alloys were traditionally used for lightweight components, thin walled casting parts and complex shaped loading parts [209]. Among Al alloys, the Al-Si-Mg system has been widely investigated and used in the automotive and aircraft industries [283]: Table 5 lists some of the most important alloys and the correspondent chemical composition.

**Table 5.** Principal Al-Si-Mg cast alloys [281]

| Aluminium alloys | Chemical composition | | | | | | | |
|---|---|---|---|---|---|---|---|---|
| | **Si** | **Mg** | **Fe** | **Cu** | **Mn** | **Zn** | **Ti** | **Ni** |
| **A356** | 6.5÷ 7.5 | 0.20÷ 0.45 | <0.60 | <0.25 | <0.35 | <0.35 | <0.25 | - |
| **A357** | 6.5÷ 7.5 | 0.45÷ 0.60 | <0.15 | <0.05 | <0.03 | <0.05 | <0.20 | - |
| **A360 / (AlSi10Mg)** | 9.0÷ 10.0 | 0.40÷ 0.60 | <2.0 | <0.60 | <0.35 | <0.50 | - | <0.50 |
| **A413 (AlSi12)** | 11.0÷ 13.0 | <0.10 | <2.0 | <1.0 | <0.35 | <0.50 | - | <0.50 |

In the last few years Al based LPBF parts have been strongly and widely investigated and studied (Table 4) owing to the possibility to produce 3D metal structures with, theoretically, any shape and geometry, combined with high performing materials such as Al-Si-Mg alloys. On the other hand, the LPBF

processability of Al alloys involves a complex and wide number of challenges. Al powders inherently possess low density, poor flowability, high thermal conductivity and high reflectivity. As a consequence, high laser power is required to completely melt the powder bed and overcome the poor absorption and rapid heat dissipation. Notwithstanding this, too high laser power can provoke composition modification due to excessive vaporization, melt track instability and defects generation. Furthermore, the high Al affinity to oxygen promotes the creation of oxide layers during the laser scanning and contributes to porosity enhancement [189].

Among the Al-Si-Mg alloys numerous papers focused the attention on the processability of AlSi10Mg alloy by LPBF: they correlate the microstructures, corrosion resistance, residual porosity, hardness, tensile strength, yield strength, and elongation to break, in some cases after different heat treatments, to the process parameters adopted [284–295]. Table 6 lists some of these studies, highlighting the principal aims and the main findings on AlSi10Mg. On the other hand, the AlSi7Mg alloy processed by LPBF has not been widely studied: in the next sub-chapters a presentation of the densification efforts, microstructures, mechanical properties and post-processing heat treatments of AlSi10Mg and AlSi7Mg aluminium alloys will be presented.

**Table 6.** The main recent researches focused on AlSi10Mg processed by LPBF [153].

| Research Goal | Results | Reference |
|---|---|---|
| **Microstructure** | Fine microstructure with sub-micron-sized cells. | [296] |
| | High hardness (127 ± 3 $Hv_{0.5}$). | |
| | Morphological and crystallographic texture . | |
| **Porosity, tensile and creep responses** | Higher tensile strength than parts with similar composition produced by die casting. | [210] |
| | Superior creep resistance compared to cast alloy. | |
| **Hydrogen porosity** | Moisture presence on particles surface and dissolved hydrogen inside metal powder promote the creation and growth of metallurgical pores in the laser track that can be reduced by drying the powder. Varying the process parameters affects the duration of laser-material interaction during LPBF, influencing hydrogen porosities generation. | [191] |
| **Porosity** | Full dense components, with density around 99.8 %, can be fabricated by optimizing the choice of process parameters and scanning strategies. | [213] |
| **Microstructure, high cycle fatigue, fracture** | High fatigue resistance. | [290] |
| | Fatigue life can be enhanced and combining 300 °C platform heating and post-processing T6 treatment, nullifying the fatigue resistance anisotropy for 0°, 45° and 90° building orientations. | |
| **Heat treatment** | Solution heat treatment at 550 °C for 2 h reduces the tensile strength of as-fabricated material from 434.25 ± 10.7 MPa to 168.11 ± 2.4 MPa, while increases the elongation at break significantly from 5.3 ± 0.22 % to 23.7 ± 0.84 %. | [292] |
| **Precipitation hardening** | The ageing response of the material is strongly connected on Solution Heat Treatment (SHT) duration. The fine microstructure of LPBF parts requires longer SHT to stabilise the microstructure and strengthening the material, with and without ageing. | [294] |

| | | |
|---|---|---|
| **Phase analysis, microstructure characterization** | A definite quantity of Si dissolved in the Al matrix to generate cellular-dendritic α-Al phase, with a cell size around 500 nm. $Mg_2Si$ precipitated, which harden the material, formed during LPBF. Eutectic Al-Si phase was identified in sub-micrometric network surrounding the Al phase. | [295] |
| **Microstructure, heat treatments, hardness and tensile properties** | Ultra-fine microstructure with submicron-sized cells. | [178,297] |
| | High hardness, yield and ultimate tensile strength. | |
| | Effect of T2, T4 and T6 post-processing heat treatments. | |
| **Corrosion resistance** | Microstructural investigations showed that α-Al preferentially dissolves at laser tracks borders. | [286,288, 289] |
| | Resistance to pitting corrosion can be increased and corrosion rate can be lowered by modifying surface conditions by means of shot peening or polishing. | |

### 3.1.1 Microstructure and densification

During slow solidification of Al-Si alloy, the solid solution of silicon in aluminium breaks down easily leading to a very coarse microstructure constituted by continuous eutectic structure of Al and Si, with dispersed primary α-Al [280,298]. An example of microstructure is reported in Figure 31 for the case of AlSi10Mg alloy: the white particles are composed of primary α-Al phase while the darker needles in the matrix are constituted of eutectic α + Si phase.

On the other hand LPBF parts made in Al-Si possess a unique micro- and macro-structure generated by extremely fast repeated melting and subsequent rapid cooling of the material. As reported by Lam et al. [295] in the case of AlSi10Mg, two different microstructures can be detected: a cellular-dendritic structure of α-Al and a network of eutectic Si phase at α-Al phase boundaries. Adopting TEM analysis the dimension of Al cellular dendrites was attested to be around 500 ÷ 1000 nm, that is, much lower than in the case of as-cast components. Prashanth et al. [299] observed this particular microstructure also in the case of Al-12Si alloy, and described how LPBF kinetically promoted the solidification of α-Al into a cellular

morphology, and the extended solubility of Si into Al phase. The residual amount of Si was preferentially found at the cellular boundaries, which had a thickness of about 200 nm. The overall macrostructure of AlSi10Mg specimens fabricated by LPBF, composed by overlapping melt pool, was strictly influenced by scanning strategy and process parameters choice. An example of the different macrostructures obtained by modifying the scanning strategy during LPBF processing of AlSi10Mg are showed in Figure 32 and Figure 33 [178,297]. Unidirectional scanning strategy produces parallel scan tracks inside the part, and the melt pools in the microstructure possess an almost half cylindrical shape along the vertical cross section (Figure 32). On the other hand adopting a rotated scanning strategy affect the laser tracks overlapping producing a complex macrostructure (Figure 33).

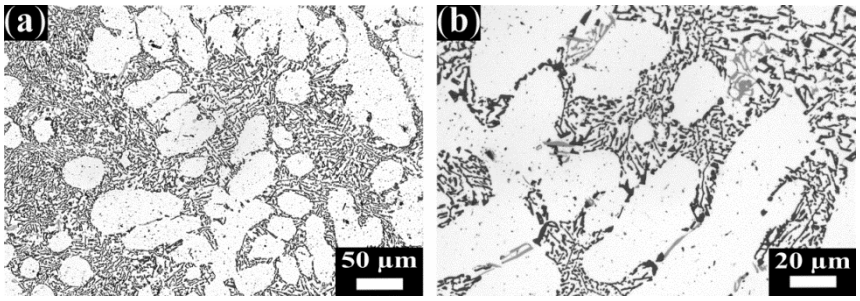


**Figure 31.** Examples of AlSi10Mg alloy microstructure, fabricated by casting process, observed by optical microscopy at (a) low and (b) high magnifications [153].

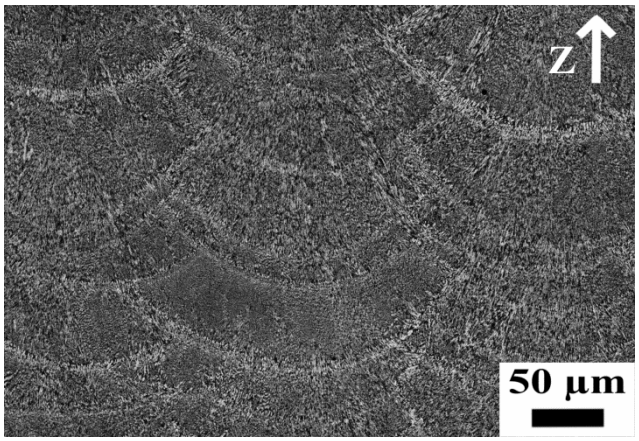


**Figure 32.** Optical microscopy of AlSI10Mg specimen fabricated by LPBF adopting an unidirectional scanning strategy (along the *x* axis). The white arrow indicates the direction of *z* axis and the building direction of the sample [153].

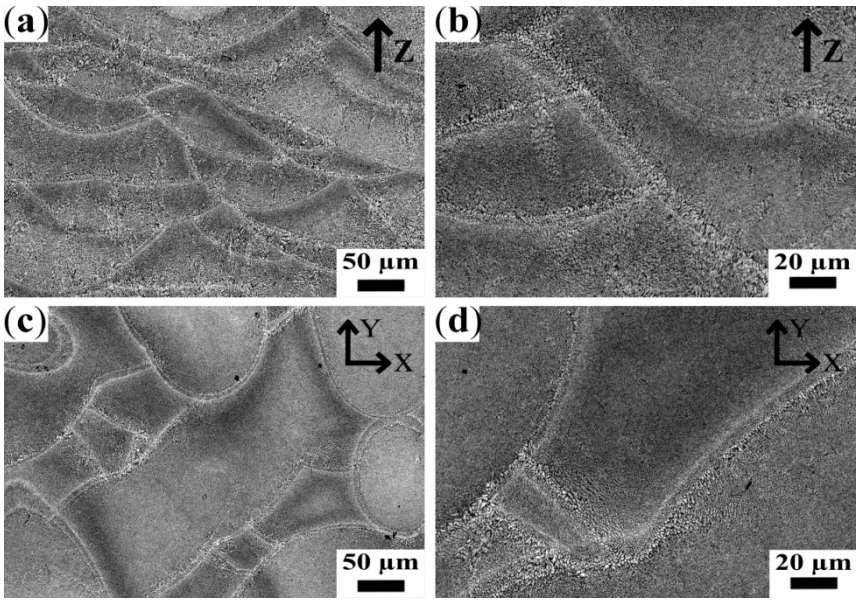


**Figure 33.** Optical micrographs of AlSi10Mg specimens fabricated by LPBF adopting a 67° rotated scanning strategy at different magnifications: (a,b) show a vertical cross section of the sample parallel to building direction (*z* axis); while (c,d) display the horizontal cross section parallel to the building plane (*x*-*y* plane).

Two other fundamental factors affecting the melting behaviour are directional cooling and solidification rate, both of which strongly influence the microstructure of LPBF components. Manfredi et al. [178,297] studied the AlSi10Mg microstructure analysing high magnifications Field Emission Scanning Electron Microscopy (FESEM) micrographs, as displayed in Figure 34. The areas named as 2 and 3 correspond to the heat affected zone (HAZ) of the adjacent melt pools: in area 1, which represents the centre of the melt pool, the very fine cellular-dendritic structure, typical of LPBF processing of Al-Si alloys, can be appreciated. As highlighted in area 4, these structures possess different sizes inside the melt pool due to different thermal gradients developed during the process. The same melt pool structure can be observed in the AlSi7Mg (A357) parts made by LPBF, as illustrated in Figure 35 [201], due to the fact that the Gaussian thermal profile of the laser beam determines a temperature gradient in the laser track [203,241]. The centreline of the melt pool presents the highest temperature while the scan track borders the lowest one. Such thermal gradient generates a consequent surface tension gradient and induces the molten metal to flow from the inner side of the track to the borders [215,296,300].

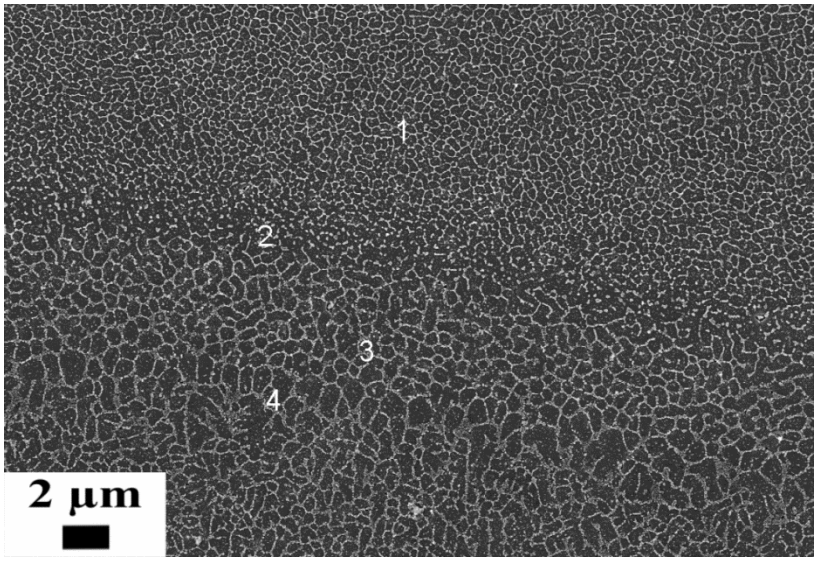


**Figure 34.** FESEM micrograph of an AlSi10Mg specimen fabricated by LPBF, investigated in the as-built conditions after polishing and chemical etching [153].

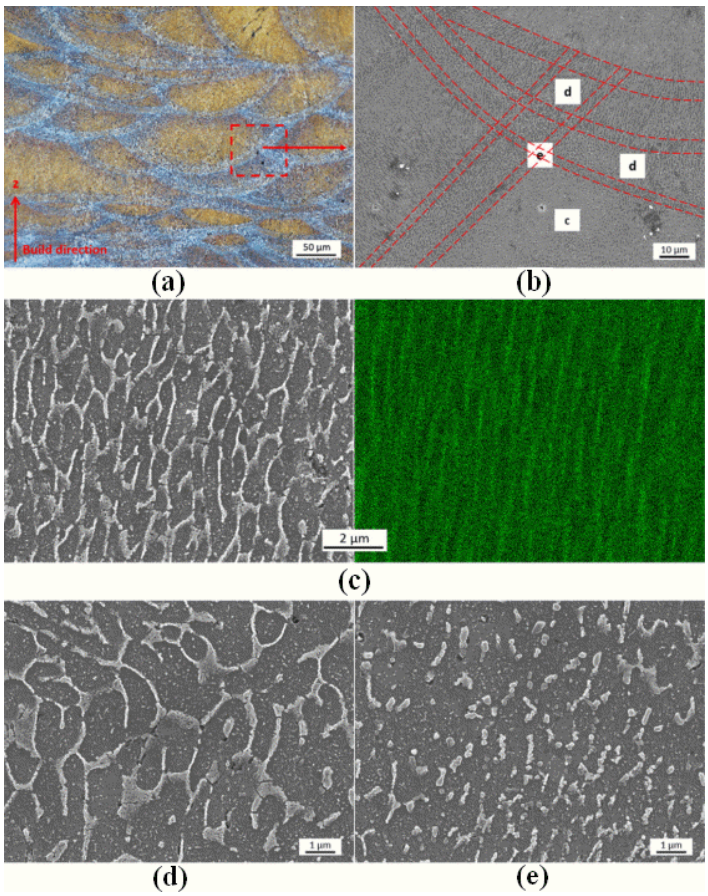


**Figure 35.** Microstructural investigation of A357 alloy specimen processed by LPBF: (a) Optical micrograph of cross section in the *z* plane; (b) SEM investigation of melt pool structure, highlighting the arrowed area at higher magnification corresponding to (c) melt pool cross section with EDS analysis (Si distribution in green colour), (d) melt pool boundary and (e) HAZ [201].

As reported by Rosenthal et al. [293], in LPBF processing of AlSi10Mg alloy the thermal gradient (G) and the growth rate (R) determine the solidification behaviour. The growth rate could be adjusted by modifying the scanning speed and the angle between the laser scan track direction and the growth direction of the solidified part. The G/R ratio determines the stability of the solidification front. Lowering the R value at constant G values provided a stable planar consolidation front, while increasing R promoted the formation of cellular, and finally dendrite solidification morphologies. The product of G and R gives the cooling rate of the system, and the higher product yields a finer microstructure. Both thermal gradients and growth rate are at a minimum at the border of the melt pool, in particular R reaches a zero value at the corner of the melt pool where the laser track results perpendicular to the heat flow direction. From the border of the melt pool G and R

increase reaching a maximum in correspondence of the melt pool centre [296]. As a consequence the microstructure fineness can vary by modifying the G and R values.

Another consequence of the directional solidification in the melt pool is the creation of a crystallographic texture inside the material. Thijs et al. [296] studied the overall texture of AlSi10Mg specimens fabricated by LPBF, and the influence of different scanning strategies on the material. It was established that cells preferentially grew along the ⟨100⟩ crystal direction, parallel to the centreline of the melt pool: the cells, constituted by face centred cubic α-Al phase, were surrounded by a diamond-like silicon phase. This specific fine microstructure determines the LPBF parts high hardness (~127 $Hv_{0.5}$). Furthermore, the cells dimensions varied between 0.7 and 0.4 μm moving towards from the melt pool border to the melt pool centre. Moreover adopting different scanning strategies could modify the component anisotropy.

Therefore, as stated before, the process and the scanning strategy can profoundly affect the microstructure and texture evolution inside the parts [293,296], and they also have a substantial impact on the material densification: both industries and research employed significant resources to comprehend and model the melting and solidification behaviours during laser melting. Furthermore, the LPBF systems available on the market (Table 2) differ for the laser source and scanning strategy adopted: in order to maximise material density and process productivity the optimisation of process parameters and scanning strategies is required for each LPBF machine. A major current focus is to investigate the generation of porosity inside the material, due to its deleterious effects on the mechanical and fatigue properties of the final parts: Figure 36 displays the hydrogen porosities and keyholes defects that can be found inside a LPBF processed part made in AlSi10Mg alloy. Indeed since the majority of LPBF fabricated components have being used in the aerospace and biomedical market, a great concern is given to the detection of pores and defects inside the parts, due to the fact that they favour premature and unexpected structural failures during operation [231].

Kempen et al. [301] studied the correct combination of laser power and scanning speed parameters in order to produce fully dense AlSi10Mg components. Following a laser energy per unit length approach, they investigated the melting behaviour of the powder bed at varying laser power, between 170 and 200 W and scanning speed from 200 to 1400 mm/s. From density measurements they determined a process window in which it was possible to produce 99 % dense parts,

without modifying the other process parameters. Indeed by the modulation of the energy density the generation of hydrogen porosities was avoided promoting a correct overlapping of the laser tracks and decreasing the defect amount inside the material.

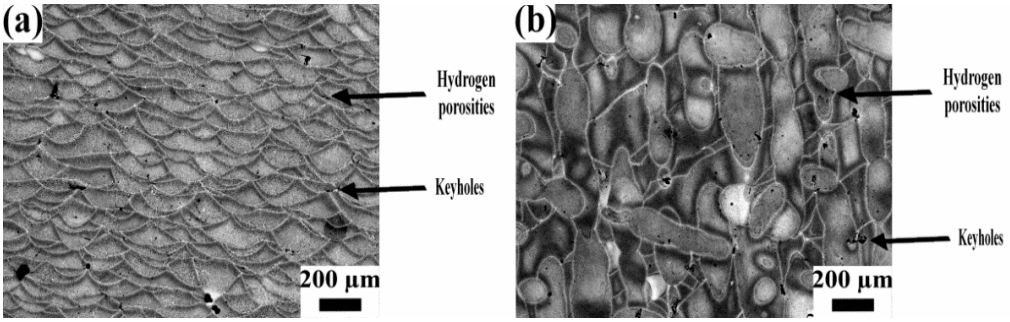


**Figure 36.** Optical micrographs of an AlSi10Mg microstructure after chemical etching in the (a) vertical and (b) horizontal cross sections. The metallurgical pores, also known as hydrogen porosities and keyhole defects are indicated in the images [153].

Similar results were obtained by Kimura et al. [209] and Rao et al. [201] in the investigation of LPBF process of two AlSi7Mg alloys, A356 alloy and A357 alloy, respectively. In the case of A356, the peak density data were obtained adopting laser power of 200, 250, 300 and 370 W coupled with laser scan speed values of 800, 1400, 1600 and 1800 mm/s, respectively, demonstrating how increasing the laser power can raise the scan speeds. Furthermore, it was shown that the high density samples could be obtained choosing an energy density between 50 and 100 J/mm$^3$, while at higher or lower energy density values densification decreases considerably. Low energy densities determined an incomplete melting of the material, leading to the formation of irregular shaped porosities filled of un-melted particles. On the other hand, specimens fabricated at high density values presented spherical porosities generated by gas presence: from chemical analysis it was established the presence of argon (67 %) and hydrogen (30 %) [209]. Concerning metallurgical pores, Weingarten et al. [191] studied the generation of these porosities during AlSi10Mg alloy LPBF processing, evaluating the effects of a pre-drying treatment of the powder. From the results appeared that drying the metal powder at 200 °C before LPBF halved the hydrogen porosities compared to un-dried powder processing, thanks to the moisture removal from particles surface induced by the heat treatment [192,193].

Similarly Aboulkhair et al. [196] studied the correlation between process parameters and defects generation inside AlSi10Mg specimens. The hydrogen

porosities were principally generated when low scanning speeds (~ 250 mm/s) were adopted, while keyholes were detected in the case of higher scanning speeds (higher than 500 mm/s). The explanation was related to the excessive energy density transferred to the powder bed. At high scanning speeds and low laser power balling phenomenon is favoured compromising the solidification front and layer consolidation. Instead, using low scanning rates and high laser power, corresponding to high energy densities, the melt pool instability is promoted. Moreover, they investigated the connection between the distance of subsequent laser tracks and material densification: incorrect scan tracks overlapping significantly promoted porosities formation inside the material [196]. Read et al. [210] adopted a statistical approach to investigate the correlation between process parameters and porosity level inside AlSi10Mg alloy specimens fabricated by LPBF. Using ANOVA, they established the porosity response as a function of the laser power, hatching distance, scanning speed, and scanning strategy. The results confirmed that the main influencing factors on the pores generation were the laser power, hatching distance and scanning speed, as also described in previous researches [189,190,215]. Since these three parameters could individually module the energy input, it was plausible that the porosity level could be decreased by varying parameter values in the range delimiting the process window. Indeed, keeping laser power fixed, it emerged that decreasing the hatching distance value substantially reduced the effect of scan speed on the porosity generation. The experiments showed that adopting an energy density around 60 J/mm$^3$ the resultant porosity inside the specimen was lowered to almost 0 % (Figure 37): this result is comparable with the threshold limit described by Olakanmi et al. [215] in their research on Al, Al-Si, and Al-Mg alloys.

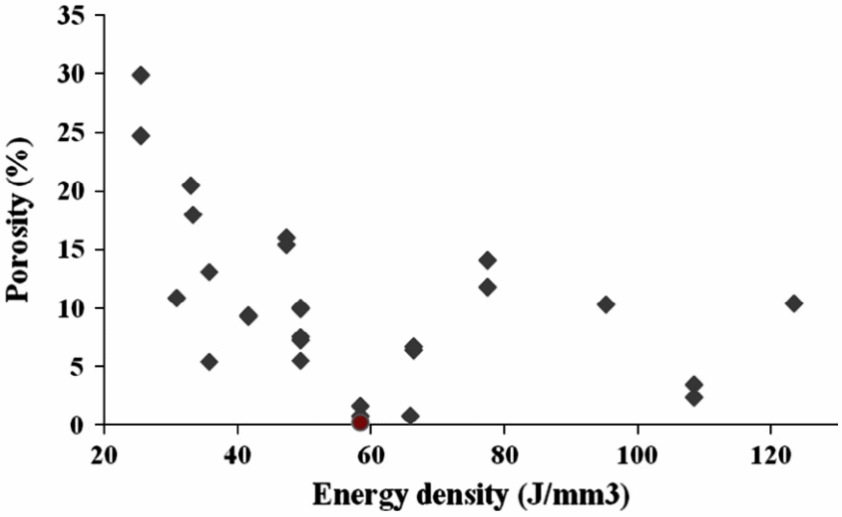


**Figure 37.** Porosity level versus energy density. The red dot indicates the lowest porosity obtained for the LPBF processing of AlSi10Mg powders [210].

The researches presented before highlighted how the process parameters do affect defects generation inside LPBF components, due to their direct effect on the energy input transmitted to the powder bed. Energy density values (per length [301], per area or per volume [210]) give an indication about the limits of the process window, but in order to optimise the process and avoid porosity formation an accurate investigation of process parameters effects is necessary.

### 3.1.2 Mechanical Properties

Focusing on the mechanical properties of LPBF parts, it has been underlined that they possess a higher hardness, a higher tensile strength and at the same time a similar ductility and a lower fatigue life than traditional cast or wrought ones. The difference in mechanical behaviour can be attributed to three main factors [295]: the ultrafine-grained microstructure, which favours grain boundary strengthening, the alloying elements present inside the supersaturate solid solution, which are responsible for solid solution strengthening, and the strengthening given by dislocations interaction [273,302].

Buchbinder et al. [303] evaluated the tensile properties of AlSi10Mg alloy specimens fabricated by LPBF adopting two different sets of process parameters: 240 W laser power and 500 mm/s scanning speed for the first one, 960 W laser power and a 1000 mm/s scanning rate for the other. From the results it appeared that laser power did not affect the ultimate tensile strength (400 ÷ 450 MPa) and

yield strength (210 ÷ 240 MPa) of the specimens while it influenced the elongation at break, resulting in an 25 % ductility increment when low laser power was employed. Moreover, it was evinced that three main factors should be considered when the elongation at break anisotropy of LPBF parts is taken under investigation: defects and pore presence, grains orientation and texture, as well as interfaces between melt tracks and layers. In contradiction to the previous study, Rosenthal et al. [293] measured an higher ductility for specimens fabricated horizontally than those fabricated vertically. The explanation of such anisotropy was evinced from fracture surface analysis and was attributed to a the different crack path during fracture: vertical samples showed a predominantly ductile failure located between weakly bonded layers, while horizontal samples fracture occurred within each layer. In good agreement with such results, Kempen et al. [287] reported a mean elongation at break of 5.5 % for horizontal specimens and 3.5 % for vertical ones. During failure, crack most probably initiated in correspondence of large porosities which act as preferential sites for inhomogeneous deformation at a high stress level (around 395 MPa). Comparing vertical and horizontal samples the pores amount appeared to be greater in the vertical specimens rather than in the horizontal ones, corroborating the tensile results. Rao et al. [201] related the higher tensile strength of horizontal A357 samples to the Si phase distribution in the melt pool. While in the centre of the melt pool the Si network appears continuous and elongated, at the borders and in the HAZ the Si particles appear discontinuous with a scale of few hundred nanometers (Figure 35). Such disconnected Si cells easily act as stress concentration areas for cracking and lead to the mechanical properties anisotropy measured in the LPBF parts. Read et al. [210] determined the presence of thick oxide layers on the un-melted particles during the investigation of the fracture surfaces of broken tensile specimens: these un-bonded areas promoted the creation of large cracks during fracture. From electron microscopy observation, these un-bonded sections emerged as flat or faceted, in contrast to ductile deformed fracture regions where samples surface appeared constituted by very fine dimples [190]. Examples of AlSi10Mg LPBF fracture surfaces are reported in Figure 38, while the typical defects of LPBF are illustrated in Figure 39, Figure 40 and Figure 41: porosities (Figure 39), oxide layers (Figure 40), and un-melted powders (Figure 41) results extremely deleterious for the static and dynamic mechanical properties of the components [210,297].

Moreover, porosity has the most detrimental effects on the fatigue properties, especially when the pore size exceeded a certain value. Mower and Long [304] evaluated the fatigue properties of AlSi10Mg through fully-reversed bending tests

(frequency equal to 20 ÷ 25 Hz). For any prescribed lifetime, the maximum endurance limit of the LPBF specimens (as-built conditions) was 30 % lower than the reference wrought 6061 aluminium alloy specimens. This different behaviour was explained by the presence of defects and porosities inside the LPBF material, which acted as stress concentration sites that favoured crack initiation and propagation.

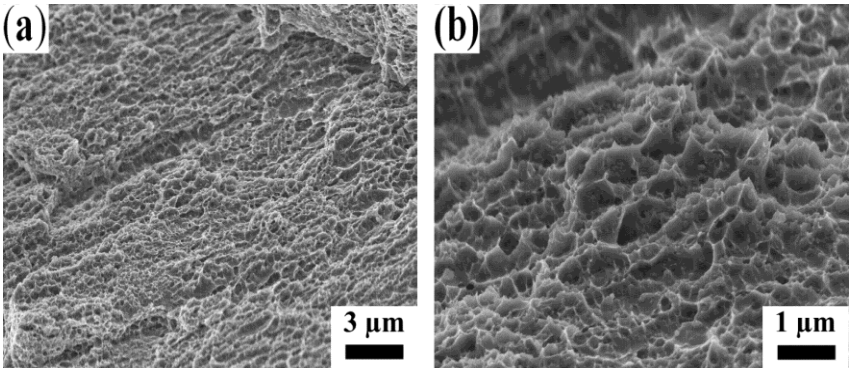


**Figure 38.** Examples of fracture surface of an AlSi10Mg alloy specimen produced by LPBF observed at FESEM, at (a) low and (b) high magnifications [153].

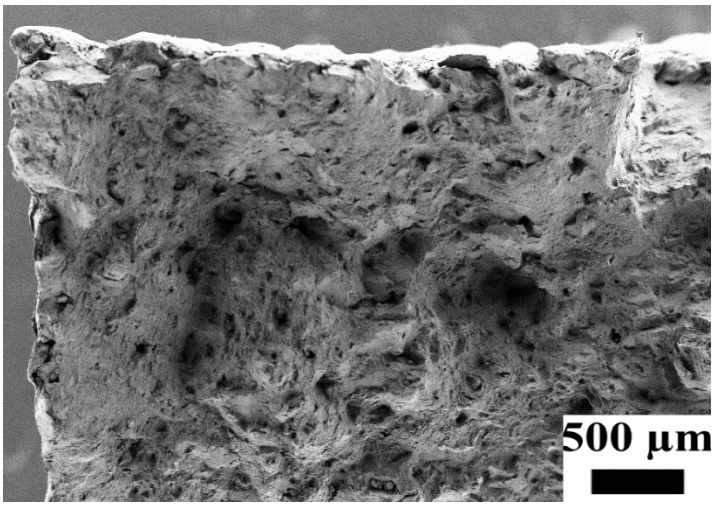


**Figure 39:** Example of fracture surface of an LPBF AlSi10Mg specimen after tensile test observed at FESEM [153].

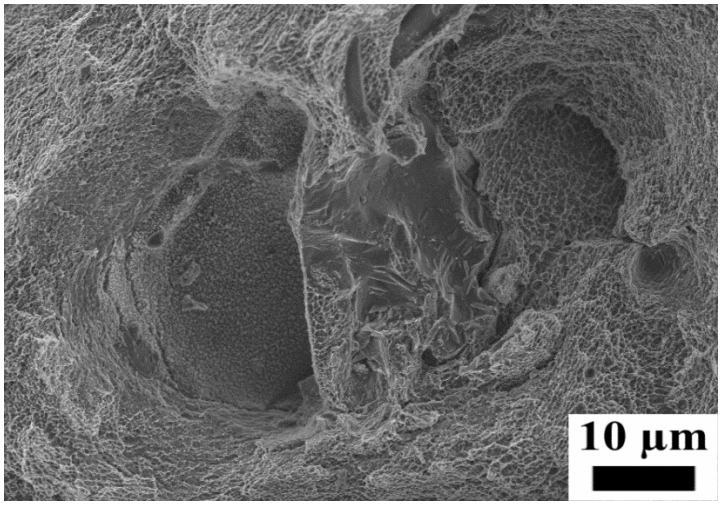


**Figure 40.** FESEM micrograph of the fracture surface of a LPBF specimen after tensile test: the central smooth area represents a fragile rupture area corresponding to oxide layers presence [153].

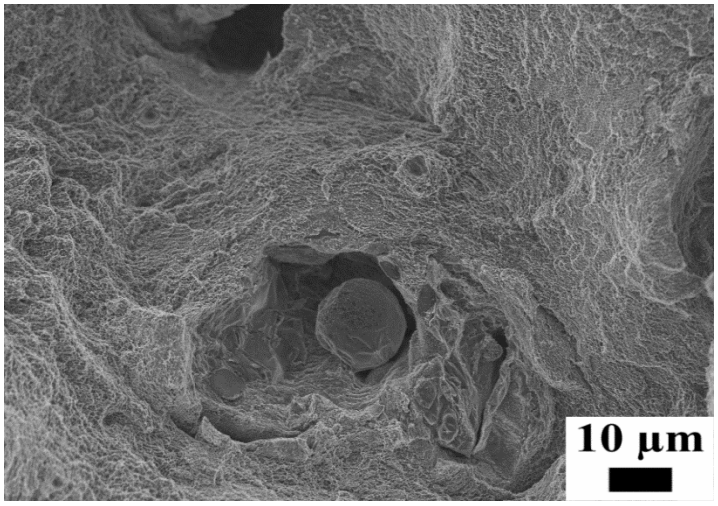


**Figure 41.** FESEM micrograph showing an un-melted powder particle inside the fracture surface of an AlSI10Mg alloy tensile sample produced by LPBF [153].

### 3.1.3 Post-processing heat treatments

As described before, LPBF parts present a great amount of thermal residual stresses which can lead to distortion and warping of the pieces and also alter the final mechanical properties. Commonly a stress relieving heat treatment is performed on the as-fabricated LPBF components in order to reduce the amount of residual stresses and at the same time to maintain good dimensional and physical

stability of the part. A major effect of stress relieving treatment is to influence the mechanical properties of the parts, significantly reducing tensile strength and increasing elongation at break values. As an example, Mertens et al. [284] investigated the tensile properties of AlSi10Mg samples before and after a stress relieving treatment performed at 250 °C for 2 h. Compared to the as-built conditions, after stress relieving the elongation at break increased of 80 %, while yield and ultimate tensile strength slightly decreased of 12 and 2 %, respectively. Kimura et al. [209] investigated different stress relieving temperatures on A357 samples and their effects on the tensile properties. From the results appeared that annealing at low temperatures (150 °C for 5 h) did not affect either the tensile strength (400 MPa) and the elongation at break (almost 12 %) compared to the as-fabricated conditions, while annealing for 5 h at 200 °C and more considerably increased the ductility and reduced the strength. For instance, at 350 °C for 5 h the tensile strength decreased to 180 MPa and the elongation raised to 35 %. Increasing the annealing temperature from 150 to 250 °C favoured the diffusion of Si and the migration of the cells boundaries, consequently weakening the dislocation hardening (reduction of tensile strength and increase of ductility). At 350 °C temperature for 5 h, the microstructure was further modified and the cell boundaries disappeared, increasing the elongation to break of the specimens due to the higher dislocation mobility.

In traditional casting, the Al-Si-Mg alloys are commonly strengthened through precipitation hardening [281,305–307], which consists of a solution heat treatment followed by quenching and artificial ageing: depending on the alloy, temperature and duration of the solution and ageing treatments vary considerably. Indeed the Si and Mg contents have a substantial effect on the age hardening capacity of the alloy [298]. For example, in the case of casting parts made by AlSi7Mg, the common solution treatment is made at 540 °C for 8 h while the ageing treatment at 170 °C for 3 to 5 hours [281]. Instead in the case of AlSi10Mg (higher Si content and lower Mg one), the solution and ageing treatments are carried out at 530 °C for 5 h and 160 °C for 12 h, respectively [281,297].

Adopting a precipitation hardening on LPBF materials modifies the microstructure to a great extent, as pointed out by Brandl et al. [290]. In their study, they showed how the as-built microstructure, constituted by cellular α-Al dendrites and interdendritic Si particles, was modified by a heat treatment, and that eutectic globular Si particles, homogeneously distributed inside the α-Al matrix, were obtained. After the heat treatment, all the microstructural differences, such as different grain size, heat affected zone, and melt pools, were eliminated. Li et al.

[292] investigated the effect of different treatments, and highlighted how the microstructure became coarser when the solution temperature was increased from 450 to 550 °C, and in particular after artificial ageing (at 180 °C for 12 h). It was observed that when as-built LPBF AlSi10Mg specimens were solution heat treated at 450 °C for 2 h, the mean Si particle size was less than 1 μm. When a 550 °C solution temperature was adopted, Si particles rose to 4 μm, instead, when a subsequent artificial ageing was applied, they again became coarser, reaching a mean dimension of 5 μm. During the solution heat treatment and artificial ageing, the supersaturated Al phase rejected Si, which started to agglomerate in small particles.

The great microstructure modification provided by the post-processing heat treatment appears fundamental to improve the ductility behaviour of LPBF as-built parts, maintaining the high tensile properties [192,284,297]. In the same study presented before, Li et al. [292] described how each solution heat treatment reduces the tensile strength to a great extent, compared to the high values of as-built parts (UTS = 434 MPa) (Figure 42). Indeed they described that the higher the temperature, the lower the tensile properties, till minimum yield and tensile strength values, 90 and 168 MPa, respectively, were measured for 550 °C solution heat treated specimens. At the same time, the results showed an increase of elongation at break value from 5.3 % to a maximum of 23.7 %. Moreover, performing an ageing treatment after solution and quenching treatments did not increased the low mechanical properties, leading to a maximum tensile strength value of 200 MPa and maintaining the elongation at break at 23 %.

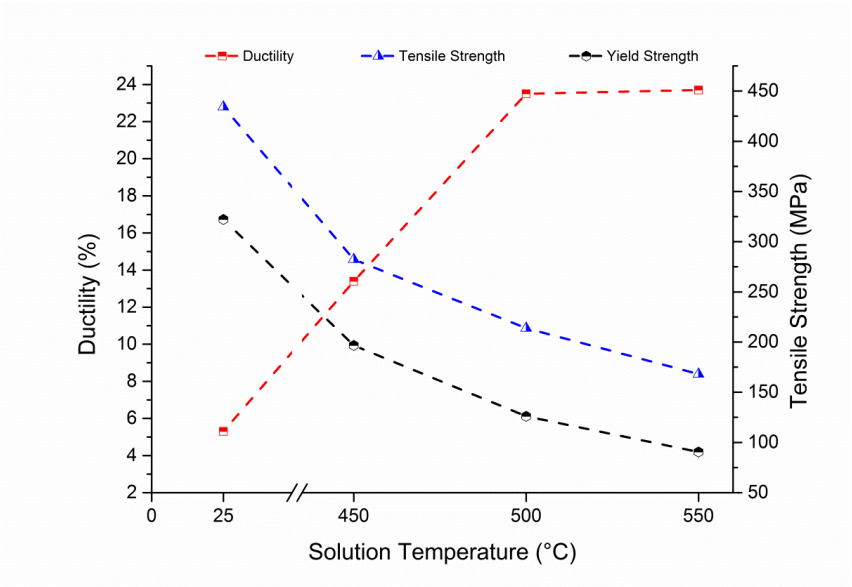


**Figure 42.** Effects of solution heat treatments, performed for 2 h at different temperatures, on tensile properties of as-built AlSi10Mg alloy specimens produced by LPBF [153].

Mertens et al. [284] measured the hardness and tensile properties of AlSi10Mg parts after several ageing treatments, performed at different temperatures and times after solution heat treatment (510 °C for 6 h) and water quenching. According to the results the best compromise was achieved performing the ageing treatment at 170 °C for 4 h. Tensile strength was lowered by 13 % while at the same time yield strength and ductility were enhanced by 30 and 220 %, respectively, compared to the as-built conditions. The different mechanical behaviour was recorded because the microstructure was strongly modified by the post-processing treatment: indeed the silicon lamella were substituted by globular silicon precipitates. Manfredi et al. [297] investigated the effects of a T4 treatment (solution treatment at 530 °C for 5 h, followed by water quenching, and then by room temperature ageing for at least two weeks) and of a T6 treatment (solution treatment at 530 °C for 5 h, followed by water quenching, and then by artificially ageing at 160 °C for 12 h). Figure 43 displays the optical micrographs of the microstructure after each heat treatment, highlighting the strong effect of such post-processing heat treatments on the material. Figure 44 reports the fracture surfaces observed at FESEM after tensile tests: it can be noticed how in the as-built conditions dimples possessed a sub-micrometric dimension (Figure 44a) while after heat treatments they significantly coarsened (Figure 44b,c) [297].

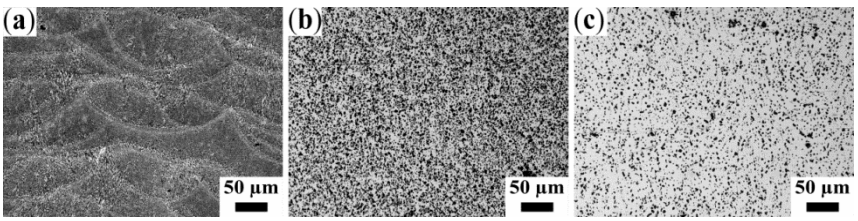


**Figure 43.** Optical micrographs of AlSi10Mg alloy specimens fabricated by LPBF and subjected to different heat treatments: (a) after stress relieving (300 °C for 2 h); (b) after T4 treatment; (c) after T6 treatment [153].

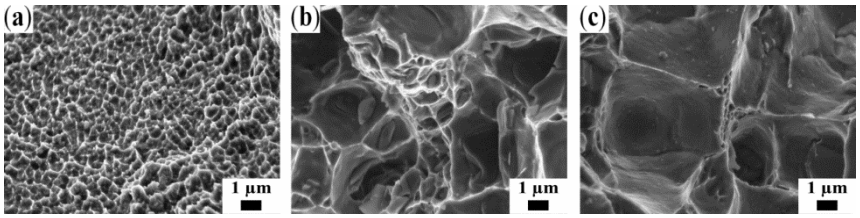


**Figure 44.** FESEM images of fracture surfaces of AlSi10Mg specimens fabricated by LPBF and subjected to different heat treatments: (a) as-built conditions; (b) after T4 treatment; (c) after T6 treatment [153].

Brandl et al. [290] measured the high cycle fatigue (HCF) properties of AlSi10Mg alloy LPBF samples. Un-notched (stress concentration factor, Kt, equal to 1) specimens were tested at 108 Hz test frequency, using a tension-tension mode with a stress ratio (R) equal to 0.1 (corresponding to a tension-tension cycle in which the minimum stress is equal to 1/10 of the maximum one). They also investigated the effects of building platform heating and T6 post-processing treatment (solution treatment at 525 °C for 6 h, followed by quenching and ageing at 165 °C for 7 h) on the fatigue resistance. From the results appeared that adopting 300 °C platform temperature and treating the specimens in the peak hardening condition, the endurance limit was considerably increased. Indeed both conditions favoured the material homogenization altering the as-built microstructure: in particular T6 treatment induced the removal of HAZ and the sphereodisation of interdendritic eutectic Si particles. As a consequence the crack initiation and propagation rate were reduced and the fatigue resistance was enhanced.

Aboulkhair et al. [294] recently established to what extent the LPBF microstructure requires a different solution treatment duration from that of the casting materials. The fine microstructure of LPBF parts required longer times than the cast one to be fully stabilized and homogenized: the precipitation behaviour was completely different in a coarse microstructure from that of an ultrafine grained

one. This statement opens new horizons to the development and optimization of post-processing heat treatments for metals alloys processed by LPBF.

## 3.2 Study and characterisation of A357 alloy processed by LPBF

As briefly described before, among Al-Si-Mg alloys, A357 (AlSi7Mg0.5) is a cast alloy extensively used in structural automotive applications such as for blocks, cylinder heads, suspension system etc. since its excellent castability and good corrosion and fatigue resistance [280]. Generally A357 is strengthened by precipitation hardening [308], particularly T6 heat treatment [309] which consists of solutionizing at high temperature, subsequent water quenching and final artificial ageing. The optimum castability of such alloy is provided by Si presence which increases the fluidity and hot cracking resistance, while the Mg presence improves the mechanical properties after T6: during heat treatment Mg and Si form $Mg_2Si$ which precipitates from α-Al solid solution and strengthens the alloy by precipitation hardening [298]. Such properties make A357 a suitable candidate for LPBF rapid solidification process.

To the author knowledge a few studies have been addressed on the production and characterisation of A357 parts made by LPBF. Rao et al. [201] investigated the effects of laser parameters and building platform temperature on density and mechanical properties of LPBF A357 parts. They correlated the mechanical properties with the ultrafine microstructure of as-built specimens, studying the relevant factors affecting strength and fracture behaviour during tensile load application. Aversa et al. [240] discussed the ageing effects of building platform heating on as-built specimens considering various temperatures from 100 °C to 190 °C. Furthermore they investigated the influence of direct ageing treatment on micro-hardness of as-fabricated samples.

Moving towards applications in industry, the present study examines the investigation of the A357 alloy produced by LPBF process and the evaluation of different post-processing heat treatments. The aim of this research is to understand the LPBF's process parameters to build dense components for industrial applications in A357 alloy and how heat treatments, a frequently used industrial process, change the microstructures and hardness of this material. Furthermore the influences on the tensile properties of machined specimens were also investigated.

### 3.2.1 Materials properties

Table 7 lists the chemical composition and size distribution of the A357 gas atomised powder used in this study, as reported by material datasheet of the supplier. A preliminary observation of powder morphology was conducted using FESEM (Appendix 1.1.1.1A.1) as shown in Figure 45a. At high magnification (Figure 45b) the particle surface oxidation is visible: thin oxide layer forms on metal powder during gas atomization process and during storage. The graph in Figure 46 illustrates the particle size distribution (volume and cumulative fraction) based on volumetric assumption, obtained by laser diffraction (Appendix A.2). Adopting the volumetric assumption the mean diameters corresponding to 10% ($D_{10}$), 50% ($D_{50}$) and 90% ($D_{90}$) of the cumulative size distribution were measured as 22, 34 and 53 μm, respectively.

**Table 7.** A357 gas atomised powder used in this study.

| Material | Chemical composition [wt.%] | Particle size range [μm] | Supplier |
|---|---|---|---|
| **A357** | Cu ≤ 0.2; Mg = 0.4 ÷ 0.7<br>Mn ≤ 0.1; Si = 6.5 ÷ 7.5<br>Fe ≤ 0.2; Zn ≤ 0.1<br>Ti = 0.1 ÷ 0.2; Al = bal. | 20 – 63 μm | LPW Technology |

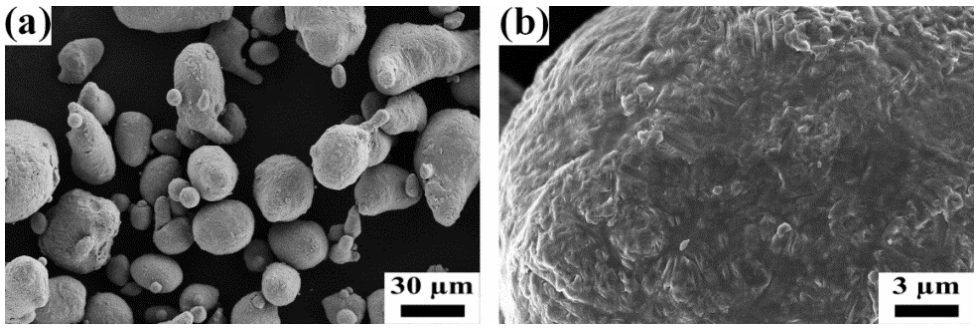


**Figure 45.** FESEM observation of A357 alloy powder at low (a) and high (b) magnification.

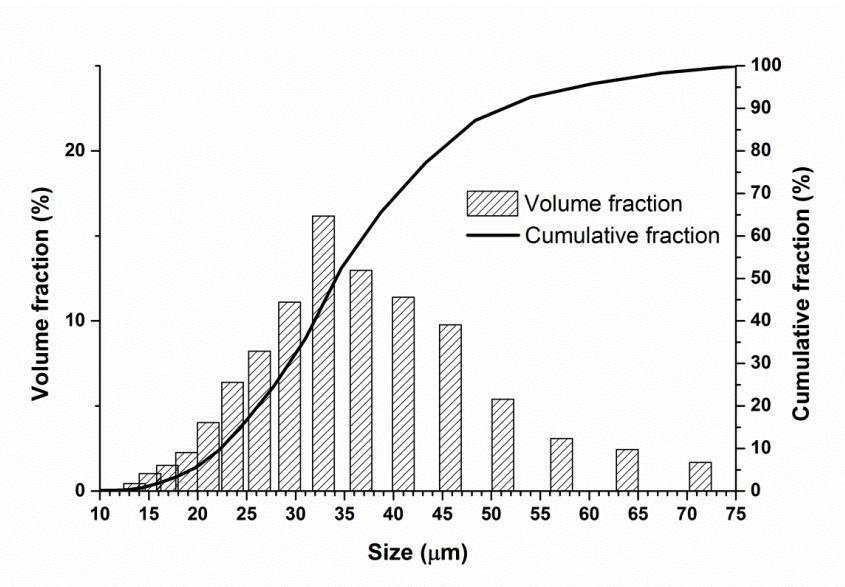


**Figure 46.** Particle size distribution (volume and cumulative fraction) of A357 gas atomised powder adopted for LPBF process.

Furthermore the polished and etched (Appendix 1.1.1.1A.1) cross sections of powder particles are presented in Figure 47. It can be observed that the internal microstructure of the powder is constituted by an eutectic phase (dark phase) and an aluminium one (bright phase). These phases appears to be uniformly distributed in the material. In particular, the aluminium phase appears to be organised in fine lamellae, with different aspect ratios, due to the high cooling rates developed during gas atomisation process, which induce the creation of non-equilibrium conditions, as in the case of melt-spinning process [310].

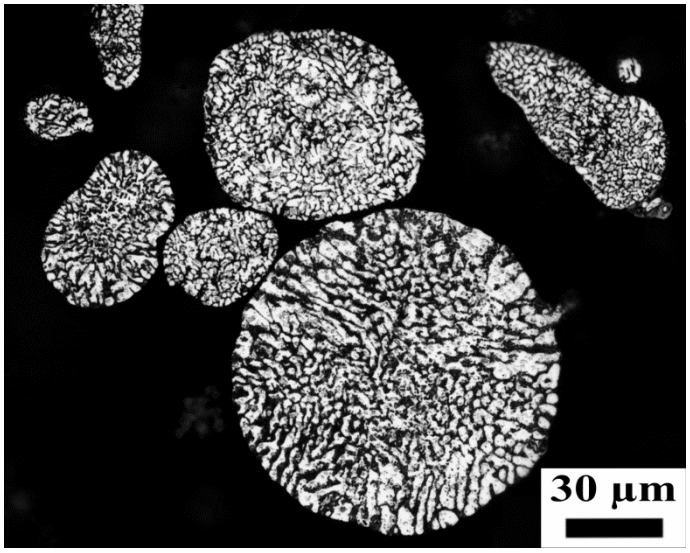


**Figure 47.** A357 powder cross sections observed at optical microscope after chemical etching.

All the specimens were fabricated using an EOSINT M270 Dual mode commercial machine, previously described in Chapter 2.3. Cubic samples (10 x10 x 10 mm) for density investigations (Appendix 1.1.1.1A.3) were produced adopting different scan speed and hatching distance values, within the ranges shown in Table 8, using a layer thickness of 30 µm and a laser power of 195 W [205]. The range of values was chosen starting from the idea of obtaining a good compromise between density and production times. Before starting the LPBF process, the building platform was pre-heated at 100 °C. Considering scanning strategy, the direction of scanning is rotated 67° between consecutive layers. This should ensure a better overlapping and more isotropic properties with respect to other scanning strategies made of layers with unidirectional vectors or at least with a cross-ply pattern.

**Table 8.** Specimens built parameters using different scanning speeds and hatching distances.

| Parameters | Values |
|---|---|
| **Scanning speed v [mm/s]** | 600 |
| | 700 |
| | 800 |
| | 1000 |
| | 1200 |
| **Hatching distance hd [mm]** | 0.10 |
| | 0.17 |
| | 0.20 |

Two different types of heat treatment were took under investigation. The first one was a stress relieving treatment which enables to reduce the amount of residual stresses inside the parts generated during the LPBF processes and eliminate the distortions and warping risks. In the case of A357 alloy the treatment was chosen based on the stress relieving of AlSi10Mg components fabricated by LPBF, since the two aluminium alloys possess similar chemical composition. According to EOS datasheet, the stress relieving treatment for AlSi10Mg is performed at 300 °C for 2 h in air.

The second treatment investigated was a T6 one. Generally performed on casting or wrought A357 parts, it is composed by a solution treatment at 540 °C for 8 hours, followed by water quenching and further ageing treatment at 160 ÷ 170 °C for 3 ÷ 5 hours [281]. In this thesis several T6 conditions were investigated to establish the peak-hardening conditions for the LPBF parts fabricated and subsequently stress relieved: Figure 48 summarise the solution and ageing treatments conditions studied. Two distinct solution conditions, solution “A” carried out at 530 °C for 5 h and solution “B” performed at 540 °C for 8 h, were combined with two ageing temperatures, 160 °C and 170 °C, with different duration times, from 0 to 12 h. To individuate the peak hardening conditions micro Vickers indentation were performed (Appendix A.4).

In order to study the mechanical properties of the material, tensile test samples were obtained with the optimised process parameters (scan speed v = 800 mm/s, hatching distance $h_d$ = 0.17 mm) by machining round bars of 110 mm length and 14 mm diameter, according to ASTM E8/EM-09 [311]. The specimens possessed a

final surface roughness $R_a$ = 0.4 µm and were tested using a Zwick Z100 tensile testing machine at room temperature using 35 N preloading and 0.008 $s^{-1}$ strain rate. All the samples were built in parallel to the *x-y* plane and tested in three different conditions, as-built, after stress relieving, after stress relieving and subsequent T6 (peak hardening conditions), respectively.

The microstructure and chemical composition were studied by optical and electron microscopy (Appendix 1.1.1.1A.5) and further X-ray Diffraction (XRD) analysis (Appendix 1.1.1.1A.6). The fracture surfaces of broken specimens were finally observed both at FESEM and along the cross section at optical microscope (Appendix 1.1.1.1A.5).

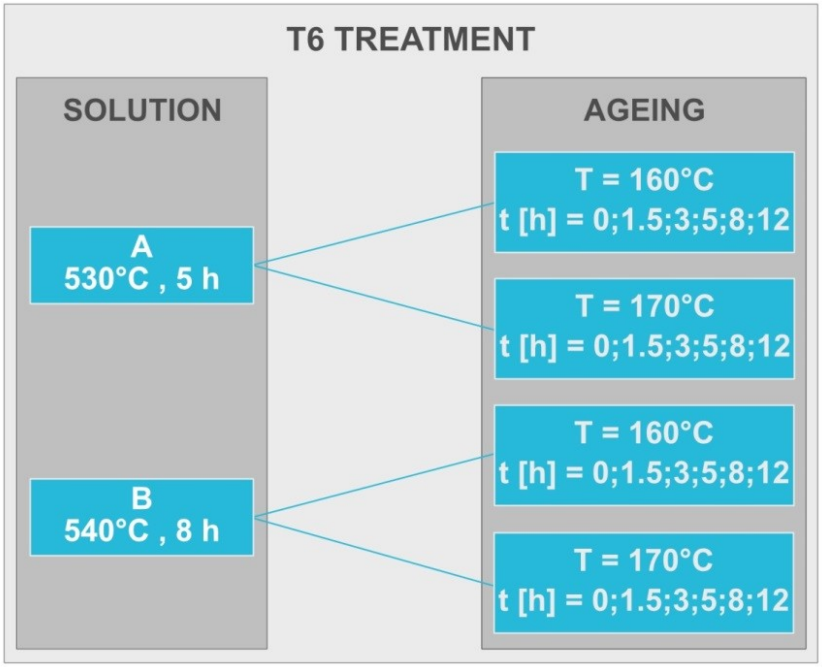


**Figure 48.** Scheme of the solution and ageing conditions investigated on the A357 alloy specimens fabricated by LPBF.

## 3.2.2 Process parameters optimisation

The optimum process conditions were defined as the conditions under which the A357 alloy samples by LPBF with the highest relative density and scanning speed were obtained. Table 9 contains the LPBF process parameters chosen for specimen fabrication, productivity and density values. Relative density of specimens was calculated assuming a theoretical value of 2.68 g/$cm^3$, adopting

Archimedes method (Appendix A.3). The productivity of the LPBF process is given by the process-related build-up rate, in according to the following equation [312]

$$Prod_{LPBF} = h_d \times t \times v \qquad \left[\frac{mm^3}{s}\right]$$

The main influencing variables to decrease the time required by laser beam to melt the powder layer and thus manufacture parts economically, are hatching distance (hd), layer thickness (t) and scan speed (v). The layer thickness and scan speed are limited amongst other factors by the available laser power. The hatching distance is limited by the diameter of the beam and typically equals approximately 0.7 times the beam diameter [312].

**Table 9.** Combination of process parameters, productivity and relative density.

| Number samples | v [mm/s] | $h_d$ [mm] | $Prod_{LPBF}$ [$mm^3/s$] | Relative density [%] |
|---|---|---|---|---|
| **1** | 800 | 0.20 | 4.80 | 99.39 |
| **2** | 1000 | 0.10 | 3.00 | 99.54 |
| **3** | 1200 | 0.20 | 7.20 | 96.00 |
| **4** | 1000 | 0.20 | 6.00 | 97.92 |
| **5** | 800 | 0.17 | 4.08 | 99.78 |
| **6** | 1000 | 0.17 | 5.10 | 99.17 |
| **7** | 800 | 0.10 | 2.40 | 99.81 |
| **8** | 1200 | 0.17 | 6.12 | 98.08 |
| **9** | 1200 | 0.10 | 3.60 | 99.94 |
| **10** | 600 | 0.10 | 1.80 | 99.45 |
| **11** | 600 | 0.17 | 3.06 | 99.09 |
| **12** | 600 | 0.20 | 3.60 | 99.36 |
| **13** | 700 | 0.10 | 2.10 | 99.16 |
| **14** | 700 | 0.17 | 3.57 | 99.17 |
| **15** | 700 | 0.20 | 4.20 | 98.97 |

Considering the results, it is possible to see that for $h_d$ of 0.20 mm, increasing the scan speed from 800 to 1200 mm/s, there was a rapid decrease in density but a rapid increase of the productivity. Starting from the assumption of reaching a final density greater than 99.5 % and a good productivity, it was considered the sample 5 fabricated with v of 800 mm/s and $h_d$ of 0.17 mm to fabricate the specimens for

the mechanical tests. This sample shows a slightly lower density with respect to sample 9 but it has a higher productivity than it.

### 3.2.3 T6 treatment optimisation

Figure 49 shows the results of microhardness measurements for the two different solution treatments and two different ageing temperatures tested. Porosity level in the T6 treated specimens was measured by Archimedes method, but not noticeable differences with the as-built conditions were observed. Focusing on the ageing time influence, it can be noticed that for the solution B, samples over-ageing started after 3 h, instead for the solution A the over-ageing began only after 5 h. Considering the temperature, ageing at 160 or 170 °C seemed do not affect the peak hardening conditions, while, on the contrary, a slight difference could be observed in the pre-aged and over-aged conditions.

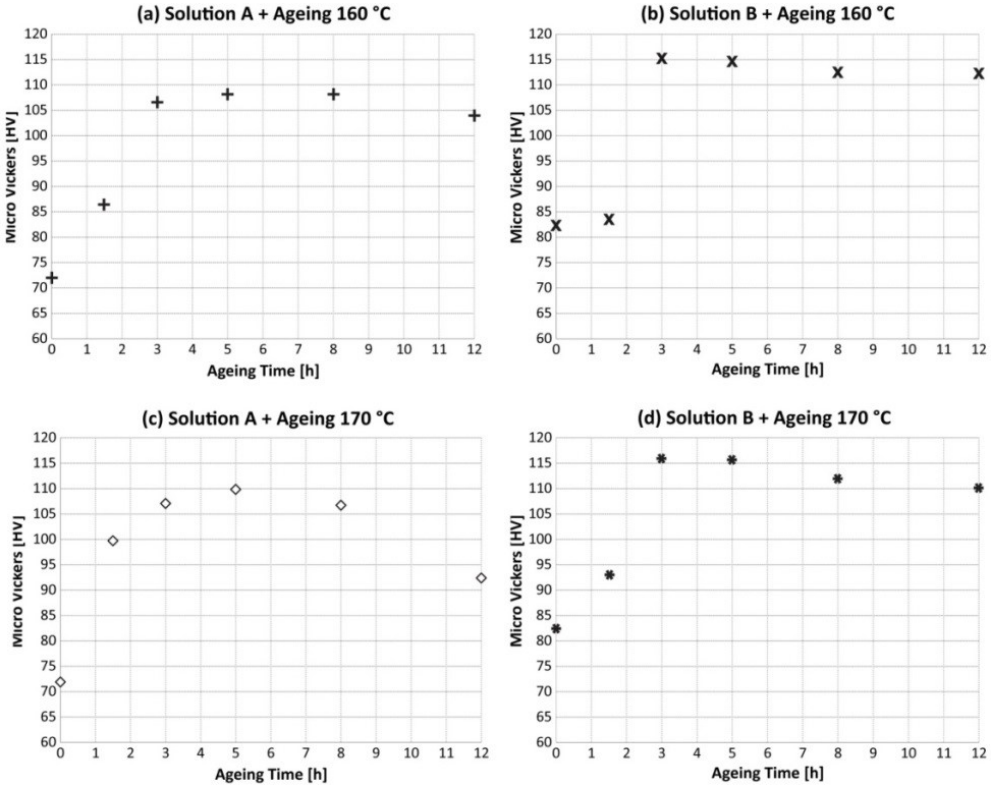


**Figure 49.** Vickers microhardness ($HV_{0.1}$) mean values obtained for samples after different T6 conditions.

Vickers microhardness measurements are reported in Table 10. The highest hardness was obtained in the as-built conditions, so without treatment, while the lowest value was obtained after the stress relieving. Analysing in detail the results

of T6 treatment, it appears that a maximum hardness of 116 $HV_{0.1}$ was reached for samples $T6_{B,170,3}$. In the case of no ageing conditions, the mean hardness for the 8 h solution treated was 82 $HV_{0.1}$, 14% higher than the 5 h ones, while after 12 h ageing the maximum hardness reached is 112 $HV_{0.1}$. This last value was 20% higher than the mean hardness of the samples treated at $T6_{A,170}$ (92 $HV_{0.1}$).

**Table 10.** Hardness measurements on LPBF A357 samples in different conditions.

| LPBF A357 Specimens | $HV_{0.1}$ | S.D. |
|---|---|---|
| **As-built** | 119 | 2 |
| **Stress relieved** | 80 | 2 |
| **Stress relieved + $T6_{B,170,3}$** | 116 | 2 |

All the data provided show a net difference between the two solution treatments A and B, particularly they underline the great improvement given by longer solution treatments to hardness rather than by shorter ones. As described by Aboulkhair et al. [294] in the case of precipitation hardening treatment material strengthening is governed by the presence of precipitates (Orowan strengthening), solid solution strengthening and dislocation strengthening. In the case of A357 fine Si particles and Mg precipitates act as obstacles to the dislocation motion in peak hardening conditions: the microstructural characterization of the $T6_{B,170,3}$ specimens is given in the following section of the study. On the other hand during over-ageing the Orowan strengthening effect is depressed and hardness reduces. This feature can be observed for both $T6_A$ and $T6_B$ at 12 h ageing time (Figure 49).

From the micro hardness measurements prolonging the solution treatment from 5 h to 8 h considerably varied the material behaviour in the early stages of ageing and in the peak hardening conditions. Longer solution treatments differently from shorter ones favour higher diffusion of Si inside the microstructure, completely homogenizing the LPBF microstructure and enhancing material micro hardness [294]. This behaviour appears to be opposite to the typical cast parts treatments, where shorter solution treatments are preferred to longer one [273]. These statements are consistent with previous studies in literature: as stated by Leuders et al. [313], LPBF produces very fine microstructures that require adjustments to the post-processing heat treatment conditions traditionally adopted on cast parts. In order to fully exploit the advantages of LPBF technology and fully optimise the material properties of the fabricated parts, further improvements on post-processing treatments, such as stress relieving or T6 treatment, should be explored and studied.

### 3.2.4 Microstructural investigation

In traditional castings processes, during slow cooling, the solid solution of silicon in aluminium easily decomposes with the consequent precipitation of silicon in the form of relatively coarse and rapidly growing particles. On the other hand, in LPBF process, melt powder cools down very rapidly, with a mean rate of $10^3$-$10^5$ K/s [314], creating an anisotropic and ultrafine microstructure. Figure 50 depicts the optical micrographs of the microstructure of the LPBF A357 specimens, built with optimised process parameters (Sample 5), along the vertical building direction. The repeated melting and subsequently rapid cooling of the material create complex structures composed by melt pools overlapping (Figure 50a). The shape and orientation of the melt pools depends on the scanning strategy adopted during the process [14]: using 67° rotated scanning strategy, such as in this study, melt pools growth direction repeatedly varies between each layer (Figure 50a,b).

In order to study the melt pool morphology, particularly the average width and depth values, one cubic specimen of 10 mm side was-built with unidirectional scanning and optimised process parameters (Figure 51a). The average width of melt pool was 183.0 ± 17.8 μm and the average depth 37.8 ± 12.3 μm: they were measured by image analysis according to the simplified sketch illustrated in Figure 51b. The results confirm the good consolidation obtained by choosing Sample 5 process parameters (Table 9). Indeed the average melt pool depth exceeded the 30 μm layer thickness while the average width corresponded to a balanced overlapping of the laser tracks. However rotated scanning strategy allows to reduce both porosity and residual stresses compared to unidirectional strategy, even if the melt pool dimensions do not greatly vary between the two cases [297].

As for other Al-Si-Mg alloys processed by LPBF [189] also A357 microstructure is constituted by cellular-dendritic structures of supersaturate α-Al phase surrounded by residual Si phase network, as shown in Figure 50. The high cooling rates developed during LPBF process do not allow the diffusion of Si outside the α-Al phase favouring the creation of a supersaturated solid solution constituted by very fine cellular structures (Figure 50d). The cellular dimensions are not equal inside the melt pool (Figure 50c) due to different thermal histories of the material [241]. Indeed the highest temperature is located at the centreline of the melt pool and decrease radially towards the scan track borders [296].

As in the case of AlSi10Mg [178], also in the A357 LPBF microstructure three distinctive regions with different cellular morphologies could be observed in the melt pool (Figure 52a): coarse cellular region, heat affected zone (HAZ) and fine

cellular region. The coarse cellular region (Figure 52b) and the HAZ (Figure 52c) characterized the melt pool boundaries with cellular-dendrites of few microns elongated in the direction of main heat flux. The melt pool borders represented the overlapping areas between two subsequent laser tracks and stayed at higher temperature and longer time compared to the fine cellular region of the melt pool (Figure 52d): such conditions of higher temperature and longer times favoured the Si diffusion out of the supersaturate α-Al phase and the cellular growth [201].

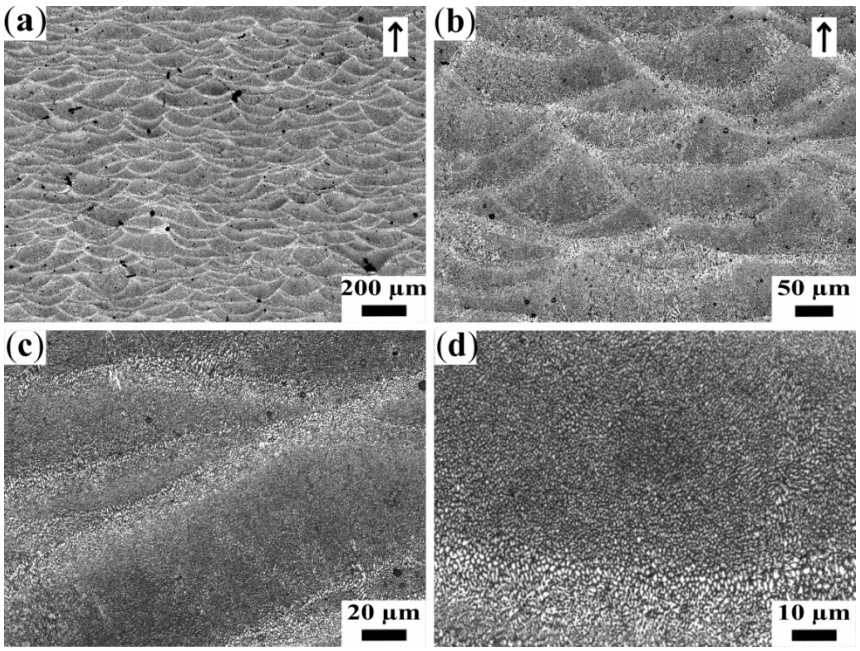


**Figure 50.** Optical micrographs of as-built A357 specimens vertical sections at different magnification. In (a) and (b) the complex melt pool structures are exposed; the black arrows indicate the building direction of the specimen. In (c) and (d) the very fine and anisotropic microstructure at melt pool borders are reported.

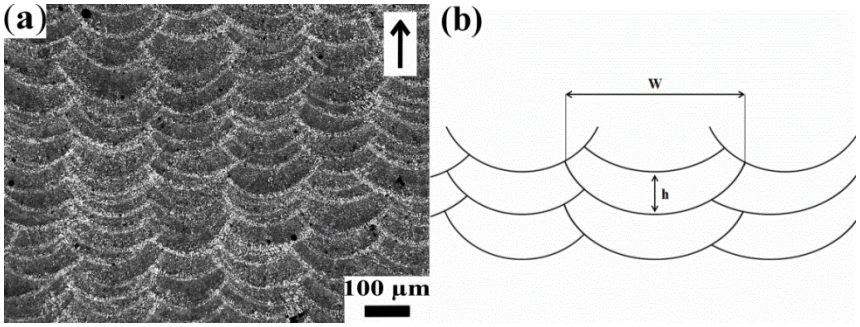


**Figure 51.** Optical microscopy of A357 specimen built with optimised parameters and unidirectional scanning strategy (a). The arrow in the upper left corner represents the building direction of the sample. On the right (b) a schematic representation of the melt

pool structure is given: w indicates the width of the melt pool while h is the depth in the centre of the melt pool.

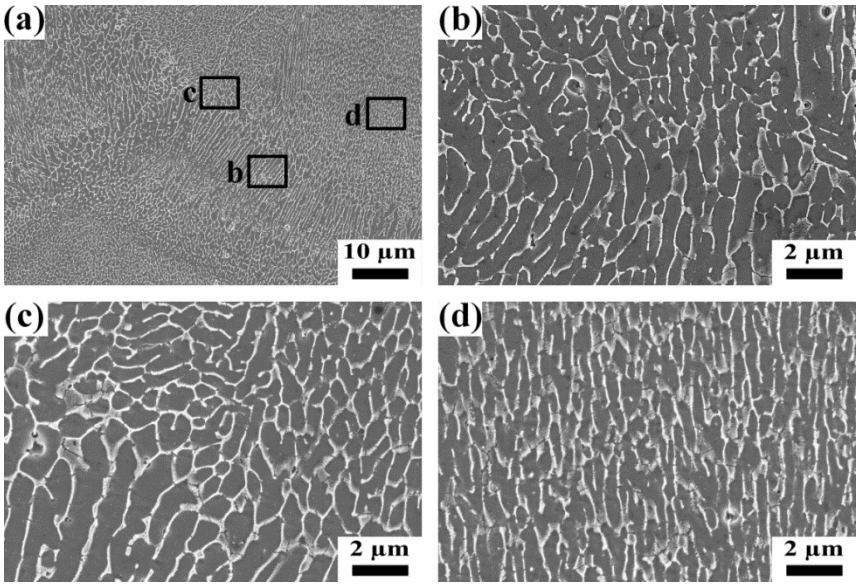


**Figure 52.** FESEM micrographs of melt pool structure in as as-built LPBF A357specimens. In (a) the overall structure is shown with three distinct areas highlighted: coarse cellular region representing the boundaries of the melt pool (b), HAZ (c) and fine cellular region which defines the melt pool centre (d).

EDS analysis of the as-built material is shown in Figure 53 (Appendix A.5). As expected silicon appeared to be mostly located at the cellular boundaries, with a mean concentration around 7.9 wt%, while in the α-aluminium phase its concentration decreased to 5.9 wt% (Figure 53c). Si concentration in supersaturate α-Al largely exceeded the maximum solubility at equilibrium conditions (~ 1.6 wt.%) [281] and it was ever greater than in the case of another rapid solidification process as melt spinning [310]. On the other hand, aluminium appeared to be homogeneously dispersed over the entire LPBF microstructure (Figure 53b). The high concentration of Si in α-Al solid solution of as-built LPBF specimens was also confirmed by XRD analysis showed in Figure 54: the Si peaks were much weaker and broader than the Al ones due to the higher Si solubility in the material [315]. Moreover, EDS analysis revealed a slight presence of Mg (Figure 53d) inside the as-built material. At the same time XRD measurements (Figure 54) displayed the presence of $Mg_2Si$ precipitates: the low signal of $Mg_2Si$ peak in the XRD pattern can be related to the small amount of Mg present in the chemical composition of A357 alloy (Table 7), as described in the study carried out by Rao et al. [201].

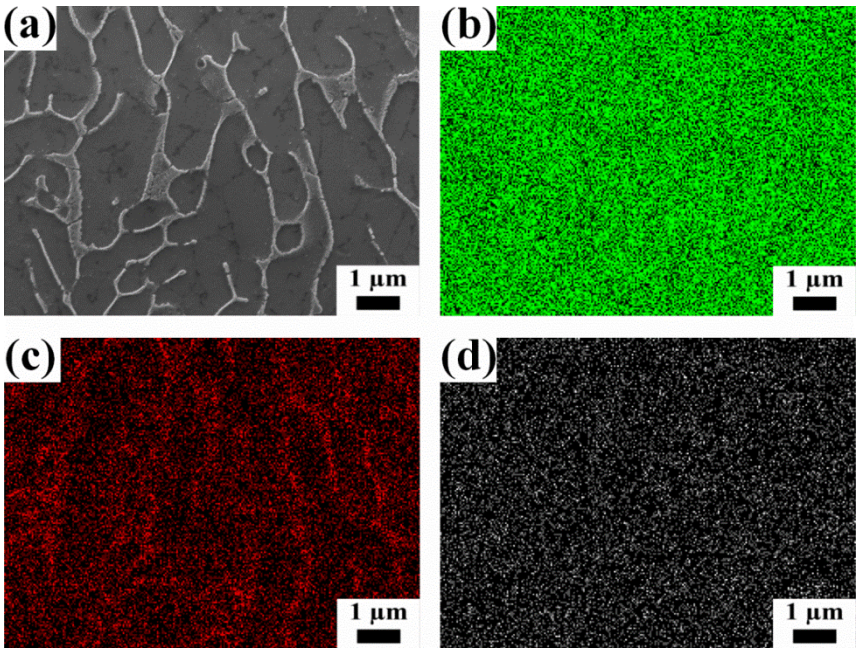


**Figure 53.** EDS analysis of as-built LPBF A357 specimens: (a) FESEM micrograph and corresponding EDS maps of (b) aluminium, (c) silicon and (d) magnesium.

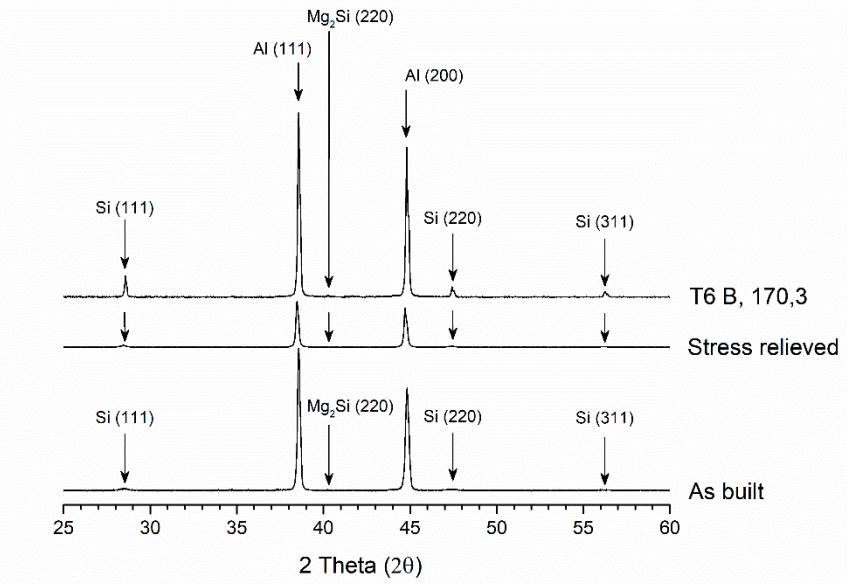


**Figure 54.** XRD patterns of A357 alloy samples in different conditions.

Post-processing stress relieving treatment reduces the residual stresses generated inside the material [316]. In Figure 55a,b the micrographs of the stress relieved specimens observed by optical microscopy are reported: it can be noted that the melt pool structures were maintained after heat treatment. FESEM

investigations (Figure 56) showed how the cellular boundaries did not disappear but became blurred compared to as-built conditions (Figure 56b,c). During the heat treatment Si was rejected from the supersaturated α-Al phase altering the sub-micrometric structure [299]. Thus the sub-micrometric Si network lost its continuity disaggregating in to smaller Si precipitates almost preserving the original shape of the cell, as shown in Figure 56d [277].

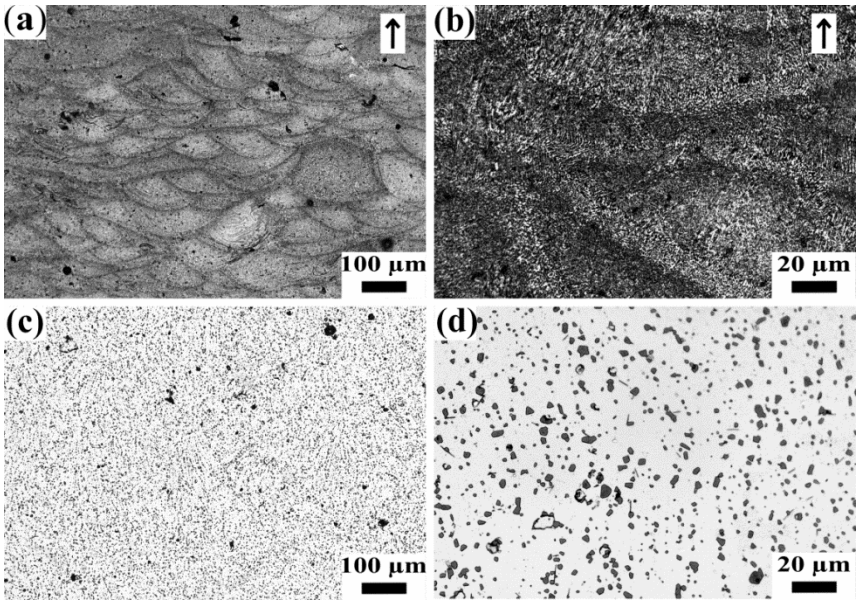


**Figure 55.** Optical micrographs of etched microstructures A357 specimens fabricated by LPBF, after stress relieving (a,b) and $T6_{B,170,3}$ heat treatment (c,d). The black arrows in the upper micrographs indicates the building direction of the specimens.

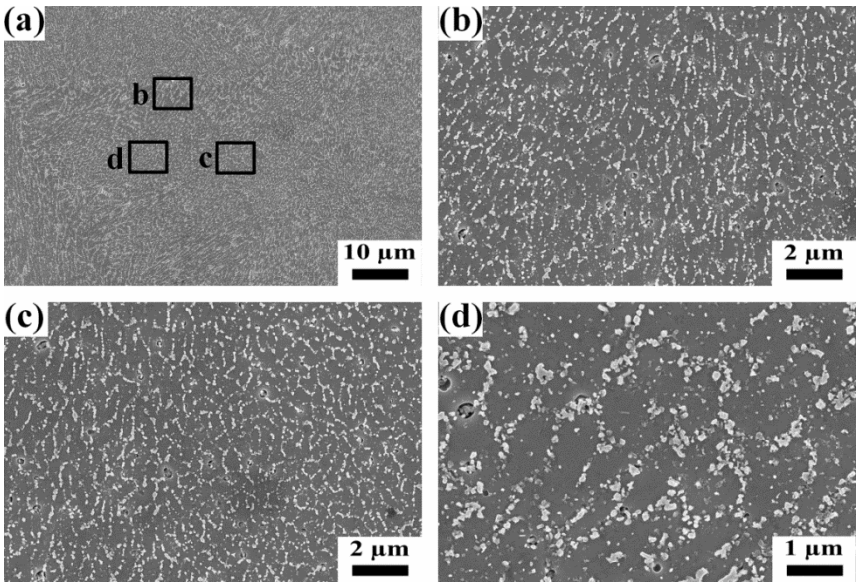


**Figure 56.** FESEM micrographs of etched microstructures of A357specimens produced by LPBF, after stress relieving. In (a) the overall structure is shown and three distinct areas are highlighted: coarse cellular region representing the boundaries of the melt pool (b), fine cellular regions within the melt pool core at different magnification (c,d).

The effects of subsequent $T6_{B,170,3}$ heat treatment can be seen in Figure 55c,d and Figure 57. T6 precipitation heat treatment totally modified the original LPBF microstructure [290] eliminating all the anisotropic features such as melt pools and laser track traces (Figure 55c). Supersaturate α-Al cellular-dendritic structures and Si network disappeared leading to a homogeneous microstructure constituted by α-Al matrix, Si particles and Mg precipitates [209]. During solution heat treatment Si diffused from supersaturate α-Al phase, dropping Si concentration inside the solid solution to equilibrium conditions [317]. By quenching and ageing treatment fine distributed particles of Si formed (Figure 55d) and further grew through a combination of Ostwald ripening and coalescence of adjacent Si particles [292]. By image analysis of FESEM micrographs Si particles dimensions were measured to be comprised between 1 and 5 µm. XRD analysis (Figure 54) showed an increase of the Si peak intensity and the presence of $Mg_2Si$ precipitates after $T6_{B,170,3}$ heat treatment. The higher intensity of silicon peaks can be attributed to the greater amount of free Si present in the form of micrometric particles (Figure 57b,c). The $Mg_2Si$ presence was further detected by FESEM investigations as showed in Figure 57d, even if the amount of Mg and precipitates in the LPBF material was very low according to EDS analysis.

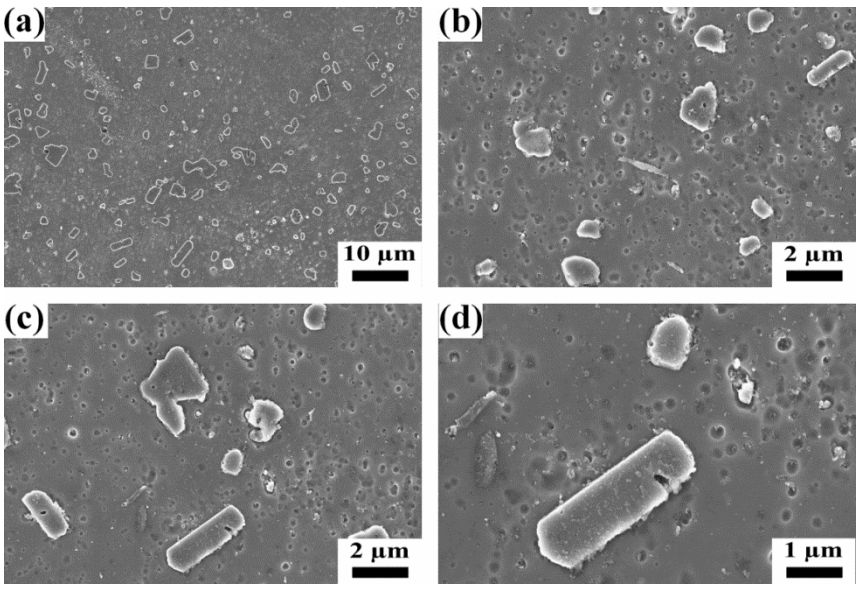


**Figure 57.** FESEM micrographs of etched microstructures of A357specimens produced by LPBF, after $T6_{B,170,3}$ heat treatment: overall microstructure (a) micrometric Si particles (b,c) and $Mg_2Si$ precipitates (d).

### 3.2.5 Tensile properties

The tensile properties of A357 sample are summarized in Table 11, while the stress-strain curves are shown in Figure 58. Compared to T6 cast parts A357 LPBF as-built specimens achieved higher tensile properties and lower ductility [318]. There are three main factors which enhance the hardness and tensile strength of LPBF parts: grain boundary strengthening, solid solution strengthening and dislocation strengthening [273]. The grain boundary strengthening was provided by the ultrafine microstructure present inside the as-built material: it can be described by the Hall-Petch relationship $\sigma = \sigma_0 + k \cdot d^{-1/2}$ where $\sigma$ is the material strength, $\sigma_0$ is the frictional stress for dislocation motion, k is the Hall-Petch coefficient, and d is the grain size [287]. The solid solution strengthening in the LPBF was favoured by the high concentration of Si and other elements (such Fe, Mg) inside the supersaturate α-Al phase (Figure 53) [277], while the dislocation strengthening was resulted of the pile-up of dislocations inside the microstructure [273].

From Figure 58 it can be observed that all post-treatments altered the tensile properties with respect to the as-built conditions. Stress relieving treatment strongly affected yield ($Rp_{,0.2}$) and ultimate tensile strength (UTS) of LPBF parts, reducing their values of 30 and 34 %, respectively. On the contrary, elongation at break increased of 36 %. During annealing the cellular boundaries inside the microstructure lost their continuity (Figure 56) and cells slightly coarsened: as a consequence the capacity of dislocation pile-ups resulted weakened [209]. Furthermore Si started to diffuse out of the solid solution decreasing the solution strengthening of the material [292]. Both these effects were responsible of the tensile and yield strength reduction and consequently of the increase of ductility.

$T6_{B,170,3}$ treatment improved the tensile strength of A357 samples after stress relieving. The $Rp_{,0.2}$ mean value raised up to 249 MPa, similar to the one obtained before any post-treatment, while E and UTS values increased of 10 % respect to annealed conditions. Tensile and yield strength increased after T6 following a trend similar to the one observed for micro hardness measurements (Table 10): after $T6_{B,170,3}$ the material was strengthened by Si and $Mg_2Si$ precipitates (Orowan strengthening), solution strengthening and dislocation strengthening [294]. Al-Si-Mg alloys are commonly strengthened by age hardening mechanism where the dispersoids present inside the microstructure (Figure 57) act as obstacles to dislocations motion enhancing the material strength [319]. Compared to stress relieving conditions $T6_{B,170,3}$ peak hardened specimens showed 38 % lower ductility: such reduction could also be related to Si and $Mg_2Si$ precipitates presence

and to reduction of dislocation motion. Although the elongation at break after $T6_{B,170,3}$ treatment was comparable to as-built conditions and furthermore fitted the same range of values of T6 A357 cast parts [319].

As already stated, LPBF parts possess an high grade of residual stresses in the as-built conditions which generate distortions and warping effects [153], so a stress reliving treatment is mandatory for industrial production of near-net-shape parts which should meet dimensional tolerances. A subsequent T6 is able to increase the mechanical properties back to values comparable to the as-built conditions and to eliminate anisotropic features such as melt pools and laser track traces (Figure 55) leading to more uniform and isotropic material [290].

**Table 11.** Tensile properties of A357 specimens produced by LPBF and tested in as-built conditions and after two heat treatments.

| Specimens | E [GPa] | $R_{p,0.2}$ [MPa] | UTS [MPa] | ε [%] |
|---|---|---|---|---|
| **As-built** | 82 ± 4 | 245 ± 4 | 386 ± 4 | 5.2 ± 0.4 |
| **Stress relieved** | 75 ± 1 | 189 ± 3 | 288 ± 5 | 8.2 ± 0.9 |
| **Stress rel + $T6_{B,170,3}$** | 83 ± 3 | 249 ± 9 | 307 ± 10 | 5.1 ± 0.3 |

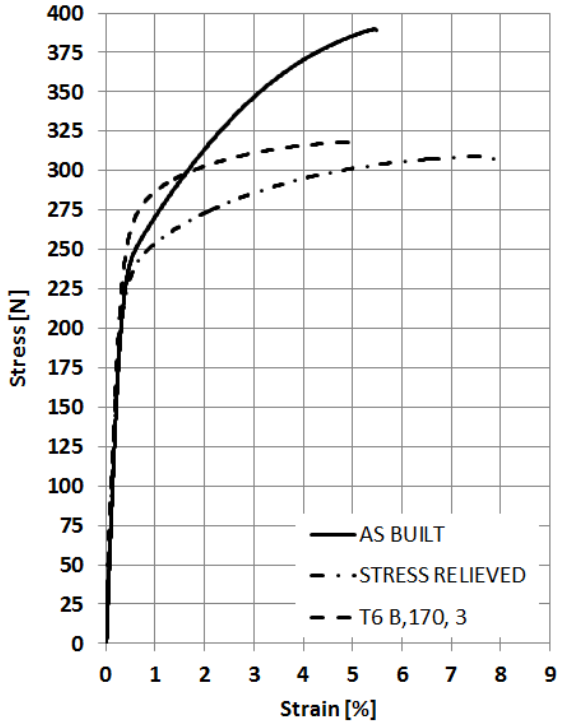


**Figure 58.** Stress strain curves of room temperature tensile tests performed on A357 specimens by LPBF in different conditions.

The fracture surfaces of different samples were analysed by FESEM and some significant micrographs are reported in Figure 59: all LPBF samples exhibited trans-granular ductile fracture. In as-built conditions fracture surface appeared to be mostly constituted by ultrafine dimples (Figure 59a,b) with a mean dimension around 500 nm, comparable to Si enriched dendrite cells present in the as-built microstructure (Figure 52). Generally dimples presence in LPBF fractography is attributed to micro-void coalescence [320] but according to Tradowsky et al. [321] the LPBF ultrafine rough morphology appears to be connected to the sub-micrometric Si network. Since Si dendrites network possessed an higher hardness and lower ductility compared to the α-Al phase, it could be possible that failure followed the pattern of the Si sub-micrometric cells during fracture, generating the ultrafine roughness in the fracture surfaces (Figure 59b). Further investigations upon crack path in the LPBF as-built microstructure during tensile load application are needed.

After stress relieving treatment (Figure 59c,d) fracture surface showed a ductile fracture mode and appeared to be constituted by fine dimples as in the case of as-

built conditions but with slightly coarsen dimensions than before (Figure 59c). Furthermore small silicon particles could be observed inside the dimples (Figure 59d): such features could be ascribed to the microstructure modification induced by the heat treatment (Figure 56). Indeed differently from as-built conditions where a continuous sub-micrometric Si network was present, after stress relieving Si dendrites lost their continuity and disaggregated in smaller Si precipitates, almost preserving the original shape of the cell (Figure 56d). As a consequence the capacity of dislocation pile-ups resulted weakened and ductility increased [209]. After $T6_{B,170,3}$ the samples showed much coarsen microstructure compared to as-built and stress relieved conditions [297], with micrometric dimples (Figure 59e) and microvoid coalescence morphology (Figure 15f) [292]. Furthermore micrometric Si particles inside the dimples could be observed: the presence of cracks could be noted inside silicon particles attesting the low ductility measured during tensile testing (Figure 59e).

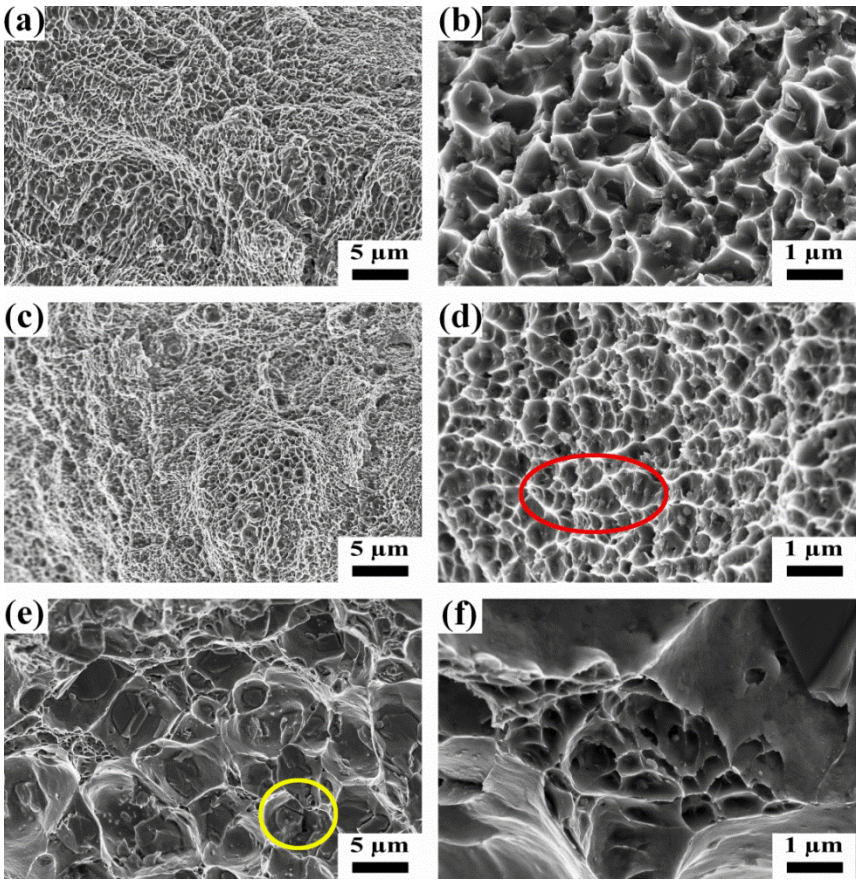


**Figure 59.** Fracture surfaces analysis through FESEM of A357 LPBF samples: (a) and (b) as-built condition, (c) and (d) after stress relieving, (e) and (f) after $T6_{B,170,3}$. The red circle in (d) highlights the presence of small aligned silicon particles inside dimples, while the yellow circle in (e) shows a cracked silicon particle.

In Figure 60 the fracture surface cross-sections of the tested specimens are reported. In the as-built and stress relieved materials (Figure 60a,b) fracture followed partially the interface between the melt pool core and boundary. Indeed the melt pool boundaries were characterized by elongated cellular-dendrites of few microns (Figure 52b) and resulted softer than the melt pool core which was instead characterized by finer cells (Figure 52d) [273]. For the $T6_{B,170,3}$ specimens instead voids were generated by de-cohesion at Si particles (Figure 60c): subsequent void coalescence favoured the fracture propagation until the sample failure.

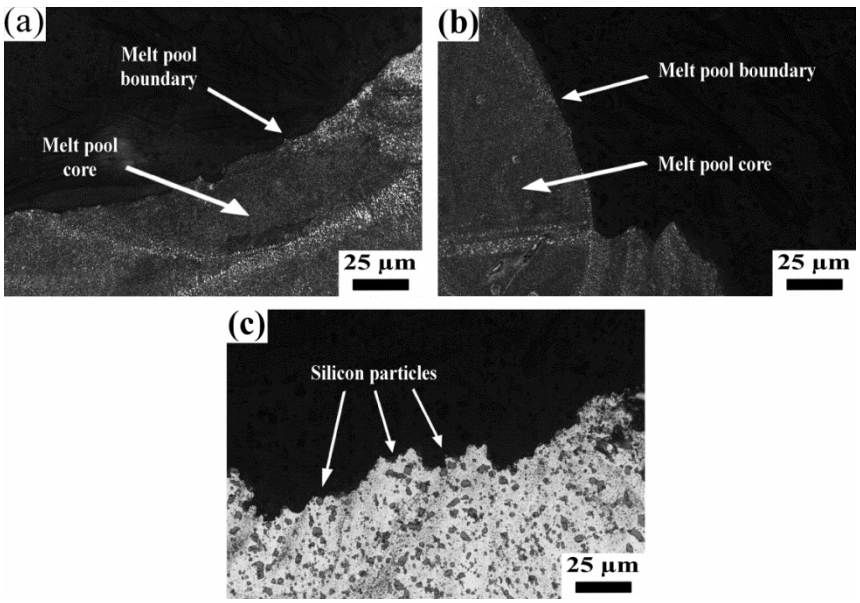


**Figure 60.** Cross-sectioned fracture surfaces analysis at optical microscope after etching: (a) as-built condition, (b) after stress relieving, (c) after $T6_{B,170,3}$.

### 3.2.6 Conclusions of the study

Processing of A357 alloy gas atomized powders by LPBF technique was investigated, through process parameters optimization and mechanical properties investigations after different heat treatments. The obtained results show that:

- Varying hatching distance and scanning speed it was possible to obtain 99 % dense A357 components through LPBF process keeping relative high productivity.

- LPBF parts possess an high grade of residual stresses in the as-built conditions which generate distortions and warping effects, so a stress reliving treatment is mandatory for industrial production of near-net-shape parts which should meet design dimensions and tolerances. However a common stress relieving treatment at 300 °C for 2 h reduces tensile strengths and hardness; therefore a following heat treatment, like a T6 precipitation hardening, could be performed.

- Due to the ultrafine microstructure LPBF fabricated parts required different heat treatment conditions compared to cast parts. Two T6 treatments on stress relieved LPBF specimens were investigated by micro hardness. From the

results appeared that longer solution treatments enabled to obtain higher hardness values and to reduce the time required to reach peak hardening conditions. A maximum hardness value of 116 $HV_{0.1}$, comparable to as-built parts conditions, was obtained after 8 h solution treatment, water quenching and 3 h ageing treatment ($T6_{B,170,3}$).

- The microstructure of A357 specimens fabricated by LPBF were analysed by optical and electron microscopy in as-built conditions and after stress relieving and T6. As expected stress relieving favoured the diffusion of Si out of the α-Al supersaturate phase and the disaggregation of sub-micrometric Si network maintaining the original melt pool structures. Instead subsequent $T6_{B,170,3}$ eliminated the melt pools and laser track traces leading to more uniform and homogeneous microstructure composed by α-Al matrix, Si particles and $Mg_2Si$ precipitates.

- From tensile tests of machined samples appeared that the $T6_{B,170,3}$ treatment after stress relieving was effective to increase elastic modulus and yield strength, reaching values comparable to those of as-built samples. Microstructural and fracture surfaces revealed dimples growth, which confirmed the higher ductility of the material. After $T6_{B,170,3}$ the presence of cracked Si precipitates inside microscopic dimples was detected and related to the low ductility measured during tensile tests.

# Chapter 4

# LPBF of Ti-6Al-4V alloy

## 4.1 State of the art

Titanium is a transition element, with a melting point of about 1678 °C, which undergoes an allotropic transformation in the solid state at 882 °C, referred to as β-transus temperature [280], in which a change from the α phase (hexagonal closed-packed structure, hcp) to β one (body-centred cubic structure, *bcc*) occurs. Thanks to the presence of a stable and inert oxide layer, which spontaneously forms on its surface, chemical pure Ti has an elevated corrosion resistance and biocompatibility, and is widely considered to be the most compatible metal for the human body. Furthermore, by adding α-stabilizer elements (Al, C, O, N, B), or β-stabilizer elements (Fe, Mo, V, Cr, Ni, Cu, W, Co, Nb, Ta) the α → β transition temperature can be modified. Therefore, depending on the chemical composition and allotropic structure, titanium alloys are classified as α alloys, near-α alloys, metastable β alloys, β alloys and α + β alloys [280,322]. α and near α alloys exhibit low values of tensile strength at room temperature but superior corrosion resistance. Compared with the α one, the β phase induces a lower resistance to plastic deformation and higher ductility, and a significant anisotropy of physical and mechanical properties. The α + β alloys possess higher strength due to the biphasic microstructure, whereas β alloys possess a low elastic modulus and superior corrosion resistance [322,323]. Among these alloys, Ti-6Al-4V has now the greatest commercial importance, combining more than 50 % of the sales of Ti based materials both in Europe and the United States [280].

Ti-6Al-4V alloy offers significantly high strength-to-density ratio and resistance to corrosion and fracture-related properties together with high creep and fatigue resistance. For these reasons this alloy has been used since many decades in aerospace, automotive and biomedical sectors, although the high costs of production and manufacturing of such material [251]. For example, in aircraft manufacturing Ti-6Al-4V is used for most of the fans for by-pass engines, blades

and discs in the low and intermediate sections of the compressors of jet engines (with temperatures of about 300 °C) (Figure 61) [280,324]. At the same time, such titanium alloy have been applied in several biomedical devices thanks to its high strength and fatigue properties at room temperature, together with a high biocompability and a higher resistance to corrosion compared to the other biomedical alloys [325,326]. The feasibility of Ti-6Al-4V has been considerably useful in the fabrication of cardiovascular, craniofacial, dentistry and particularly orthopaedic implants [327].

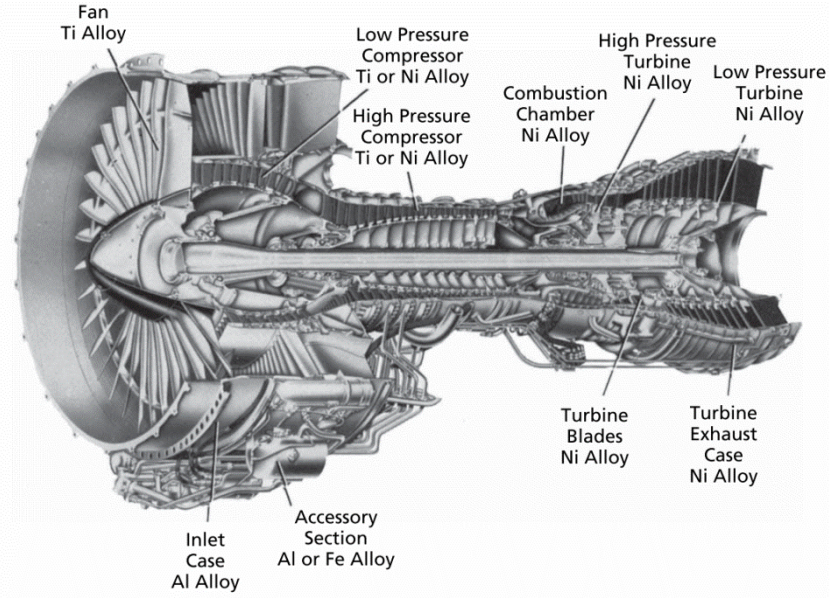


**Figure 61.** Material distribution in a common jet engine [324].

The most employed Ti-6Al-4V components are generally manufactured via conventional forming operations (forging, cold and hot forming, hydroforming), machining processes (drilling, milling, turning), and alternative machining techniques such as laser cutting and water-jet cutting. Due to its relatively low ductile yield and high tensile strength, machining of titanium and its alloys represents a considerable manufacturing challenge. The low elastic modulus may cause greater "springback" effect, which is a geometric change underwent from a part at the end of the forming process. Therefore, the need to have rigid setups can induce high pressure and temperature in the tool contact zones. This can represent a problem since at higher temperatures the titanium becomes more chemically reactive. In addition, over-heating of the surface can result in interstitial absorption of nitrogen and oxygen, that can create a series of micro cracks which reduce the performance and the fatigue properties. For such reasons, the conventional cutting

speed values for titanium alloys machining are relatively low, involving longer and more expansive productions with respect to aluminium alloys or steels. Moreover, Ti alloys possess higher production costs: a Ti ingot can cost about 90 times one steel ingot. Considering also that traditional machining often reaches high buy-to-fly ratios (up to 40:1), the overall cost to fabricate titanium components represents a crucial issue.

The numerous drawbacks of traditional production routes of Ti-based materials offer to AM technologies the occasion to demonstrate their ability to realize near-net-shape parts with comparable or higher features and with a not negligible cost reduction [34]. Furthermore, the complex thermal evolutions and the high temperature gradients of the different AM processes combined with the allotropy of Ti and its alloys give the possibility to widely modify their microstructure and mechanical properties.

Ti-6Al-4V processed by PBF has been widely studied and characterized in the past years, and up to nowadays it has been one of the first materials made by AM to be standardized (ASTM F2924-14 [73] and ASTM F3001-14 [73]) and largely applied in final applications [328–333]. In the next sub-chapters a description of the main features in densification, microstructure, mechanical properties and post-processing treatments of Ti-6Al-4V will be presented.

### 4.1.1 Microstructure and densification

The high performances of Ti-6Al-4V alloy depend on the particular α + β microstructure achievable for this alloy: the ratio between these two phases, their shape and their organisation strongly affect the mechanical properties and the chemical resistance too [280,334]. Commonly size, aspect ratio and morphology of the α and β phases can be controlled and improved by thermomechanical processing, accurately evaluated on the basis of the Ti-6Al-4V phase diagram (Figure 62). For example, working in the α + β temperature range results in α phase (primary α phase) with an equiaxed or globular shape (Figure 63) while exceeding the β transus temperature (β field of the phase diagram) large prior-β grains can be obtained (Figure 64). The fraction of primary α can be controlled by the final working temperature and/or the subsequent post-processing heat treatment [335] while its shape highly depends on the cooling rate. As shown in Figure 65, increasing the cooling rate favours the creation of very fine acicular morphologies: in the case of rapid quenching, martensite species such as α’ and α’’ are generated due to the very high cooling rates [334,336,337]. Foreign elements, such as oxygen,

nitrogen, carbon, have been used as grain refiners and strengthening additions [337]. Oxygen for example is a potent α-phase interstitial solid-solution strengthener because of its ability to modify the lattice parameters ratio (c/a) of the α hexagonal crystal [184,185,338]. Higher O concentrations inside the composition cause a greater increase in the *c* axis than the *a* axis, reducing the number of slip planes and inducing an increase in hardness and strength of titanium alloys [184]. Furthermore oxygen has an α-stabilizing effect which causes the rising of the β-transus temperature, almost with a linear dependence [187].

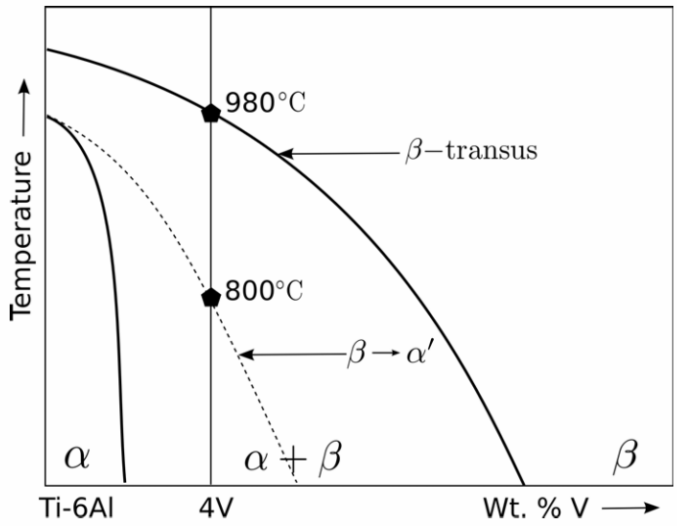


**Figure 62.** Ti-6Al-4V phase diagram [339].

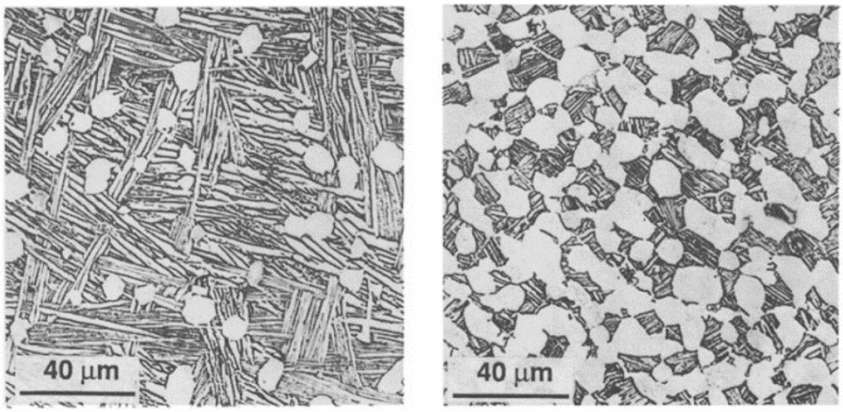


**Figure 63.** Ti-6Al-4V microstructure after α + β processing and solution heat treatment [335].

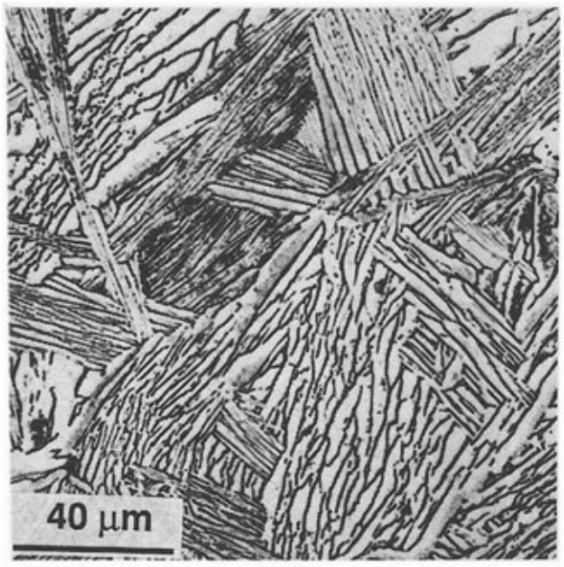


**Figure 64.** Ti-6Al-4V microstructure after β processing [335].

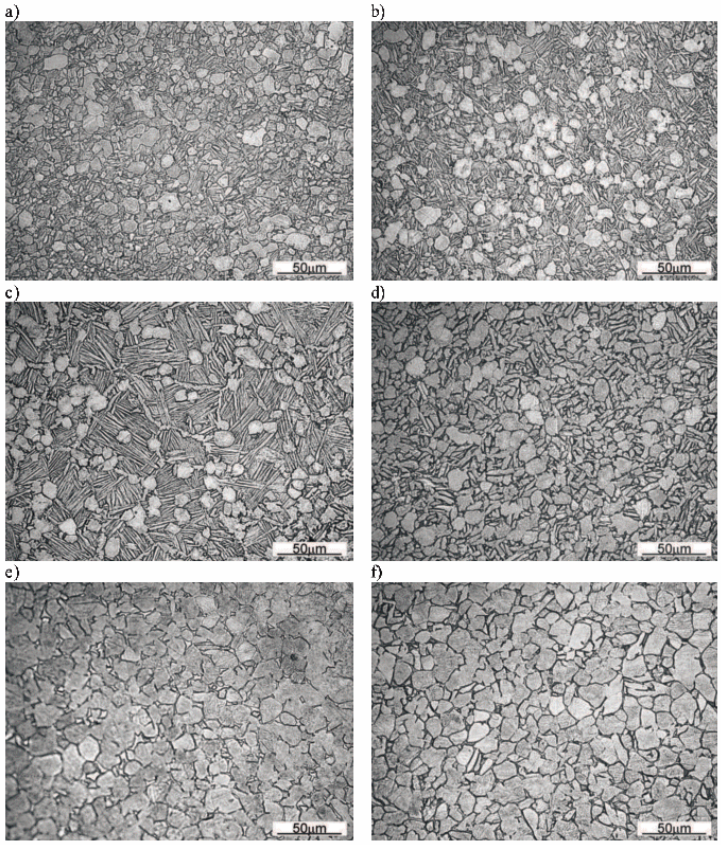


**Figure 65.** Ti-6Al-4V microstructures after cooling from 950 °C at different cooling rates: (a) 7.1 °C/s; (b) 3.2 °C/s; (c) 0.9 °C/s; (d) 0.23 °C/s; € 0.061 °C/s; (f) 0.011 °C/s [337].

As visible in Figure 66, AM manufacturing processes enable to obtain higher tensile strength compared to as-cast and wrought parts. Indeed Ti-6Al-4V parts produced by LPBF are mainly composed by ultrafine α' martensite [228,340,341]: the β→α' martensitic transformation is activated during the extremely-rapid cooling of the melt material [253,342].

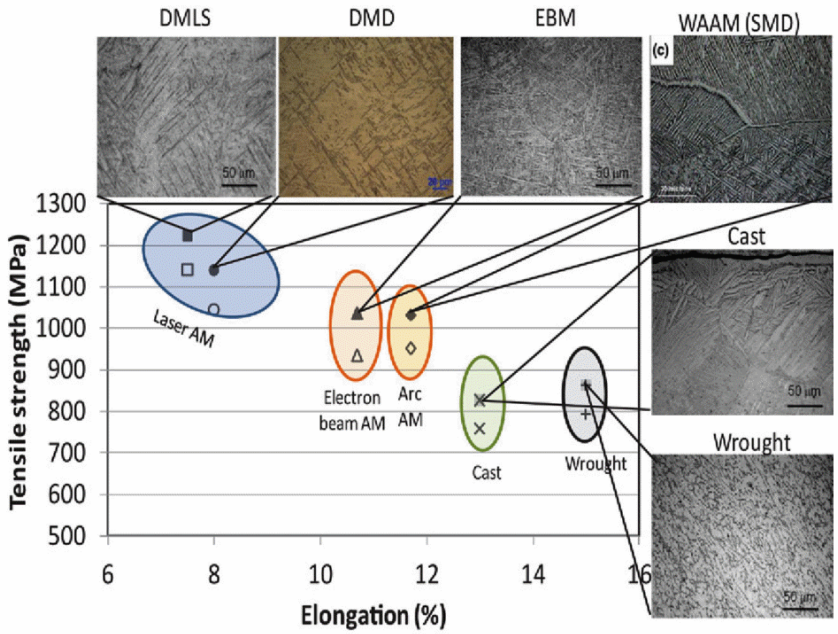


**Figure 66.** Microstructures and relative mechanical properties of Ti-6Al-4V alloy parts produced with different processes [251].

As described by Sun et al. [29], during LPBF there is not enough time for the diffusion of V atoms out of the β phase, enabling the martensitic transformation from the *bcc* β phase to the hcp α' to take place. α' martensite first nucleates and grows inside the original columnar crystals β, forming paralleled primary α', then diffuses throughout the grain boundary. Afterwards, fine secondary α' appears and grows in the boundary of primary α' (Figure 67). Do and Li [253] investigated the effect of three different energy inputs and measured the martensitic lath length in each processing condition. It was found that the increase in laser energy densities noticeably favours the increase in α' lath size. The reason of this phenomenon is correlated to the different cooling rate during LPBF process. Higher scanning rates, can induce an increase in the cooling rate during metal solidification, consequently reducing the α' lath length. On the contrary, with low laser scanning velocities, and so higher energy densities values, the cooling rate decreases enlarging martensite phase.

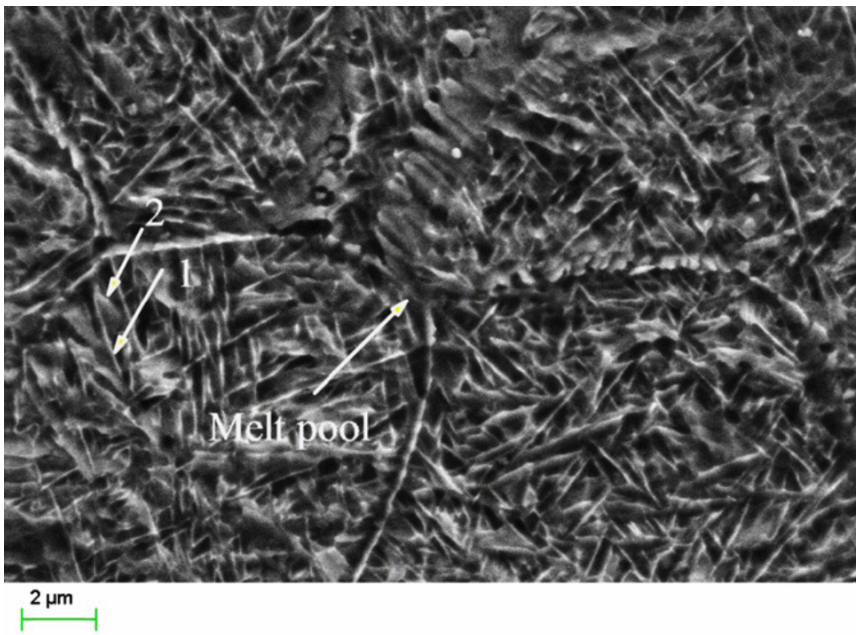


**Figure 67.** LPBF Ti-6Al-4V microstructure showing the martensite structure of the as-built material: the arrow identify the melt pool border and the acicular shape of primary and secondary α' phases [29].

As for other materials processed by LPBF, also Ti-6Al-4V presents an epitaxial growth during the laser processing. Layer by layer, the laser beam remelts also the surface of the previous consolidated layers: in the bulk material temperature increases between 575 and 995 °C, corresponding to martensite start ($M_S$) and β-transus temperatures, respectively [143,340,343]. In such conditions the α' transformation into α + β phases is promoted and favoured creating elongated grains along the building direction [343]. These grains grow along the main heat flow direction and possess a mean length of some millimetres and a mean micrometric width (Figure 68) [228,344–346]. As in the case of α' phase dimensions, also the prior β grains depend on the adopted process parameters. Indeed the width of the columnar grains fits approximately the width of the scan track: raising the heat input would enlarge the scan track width and coarsen the microstructure. Furthermore it must be considered that scanning strategy and scanning speed directly influence the thermal gradients inside the parts and consequently determine the orientation of the columnar grains [272,345]. Thijs et al. [228] found that adopting a unidirectional scanning strategy the elongated grains appeared parallel to each other and tilted 19° away from the building direction, while using a cross-hatching strategy, two grain directions were introduced, one parallel to the building direction while the other tilted of 25°. Similar results were obtain by Simonelli et al. [255] who found that

the elongated grains are inclined of 20° respect to the building direction when a rotated scanning strategy (in this case 67° rotation) was adopted.

Within these grains it is possible to observe the presence of martensitic needles, organized in an herringbone structure and mainly inclined of 40° respect to the building direction [296,342,345,347]. Simonelli et al. [255] deeply studied the relation between prior-β grains and α' martensite through high-resolution EBSD analysis. From the analysis conducted, it was reasonable to believe that the α' grains precipitate in order to satisfy the self-accommodation of the neighbouring α grains. According to this fact, small groups of α' variants prefer to adopt just to two types of possible grain boundary misorientation angles, in order to minimize the average strain energy generated by the β → α' martensitic transformation. From variant frequencies distribution it was established that the overall α' texture appears random because of the elevated number of micrometric α' grains, precipitated from the prior-β grains, that grow in multiple direction and random orientation.

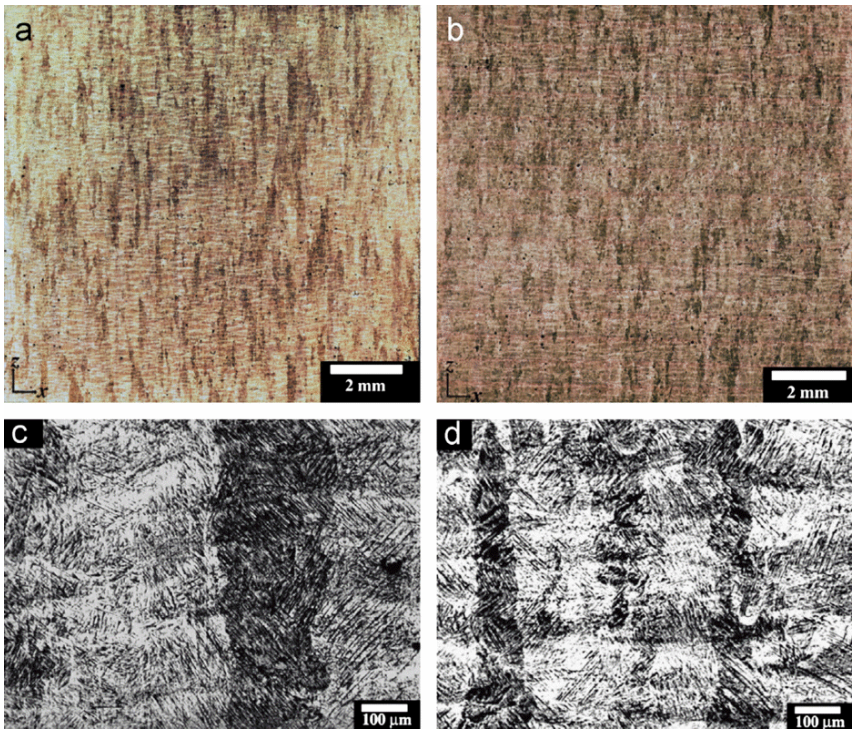


**Figure 68.** Optical micrographs showing the β columnar grains in the microstructure of Ti-6Al-4V alloy specimens processed by means of LPBF, along the building direction: (a,c) vertical samples; (b,d) horizontal samples [345].

As stated before, varying the process parameters modifies the energy input and consequently the thermal history of the material. In an innovative study, Xu et al. [314] investigated the evolution of α' phase during LPBF process, varying the laser parameters, and obtaining an ultrafine α + β lamellar structure adopting a commercial LPBF machine. Firstly they investigated the influence of layer thickness value upon the β columnar width: adopting 30 μm layer thickness, the mean columnar grains width was 15 μm, while with thicker powder layers, up to 60 and 90 μm, the mean width increased to 70 μm. Furthermore, the influence of the focal offset distance (FOD) upon the microstructure was found to be significantly important: this parameter represents the relative position between the laser focal plane and the surface of powder layer and directly influences the amount of energy density delivered to the powder bed [348]. Adopting 60 μm layer thickness and an energy density of 50.62 J/mm$^3$, the variation of FOD parameter between 0 and 4 mm resulted in a different evolution of α' martensite (Figure 69). Indeed with high FOD values the microstructure appeared predominantly composed by α' martensite, while reducing FOD induced the formation of an ultrafine α + β lamellar structure. The reason is related to the variation FOD values has upon the laser spot size: a decrease in the FOD value will reduce the laser spot diameter and so imply an increase in the energy density input. As a consequence the temperature within the melt pool will increase and favour the martensite transformation.

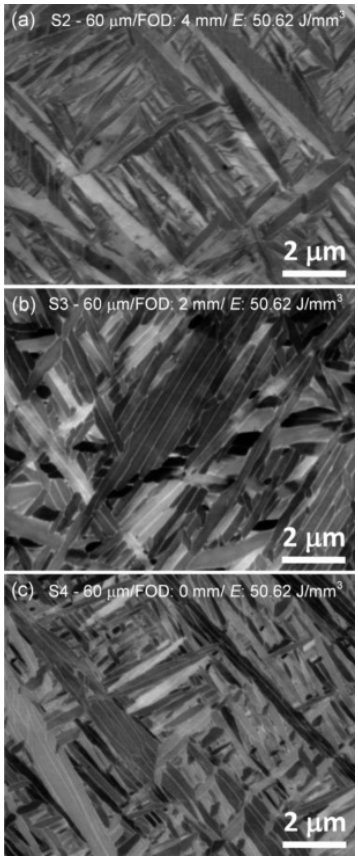


**Figure 69.** Microstructures of Ti-6Al-4V alloy parts fabricated by LPBF adopting different focal offset distance values: (a) 4 mm; (b) 2 mm; (c) 0 mm. It can be noticed how the α' martensitic microstructure present in (a), is transformed into α + β lamellar structure in (b) and (c) [314].

As for the other materials, process parameters optimisation represents a crucial step in the development of Ti-6Al-4V for LPBF, and several studies investigated this matter in order to understand the main relations between melting behaviour and laser parameters adopted [29,349–352]. Gong et al. [350] investigated the process window for Ti-6Al-4V parts made by LPBF and studied the generation of defects inside the material. The process window they evaluated, exposed in Figure 70, can be divided in four zones: "full dense material" (ZONE I), "over melting region" (ZONE II), "incomplete melting region" (ZONE III) and "over heating region" (ZONE OH). Fully consolidated samples were produced only in the ZONE I, while in the ZONE II and ZONE III all the parts produced contained numerous porosities. The difference between these two zones depends on the mechanism which induced the porosity formation. In the case of ZONE II the excess of energy caused the over melting of the material and the entrapment of gas inside the melt material, creating

spherical porosities inside the part. On the other hand in the ZONE III the lack of energy was responsible of defect generation, leaving un-melted particles and irregular shaped pores. On the other hand, in the case of ZONE OH the presence of high residual strains inside the parts, caused by the excess of heating, produced the deformation and the failure of the part during the process.

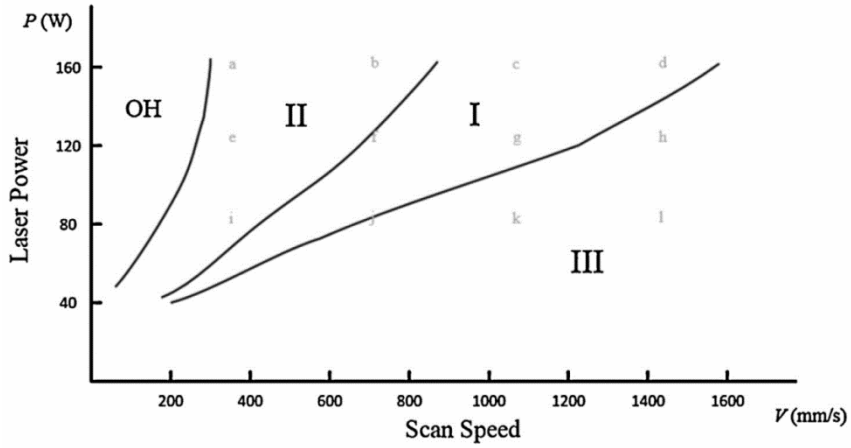


**Figure 70.** Process window for LPBF processing of Ti-6Al-4V alloy. Four regions can be distinguished: (I) full dense material, (II) over melting, (III) incomplete melting, (OH) overheating regions [350].

As already stated, also laser scanning speed and layer thickness influence the melt flow behaviour, affecting both surface structure and porosity development. As described by Qiu et al. [351] high values of scanning speed can increase the melt flow instability and the Marangoni effect, due to the higher evaporation and thermal gradient created inside the material. As a consequence, large melt surface areas and longer melt pool are created during the process. Almost the same effects are obtained when high values of layer thickness (up to 100 μm) are used. The increased volume of powder processed during every layer increases the amount of melt material and melt surface areas, which affect the evaporation phenomenon and the stability of the laser track. Sun et al. [29] adopted the Taguchi method in order to maximize the density value of the parts, keeping the scanning speed constant at 200 mm/s and varying the other process parameters and scanning strategy. According to the results from S/N data analysis, the most influent factor on density value is layer thickness, followed by scanning strategy, linear energy density and finally hatching distance. Raising layer thickness drastically reduces density, while, on the other hand, density value arrives at a maximum when the linear energy density reaches 0.4 J/mm, and then it decreases. Regarding hatching distance, density values are comprised in a narrow range when scan spacing value is modified. Small

hatching distances increase the overlapping region of adjacent scanning lines and uniform energy distribution contributes to the complete melting of the powders. Finally, it was found that the best scanning strategy to maximize density was the *x-y* inter-layer stagger scanning one, as described in Figure 71.

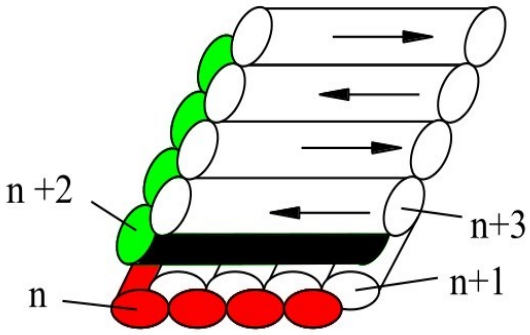


**Figure 71.** X–Y inter-layer stagger scanning strategy adopted during LPBF process in the study of Sun. et al. [29]**.**

### 4.1.2 Mechanical Properties

In the past few years LPBF Ti-6Al-4V has been widely investigated due to its high importance as structural material in aerospace, biomedical and several other industrial sectors [304,348,353–355]. The mechanical response of the as-built material strictly depends on the microstructural features, such as α' martensite and prior-β grains structures [342,344] and interior defects [256,340].

In Table 12 the tensile properties of Ti-6Al-4V parts made by LPBF are listed and compared to traditional manufactured components, highlighting the corresponding microstructure. Thanks to its intrinsic high strength and stiffness, α' martensite provides high tensile strength: UTS and YS of LPBF parts generally overtake the properties possessed by casting or wrought materials, which are characterized by α +β microstructures [342,355]. At the same time, the intrinsic low ductility of α' strongly reduces the elongation at break, as shown in Figure 72. In order to improve ductility, in two different studies Xu et al. [314,348] modified the process parameters, favouring the martensitic phase transformation and obtaining ultrafine lamellar α + β structure inside the parts. From the results appeared that the specimens showed both higher YS (1106 ± 6 MPa) and elongation at break values (up to 11.4 ± 0.4 %) compared to the as-built conditions. The ultrafine laths dimensions induced the high mechanical properties while the substitution of the

brittle α' phase with the more ductile β one, increased the elongation at break of the specimens.

**Table 12.** Mechanical properties and corresponding microstructures of LPBF, cast or wrought Ti-6Al-4V materials.

| Process & Microstructure | Mechanical Properties | | | Reference |
|---|---|---|---|---|
| | YS [MPa] | UTS [MPa] | ε [%] | |
| **LPBF as built Acicular α'** | 1040 | 1140 | 8.2 | Facchini et al. [355] |
| **Hot Working Globular α + β** | 790 | 870 | 18.1 | |
| **LPBF as built Fine α' in columnar prior-β** | 1143 | 1219 | 4.9 | Rafi et al. [356] |
| **LPBF stress relieved Fine acicular α'** | 1137 | 1206 | 7.6 | Vilaro et al. [340] |
| **Casting Globular α + β** | 865 | 980 | 13.5 | |
| **LPBF stress relieved α' martensite** | 972 | 1034 | 5.5 | Mower et al. [304] |
| **Wrought α + β lamellae in α matrix** | 945 | 972 | 10 | |

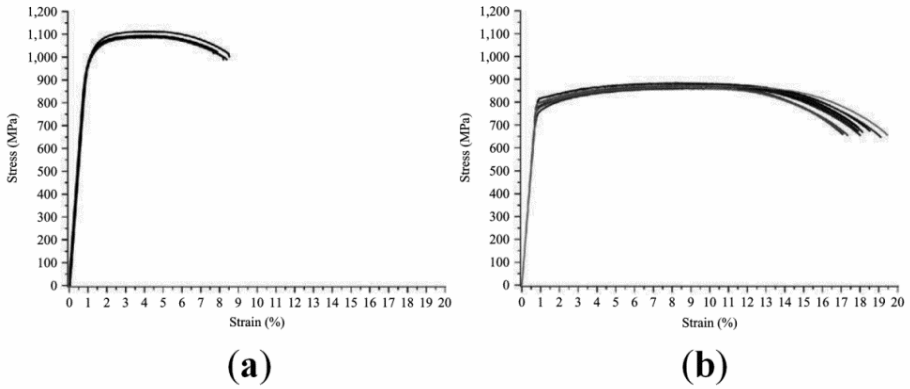


**Figure 72.** Stress strain curves of Ti-6Al-4V specimens in (a) as-built LPBF conditions and (b) hot worked and annealed conditions [355].

β columnar grains influences the mechanical behaviour of LPBF parts generating anisotropy in the tensile properties and fracture behaviour [346,353,356,357]. Qiu et al [345] demonstrated how vertical specimens possessed an elongation at break value between 7 and 10 %, slightly higher than horizontal samples one (between 4 and 6 %). Because the vertically samples have columnar β grains parallel to the building and loading direction, during fracture tortuous crack paths and rougher profiles preferentially formed. In the case of the other building orientations, instead, the β grains are nearly perpendicular to the loading direction and the crack deflection is lowered. The fracture surface appeared to be different between samples realized with the two building strategies: vertical specimens showed rougher fracture surfaces made of fine dimple structure while the horizontal ones presented smoother surfaces constituted of lamellar/cleavage fracture pattern (Figure 73). Furthermore the surface fracture analysis revealed the presence of a significant higher number of opened up porosities in horizontal samples than in the vertical ones: although it was established that the mechanical response anisotropy was much more influenced by β columnar grains rather than pores distribution [344]. It was observed that the surface roughness of the central portion of fracture surfaces in the vertically built specimens was higher than the other building orientations. This feature derives from the fact that vertical oriented parts preferentially fracture either along hexagonal phase boundaries or along the prior-β columnar grains.

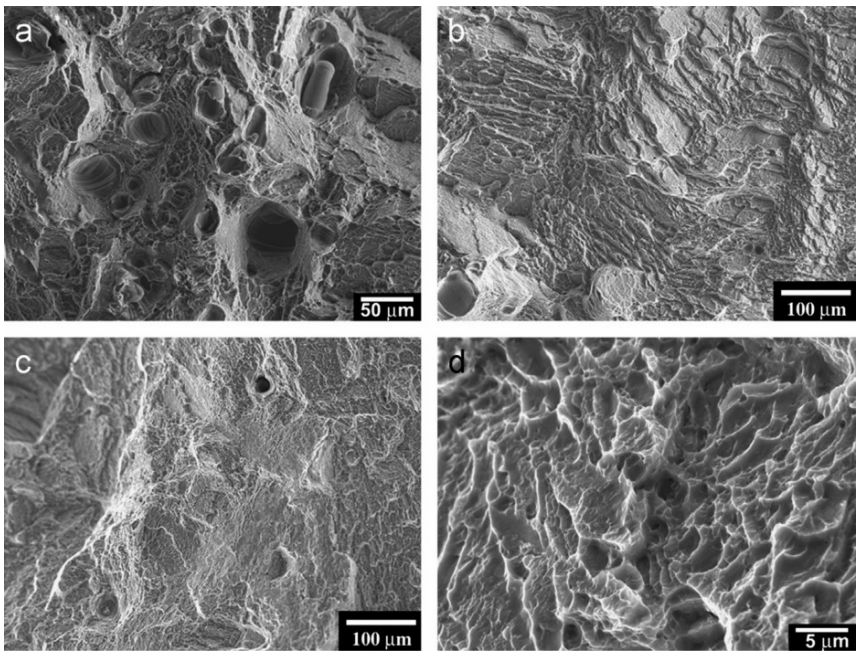


**Figure 73.** Fracture surfaces of as-fabricated LPBF Ti-6Al-4V alloy specimens, built in different building orientations: (a,b) horizontally samples, (c,d) vertical samples [345].

The tensile properties anisotropy of LPBF was also studied and investigated by Simonelli et al. [344]: the mechanical test results are listed in Table 13 while the building orientations adopted are illustrated in Figure 74. Differently from Qiu et al. [345], horizontal specimens, fabricated parallel to the building platform, possessed higher tensile strength than the vertical ones (Figure 73) due to the less presence of porosities and infra-layers defects. During loading, in the case of vertical orientations the layers inside the material are perpendicular to the loading direction as also the interlayer defects. In such conditions, lower stresses are necessary to open up the defects and to favour the nucleation and coalescence of voids. On the opposite way when an horizontally built specimen is subjected to tensile test, layers and defects are parallel to the loading axis and so higher stress levels are necessary to open them up. In both vertical and horizontal samples, fractography investigations revealed that the fracture was mainly trans-granular, with a mixed mode of brittle and ductile failure mechanism [356,358]. Differently from tensile strength and ductility, elastic modulus seems not to be affected by building orientation or even scanning strategy. Both the different orientation of prior-β grains and weak α' (or α) texture does not influence the Young modulus [344].

**Table 13.** Tensile properties of three different oriented Ti-6Al-4V specimens sets, fabricated by LPBF technology adopting a 67° rotated scanning strategy [344].

| Building Orientations | *xy*-plane | *xz*-plane | *zx*-plane |
|---|---|---|---|
| **E [GPa]** | 113 ± 5 | 115 ± 6 | 119 ± 7 |
| **$Rp_{0.2}$ [MPa]** | 1075 ± 25 | 978 ± 5 | 967 ± 10 |
| **UTS [MPa]** | 1199 ± 49 | 1143 ± 6 | 1117 ± 3 |
| **Elongation at break [%]** | 7.6 ± 0.5 | 11.8 ± 0.5 | 8.9 ± 0.4 |

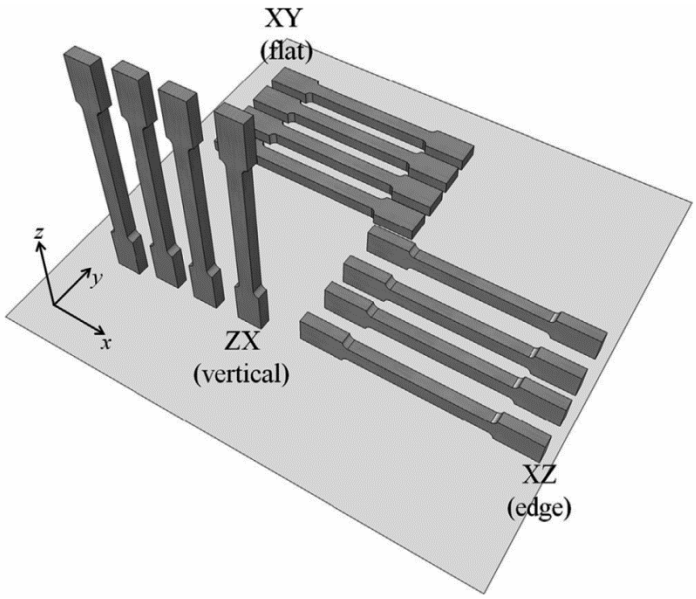


**Figure 74.** Three different building orientations used to investigate the anisotropy level in the mechanical performances of Ti-6Al-4V specimens fabricated by LPBF adopting a 67° rotated scanning strategy [344].

A part from tensile strength and ductility, fatigue resistance represents a fundamental material property for aerospace and biomedical applications: many studies have been focused on this property for Ti-6Al-4V by LPBF (Figure 75) [357–363]. Generally LPBF fatigue life is noticeable lower than conventionally wrought or cast parts. Three main factors have been found to be directly responsible of the poor fatigue resistance: ultrafine microstructures [359,364,365], interior defects [33,366] and rough surfaces [357].

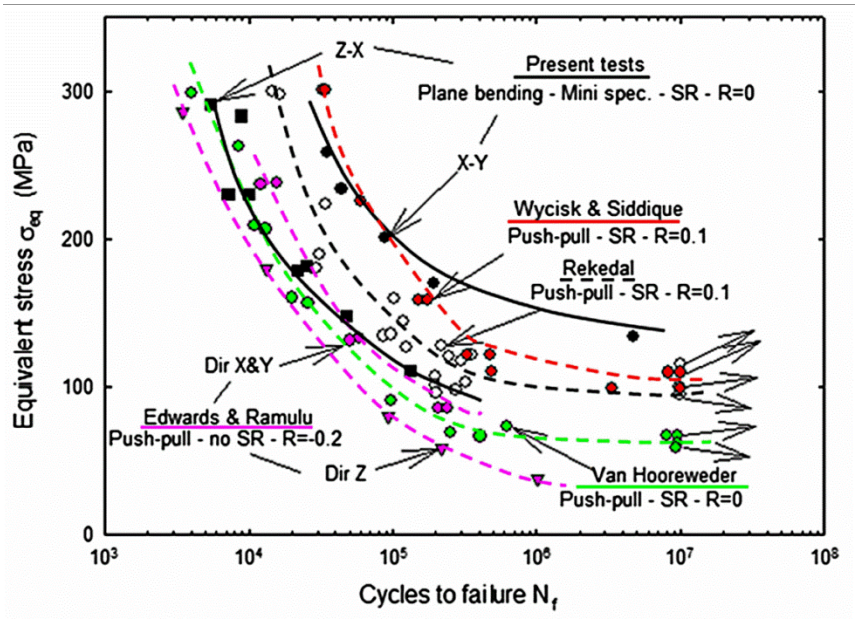


**Figure 75.** Literature review of the fatigue behaviour of Ti-6Al-4V alloy parts fabricated by LPBF [367].

Firstly the α' martensite phase, with its intrinsic brittle mechanical behaviour, reduces the fatigue life of LPBF part compared to the biphasic α + β microstructure of traditional manufactured materials [359]. Secondly, internal porosities such as metallurgical pores created by entrapped gas and un-fused particles act as stress concentrations and sites for fatigue crack initiation (Figure 76) [304,313,353]: generally post-processing HIP is performed to reduce the amount of porosity and to consequently increase the crack initiation time and the fatigue resistance [304,313,361]. Together with internal porosities, low surface finishing plays a dominate role in crack initiation in the as-fabricated parts [353,368]. It has been showed that surface treatments, such as polishing, machining and shot peening, enhance the fatigue resistance [368]. In their study Wycisk et al. [357] investigated three conditions of surface quality of Ti-6Al-4V LPBF parts, respectively as-built ($R_a$ = 13 μm), polished ($R_a$ = 0.5 μm) and shot-peened ($R_a$ = 2.9 μm). The fatigue limit of the as-built samples was 210 MPa and the crack initiation occurred at the rough outside surface, as shown in Figure 77. Instead polished and shot-peened specimens showed an higher fatigue limit, 510 and 435 MPa respectively. In both case the crack initiation was found to be present inside the material from internal pores and defects (Figure 76). As for the tensile properties the fatigue ones vary depending on the building orientation chosen during the process. Horizontal samples generally show higher fatigue strength compared to vertical specimens,

due to the perpendicular orientation of β columnar grains to cyclic stress direction and to the lower interlayer defects presence [353,367].

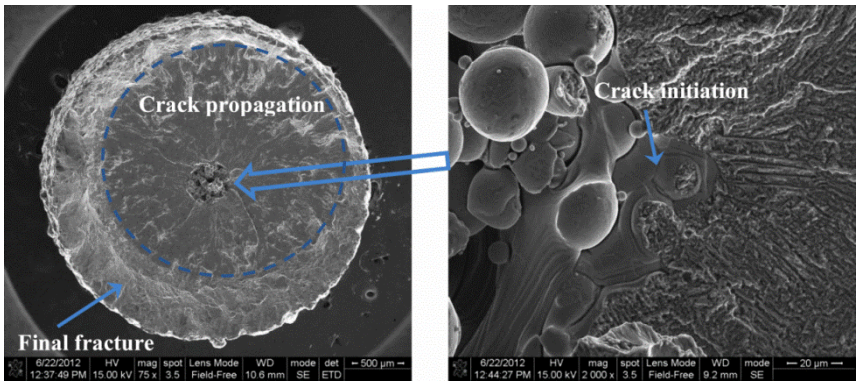


**Figure 76.** Fractography investigation of Ti-6Al-4V alloy fatigue specimen produced by LPBF: crack initiated from central double-conical defect [366].

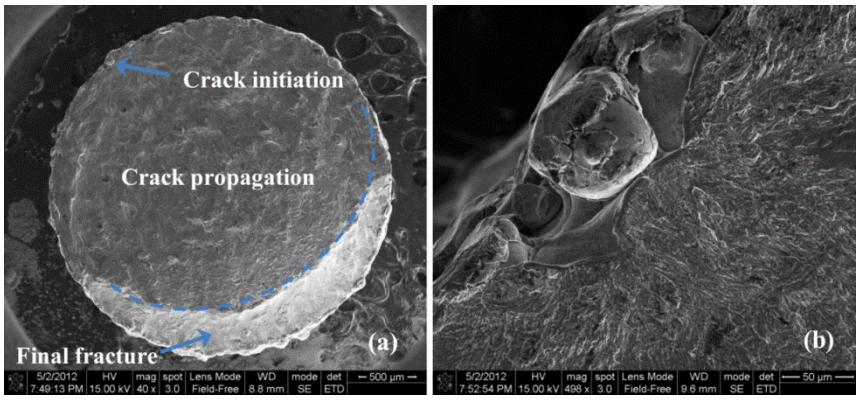


**Figure 77.** Fracture surface of Ti-6Al-4V fatigue specimen fabricated by LPBF. At high magnification (b) it can be noticed that the crack initiated from surface defect [366].

### 4.1.3 Post-processing heat treatments

In order to overtake the mechanical properties limitations of LPBF, such as low ductility and fatigue resistance, post-processing heat treatments are generally performed. These treatments can be designed to reduce the amount of residual stresses or to decompose the α' martensite generating α + β microstructure or to close the porosities and defects present inside the material [304,361,369–373]. Table 14 lists the tensile properties of Ti-6Al-4V specimens fabricated by LPBF and then subjected to various heat treatments. In the case of α/β titanium alloys the post-processing heat treatments can be commonly divided in sub-transus or super-transus treatments depending on the β transus temperature. Varying the chemical

composition, e.g. adding α and/or β stabilizers, alters the α/β phase stability and consequently the transus temperature. For example Ti-6Al-4V Grade 5 has an oxygen content between 0.13 and 0.2 wt.% and the β transus temperature is 1010 °C, while in the case of Ti-6Al-4V Grade 23, which has an oxygen content lower than 0.13 wt.%, the transus temperature is 975 °C [374–376]. Regarding LPBF Ti-6Al-4V, sub-transus heat treatments generally reduce the mechanical strength and improve the ductility thanks to the residual stresses relief and martensite transformation (Table 14) [254,313,314,340,347,363,377]. However, such relative low temperature treatments are not able to erase the columnar β grains and avoid anisotropy [255]. Instead super-transus heat treatments generate equiaxed α + β microstructures eliminating the laser tracks and anisotropic features of LPBF parts. At slow cooling rates, such post-processing treatments are able to enhance the material ductility to the detriment of the mechanical strength [313,340,347,363]. On the other hand, Hot Isostatic Pressing (HIP), usually performed at more than 900 °C and 100 MPa, is able to generates equiaxed α + β microstructures, to close porosities and fuses un-melted particles considerably increasing both static and dynamic mechanical performances [340,345,361,363].

**Table 14.** The main recent researches focused on the mechanical properties of Ti-6Al-4V alloy by LPBF and subjected to different post-process heat treatments. The tensile properties are also related to the specimens building orientation adopted during fabrication: the horizontal samples possess the main axis parallel to the building platform plane (*x-y* plane), while vertical ones has the main axis parallel to the building direction (*z* plane) [378].

| Post treatment | Orientation | Mechanical Properties | | | | Ref. |
|---|---|---|---|---|---|---|
| | | E [GPa] | YS [MPa] | UTS [MPa] | ε [%] | |
| **540 °C, 5 h water quench** | Horizontal | 112.6 | 1118 | 1223 | 5.36 | [347] |
| **640 °C, 4 h** | Horizontal | - | 1104 | 1225 | 7.4 | [377] |
| | Horizontal | - | 11403 | 1214 | 3.2 | |
| | Vertical | - | 1152 | 1256 | 3.9 | |
| **700 °C, 1 h 10 °C/min cool** | Vertical | 117.4 | 1051 | 115 | 11.3 | [361] |
| **705 °C, 3 h air cool** | Horizontal | 114.6 | 1026 | 1082 | 9.04 | [347] |
| **730 °C, 2 h** | Horizontal | 101 | 965 | 1046 | 9.5 | [340] |
| | Vertical | 110 | 900 | 1000 | 1.9 | |
| **800 °C, 2 h** | Vertical | - | 962 | 1040 | 5 | [313] |
| **850 °C, 2 h** | Horizontal | 114.7 | 955 | 1004 | 12.84 | [347] |
| **850 °C, 5 h** | Horizontal | 112.0 | 909 | 965 | - | [347] |
| **900 °C, 2 h 700 °C, 1 h 10 °C/min** | Vertical | 118.8 | 908 | 988 | 9.5 | [361] |
| **940 °C, 1 h air cool; 650 °C, 2 h air cool** | Horizontal | 115.5 | 899 | 948 | 13.59 | [347] |
| **950 °C, 0.5 h** | Horizontal | 118 | 960 | 1042 | 13 | [379] |
| **950 °C, 1 h water quench; 700 °C, 2 h air cool** | Horizontal | 103 | 944 | 1036 | 8.5 | [340] |
| | Vertical | 98 | 925 | 1040 | 7.5 | |
| **1020 °C, 2 h furnace cool** | Horizontal | 114.7 | 760 | 840 | 14.06 | [347] |
| **1050 °C, 2 h in vacuum** | Vertical | - | - | 986 | 13.8 | [363] |
| **1050 °C, 2 h** | Vertical | - | 798 | 945 | 11.6 | [313] |

| | | | | | | |
|---|---|---|---|---|---|---|
| **1015 °C, 0.5 h air cool; 730 °C, 2 h air cool** | Horizontal | 112.8 | 822 | 902 | 12.74 | [347] |
| **1015 °C, 0.5 h air cool; 843 °C, 2 h furnace cool** | Horizontal | 114.9 | 801 | 874 | 13.45 | [347] |
| **1050 °C, 1 h water quench; 820 °C, 2 h air cool** | Horizontal<br>Vertical | 96.7<br>95 | 913<br>869 | 1019<br>951 | 8.9<br>7.9 | [340] |
| **900 °C 100 MPa, 2 h; 700 °C, 1 h 10 °C/min cool** | Vertical | 115.4 | 885 | 973 | 19 | [361] |
| **920 °C 100 MPa, 2 h** | Vertical | - | 912 | 1005 | 8.3 | [313] |
| **920 °C 100 MPa, 2 h** | Vertical | - | - | 1088 | 13.8 | [363] |
| **600-700 °C, 2 h furnace cool; 920 °C 103 MPa, 4h furnace cool** | Horizontal<br>Vertical | -<br>- | 1000<br>930 | 1100<br>1020 | 12.5<br>15.5 | [345] |
| **1050 °C 100 MPa, 2h** | Vertical | - | - | 1007 | 13.5 | [363] |

The LPBF material is originally constituted of fine acicular α'martensite. Since α' is supersatured in vanadium and β phase can solubilize a significant amount of it, during heating vanadium atoms diffuses from α' and β phase begins to nucleate at α' boundaries. Sallica et al. [369] conduced DSC analysis (Figure 78) on as-built and annealed part. It appeared that the exothermic peak, corresponding to α' decomposition, was comprised between 760 °C and 850 °C while the onset temperature of the endothermic peak of the α → β phase transformation appeared at mostly 40 °C lower temperature. An example of such mechanism is shown in Figure 79a: after heating at 780 °C the ultrafine α' microstructure was transformed to a mixture of α fine needles and β grains [347].

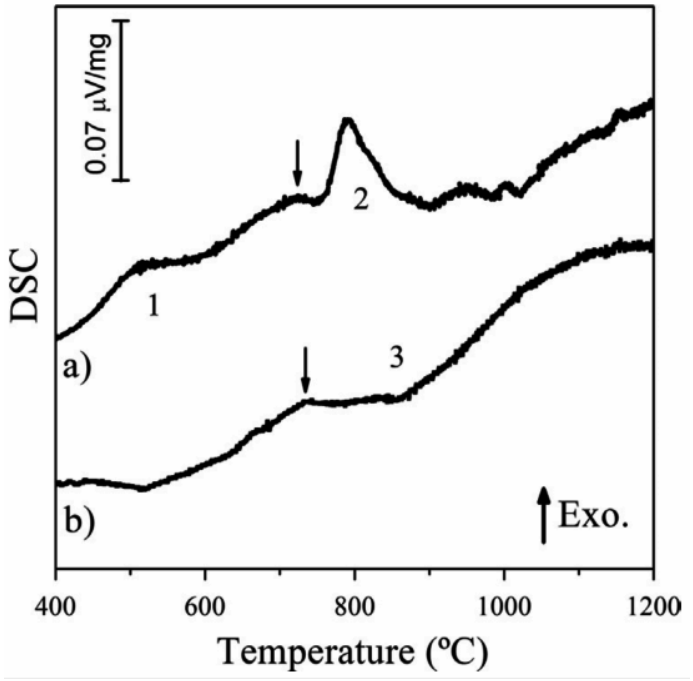


**Figure 78.** DSC thermograms of Ti-6Al-4V produced by LPBFin the (a) as-built conditions and (b) after 1050 °C annealing heat treatment. The numbers indicate (1) the residual stress relaxation exothermic peak, (2) the α' martensite transformation exothermic peak and (3) the α → β transformation endothermic peak, respectively [369].

Temperature increase up to 850 °C and 950 °C favoured the α plates coarsening (Figure 79b) but did not affect the columnar β grains (Figure 80a). Heating at 1015 °C, above β transus temperature, erased the LPBF footprints and columnar grains and favoured the β grains growth (Figure 79c and Figure 80b). When treating below the β transus, residence time is less influencing the grain growth because α and β phases hinder each other, instead, when the material is kept over β transus temperature the effect of residence time is much higher and β phases can grow easier. Cooling rate has a comparable influences on microstructure evolution: below β transus, the α fraction is fairly large and the influence of cooling rate is minimal, while above β transus the cooling rate determines the final dimension and morphology of α phase [347].

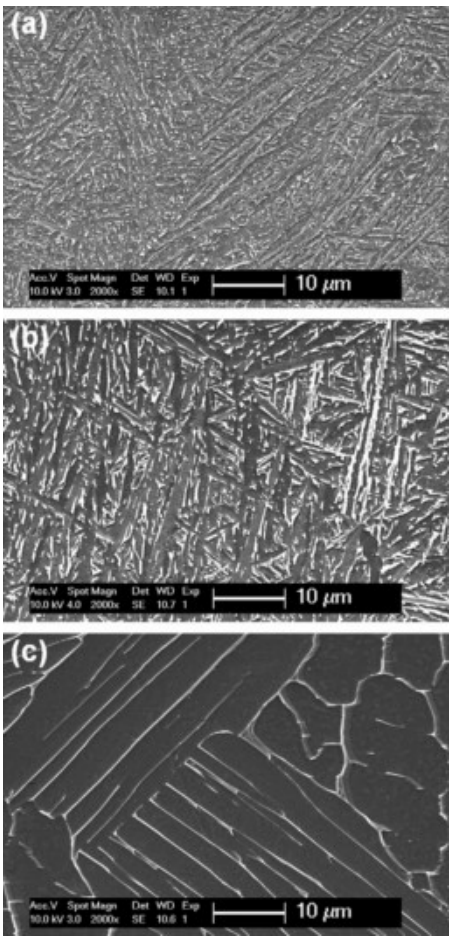


**Figure 79.** Microstructural evolution of Ti-6Al-4V alloy samples produced by LPBF and subjected to different annealing treatments performed at different temperatures for 2 h: (a) 780 °C, (b) 843 °C and (c) 1015 °C. The dark and bright areas in the images were identified as α phase and β phase, respectively [347].

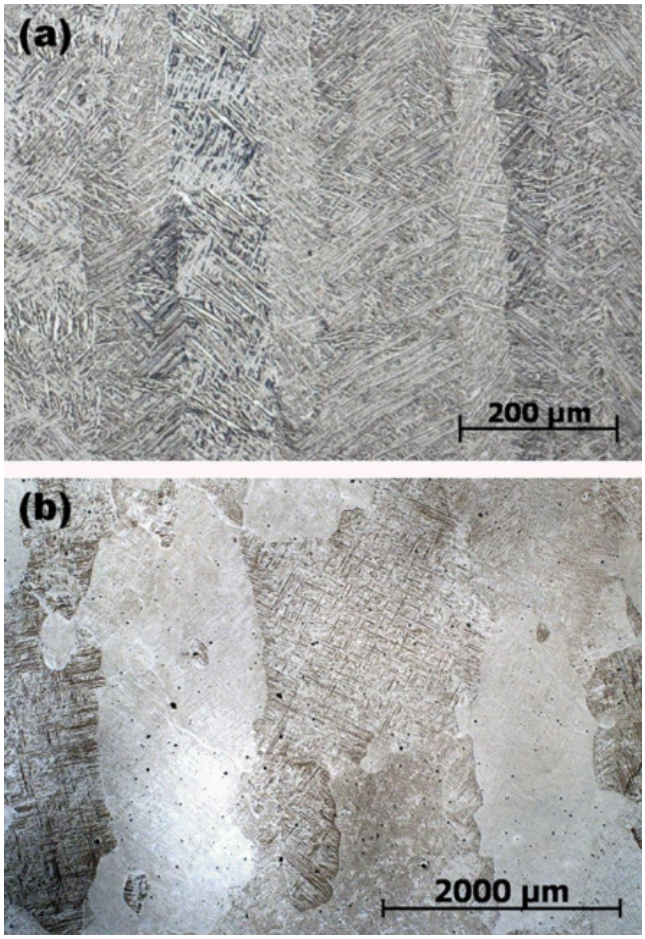


**Figure 80.** Vertical cross section of Ti-6Al-4V parts fabricated by LPBF and subjected to different heat treatments: (a) annealing at 940 °C for 1 h then followed by heating at 650 °C for 2 h; (b) heating at 1015 °C for 2 h followed by water quenching [347].

An example of the correlation between microstructure, thermal treatments and mechanical properties of LPBF Ti-6Al-4V was described by Kasperovich et al. [361]. As displayed in Figure 81, they performed different post-processing heat treatments on as-built LPBF specimens and compared the corresponding microstructures and mechanical properties (Figure 82, LPBF is named SLM) with wrought reference material.

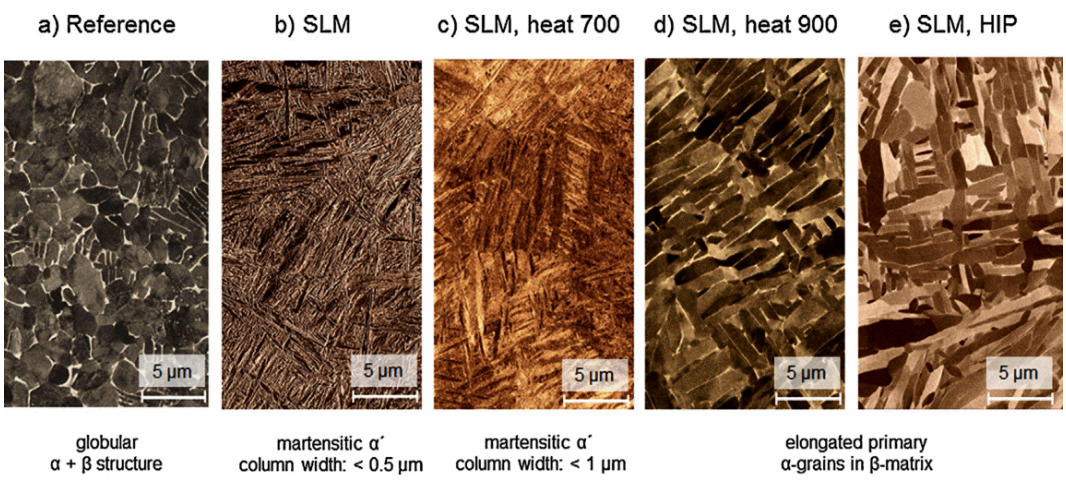


**Figure 81.** Ti-6Al-4V microstructures in (a) wrought conditions (used as reference), (b) LPBF as-built conditions (LPBF) and (c-e) after different heat treatments [361].

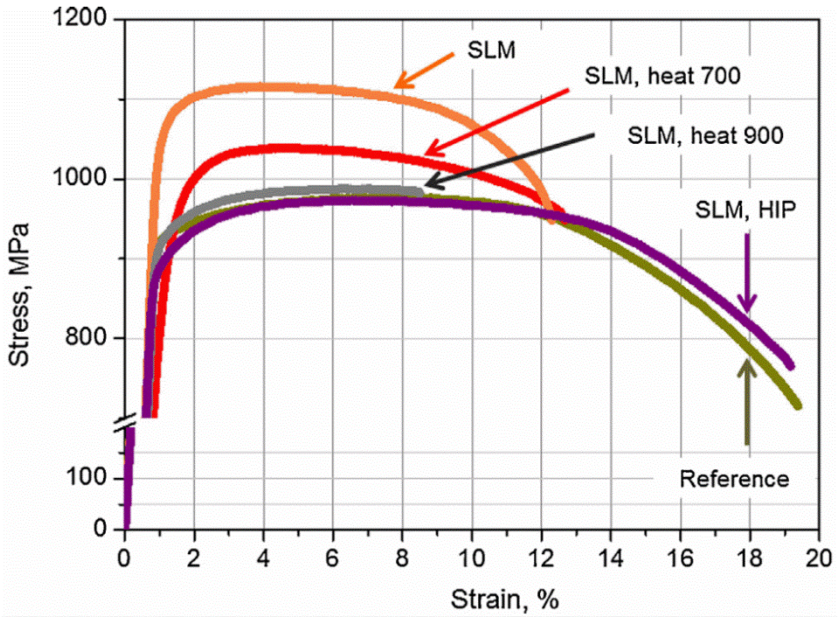


**Figure 82.** Stress-strain curves of Ti-6Al-4V alloy parts in as-wrought conditions (Reference), in SLM as-built conditions and after different post-processing heat treatments [361].

The typical microstructure of traditional wrought material (Figure 81a), constituted by α-globular phase dispersed in an biphasic α + β matrix, provided good compromise between tensile strength and ductility (YS = 914 ÷ 931 MPa; UTS = 973 ÷ 1002 MPa; ε = 18.8 ÷ 19.6 %) instead LPBF specimens (Figure 81b) showed superior strength and reduced ductility due to α' martensite presence (YS

= 984 ÷ 988 MPa, UTS = 1151 ÷ 1157 MPa, ε = 10.2 ÷ 11.3 %). Heating at 700 °C for 1 h favoured the beginning of martensite transformation, obtaining an overall microstructure constituted by fine α needles and enlarging of β columnar grains width (Figure 81c). This type of heat treatment leaded to lower UTS and higher YS values than the as-built conditions (UTS = 1115 ÷ 1116 MPa; YS = 1045 ÷ 1054 MPa): such annealing was considered as possible stress relieving treatment for LPBF parts, although ductility improvement was not considerably high (ε = 9.5 ÷ 12.3 %). Further temperature increase to 900 °C produced a microstructure made of elongated α grains embedded in α + β grain boundaries (Figure 81d,e): chemical analysis showed a phase distribution of 93.5 % α-Ti and 6.5 % β-Ti, with only 2 % vanadium inside the alpha phase and more than 20 % inside the β one. Relative tensile strength decreased compared to previous conditions (UTS = 973 ÷ 988 MPa, YS = 885 ÷ 908 MPa). Although ductility values showed big difference between annealed and HIPped conditions (ε = 9.5 % and ε = 19.0 %, respectively). Indeed HIP suppressed the interior defects greatly improving the elongation at break to values comparable with wrought reference conditions (Figure 82): porosity content was lowered from and initial content of 0.5 % in the as-built conditions to 0.01 % in the HIPped one. A part from ductility improvement, also fatigue resistance improved considerably thanks to defects elimination: indeed while LPBF as-built specimens resisted up to 5.6 x $10^3$ cycles, HIPped ones reached 3 x $10^5$ cycles, almost two orders of magnitude higher. These results confirm the general opinion that residual porosities, un-fused particles and interior defects in general, are the principal causes for LPBF poor fatigue resistance [304,313,360,363].

## 4.2 Study and characterisation of Ti-6Al-4V alloy processed by LPBF

Among the industrial application of Ti-6Al-4V alloy, Ti-6Al-4V grade 5 and grade 23, also known as Ti-6Al-4V Extra Low Interstitial (ELI), are the commercial grades most used in the aerospace and biomedical sectors. The principal difference between these two metal systems consists in the lower oxygen content present in the ELI grade: according to standards, Ti-6Al-4V grade 5 contains an O % not superior to 2000 ppm while in Ti-6Al-4V ELI O % does not exceed 1300 ppm [72,73]. Oxygen acts as solid solution toughener, increasing tensile strength and decreasing ductility and fatigue life [335].

In the past years several studies have been addressed on the investigation of the mechanical and fatigue properties of Ti-6Al-4V made by LPBF. Most of the studies

have been performed adopting Ti-6Al-4V grade 5 [250,380] or ELI grade [254,342,343,353,356]: most all of the researchers focused on the correlation between LPBF parts microstructure and mechanical performances also considering the effects of LPBF process parameters [253,342,350,381] and possible post-processing heat treatments [304,346,361]. However to the author knowledge no studies have been carried out on the comparison of the fatigue properties of Ti-6Al-4V grade 5 and grade ELI parts made by LPBF.

The aim of the following research focuses on the comparison of the mechanical and fatigue properties of Ti-6Al-4V parts fabricated by commercial LPBF machine with different post-processing heat treatments, building directions and oxygen content. The raw material consisted in two sets of Ti-6Al-4V gas atomised powders, with low and high oxygen content, respectively, in order to simulate the processing of Ti-6Al-4V ELI and Ti-6Al-4V grade 5, respectively. Tensile and fatigue specimens were fabricated parallel to the building platform and parallel to the building direction and subsequently machined. Three different post-processing conditions were investigated: stress relieving, stress relieving plus heat treatment and stress relieving plus HIP. Moreover the microstructure and chemical compositions were analysed and correlated to the microhardness, tensile and fatigue properties.

### 4.2.1 Materials properties

Two different Ti-6Al-4V gas atomised powders were provided by Falcontech company, one with low oxygen content (< 1000 ppm) and the other with high oxygen content (> 1600 ppm): Table 15 lists the chemical composition and the particle size distribution as provided by the supplier. The powders morphology was preliminary investigated by field emission scanning electron microscopy (FESEM) analysis (Appendix 1.1.1.1A.1) as shown in Figure 83. Both the Ti-6Al-4V powders appeared to possess spherical shape, with the smaller particles adhering at bigger spheres surfaces.

**Table 15.** Chemical composition and particle size distribution of the Ti-6Al-4V gas atomised powders processed.

| Material | Chemical composition | Particle size distribution [μm] |
|---|---|---|
| **Ti-6Al-4V low oxygen content (LO)** | Al = 6.04 wt.%<br>V = 3.94 wt.%<br>C = 0.013 wt.%<br>Si = 0.012 wt.%<br>O = 918 ppm<br>N = 31 ppm<br>H = 13 ppm<br>Ti = bal. | $D_{10}$ = 21<br>$D_{50}$ = 39<br>$D_{90}$ = 60 |
| **Ti-6Al-4V high oxygen content (HO)** | Al = 6.12 wt.%<br>V = 4.02 wt.%<br>C = 0.013 wt.%<br>Si = 0.012 wt.%<br>O = 1645 ppm<br>N = 91 ppm<br>H = 35 ppm<br>Ti = bal. | $D_{10}$ = 21<br>$D_{50}$ = 40<br>$D_{90}$ = 62 |

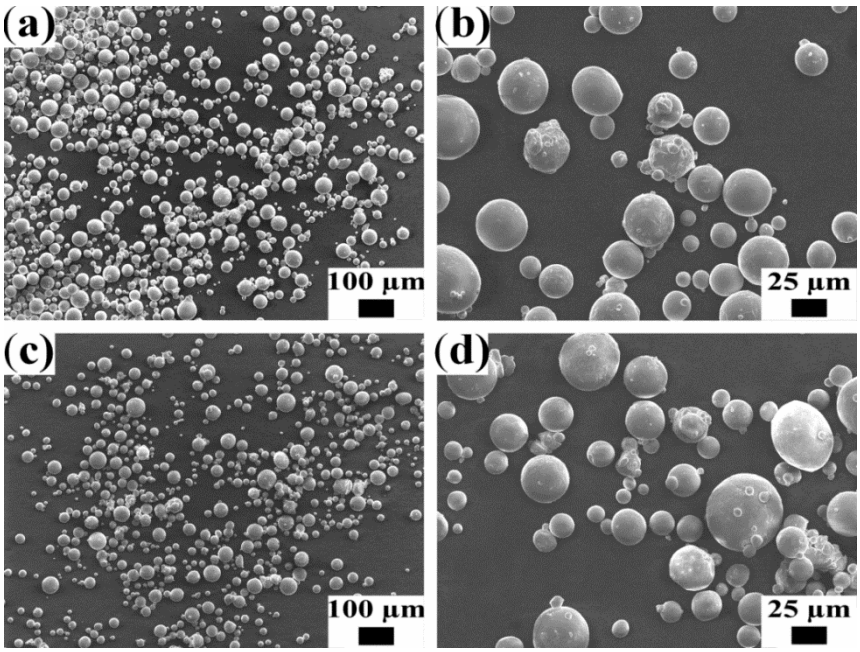


**Figure 83.** Ti-6Al-4V gas atomised spherical powders with two different oxygen contents at different magnifications: (a,b) low oxygen (< 1000 ppm), (c,d) high oxygen (> 1600 ppm) content.

The LPBF process was performed adopting a commercial EOSINT M280 EOS GmbH machine, equipped with a 400 W Yb fibre laser, with a laser spot diameter of 100 µm (previously described in Chapter 2.3). Both the powders were processed adopting the same process parameters: 280 W laser power, 1200 mm/s scanning speed, 30 µm layer thickness, 0.14 mm hatching distance and 0.015 mm beam offset. The scanning strategy adopted was a X rotated one with 45 ° rotation angle between subsequent layers. During the process the building platform was maintained at 100 °C in order to reduce the large amount of residual stresses, while the oxygen concentration inside the process chamber was kept below 0.1 % by using argon inert gas flow.

All the specimens were stress relieved in vacuum at 830 °C for 4 h, with an mean cooling rate of 5 °C/min, in order to reduce the amount of residual stresses and to avoid distortions. After heat treatment the samples were removed from the building platform by wire electrical discharge machining. To investigate the mechanical properties, both tensile and fatigue specimens were fabricated parallel to the building platform (horizontal specimens), and parallel to the building direction (vertical specimens) as shown in Figure 84. The tensile specimens were obtained by fabricating round bars of 75 mm length and 10 mm diameter then

machined according to ASTM E8/E8M standard [311]. Similarly the fatigue specimens were obtained by machining round bars of 80 mm length and 14 mm diameter according to the scheme illustrated in Figure 85: the average surface roughness $R_a$ of the machined samples was 0.8 μm.

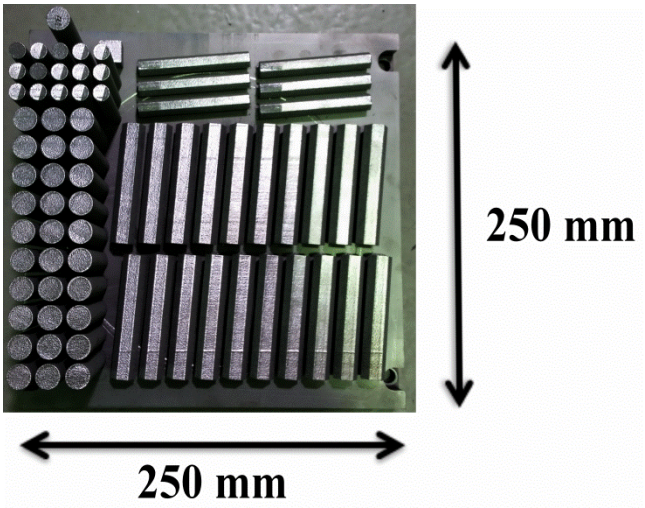


**Figure 84.** Example of Ti-6Al-4V specimens fabricated by LPBF adopting an EOSINT M280 machine. The samples were produced starting from the LO and HO Ti-6Al-4V gas atomised powders.

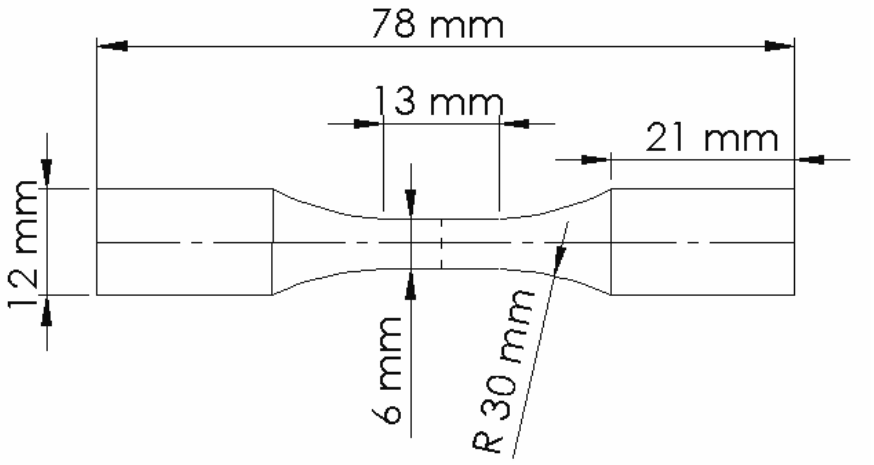


**Figure 85.** Dimensions of the fatigue specimens adopted in this study, according to the standard ASTM E466 [382].

Figure 86 summarises the samples conditions investigated in this study: for each condition 5 and 10 specimens were tested for tensile and fatigue tests,

respectively, with a total number of 90 samples processed for each powder. In order to reduce the amount of defects and porosities on the mechanical performances a HIP treatment was performed on part of the specimens ("Stress relieving + HIP" in Figure 86). The post-processing treatment was carried out at 930 °C for 4 h with 100 MPa argon pressure adopting a Avure QIH-9 Hot Isostatic Press. Furthermore, in order to distinguish the effect of microstructure and porosities on the mechanical properties a heat treatment at 930 °C for 4 h in vacuum conditions was also performed on the remaining part of samples ("Stress relieving + heat treatment" in Figure 86).

The tensile test were performed using a Zmart.Pro electro-mechanic machine, Zwick Roell company, with a 150 N pre-loading and 0.25 mm/min deformation rate at room temperature. The fatigue tests were performed using a servo-hydraulic dynamic test system equipped with a DOLI RMC7 test system. The experiments were carried out adopting a stress ratio R = -1 (symmetrical push-pull loading conditions) and a testing frequency of 50 Hz at room temperature. The fatigue endurance limit of the fatigue tests was defined as $10^7$ cycles, while the maximum stress ($\sigma_{max}$) varied between 450 and 700 MPa, with single steps of 50 MPa: two specimens were tested for each loading conditions.

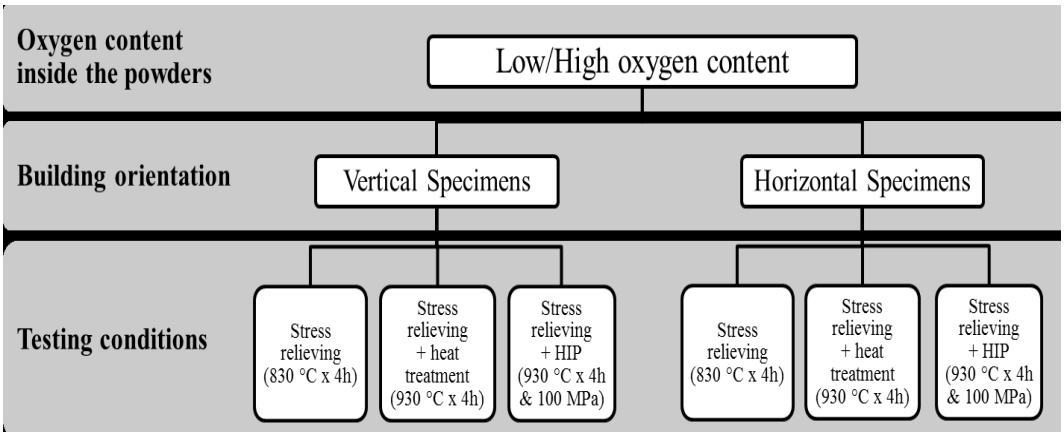


**Figure 86.** Mechanical testing conditions for Ti-6Al-4V specimens fabricated by LPBF starting form metal powder containing two different oxygen content, low (918 ppm) and high (1645 ppm), respectively.

Microstructural investigation was carried out by optical and electron microscopy on both vertical and horizontal cross sections of the specimens, after polishing and chemical etching treatment (Appendix 1.1.1.1A.5). The internal porosity was measured for both horizontal and vertical sections of the samples by image analysis of 20 optical micrographs, taken at the magnification of 200x: Image

J software was adopted to identify and measure the amount of pores present in each micrograph. The phase composition inside the alloy was investigated by X ray diffraction (Appendix 1.1.1.1A.6) while the oxygen content was evaluated by inert gas fusion technique using a ONH Analyser (LECO ONH 836), as listed in Table 16.

**Table 16.** Oxygen content inside Ti-6Al-4V samples produced by LPBF and subjected to different post-processing heat treatments. The data were obtained by inert gas fusion analysis and reported according to the standard ASTM E29 [383].

| | **Sample** | **Oxygen content [%]** |
|---|---|---|
| Low oxygen | As-built | 0.10 |
| | After stress relieving | 0.10 |
| | After stress relieving + heat treatment | 0.10 |
| | After strss relieving + HIP | 0.11 |
| High oxygen | As-built | 0.18 |
| | After stress relieving | 0.18 |
| | After stress relieving + heat treatment | 0.19 |
| | After strss relieving + HIP | 0.19 |

After being processed by LPBF the samples showed a slightly higher oxygen content which was almost maintained after post-processing heat treatment. The fatigue and tensile fractographs were investigated by stereomicroscopy, adopting a Leica EZ4W microscope, and by field emission scanning electron microscopy (FESEM) together with energy-dispersive X-ray spectroscopy (EDS).

## 4.2.2 Microstructural investigation

Figure 87 and Figure 88 show the optical micrographs of the stress relieved Ti-6Al-4V specimens, with low and high oxygen contents. The microstructure appeared to be constituted by very fine mixture of α + β (Figure 88c,d), in which α phase was present as fine needles [347]. The origin of such particular microstructure began with the LPBF process, during which the very high cooling rates induced the α' martensite creation which was later transformed into α + β phases (Figure 88a,b) by stress relieving treatment at 830 °C [355,369]. The internal porosity, measured by image analysis of the optical micrographs, was 0.15 ± 0.06 %.

Figure 89 illustrates the microstructure of the specimens observed by FESEM analysis and compares the microstructural features between low and high oxygen

content conditions. In order to investigate the effect of oxygen content in the samples, the α lamellae and the β phase amount were measured by image analysis: from the results α grains had a mean thickness of 1.1 ± 0.3 μm in the case of low oxygen level and 0.9 ± 0.2 μm in the case of high oxygen.

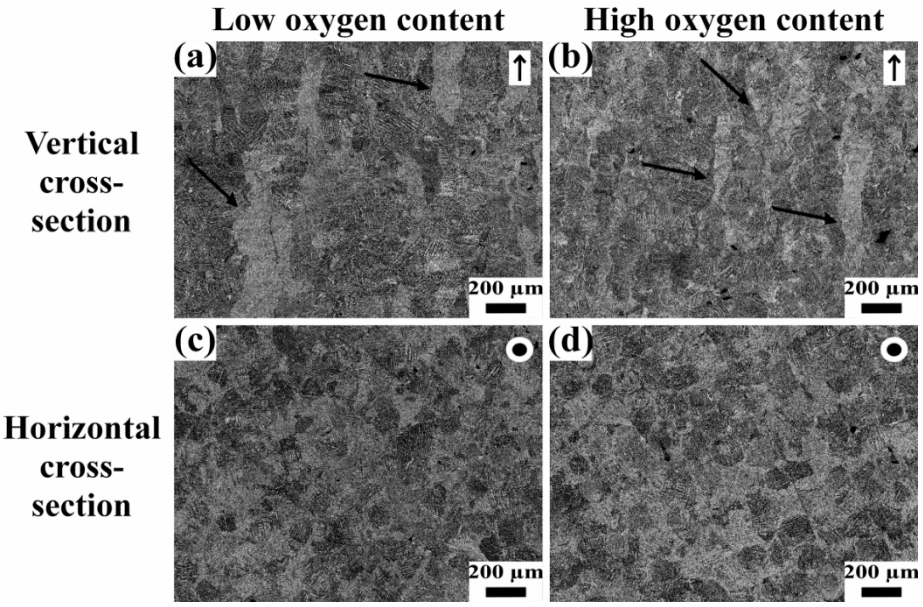


**Figure 87.** Optical micrographs of the vertical and horizontal cross-sections of Ti-6Al-4V specimens fabricated by LPBF with two different oxygen amounts, low and high concentration, respectively, after stress relieving treatment. The black arrows and circles in the upper-right corner of the imagines identify the building direction of the sample, while the black arrows in the micrographs of the vertical cross-section indicate the beta columnar grains present in the microstructure.

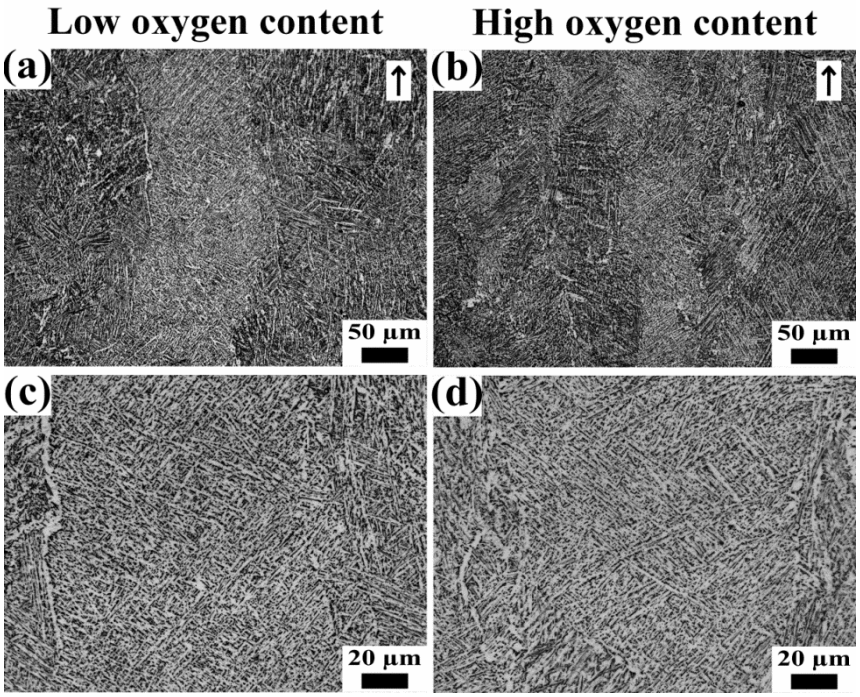


**Figure 88.** Optical micrographs of the vertical cross-sections of Ti-6Al-4V specimens fabricated by LPBF with two different oxygen amounts, low and high concentration, respectively, after stress relieving treatment, at different magnifications. The black arrows in the upper-right corner of the imagines identify the building direction of the sample.

Such results appeared in accordance with other studies present in literature [313,361]: Simonelli et al. [344] found that after heating the LPBF samples at 730 °C for 2 hours the average α grains thickness was 1.2 ± 0.3 µm, and found that the post-processing heat treatment did not greatly affect the α grains morphology since the temperature adopted was considerably lower than β-transus one (close to 1000 °C). On the other way, by comparing the two oxygen contents, the microstructure analysis carried out could suggest how the different oxygen amount in the chemical composition did not strongly affect the microstructure evolution of the material. Indeed since oxygen stabilises the hexagonal phase, the α lamellae are supposed to be larger and wider in the case of higher oxygen content rather than in the case of lower concentration. As a proof of such statement, the micrographs showed in Figure 89 as well as the results obtained from image analysis confirm such effort showing a slightly difference between the two conditions.

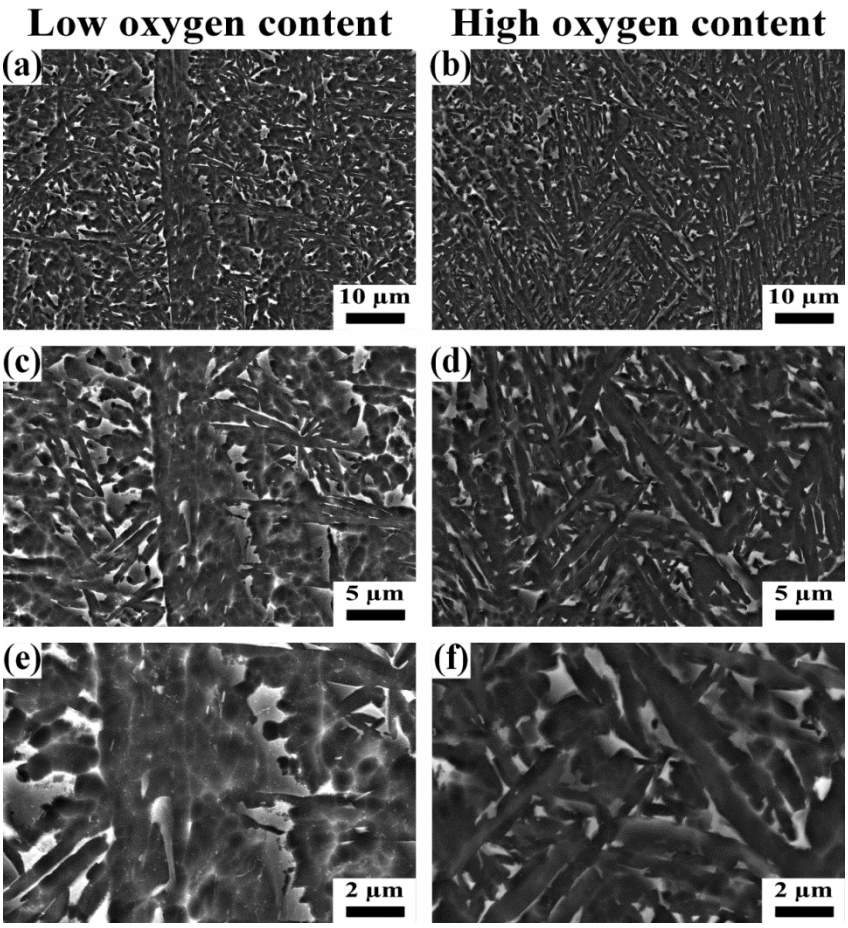


**Figure 89.** FESEM micrographs at different magnifications of Ti-6Al-4V specimens produced by LPBF, with two different oxygen content in the chemical composition, after stress relieving treatment.

Moreover, the presence of β columnar grains could be observed in Figure 87a,b as well as in Figure 88a,b. Such microstructural features are characteristic of Ti based alloys, processed by LPBF [45,384] and could be still identified after stress relieving: indeed when heated the α' martensite inside the β grains transformed in a mixture of α+ β phases which prevented the excessive grain growth and conserved the shape of the original columnar grains [344,347]. Along the vertical plane (Figure 87a,b) it could be noticed that the prior β grain boundaries appeared aligned to the building direction while in the horizontal plane (Figure 87c,d) the cross-section of the β was exposed, as widely reported in literature [228,255,355]. The nature of β grains derives from the epitaxial growth provoked during LPBF process, particularly from the layer by layer remelting phenomenon. Indeed due to the repeated and subsequent exposures of the material to the laser source, inside the

part temperature arises up to 995 °C exceeding both the martensite starts ($M_S$) and β-transus temperatures [143,340,343]. In such conditions the transformation of α' martensite into β phase favoured and microstructure evolves with the creation of columnar grains through the material.

The columnar grains growth followed the main heat flow direction along the vertical building direction of the part developing through numerous layers and reaching several millimetres length [45,384] as highlighted in Figure 87a,b. Moreover, as showed in Figure 88a, the average width of the columnar grains was closed to the hatching distance dimensions, almost 140 μm, since hatching distance represented the distance between two different laser scans and so an area of the part where the material was scanned and locally melted repeatedly during LPBF [228,344–346]. The orientation of these grains depended on the process parameters and on the scanning strategy adopted [272,345]: from Figure 87a,b appeared that β grains possessed a mean orientation parallel to the building direction with a tilted growth between consecutive layers. Such phenomenon could be related to the rotated scanning strategy adopted during LPBF fabrication of the specimens, which repeatedly altered the thermal gradient generated inside the part and the main heat flow direction [272,345].

On the other hand, since oxygen behaves as α phase stabilizer in Ti alloys [185], the approximate amounts of α and β phase in the low and high oxygen content specimens were investigated by image analysis [347]: studying the optical micrographs at different magnifications appeared that the specimens with lower oxygen content presented an higher β phase percentage (~ 18 %) while in the case of higher oxygen amount the β percentage decreased (~ 10 %). The chemical composition of these specimens was further investigated by mineralogical analysis, as exposed in Figure 90. From the results the peaks of β phase (Ti body centred cubic, *bcc*, crystal) appeared slightly more intense in the low oxygen content samples rather than in the high oxygen content ones. Such result can describe how the β phase was apparently more present in the low oxygen conditions rather than in the high oxygen ones.

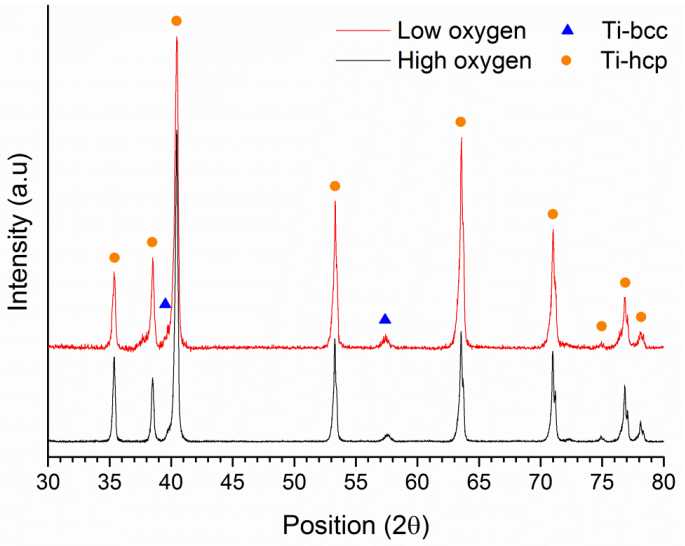


**Figure 90.** XRD patterns of Ti-6Al-4V specimens fabricated by LPBF, with two different oxygen contents in the chemical composition, after stress relieving.

Figure 91 and Figure 92 display the optical micrographs of the specimens subjected to stress relieving and further heat treatment at 930 °C for 4 hours, for both low and high oxygen contents. As it can be noticed from Figure 91a,b, the original microstructure of stress relieved samples disappeared and the original β columnar grains appeared more blurred and not well defined as before. This effort could be related to the effect of the second heat treatment at high temperature which favoured the growth of α + β phases at the columnar grains boundaries. However heating at sub-transus temperatures did not allow the complete modification of β grains which did not disappear completely [340,344,347]. The porosity level inside the specimens was measured by image analysis as 0.39 ± 0.11 %, higher than in the case of stress relieved specimens. The porosity increase in the specimens could be related to the application of the heat treatment at 930 °C with favoured the enlargement of the metallurgical pores inside the material [385].

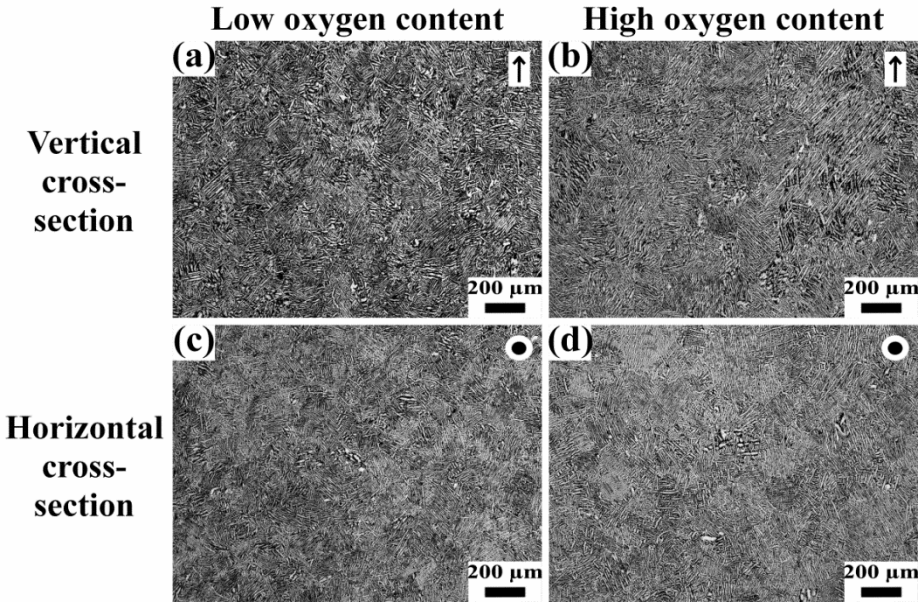


**Figure 91.** Optical micrographs of the vertical and horizontal cross-sections of Ti-6Al-4V specimens fabricated by LPBF with two different oxygen amounts, low and high concentration, respectively, after stress relieving and heat treatment at 930 °C for 4 hours. The black arrows and circles in the upper-right corner of the imagines identify the building direction of the sample.

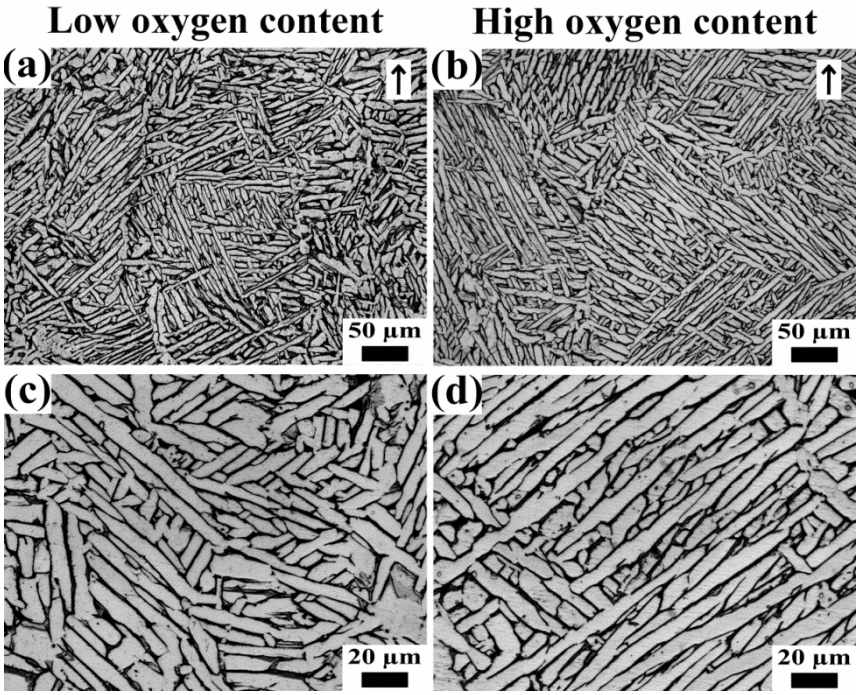


**Figure 92.** Optical micrographs of the vertical cross-sections of Ti-6Al-4V specimens fabricated by LPBF with two different oxygen amounts, low and high concentration, respectively, after stress relieving and heat treatment at 930 °C for 4 hours, at different magnifications. The black arrows in the upper-right corner of the imagines identify the building direction of the sample.

After heating at 930 °C the laser tracks and anisotropy almost completely vanished, particularly in the horizontal cross-section (Figure 91c,d). At higher magnification, as shown in Figure 92, microstructure appeared constituted by α lamellae, longer and wider than in the stress relieved conditions, surrounded by β phase. Moreover the effect of performing a second heat treatment on the microstructure can be noticeably appreciated in Figure 93: α grains possessed an average thickness of 4.1 ± 0.7 µm in the case of low oxygen concentration and 4.2 ± 1.0 µm in the case of high oxygen amount. Heating the material at high temperature favoured the migration of the alloying elements inducing the β phase enrichment and the α lamellae growth.

However as it could be observed from optical and FESEM micrographs (Figure 92 and Figure 93) that the effect of oxygen on the microstructural evolution of the different materials investigated was less appreciable than in the case of stress relieved samples. This effort was also confirmed from the measurement of β phase amount in the specimens: in the case of low oxygen content, the amount of β phase

was 37 % while in the case of high oxygen content was 33 %. Similar conclusions could be stated observing the XRD analysis shown in Figure 94. Compared to the stress relieved conditions (Figure 90) the principal peaks of *bcc* β phase (2θ = 39.5°; 57.2°) appeared more defined and intense. Such results could attest a bigger presence of β phase in the stress relieved and heat treated specimens compared to previous conditions. However, the difference between low and high oxygen content remained very light also in the XRD patterns, showing the same trend observed with the image analysis results.

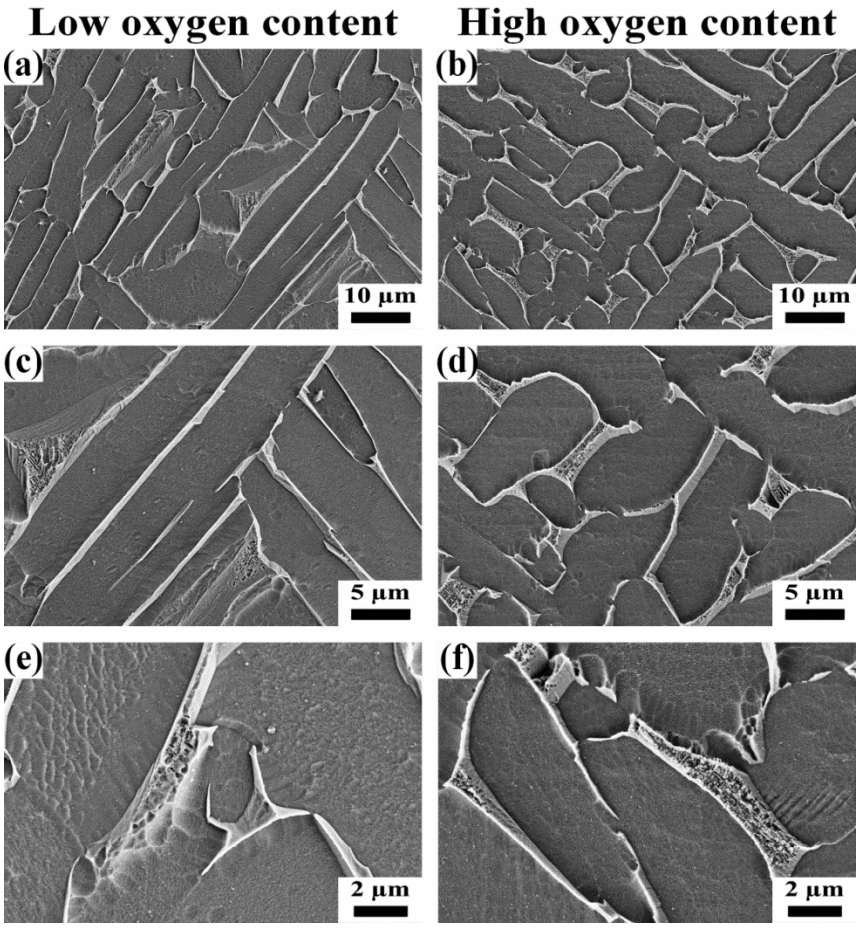


**Figure 93.** FESEM micrographs at different magnifications of Ti-6Al-4V specimens produced by LPBF, with two different oxygen content in the chemical composition, after stress relieving and heat treatment at 930 °C for 4 hours.

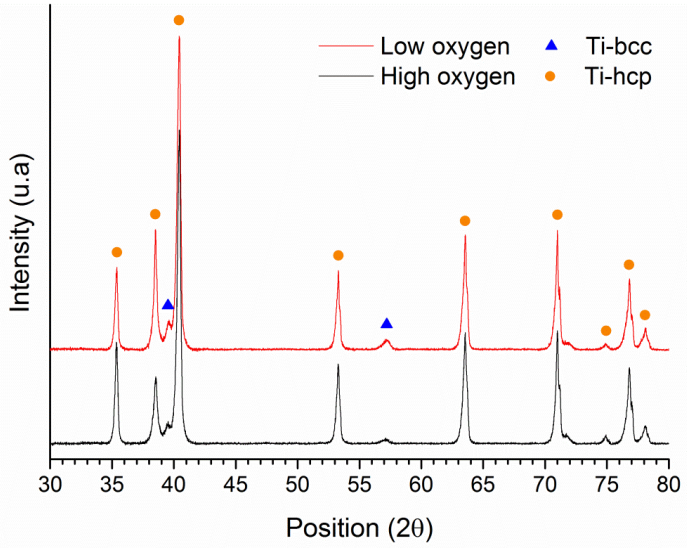


**Figure 94.** XRD patterns of Ti-6Al-4V specimens fabricated by LPBF, with two different oxygen contents in the chemical composition, after stress relieving and heat treatment at 930 °C for 4 hours.

Similarly, another set of stress relieved specimens were subjected to a second heat treatment: in this case a HIP treatment at 930 °C for 4 hours, with the use of 100 MPa external pressure was adopted. HIP enabled to close the majority of defects and pores inside the material [345]: the porosity level inside the samples was measured by image analysis as less than 0.1 %.

Figure 95 and Figure 96 show the optical micrographs of the specimens subjected to stress relieving and HIP, for both low and high oxygen content. The microstructure appeared constituted by α + β lamellae both in the vertical cross-section (Figure 95a,b) and in the horizontal cross-section (Figure 95c,d). As indicated in Figure 95a,b the original β grains of stress relieved could be still observed along the building direction, since also HIP process was carried out at sub-transus temperature [369].

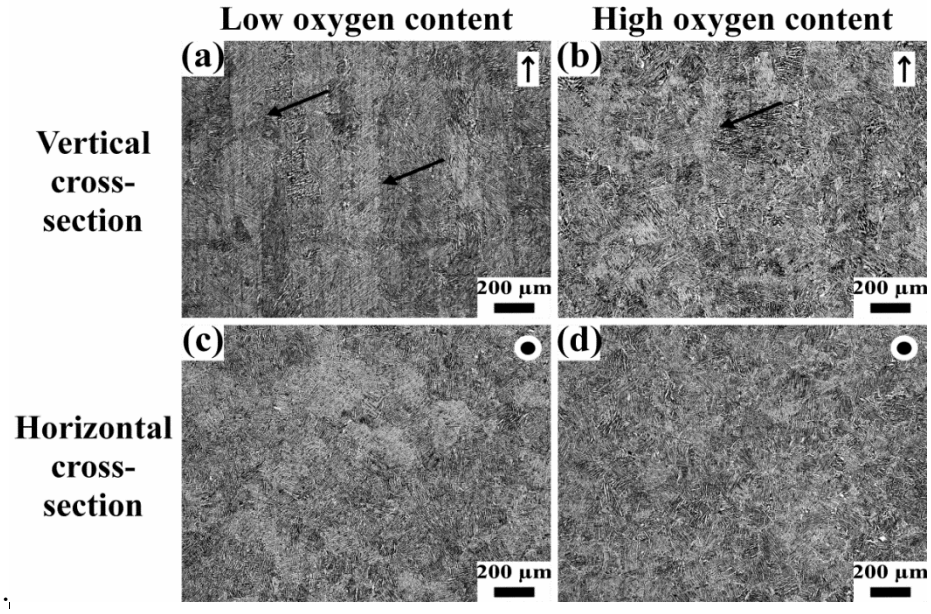


**Figure 95.** Optical micrographs of the vertical and horizontal cross-sections of Ti-6Al-4V specimens fabricated by LPBF with two different oxygen amounts, low and high concentration, respectively, after stress relieving and HIP at 930 °C for 4 hours with 100 MPa pressure. The black arrows and circles in the upper-right corner of the imagines identify the building direction of the sample, while the black arrows in the micrographs of the vertical cross-section indicate the beta columnar grains present in the microstructure.

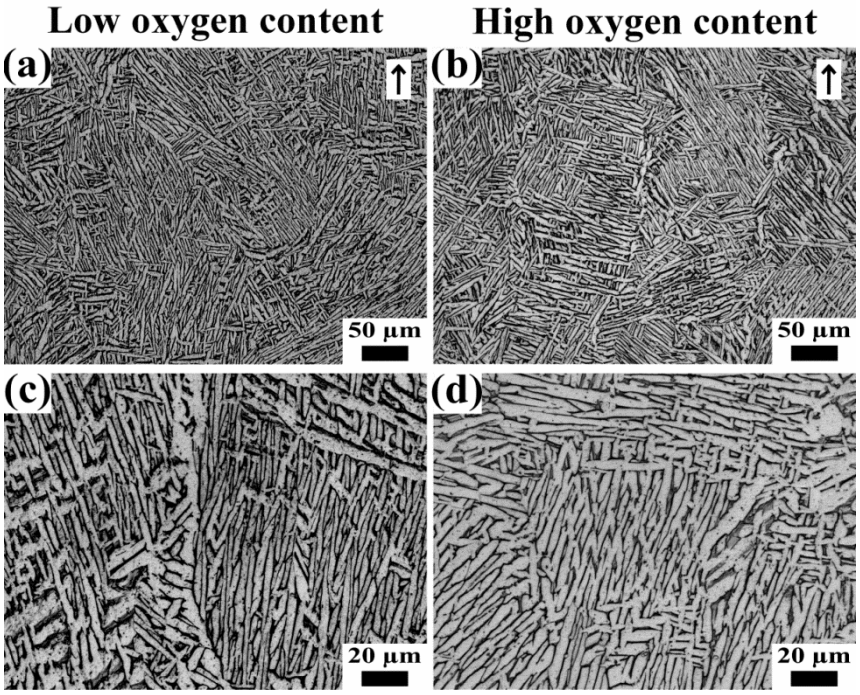


**Figure 96.** Optical micrographs of the vertical cross-sections of Ti-6Al-4V specimens fabricated by LPBF with two different oxygen amounts, low and high concentration, respectively, after stress relieving and HIP at 930 °C for 4 hours with 100 MPa pressure, at different magnifications. The black arrows in the upper-right corner of the imagines identify the building direction of the sample.

Comparing stress relieved and HIPped specimen with the stress relieved and 930 °C heat treated ones, the overall microstructure appeared slightly finer with smaller α lamellae: from image analysis α grains mean thickness was measured as 3.9 ± 0.6 µm and 4.0 ± 0.7 µm in the case of low oxygen and high oxygen content, respectively. The explanation of such discrepancy could be the different cooling rate between HIP and the other heat treatment investigated: in the first process the cooling rate was kept at 5 °C/min while in the case of 930 °C heat treatment the cooling rate was probably lower, leading to slightly coarser microstructure.

In addition also FESEM micrographs in Figure 97 show a finer lamellae thickness in the stress relieved and HIPped specimens than in the stress relieved and heat treated samples. The difference in β phase amount appeared less distinct than in the case of stress relieved specimens as also observed in the case of stress relieved and heat treated samples: from optical micrographs analysis the low oxygen content showed 35 % of β phase while in the case of high oxygen amount the β amount was less than 32 %. Furthermore, the XRD analysis in Figure 98

displays the patterns of the stress relieved and HIPped specimens with two different oxygen content: as it could be observed there was a slight difference in the β phase signal between the two conditions investigated. Such results could be compared with the ones obtained with the XRD patterns illustrated before in Figure 94, showing no significant difference as expected.

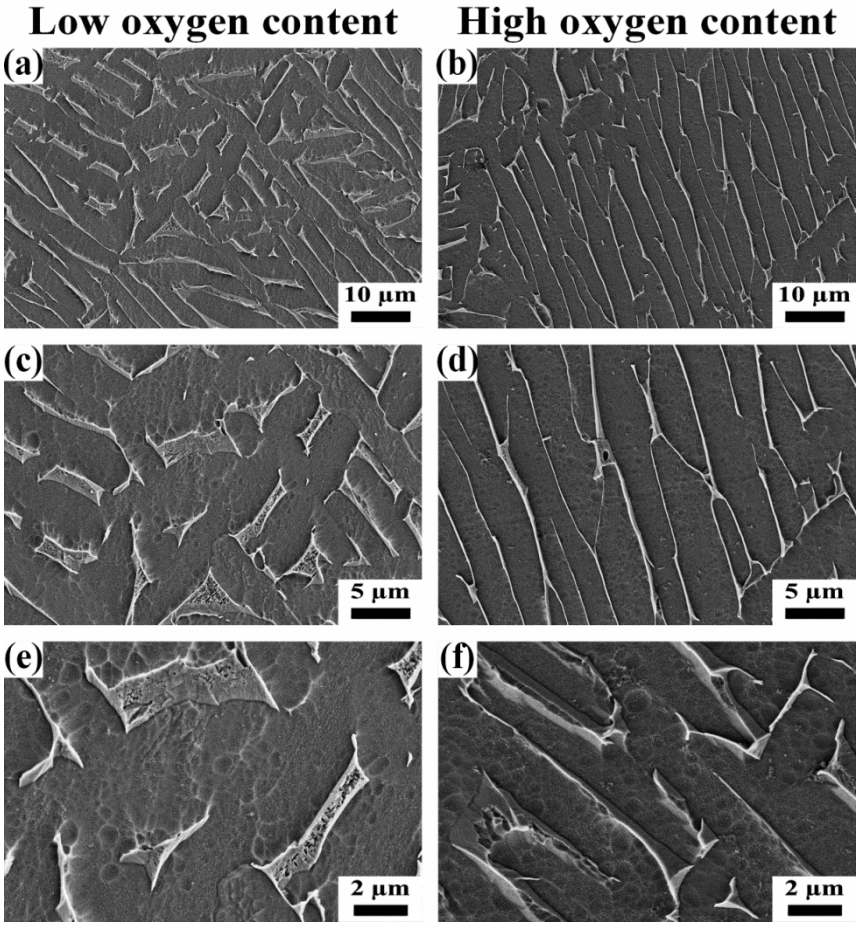


**Figure 97.** FESEM micrographs at different magnifications of Ti-6Al-4V specimens produced by LPBF, with two different oxygen content in the chemical composition, after stress relieving and HIP at 930 °C for 4 hours with 100 MPa pressure.

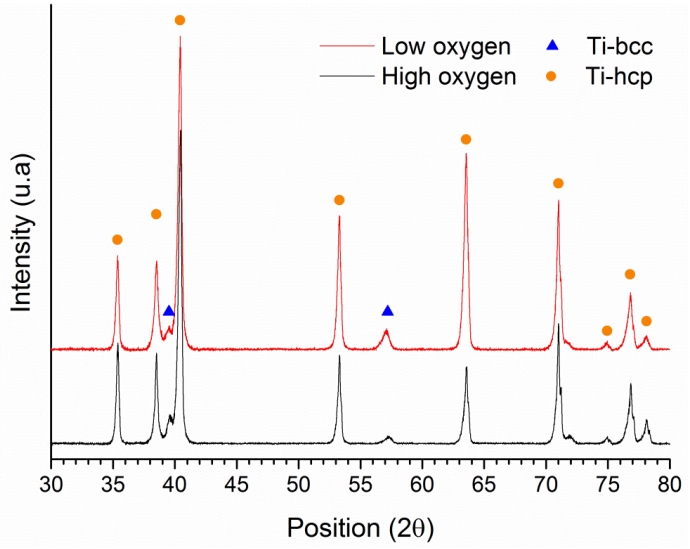


**Figure 98.** XRD patterns of Ti-6Al-4V specimens fabricated by LPBF, with two different oxygen contents in the chemical composition, after stress relieving and HIP at 930 °C for 4 hours with 100 MPa pressure.

### 4.2.3 Mechanical properties

The Ti-6Al-4V specimens fabricated by LPBF were tested in different post-processing conditions for both low and high oxygen content samples. Tensile and fatigue properties were measured and investigated for both vertically and horizontally built samples. Table 17 lists the tensile properties while Figure 99 displays the related stress-strain curves.

**Table 17.** Tensile properties of Ti-6Al-4V specimens fabricated by LPBF with two different gas atomised powders, with low and high oxygen content, respectively, tested in different conditions for both vertical and horizontal building direction.

| **Low oxygen content** | | | | | |
|---|---|---|---|---|---|
| **Conditions** | **Building direction** | **Mechanical Properties** | | | |
| | | **E [GPa]** | **YS [MPa]** | **UTS [MPa]** | **ε [%]** |
| **Stress relieving** | Vertical | 123±11 | 850±2 | 930±1 | 13.8±0.9 |
| | Horizontal | 126±13 | 895±6 | 956±4 | 14.5±0.8 |
| **Stress relieving + heat treatment** | Vertical | 118±7 | 695±36 | 808±13 | 11.9±0.5 |
| | Horizontal | 119±5 | 756±11 | 842±11 | 12.2±1.1 |
| **Stress relieving + HIP** | Vertical | 120±8 | 748±25 | 846±10 | 16.8±0.5 |
| | Horizontal | 117±7 | 789±4 | 871±5 | 17.6±1.1 |
| **High oxygen content** | | | | | |
| **Stress relieving** | Vertical | 127±8 | 1006±3 | 1060±3 | 12.8±1.3 |
| | Horizontal | 123±12 | 1008±9 | 1064±7 | 13.9±0.9 |
| **Stress relieving + heat treatment** | Vertical | 129±22 | 837±7 | 923±9 | 11.2±1.2 |
| | Horizontal | 123±6 | 863±8 | 929±4 | 13.0±0.9 |
| **Stress relieving + HIP** | Vertical | 122±9 | 863±8 | 947±4 | 14.3±0.6 |
| | Horizontal | 125±12 | 895±10 | 964±6 | 17.2±0.8 |

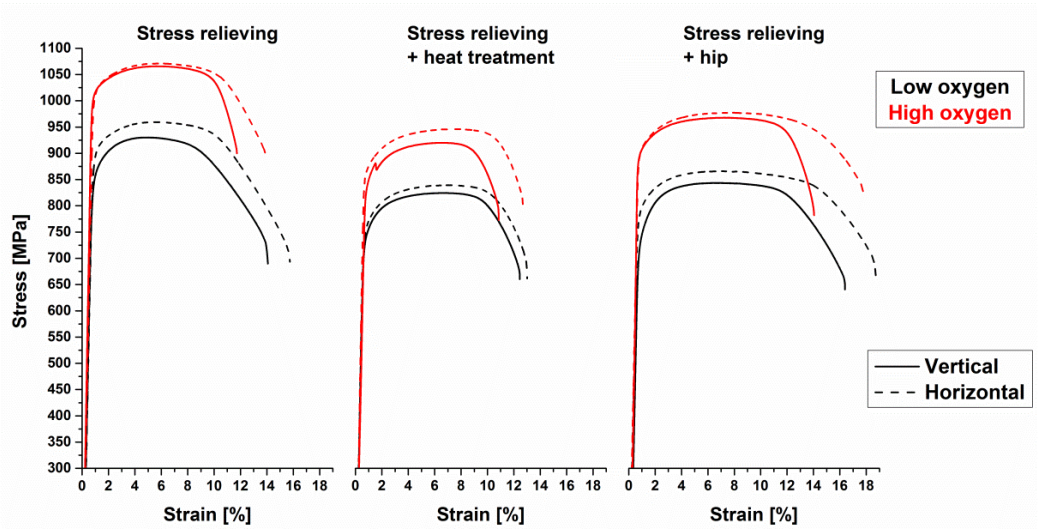


**Figure 99.** Stress-strain curves of Ti-6Al-4V specimens, fabricated by LPBF with two powders batches with low and high oxygen content, respectively, and tested in different conditions. The tensile tests were performed for both vertically and horizontally build specimens.

From the results some main considerations can be taken:

- Stress relieved specimens possessed the highest tensile strength while on the other hand applying a second heat treatment reduced the tensile strength;
- HIP enabled to increase considerably the elongation at break of the stress relieved samples;
- Horizontally built specimens had slightly higher tensile strength and longer elongation at break compared to the vertically built ones;
- High oxygen content provided higher tensile strength and elastic modulus and lower ductility compared to the low oxygen content conditions;

In the case of Ti-6Al-4V alloy post-processing treatments modify the original microstructure of the LPBF samples and favour the α' martensite transformation and the coarsening of α and β phases. Due to this microstructural modification the stress relieved samples generally possess lower tensile strength and higher elongation at break compared to the as-built conditions [344]. As expected the results obtained in this study were similar to the ones described in other studies [313,347] and comparable to those exposed in Table 12. Indeed while as-built specimens generally show YS and UTS around 1100 and 1200 MPa, respectively,

and an elongation at break lower than 10 % (Figure 72), for the stress relieved specimens tested the YS and UTS varied in the ranges of 850 ÷ 1008 MPa and 930 ÷ 1070 MPa, respectively, and ε varied between 12.8 and 14.8 %. A part from the transformation of α' martensite, the increase of ductility was also favoured by the growth of ductile β phase at the grain boundaries of α grains [344]. Even if the amount of β phase was limited in the stress relieved conditions (Figure 90) it enabled an easier slip transfer at the interface within the α phase increasing the elongation at break during tensile loading [344].

Figure 100 and Figure 101 show the fracture surfaces of the stress relieved specimens at different magnifications for both the vertical and horizontal specimens. As described in other studies, LPBF parts fracture is commonly ductile with fracture surface profiles rough and dimpled [344]. The fine dimension of the dimples could be related to the fine microstructure present inside the material, (Figure 89). Furthermore from the fracture surface profile it could be deduced that the predominant fracture was intergranular and during tensile loading cracks propagated preferentially along the boundaries of the α grains [364]. As highlighted in Figure 102, the presence of porosities and defects could be observed on the fracture surfaces. Due to the fact that the overall fracture surface appeared rough it was difficult to establish if the fracture began and propagated in correspondence of pores and defects in the material [344]. However the fracture surface inside and close to the defect appeared flat and smooth (Figure 102b,d), which could be related to a fragile rupture of the material in those areas.

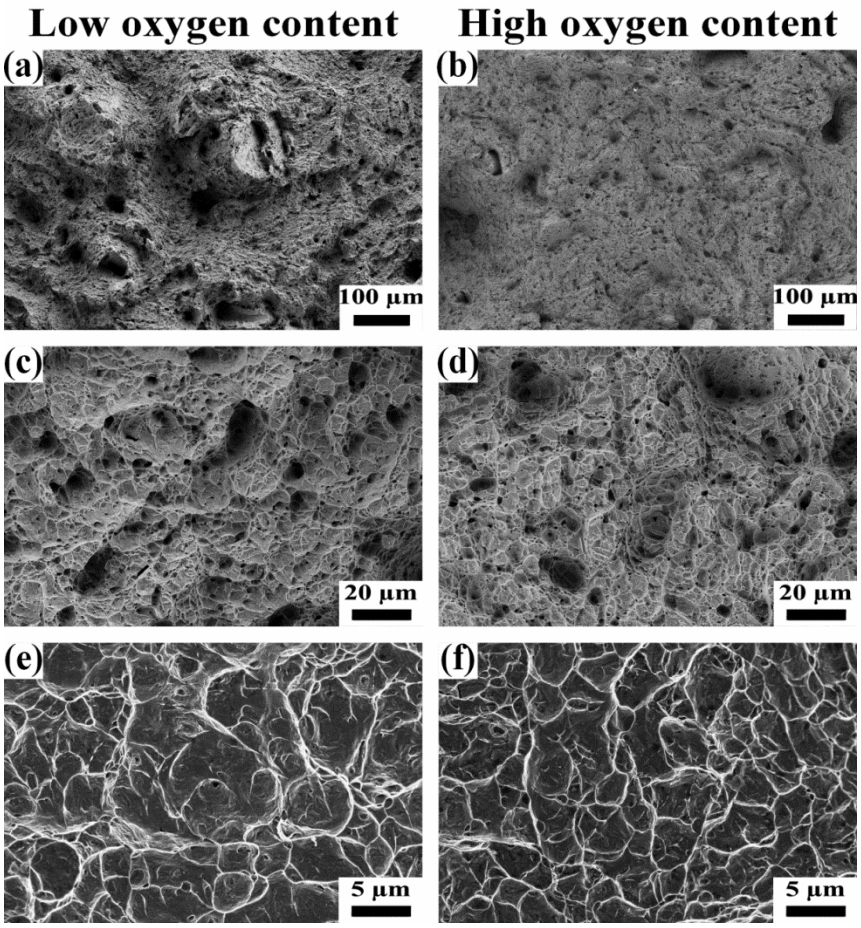


**Figure 100.** Fracture surface FESEM investigation of the vertical stress relieved Ti-6Al-4V specimens after tensile test. The FESEM micrographs were acquired at different magnifications for both the low and high oxygen conditions.

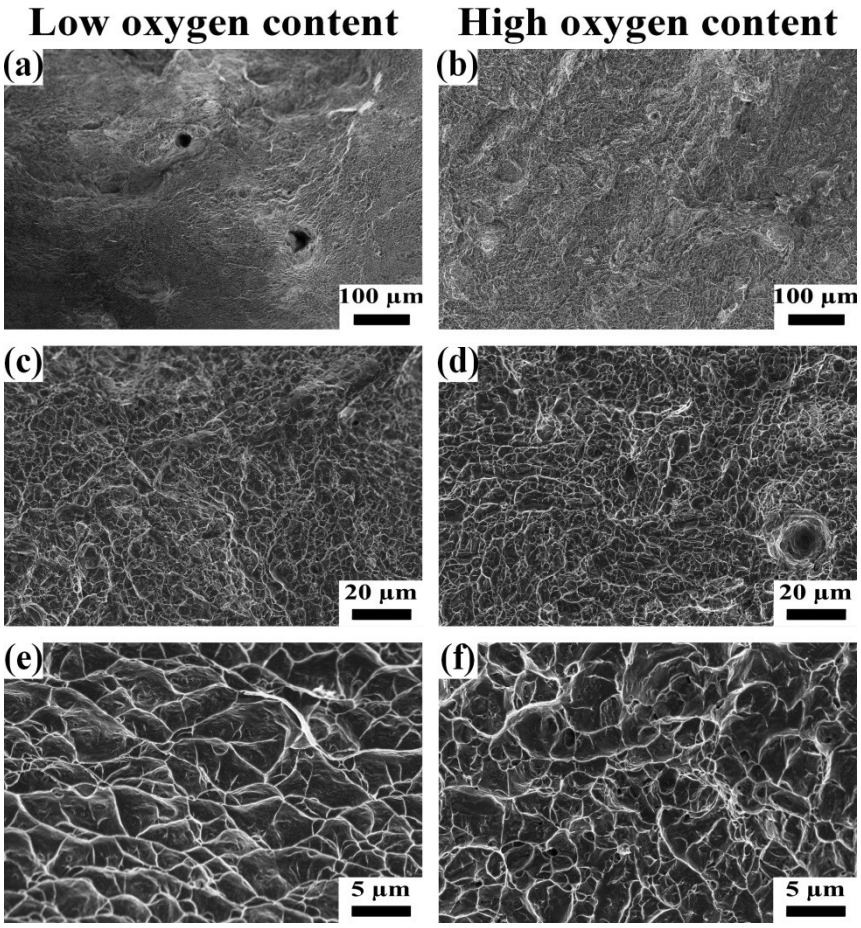


**Figure 101.** Fracture surface FESEM investigation of the horizontal stress relieved Ti-6Al-4V specimens after tensile test. The FESEM micrographs were acquired at different magnifications for both the low and high oxygen conditions.

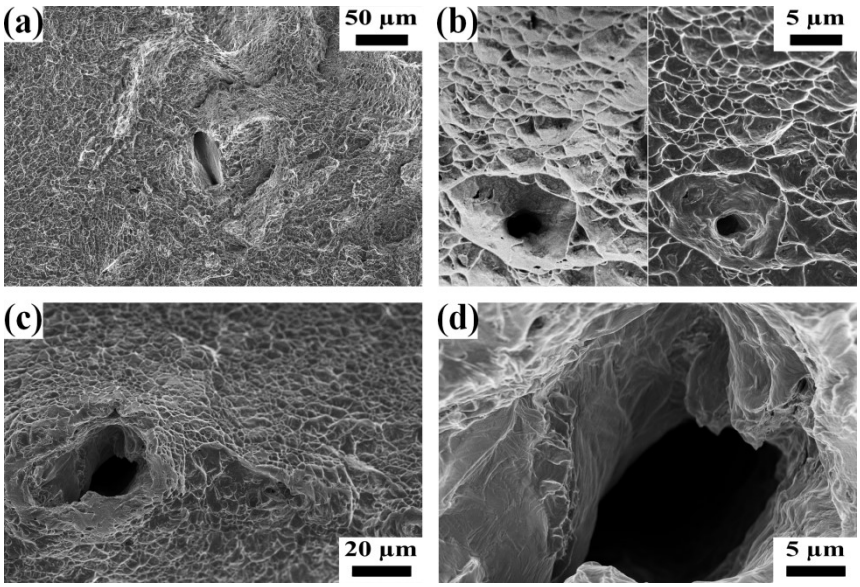


**Figure 102.** Defects and pores observed by FESEM analysis on the fracture surfaces of (a,b) vertical and (c,d) horizontal stress relieved specimens, at different magnification.

By further heat treatment or HIP at 930 °C the tensile strength of the material decreased compared to the stress relieved conditions: the fracture surfaces for both vertical and horizontal specimens are illustrated in Figure 103 and Figure 104 in the case of heat treated specimens, while for the HIPped samples are shown in Figure 105 Figure 106. The overall surface appeared rough and fine dimpled, however the dimple dimensions increased compared to the previous stress relieved conditions. The reduction of tensile strength attested between 11 and 18 % compared to the stress relieved conditions. Such results could be also compared with the micro-Vickers indentations results listed in Table 18: as it can be noted the highest hardness was measured in the stress relieved conditions while after applying a second heat treatment hardness values lowered. The main reason could be ascribed to the enlargement of the lamellar α and β grains in the microstructure (Figure 93 and Figure 97) which offered less strengthening to material [361]. Moreover, the increase of ductile and soft β phase presence inside the microstructure reduced the tensile strength and hardness and increased ductility [313,386].

**Table 18.** Micro-Vickers hardness results for Ti-6Al-4V specimens produced by LPBF, with two different content of oxygen inside the original powders, in different post-processing conditions.

| Conditions | Low oxygen | High oxygen |
|---|---|---|
| | Hardness [$HV_{0.3}$] | Hardness [$HV_{0.3}$] |
| **Stress relieving** | 317 ± 7 | 369 ± 7 |
| **Stress relieving + heat treatment** | 291 ± 3 | 334 ± 9 |
| **Stress relieving + HIP** | 314 ± 4 | 349 ± 9 |

As a fact the grain growth and β phase presence favoured the dislocations motion inside the material providing an higher elongation at break during tensile loading. Although in the stress relieved and heat treated specimens (Figure 99) ε appeared slightly lower than the previous stress relieved conditions while on the contrary in the HIPped samples ε reached higher values (almost ~ 19 %). Considering that the microstructure of stress relieved and heat treated samples (Figure 92) did not differ considerably from the one possessed by the stress relieved and HIPped specimens (Figure 96), the ductility difference between the two conditions could be related to the porosity presence in the stress relieved and heat treated samples. Moreover, as listed in Table 19, the dimples dimensions varied depending on the post-processing treatment, following the same trend shown by the stress-strain curves.

**Table 19.** Average dimples dimensions in the tensile fracture surfaces, built with low and high oxygen content, tested in different conditions, and analysed by FESEM.

| Dimples average dimensions | | |
|---|---|---|
| **Conditions** | **Low oxygen [µm]** | **High oxygen [µm]** |
| **Stress relieving** | 4.1 ± 1.8 | 2.3 ± 0.9 |
| **Stress relieving + heat treatment** | 12.3 ± 4.3 | 10.8 ± 4.9 |
| **Stress relieving + HIP** | 7.2 ± 2.2 | 6.9 ± 1.7 |

What is worth to note was the difference between the heat treated samples and the HIPped ones regarding the dimples dimension. Indeed even if in the heat treated conditions dimples were bigger and coarser than in the HIPped ones, stress-strain curves showed a lower elongation at break. A possible explanation of such discrepancy between ε and dimples dimension could be the presence of pores and

defects which strongly affected the samples rupture. As reported before, the porosity level inside the stress relieved and heat treated specimens was greater than in the stress relieved and HIPped ones (almost four times more): such statement could have the main reason for the differences between these two conditions.

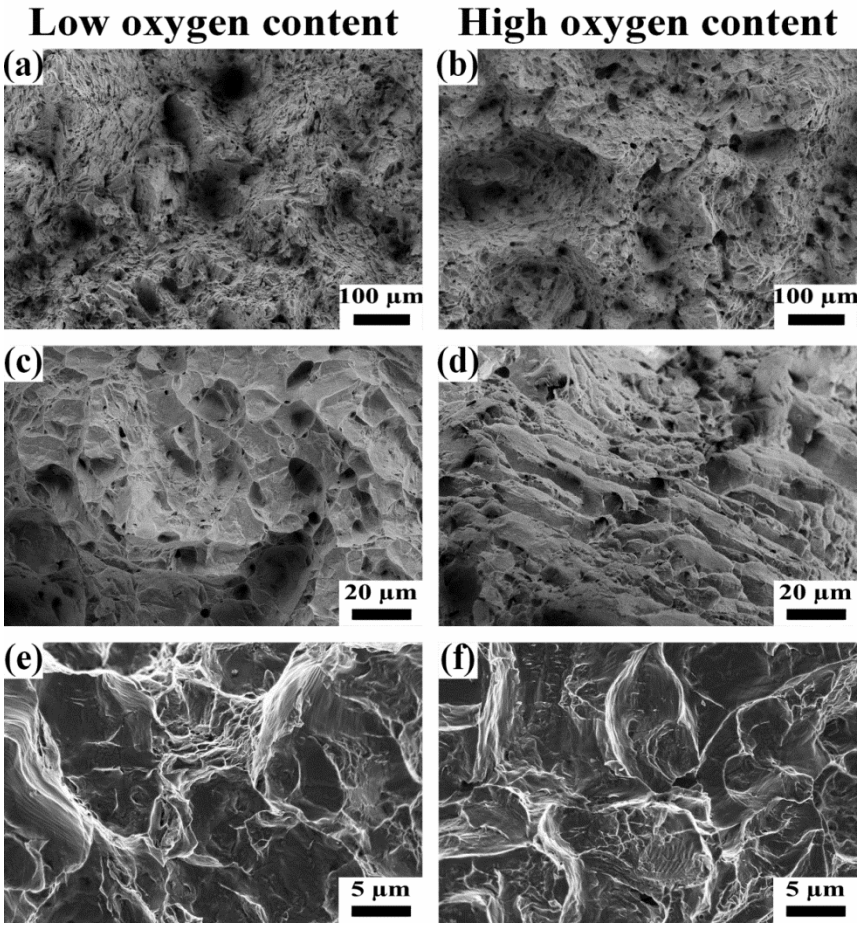


**Figure 103.** Fracture surface FESEM investigation of the vertical stress relieved and heat treated Ti-6Al-4V specimens after tensile test. The FESEM micrographs were acquired at different magnifications for both the low and high oxygen conditions.

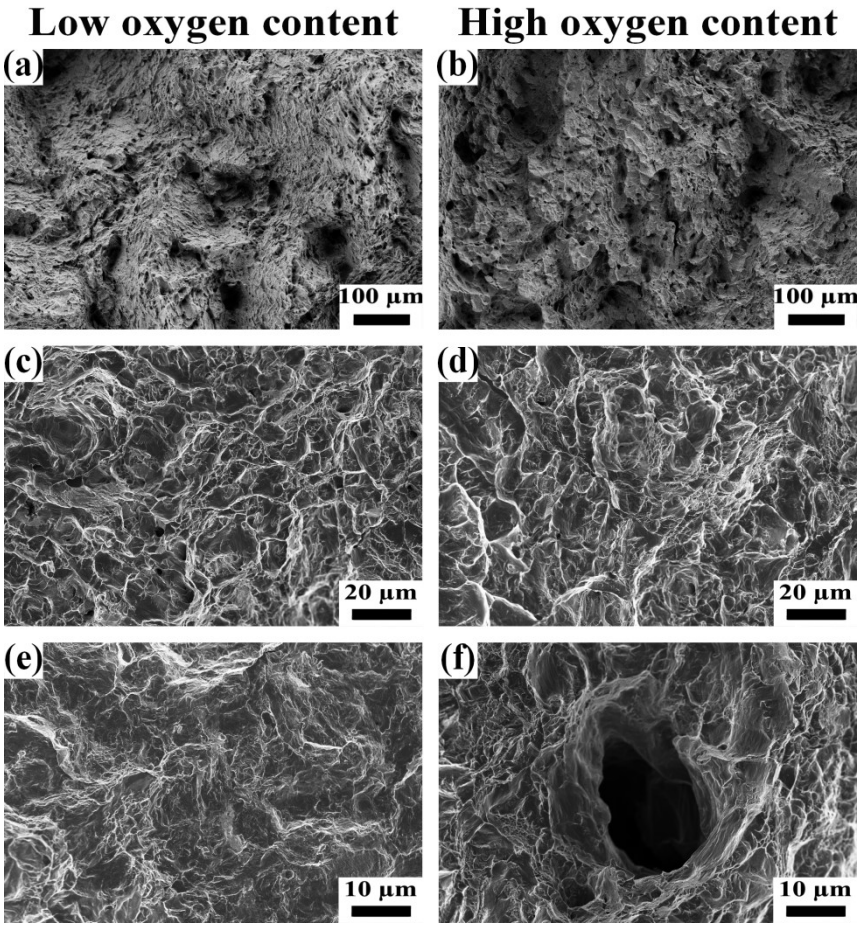


**Figure 104.** Fracture surface FESEM investigation of the horizontal stress relieved and heat treated Ti-6Al-4V specimens after tensile test. The FESEM micrographs were acquired at different magnifications for both the low and high oxygen conditions.

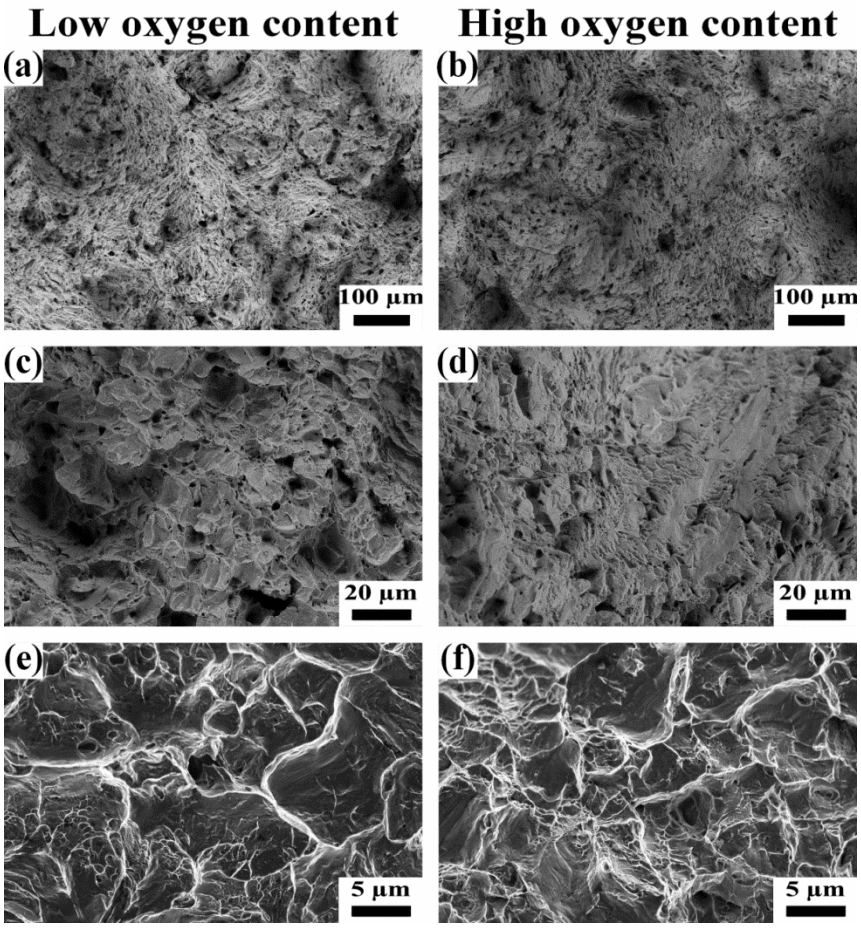


**Figure 105.** Fracture surface FESEM investigation of the vertical stress relieved and HIPped Ti-6Al-4V specimens after tensile test. The FESEM micrographs were acquired at different magnifications for both the low and high oxygen conditions.

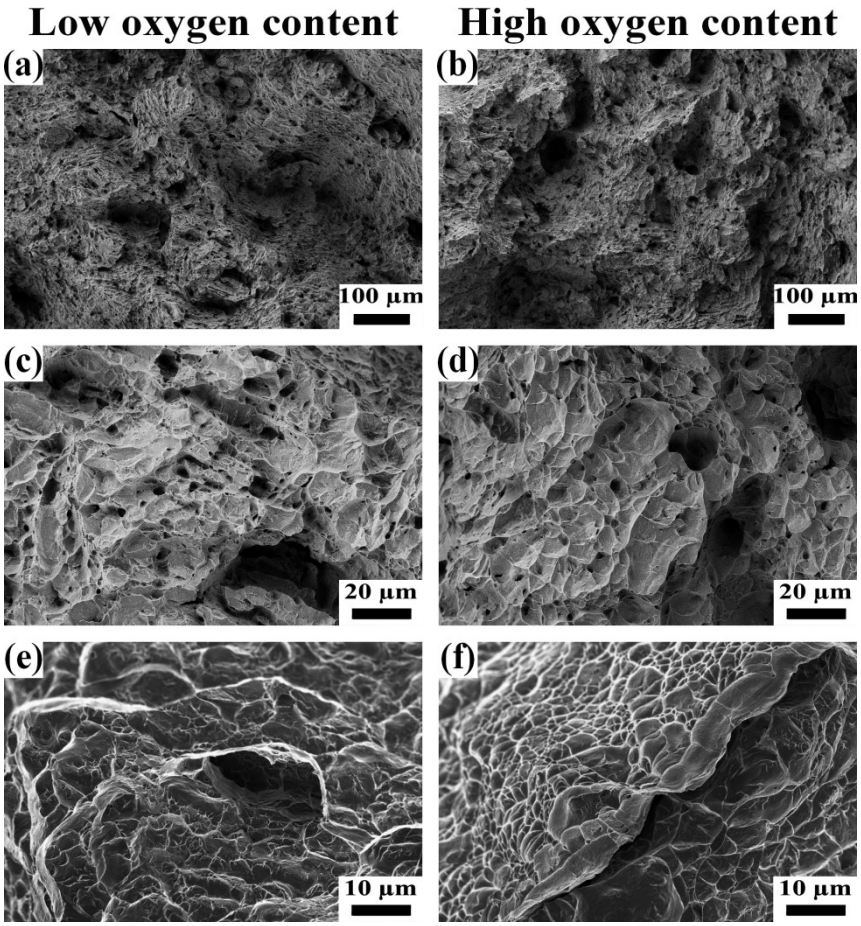


**Figure 106.** Fracture surface FESEM investigation of the horizontal stress relieved and HIPped Ti-6Al-4V specimens after tensile test. The FESEM micrographs were acquired at different magnifications for both the low and high oxygen conditions.

Moreover a large amount of porosities could be observed in the stress relieved and heat treated specimens (Figure 103 and Figure 104), which could justify the lower specimens ductility manifested during tensile loading: examples of defects and porosities observed are reported in Figure 107. Figure 107c,d displays the shape and morphology of fracture surface in correspondence of un-melted particles. Since gas-atomised powder possess an oxide layer upon surface, in the case of incomplete melting such thin ceramic layer represents a crucial interruption in the material continuity. As a consequence during mechanical loading these defect act as stress concentration sites, lowering the material strength and favouring fragile fracture behaviour: as a fact Figure 107d shows the smooth cleavage planes, orientated along preferential crystallographic directions, of the oxide layer, signs of fragile rupture of the material [345].

In the case of HIPped samples instead the defects concentration on the fracture surface appeared very low thanks to the combination of high temperature and pressure used during the treatment which helped to close the defects present inside the material. However some porosities and cracks were detected in the HIPped fracture surfaces, as displayed in Figure 106. Moreover in both heat treated and HIPped conditions, terrace-like features were present on the fracture surfaces, as highlighted in Figure 107b. The observation and the description of such microstructural features had been object of discussion in previous studies [344,345]. At high magnification, these terrace features appeared constituted by several α laths with repeated orientation within one prior β columnar grain: most probably these terrace-like features could have originated due to the crack propagation along α grain boundaries, through prior β grain.

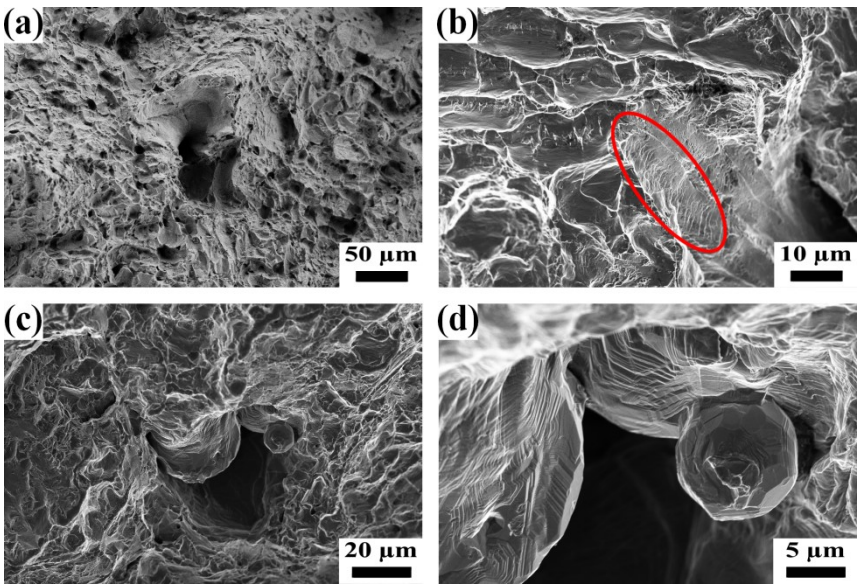


**Figure 107.** FESEM micrographs of fracture surfaces of (a,b) vertical and (c,d) horizontal Ti-6Al-4V samples after stress relieving and heat treatment at 930 °C. In (b) an example of terrace-like features related ti α phase cleavage (red circle) was observed, while in (c,d) un-melted particles with fragile smooth fracture surfaces were detected.

A part from the effects of post-processing heat treatments on tensile properties, from the stress-strain curves presented in Figure 99 it could be seen that the horizontally built specimens displayed slightly higher tensile strength and elongation compared to the vertically fabricated ones.

Such mechanical behaviour had been previously observed and discussed in several studies on Ti-6Al-4V alloy processed by LPBF [343–345,354]. As

described by Rafi et al. [358] the anisotropic mechanical response of LPBF parts related to the building orientation adopted can be attributed to the distribution and orientation of defects inside the parts. During tensile loading of vertically built samples the layers within the component are perpendicular to the loading direction and as a consequence many interlayer defects appear perpendicular to the loading axis. In such conditions the defects can be easily open up with relatively low stress levels. Instead in the case of horizontally built samples the inner layers are parallel to the main tensile loading direction and any interlayer defects are parallel to main loading axis. As a consequence an higher stress level is necessary to open up the defect compared to the case before. Moreover it must be noted that vertically built samples possess an higher number of layers and so an higher number of interlayer defects, than the horizontally fabricated specimens: such observation can explain the lower mechanical properties measured within this study [344]. A second explanation of the mechanical anisotropy could be related to the presence of β columnar grains originated during the LPBF process. Indeed while the vertically fabricated samples possessed the elongated grains parallel to the loading direction, in the case of the horizontally built specimens the prior β grains resulted perpendicular to the stress axis. The different orientation of the β grains respect to the loading direction could be related to the different ductility measured during tensile tests [345]. Furthermore, as described by Simonelli et al. [344], the surface roughness in the fracture profiles appeared to be higher in the case of vertical specimens than in the case of the horizontal ones. This feature can be related to the different orientation of the columnar grains respect to the loading direction, and consequently, to the different crack path during fracture: in the case of vertical samples, the crack path appeared tortuous and so the fracture profile appeared rougher than in the case of the horizontal specimens [344].

Finally from the tensile results (Table 17) and micro-Vickers hardness data (Table 18), the different effect of oxygen amount on the mechanical properties of the parts could be appreciated: with high oxygen content the tensile strength, elastic modulus and hardness increased between 11 and 20 % while ductility decreased between 2 and 10 %, for all the post-processing conditions investigated. Another proof of such behaviour can be obtained after comparing the dimpled fracture surfaces observed. Indeed as reported in Table 19 the dimples dimension varied according to the same trend showed by the stress-strain curves: at higher oxygen contents correspond higher strength, lower elongation at break and smaller dimples. Such difference must be related to the solution strengthening effect induced by oxygen inside the Ti-6Al-4V alloy. Oxygen increases the lattice parameters ratio

(c/a) of the α hexagonal crystal by occupying the octahedral interstices in the crystal [184,185,387]. By modifying the c/a ratio oxygen restricts the number of slip planes consequently increasing hardness and strength while reducing ductility in Ti-6Al-4V [184].

### 4.2.4 Fatigue properties

In this study the effects of the post-processing conditions, building orientation and oxygen content on the fatigue resistance Ti-6Al-4V specimens fabricated by LPBF were took under investigation. The results obtained are exposed in the S-N graphs of Figure 108: as in the case of the tensile properties some main considerations can be taken from the observation of the S-N plots:

- The highest fatigue resistance was measured for the stress relieved and HIPped specimens which reached the fatigue endurance limit of $10^7$ cycles at 500 MPa cyclic stress; the rest of the tested samples broke for a lower number of cycles at lower applied stresses, particularly the stress relieved and heat treated samples which displayed the lowest endurance limit (less than $10^6$ cycles).
- In stress relieved conditions horizontally built specimens showed slightly higher fatigue resistance than the vertically built ones, while after further heat treatment the anisotropy disappeared leading to more homogeneous fatigue properties.
- In the stress relieved conditions it was possible to observe that samples with low oxygen content possessed a slightly higher fatigue resistance than the specimens with high oxygen amount; such difference in the fatigue response tended to disappear after further heat treatment.

In order to investigate the crack nucleation site, the propagation behaviour and the final rupture during the fatigue tests, the fracture surfaces were observed by stereomicroscopy and FESEM analyses. Figure 109 and Figure 110 illustrate the fracture surface of stress relieved specimens, vertically oriented with low and high oxygen content, respectively. As shown in the Figure 109a and Figure 110a the overall fracture surface was divided in three main area, crack initiation, crack propagation and final fracture area, respectively. These regions distinguish the principal steps in the material fracture during fatigue tests: particularly the crack

initiation (Figure 109b and Figure 110b) commonly takes up much of the overall fatigue life compared to the other steps [358].

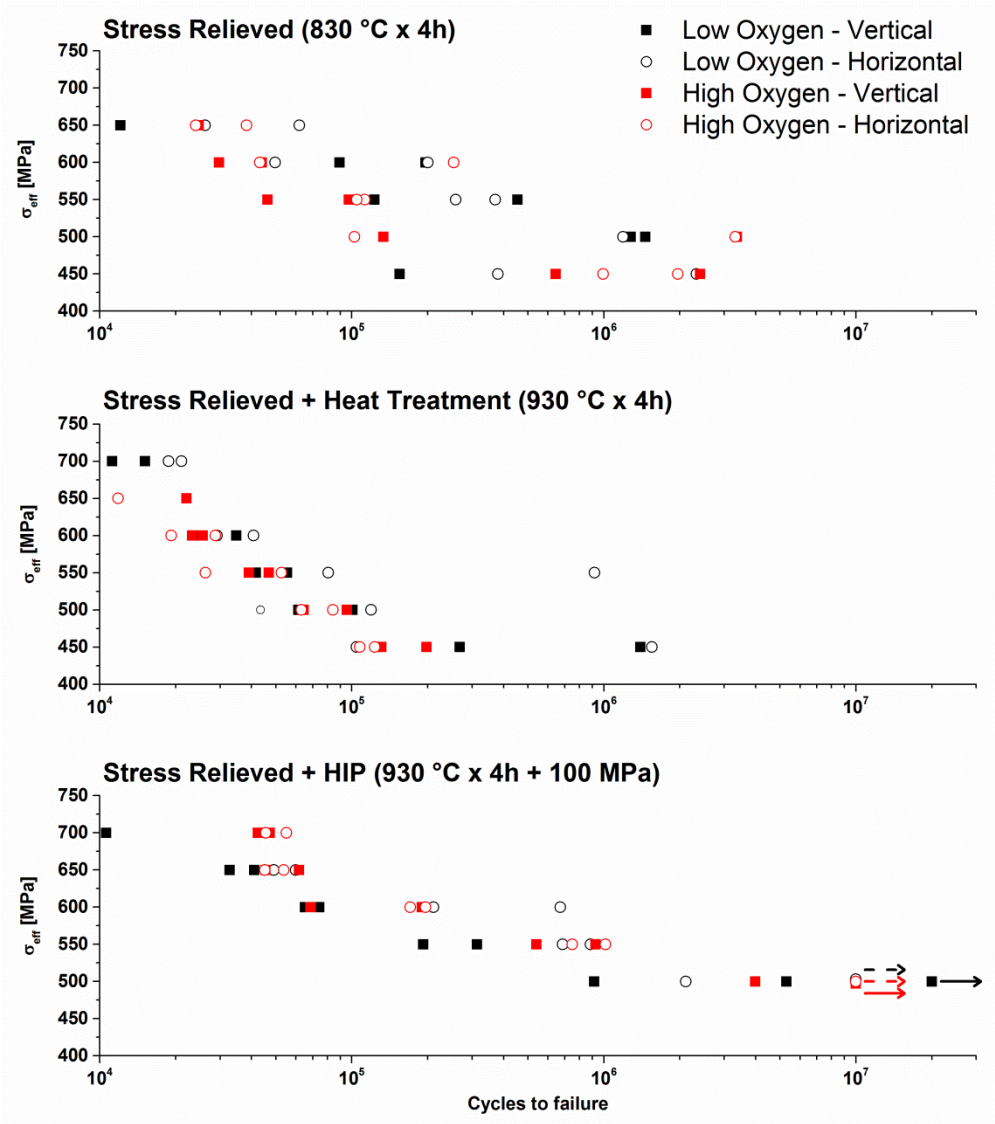


**Figure 108.** Fatigue tests results on Ti-6Al-4V specimens produced by LPBF, with two different oxygen contents inside the original powders, and tested in three different conditions for both the vertical and horizontal building direction.

Fatigue crack initiation depends on many factors such as microstructural inhomogeneity, surface roughness, presence of porosities, defects and secondary particles, notches etc. Generally the main failure reasons are represented by the presence of pores, defects and un-melted particles in proximity of the surface and

by the very low surface roughness [361,363,388]. Porosities, cracks or un-melted particles act as stress accumulation sites promoting and accelerating the nucleation of the crack [304]. In the case of smooth and defect-free Ti-6Al-4V parts fatigue crack initiation can differ considerably depending on the particular microstructure present inside the material [358,365,389]. In the case of lamellar microstructures, such the ones observed previously in this study (Figure 88,Figure 92 and Figure 96), crack initiation can occur by cross-colony slip band fracture [358]. The longer slip path is expected to easily provoke slip-off of the intense slip band, leading to crack nucleation even at low stress levels: by microstructure refinement and homogenization it is possible to enhance the fatigue resistance of Ti-6Al-4V parts by restraining both crack initiation and propagation [365].

In the case of metallic parts fabricated by LPBF and AM techniques, which generally possess much finer microstructures than the wrought or cast components ones, fatigue life is considerably lower and crack initiation is sited close to the surface. Such poor mechanical performance is provoked by the presence of pores and interlayer defects which highly weaken the material, together with low surface fineness, which considerably affects the fatigue properties [14,251].

In this study from the investigation of the specimens fabricated by LPBF and subsequently stress relieved, the river patterns observed in Figure 109a and Figure 110a suggested that the crack most probably nucleated in correspondence of an agglomeration of sub-surface defects (Figure 109c,d and Figure 110c,d). Depending on the defect kind, size and location, the material behaviour during

tensile-tensile fatigue tests varied considerably, producing a consistent scatter of fatigue life results [368], as shown in the first plot of Figure 108.

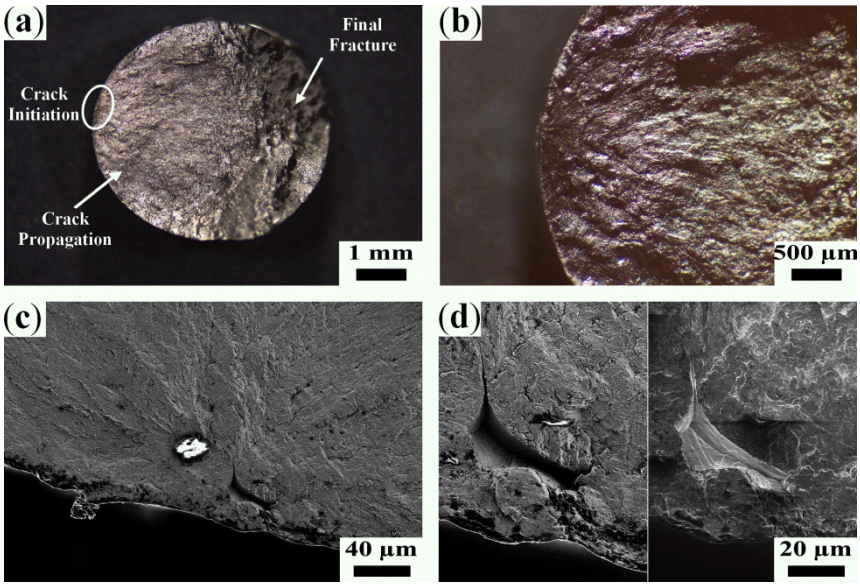


**Figure 109.** Fatigue fracture surfaces of vertical stress relieved Ti-6Al-4V specimen, with low oxygen content, observed by stereomicroscopy (a,b) and FESEM analysis (c,d): (a) overall fracture surface showing the crack initiation site, the crack propagation and final fracture areas; (b-d) crack initiation site observed at progressively higher magnification.

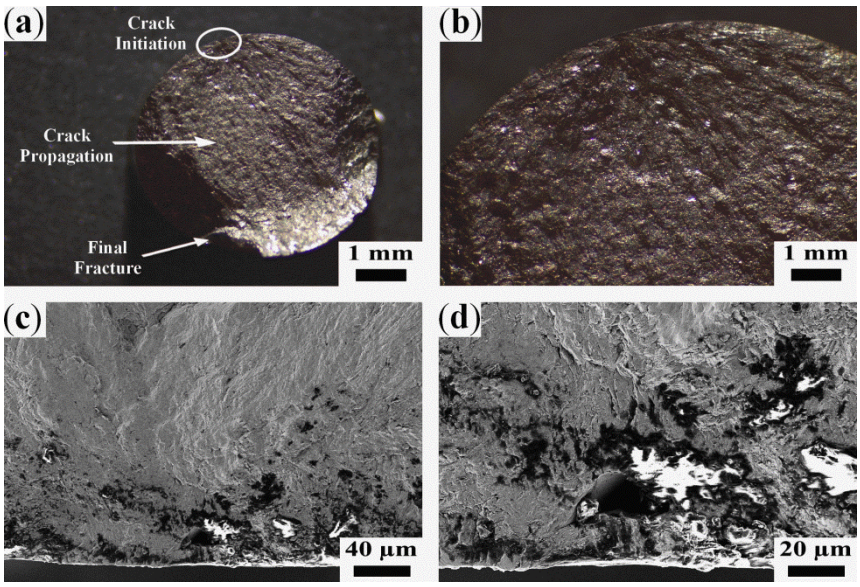


**Figure 110.** Fatigue fracture surfaces of vertical stress relieved Ti-6Al-4V specimen, with high oxygen content, observed by stereomicroscopy (a,b) and FESEM analysis (c,d): (a)

overall fracture surface showing the crack initiation site, the crack propagation and final fracture areas; (b-d) crack initiation site observed at progressively higher magnification.

After initiating, crack began to propagate towards the center of the sample, reducing the effective stress-bearing area and consequently increasing the true cyclic stress. Figure 111a,b highlight the crack propagation region, showing the typical flat and striated fracture surface of fatigue tests, originated due to the repeated re-sharpening of the material during cyclic loading. Once the loading section was reduced to the critical state, the true cyclic stress exceeded the material strength and momentary break of the specimen took place: Figure 111c,d display the final fracture area and show how the specific fracture surface appeared rough and finely dimpled.

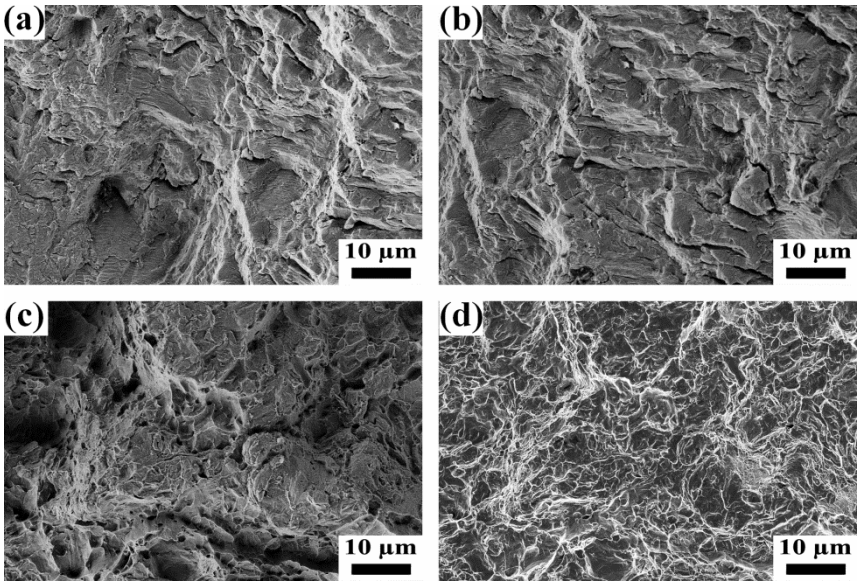


**Figure 111.** FESEM investigation of fatigue fracture surface of stress relieved Ti-6Al-4V specimens: (a,b) crack propagation areas; (c,d) final fracture area observed with two detectors mode, respectively.

Another example of defect detected on the fracture surface is exposed in Figure 112: the sharp apostrophe-shaped imperfection (Figure 112a), with an average width of 20 µm and a length of almost 40 µm, represented a substantial discontinuity in the material which considerably decreased the mechanical resistance. Moreover, it could be observed at higher magnifications (Figure 112b-d) that the fracture surface in correspondence of such defect was constituted by submicrometrical terrace-like features. Typically they are related to the fragile rupture of oxide species along preferential crystallographic directions [345], as observed before in Figure 107d. This consideration was also confirmed by the EDS analysis, displayed

in Figure 114 which showed an increase in the oxygen concentration in correspondence of the apostrophe-shape defect. Moreover from EDS analysis it could be noted that, a part from oxygen mostly located close to the sample surface in correspondence of subsurface defects (Figure 110), the other major constituents of the alloy appeared homogeneously distributed inside the material.

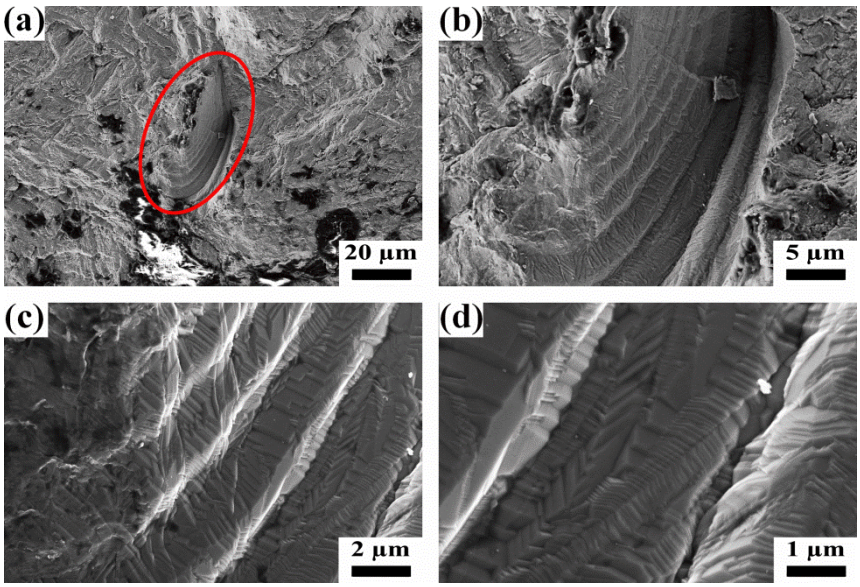


**Figure 112.** FESEM analysis of a defect present on the fracture surface of the stress relieved Ti-6Al-4V specimens.

From the investigation of fracture surface no appreciable differences between specimens built with low and high oxygen content were pointed out. The slightly lower fatigue strength measured for the specimens fabricated with a high oxygen content (upper plot in Figure 108) could be related to the strengthening effect given by oxygen to the alloy, which reduced ductility and strength life and favoured crack initiation [186,363].

Furthermore, the different building direction adopted to manufacture the samples induced a light anisotropy in the fatigue strength results: horizontally built specimens resisted for an higher number of cycles compared to the vertically built ones. Figure 113 shows an example of the fracture surface in the case of horizontal stress relieved specimens: as it can be observed crack initiated at sample surface as in the case of vertical specimens.

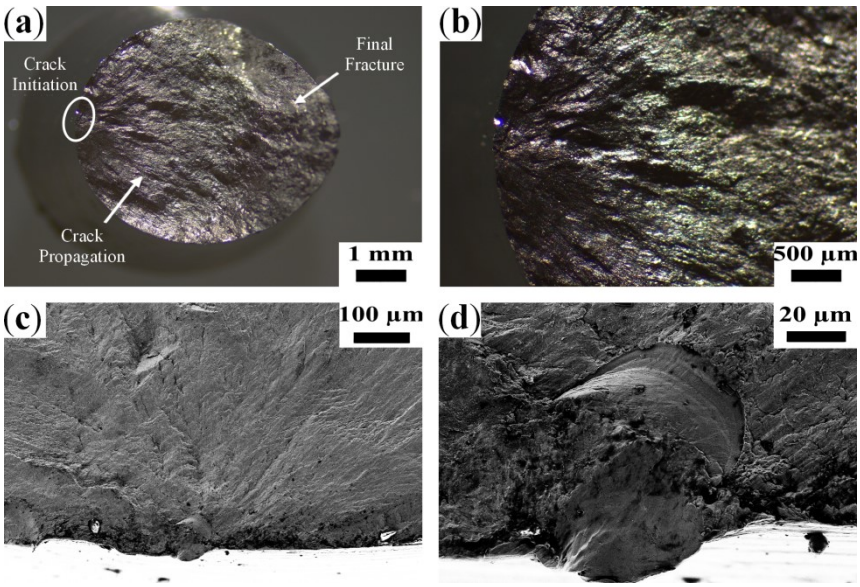


**Figure 113.** Fatigue fracture surfaces of horizontal stress relieved Ti-6Al-4V specimen observed by stereomicroscopy (a,b) and FESEM analysis (c,d): (a) overall fracture surface showing the crack initiation site, the crack propagation and final fracture areas; (b-d) crack initiation site observed at progressively higher magnification.

A possible explanation could be the different orientation of β columnar grains which altered the propagation path of the crack. When the columnar grains were perpendicular to the direction of the cyclic stress direction, they offered an higher resistance to the crack propagation increasing the fatigue resistance [353,367]. Moreover it could be considered that the vertically oriented specimens contained an higher number of interlayers defects than the horizontally built ones, which could greatly accelerate the crack propagation and final rupture of the material [353].

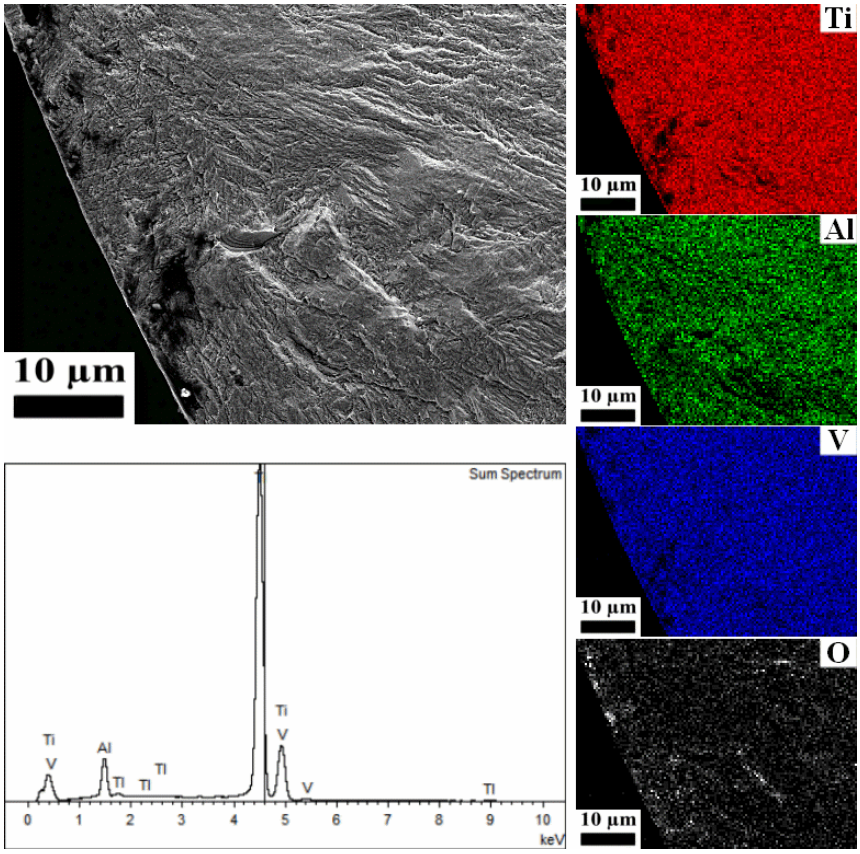


**Figure 114.** EDS analysis on the fracture surface of Ti-6Al-4V stress relieved specimens.

Regarding the stress relieved and heat treated specimens, from Figure 108 it could be observed how the overall fatigue strength was lower compared to the other conditions. The maximum fatigue life exceeded $10^6$ cycles for 450 MPa applied stress in the case of two samples with low oxygen content while for higher stresses all the specimens resisted less than $10^5$ cycles. It is worth to note that differently from the stress relieved conditions, the heat treated specimens showed less scattered results: the explanation could be related to the more homogeneous microstructure present inside the material (Figure 91). However some porosity was present inside these pieces and affected the fatigue properties. Indeed at 550 MPa the horizontal specimen, with a low amount of oxygen, showed an higher resistance than the others: Figure 115 reports the fracture surface investigation carried out on the sample. In this case fracture initiated at a certain distance (Figure 115a,b) from the sample surface, at almost 500 µm, in correspondence of a micrometric pore (Figure 115c,d): the defect was ~ 20 µm wide with smooth surfaces inside, which can be related to fragile rupture. Since the spherical shape of the pore, this type of porosity could be originated to enclosed gasses or un-melted particles [14]. The higher

fatigue resistance of the sample mostly derived from the higher distance of the crack initiating defect from the surface, which increased considerably the crack initiation time during fatigue test, and consequently the entire fatigue life of the specimen.

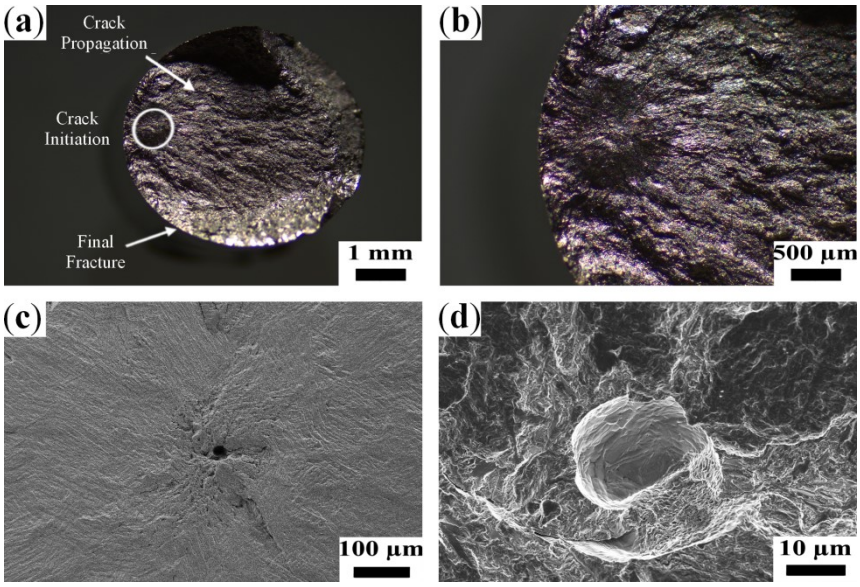


**Figure 115.** Fatigue fracture surfaces of the horizontal stress relieved and heat treated Ti-6Al-4V specimen tested at 550 MPa, observed by stereomicroscopy (a,b) and FESEM analysis (c,d): (a) overall fracture surface showing the crack initiation site, the crack propagation and final fracture areas; (b-d) crack initiation site observed at progressively higher magnification.

At the same time the lower fatigue resistance showed by the rest of heat treated specimens could be related to the higher porosity and position of the defects in the specimens From fracture surface investigation (Figure 116 and Figure 117) appeared that crack initiated in correspondence of the surface for both the horizontal and vertical samples. Crack originated from subsurface defects (Figure 116d) and terminated with a fine dimpled fracture, similar to the tensile test fracture surfaces observed in the previous chapter (Figure 103). The coarse microstructure of heat treated samples (Figure 92) together with the higher amount of ductile β phase offered less resistance to the crack initiation and propagation compared to the finer microstructure of stress relieved specimens (Figure 88), consequently reducing the fatigue life of the material.

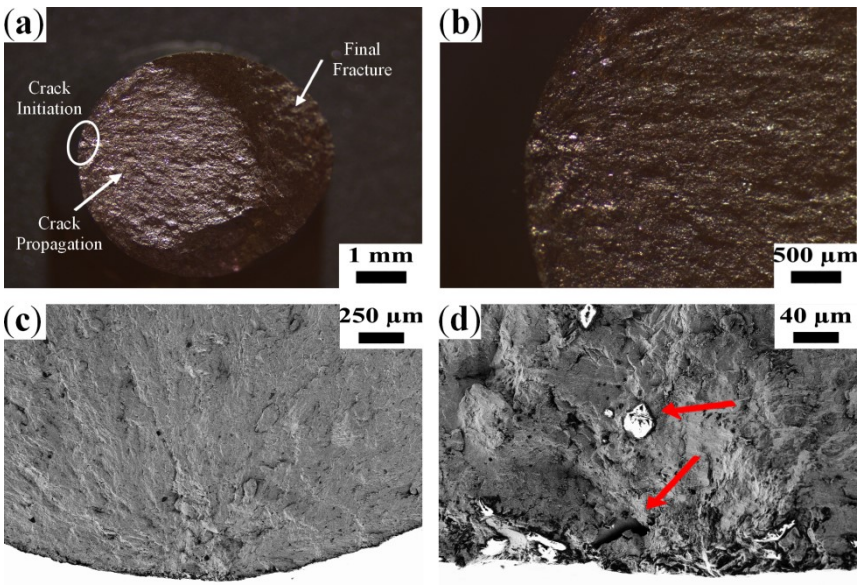


**Figure 116.** Fatigue fracture surfaces of vertical stress relieved and heat treated Ti-6Al-4V specimen observed by stereomicroscopy (a,b) and FESEM analysis (c,d): (a) overall fracture surface showing the crack initiation site, the crack propagation and final fracture areas; (b-d) crack initiation site observed at progressively higher magnification. The red arrows in (d) highlight subsurface defects which may have initiated the crack during test.

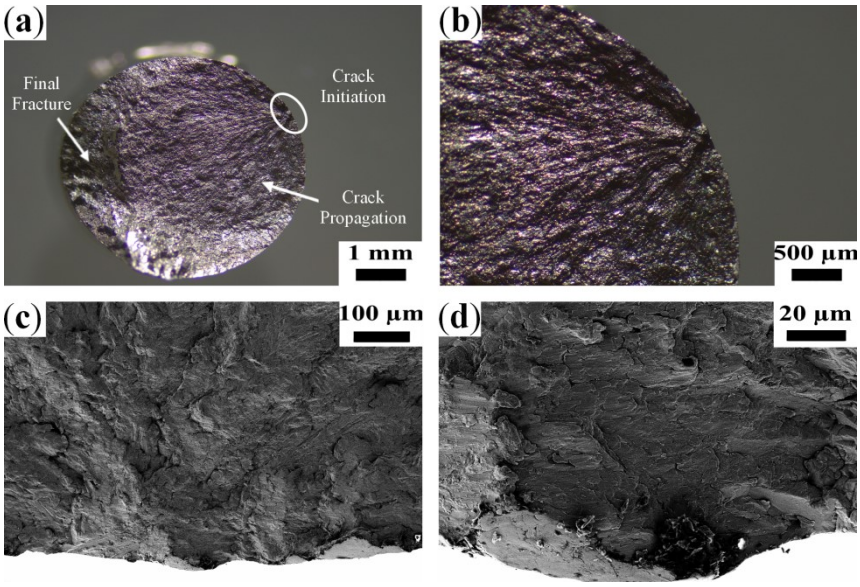


**Figure 117.** Fatigue fracture surfaces of horizontal stress relieved and heat treated Ti-6Al-4V specimen observed by stereomicroscopy (a,b) and FESEM analysis (c,d): (a) overall fracture surface showing the crack initiation site, the crack propagation and final fracture areas; (b-d) crack initiation site observed at progressively higher magnification.

From Figure 108 no substantial difference could be detected between specimens fabricated with different building orientation, probably due to the microstructural evolution of the material after heat treatment (Figure 91). Indeed since β columnar grains inside the microstructure (Figure 92) became less defined compared to the stress relieved conditions (Figure 88), most probably also the induced anisotropy decreased. As well no appreciable difference could be observed between samples with low and high oxygen content. Most probably the effect of oxygen on the strengthening of α phase was less influencing than the presence of defects and pores inside the material, which appeared to rule the fatigue resistance of the material.

By further fractography investigations, showed in Figure 118, the presence of subsurface defects was detected and related to the crack initiation. Moreover, by FESEM analysis it was possible to observe the fracture of smooth facets on the fracture surface (Figure 118c,d): such features could be related to the cleavage of α grains, nearly perpendicular to the loading direction, which represented a preferential path for material rupture during cyclic loading [388,389]. EDS maps (Figure 114) showed the presence of oxides species in the fracture surfaces, similarly to the previous case of stress relieved samples, and confirmed the nature of such defects.

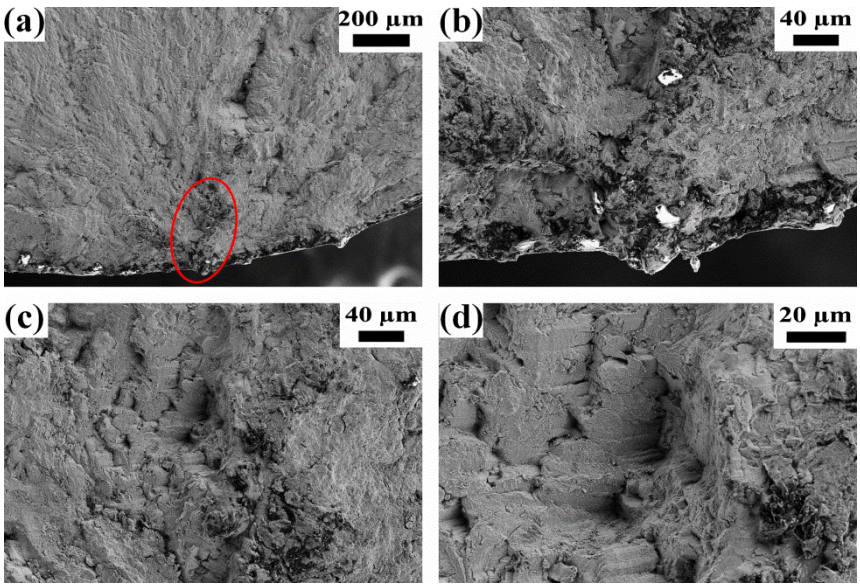


**Figure 118.** FESEM analysis of the crack initiation site in the fracture surface of the stress relieved and heat treated Ti-6Al-4V specimen (high oxygen content) at different magnification.

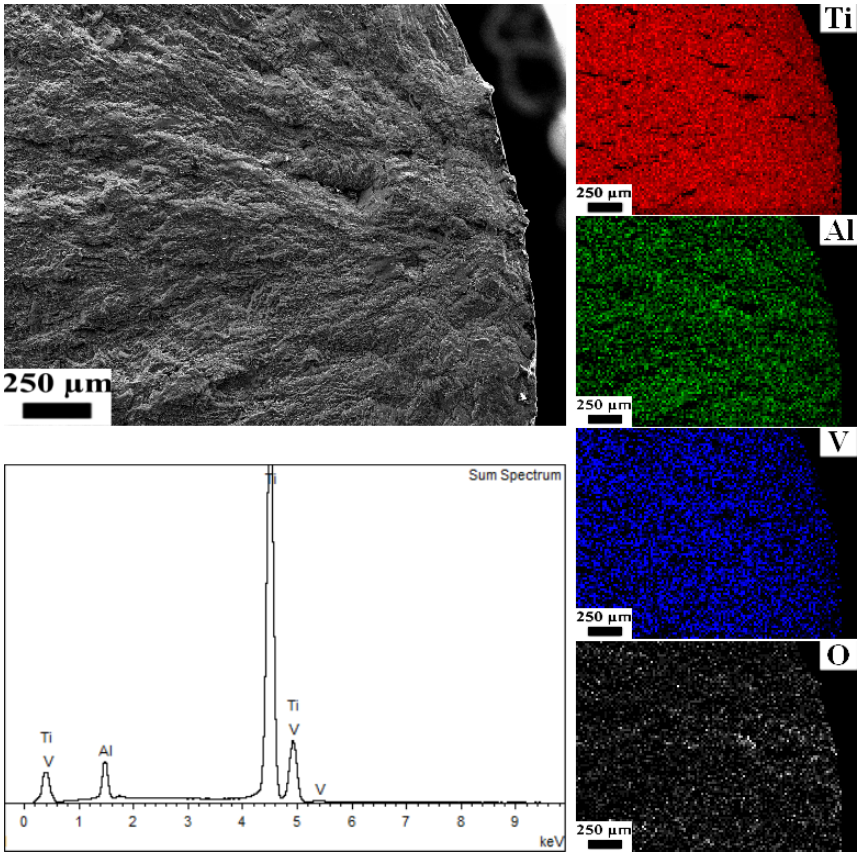


**Figure 119.** EDS analysis on the fracture surface of Ti-6Al-4V stress relieved and heat treated specimens.

Differently from the cases already described the HIPped specimens showed a consistent higher resistance during fatigue tests (Figure 108): the endurance limit of $10^7$ cycles was exceeded for an applied stress of 500 MPa. The main reason can be ascribed to the reduction of porosity level provided by HIP. Indeed, as already described in literature and in the industrial applications, such post-processing operation is able to improve the final performances by closing porosities and adjusting microstructure [361,363,368]. Moreover a part from the higher fatigue strength obtained, it could be noticed that the values measured appeared less scattered than in the stress relieving conditions due to the lower porosity inside the samples [368].

The results of fractography investigations are exposed in Figure 120 and Figure 121. As observed before for the stress relieved and stress relieved and heat treated specimens, also in the HIPped samples the crack originated at surface (Figure 120a,b) and propagated towards the center. Figure 120d highlights two

discontinuities which could have initiate the fracture during fatigue testing. Probably these defects were constituted by oxides layers or porosities with oxide layers on their surface, which were not closed during HIP treatment. EDS analysis (Figure 123) showed a small concentration of oxygen close to the initiation site which could be correlated to the oxide layers presence. Indeed HIP treatment is able to fully close most part of the pores present inside the components, but in the case of oxide layers some difficulties can develop. Indeed eliminating oxide surfaces by HIP is problematic since the material is different from the metallic matrix: finally some oxide inclusions and pores could also be find after HIP treatment.

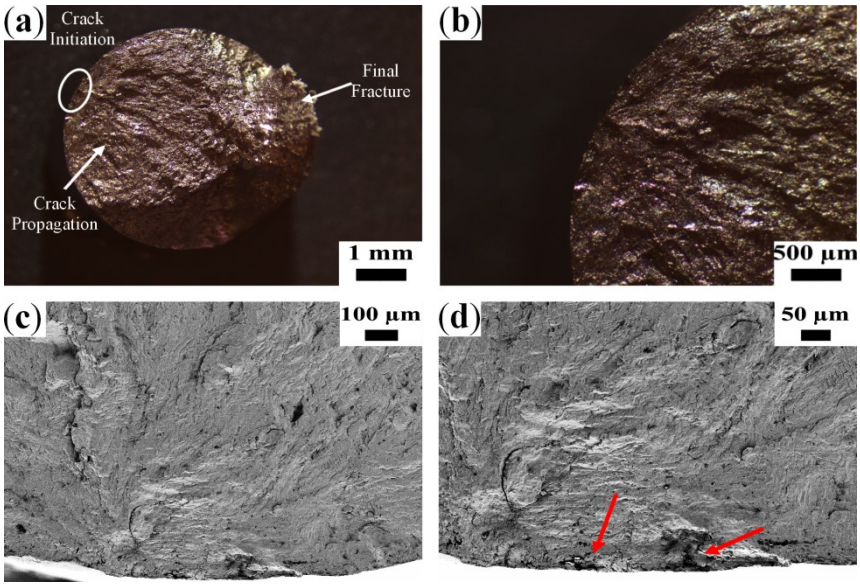


**Figure 120.** Fatigue fracture surfaces of vertical stress relieved and HIPped Ti-6Al-4V specimens (low oxygen content) observed by stereomicroscopy (a,b) and FESEM analysis (c,d): (a) overall fracture surface showing the crack initiation site, the crack propagation and final fracture areas; (b-d) crack initiation site observed at progressively higher magnification. The red arrows in (d) highlight subsurface defects which may have initiated the crack during test.

Figure 121 show some other examples of crack initiation sites found inside the HIPped specimens. As it can be seen in Figure 121a, two different features were detected and investigated: the first one (marked by red arrow) might have been a cluster of α-phase facets (Figure 121b) originated due to cleavage of the α grains, while the second one (marked by green arrow) was a smaller defect present on the surface of the sample (white particle in Figure 121c). According to Gunther et al. [388] since the crack initiating cluster of α-phase facets is bigger in size than the

porosity present in the HIPped Ti-6Al-4V sample, the cleavage of α-grains observed in Figure 121b could be related to the fatigue crack initiation [313,363].

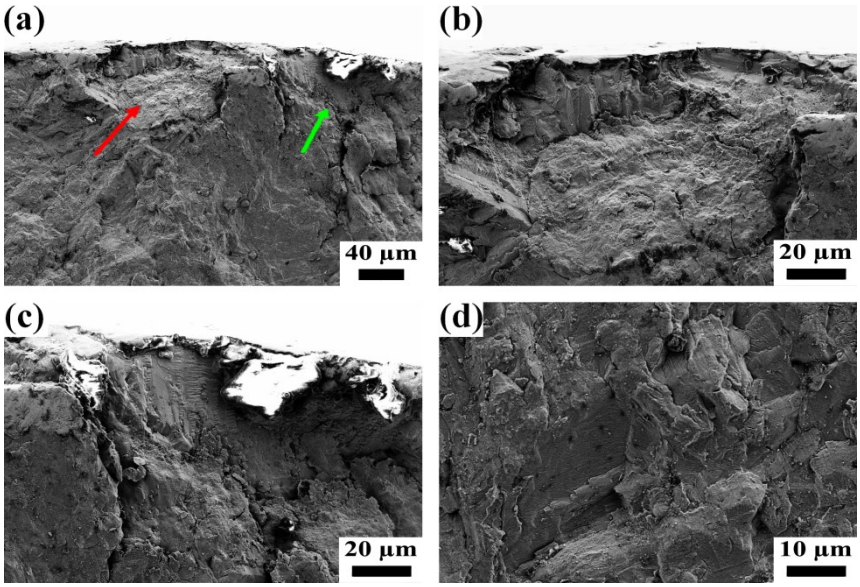


**Figure 121.** FESEM analysis of the crack initiation site in the fracture surface of the stress relieved and HIPped Ti-6Al-4V specimen (high oxygen content) at different magnification: overall crack initiation area; (b) magnification of the area marked by the red arrow; (c,d) magnifications of the area marked by the green arrow.

Moreover from the results shown in Figure 108 no appreciable differences could be noted between horizontally and vertically built specimens, in both low and high oxygen conditions. Figure 122 displays the fracture surface of horizontal fatigue specimen and shows how also in these cases, fracture initiated at sample surface. As in the case of heat treated samples, in the HIPped microstructure β columnar grains appeared less defined than the original stress relieved conditions. Such more homogeneous microstructure reduced considerably the anisotropic response of the material built with different orientations: moreover the tensile properties differed less than 5 % between the horizontally and vertically built specimens in the HIPped conditions.

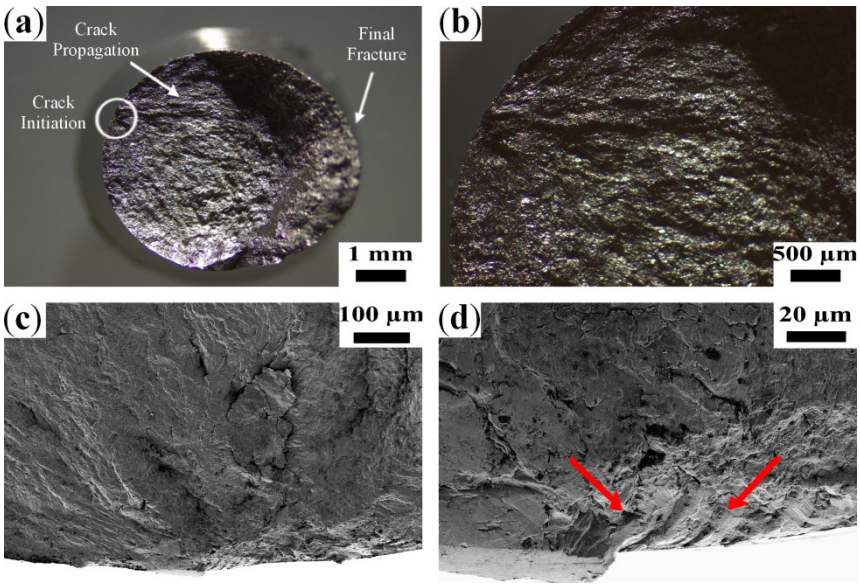


**Figure 122.** Fatigue fracture surfaces of horizontal stress relieved and HIPped Ti-6Al-4V specimens (low oxygen content) observed by stereomicroscopy (a,b) and FESEM analysis (c,d): (a) overall fracture surface showing the crack initiation site, the crack propagation and final fracture areas; (b-d) crack initiation site observed at progressively higher magnification. The red arrows in (d) highlight subsurface defects which may have initiated the crack during test.

Regarding the effect of oxygen an higher fatigue life should be possessed by samples with low oxygen content since the detrimental effect of such element on ductility and fatigue life. Instead the fatigue resistances measured in this study appeared more scattered than expected and the difference between low and high oxygen content conditions less evident. Like in the cases of the others post-processing conditions, also for HIPped specimens appears that the main factor influencing the fatigue properties was the remaining porosity present inside the material.

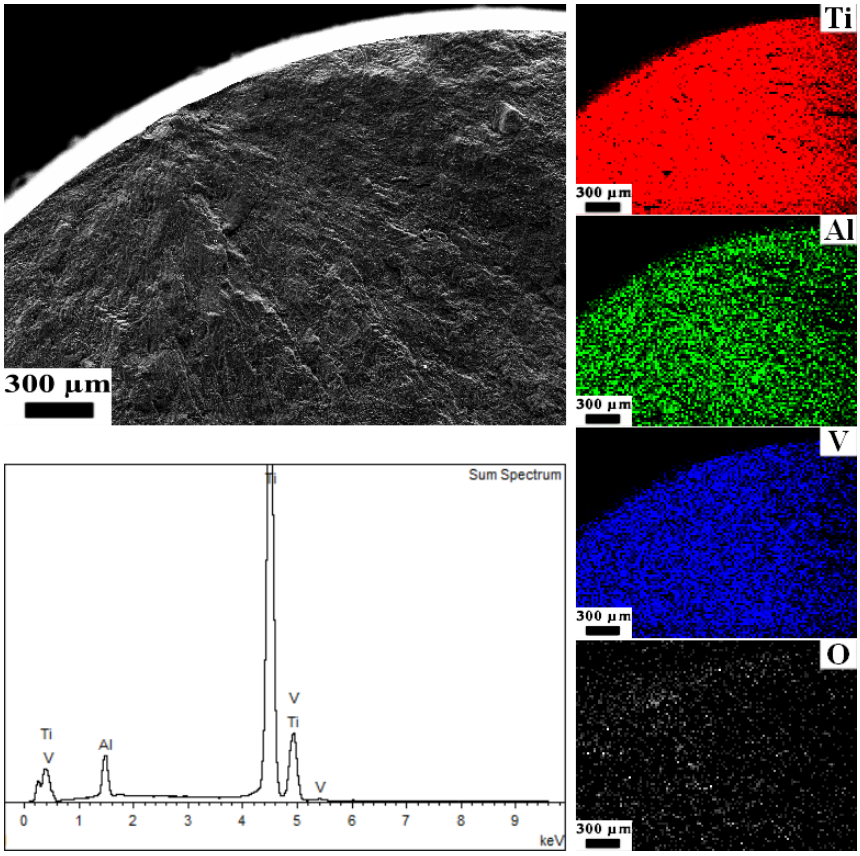


**Figure 123.** EDS analysis on the fracture surface of Ti-6Al-4V stress relieved and HIPped specimens.

In all the conditions investigated, the material cracked initially at the surface, due to the presence of sub-surface defects: porosities, cracks and oxide layers which acted as stress concentration sites and appeared to be the major responsible of the low fatigue properties of the samples [361,363,388]. Performing a HIP treatment, and consequently reducing the defects amount inside material, strongly increased the fatigue properties compared to the other conditions. Moreover the positive effect of enclosing the major part of defects and pores on fatigue life of the parts could be stated by comparing the heat treated and HIPped samples, which both possessed comparable lamellar microstructures but a different porosity level.

Further comparison of the results could show that finer microstructures promoted higher fatigue resistances: stress relieved samples, which possessed the finest lamellar structures, showed higher fatigue life than the heat treated samples which instead possessed a coarser lamellar microstructure [389]. From this point of view, further heat treatment at 930 °C, without external pressure application,

seemed to be disadvantageous for the mechanical properties since it coarsened the microstructure, reducing material strength, and did not reduce the amount of defects [313,361,363].

One positive effect given by the modification of microstructure was the homogenisation of the material and the almost complete disappear of the β columnar grains. Such microstructural features affected the mechanical response of the parts, leading to an higher resistance in the case of horizontally built samples compared to the vertically built ones [344,345,363]. Applying a subsequent high temperature treatment at 930 °C promoted the homogenisation of the microstructure and consequently of the mechanical properties of the fabricated parts.

Finally from the investigation of the fatigue resistances of Ti-6Al-4V parts appeared that the effect of oxygen on the mechanical properties was much noticeable in the stress relieved conditions compared to the other ones. As the microstructure was modified by the heat treatment, the effect of oxygen on the α/β lamellae growth lowered and consequently also the effect on the dynamic mechanical response diminished. However, even if the effect oxygen was noticeable after stress relieving, the fatigue properties were much more related to the porosity level present inside the material [313,361].

### 4.2.5 Conclusions

This study investigated the microstructural and mechanical properties of Ti-6Al-4V parts fabricated by LPBF process adopting two different gas atomised powders with two distinct oxygen content inside the chemical composition. The tensile and fatigue specimens produced were built with two different orientations, horizontal and vertical direction, and were tested in three different post-processing conditions: stress relieved, stress relieved and heat treated, stress relieved and HIPped.

Post-processing treatments altered the original microstructure of the stress relieved specimens by coarsening the fine $\alpha + \beta$ lamellar structure, increasing the amount of $\beta$ phase and erasing the $\beta$ columnar grains along the vertical building direction. The microstructural evolution of the material modified the mechanical response of the material, by increasing ductility and reducing the tensile strength and at the same time lowering the anisotropy behaviour between different oriented samples. Indeed while in the stress relieved conditions, the horizontal specimens showed higher fatigue resistance than the vertical ones, after further heat treatment the anisotropic response decreased.

Pores and other defects strongly reduced the tensile and fatigue properties of the parts produced, particularly in the stress relieving plus heat treatment conditions for which the lowest tensile strength and fatigue resistance were measured. Pores and defects acted as stress concentration sites during fatigue tests inducing the crack initiation at the surface of the specimens in all conditions investigated. As a solution, HIP process permitted to reduce the amount of pores and defects and to considerably increase elongation at break and particularly the fatigue resistance.

Varying the oxygen amount in the original metal powder slightly modified the microstructure and mechanical properties of the material produced. The strongest effect of oxygen was measured for the tensile strength and hardness, while for the fatigue response only a slight difference was observed in the stress relieving conditions, in which the specimens with low oxygen content showed higher fatigue resistance. On the other way by applying further heat treatments the difference in the fatigue resistance between low and high oxygen content was not consistently appreciable.

This study wanted to investigate which would be the most influencing factors for the fatigue response of the components fabricated by LPBF and subsequently

machined. From the results appeared that the most important factor affecting the mechanical response of the material was the porosity level present inside the parts, particularly for fatigue properties. On the contrary varying the oxygen content or the building orientation seemed less influent on the fatigue behaviour of the material. Only HIP treatment permitted to increase the fatigue life of the material over $10^7$ cycles for an applied stress higher than 450 MPa.

Since porosity appeared to be ruling the fatigue properties of the machined material, major interest should be focused on the reduction of pores and defects concentration inside the LPBF parts. Moreover, another factor which is highly influencing the fatigue properties is surface roughness. Future study would focused on the investigation of post-processing HIP treatment effects on Ti-6Al-4V parts made by LPBF and on the influence of surface roughness over the fatigue properties. The reason would be to understand which factor should be taken more under inspection for the industrial applications of parts made in Ti-6Al-4V alloy by LPBF.

# Chapter 5

# LPBF of pure copper

## 5.1 State of the art

Copper is a soft and malleable metal used as functional materials for heat exchangers and electrical devices due to their excellent thermal and electrical properties. By rolling and drawing a variety of electrical products such as wires, sheets, tubes, shaped bars can be manufactured. Since these physical properties are very impurity-sensitive, high conductivity devices require the use of copper in the pure form [281]. The most used commercially pure copper alloys adopted in electronics are the deoxidized copper, oxygen-free copper and tough pitch copper (Table 20). The use of unalloyed copper is often limited by low mechanical properties, which can be improved by cold working, grain refinement, precipitation hardening etc.: the challenge is to obtain the best compromise between electrical conductivity and mechanical strength [390].

**Table 20.** Three main copper alloys for electronic applications [391].

| Electrical Copper Alloys | Cu content [wt.%] | O content [wt.%] | P content [wt.%] | Electrical resistivity at 20 °C [mΩ/mm$^2$] | Thermal conductivity at 20 °C [W/m K] |
|---|---|---|---|---|---|
| **Tough pitch copper** | 99.00 min | 0.04÷ 0.05 | - | 58.6 | 226 |
| **Deoxidized low-phosphorus copper** | 99.90 min | 0.01 | 0.004÷ 0.012 | 49.3 | 196 |
| **Oxygen-free electronic copper** | 99.99 min | 0.001 max | - | 58.6 | 226 |

In the past years preliminary studies on LPBF processing of copper were carried out on mixed powders, particularly Cu-CuSn-CuP systems, adopting $CO_2$ laser systems [392,393] and fiber laser ones [266–268]. Similarly, many other experiments were carried out on other copper alloys, such as Cu-Cr-Zr-Ti [116] and C18400 alloys [269,270] and composites [394,395]. Although the processing of full dense components made in pure copper by LPBF represented a crucial issue for many years: up to nowadays few studies have been carried out [115].

Laser processing of pure copper involves two main challenging issues: the high reflectivity and the high thermal conductivity of copper powders. Both these limitations reduce the amount of energy available for the melting, leading to high porosity and therefore low mechanical and electrical properties. Lykov et al. [115] evaluated several process parameters combinations using a commercial laser machine, equipped with 200 W $CO_2$ laser, producing 88 % dense pure copper samples. They established that a further correction in the process parameters choice would improve the material densification during the process. Another possible solution would be to use more powerful laser systems (from 300 W to 1 KW), in order to fully melt the copper powder bed [396]. Nowadays, LPBF machines are commonly equipped with lasers with a maximum power up to 400 W, with the largest number of machines installed with a 200 W laser. Therefore the determination of LPBF process parameters for copper manufacturing using such lasers could be very attractive for industries [115].

## 5.2 Study and characterisation of pure copper processed by LPBF

This study aims to investigate the production of chemical pure copper by LPBF process with an EOSINTM270 Dual Mode machine, equipped with 200 W Yb fiber laser as stated before. Furthermore the material properties such as the chemical composition and microstructure of the fabricated materials were characterised by optical and electron microscopy, energy-dispersive X-ray spectroscopy (EDS) and X-ray diffraction (XRD).

### 5.2.1 Powder properties

Table 21 lists the chemical composition and size distribution of the oxygen free copper gas atomised powder used in this study, as reported by material datasheet of the supplier. Figure 124 shows the preliminary observation of the morphology of

the gas atomised powder by FESEM analysis (Appendix A.1). The raw powder appeared almost spherical with minor satellites, as shown in Figure 124b. Satellites particles form during gas atomisation process due to the collision between fine solidified particles and partially molten particles caused by the gas circulation in the atomising chamber [168].

**Table 21.** Oxygen free high thermal conductivity copper gas atomised powder used in this study.

| Material | Chemical composition [wt.%] | Particle size range [µm] | Supplier |
|---|---|---|---|
| **Oxygen free high thermal conductivity (OFHC) copper** | O = 0.04<br>Cu = bal. | 5 ÷ 25 | Sandvik Osprey Ltd. |

The mean size distribution was also investigated through laser granulometry adopting a frequency distribution based on volumetric assumption (Appendix A.2). The volume and cumulative fraction of the powder are exposed in Figure 125: the values of $D_{10}$, $D_{50}$ and $D_{90}$ are 6, 9.5 and 14 µm, respectively.

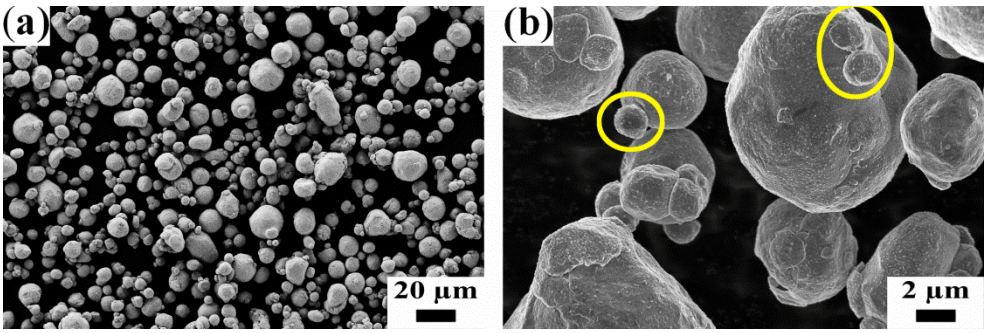


**Figure 124.** FESEM micrographs of high chemical pure Cu powders processed in this study at different magnifications (a,b). The yellow circles in (b) highlight satellites adhering on bigger particles surface.

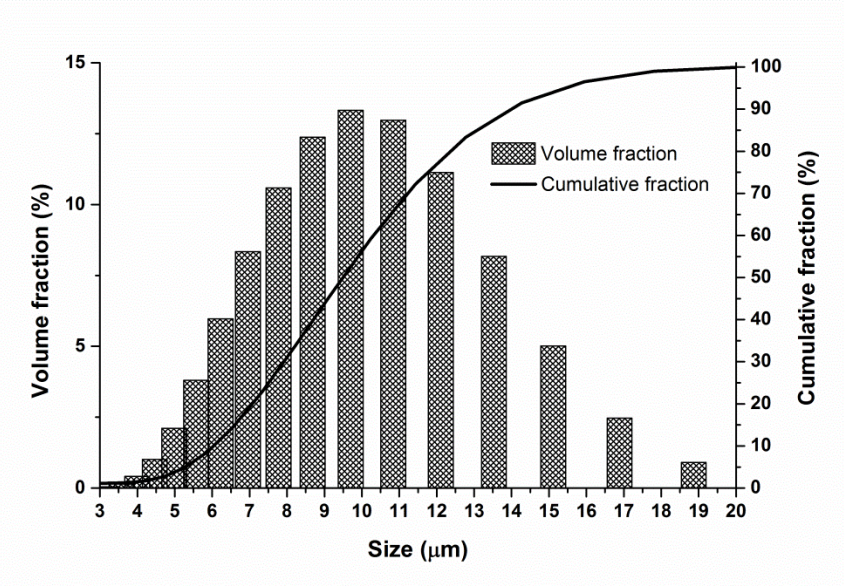


**Figure 125.** Particle size distribution of HCP Cu gas atomized powders obtained by laser granulometry.

## 5.2.2 Evaluation of porosity

This study was carried out using a layer thickness 30 μm, 67° rotated scanning strategy and building platform temperature of 100 °C. The 30μm layer thickness was chosen after several trials during which 20 and 25 μm layer thickness values were adopted. None of these trials was successful to produce final specimens for density characterisation due to the parts collapse during LPBF process. Table 22 contains the combinations of process parameters adopted for the 10 x 10 x 10 mm specimens fabrication together with the relative density measurements obtained by Archimedes method (Appendix A.3).

**Table 22.** Combination of process parameters and relative density of HCP Cu specimens made by LPBF.

| Sample | Power [W] | v [mm/s] | $h_d$ [mm] | Relative density [%] | S.D. [%] |
|---|---|---|---|---|---|
| **1** | 195 | 400 | 0.06 | 80.58 | 0.04 |
| **2** | 195 | 400 | 0.08 | 83.01 | 0.13 |
| **3** | 195 | 400 | 0.10 | 81.89 | 0.08 |
| **4** | 195 | 600 | 0.06 | 82.21 | 0.11 |
| **5** | 195 | 600 | 0.08 | 82.21 | 0.05 |
| **6** | 195 | 600 | 0.10 | 82.12 | 0.06 |
| **7** | 195 | 800 | 0.06 | 82.28 | 0.07 |
| **8** | 195 | 800 | 0.08 | 81.98 | 1.19 |
| **9** | 195 | 800 | 0.10 | 81.59 | 0.73 |
| **10** | 180 | 400 | 0.06 | 82.45 | 0.05 |
| **11** | 180 | 400 | 0.08 | 81.62 | 0.08 |
| **12** | 180 | 400 | 0.10 | 82.02 | 0.02 |
| **13** | 180 | 600 | 0.06 | 79.33 | 0.33 |
| **14** | 180 | 600 | 0.08 | 79.72 | 0.06 |
| **15** | 180 | 600 | 0.10 | 82.07 | 0.02 |
| **16** | 180 | 800 | 0.06 | 81.41 | 0.05 |
| **17** | 180 | 800 | 0.08 | 82.17 | 0.17 |
| **18** | 180 | 800 | 0.10 | 81.11 | 0.07 |

From density results it could be noted that modifying the process parameters relative density varied between 79.33 ± 0.33 % and 83.01 ± 0.13 %, with a mean value of 81.60 ± 0.16 %. The highest density value was registered for Sample 2 built using 195 W laser power, 400 mm/s scanning speed and 0.08 mm hatching distance. This specimen was used for the following microstructural investigations since its lower amount of porosity.

The density values registered were comparable with the results already obtained in literature with different laser system sources [115]. The relative low densification of LPBF parts should be correlated to the low absorptance of copper powders to infrared laser radiation [114] and to the very high thermal conductivity of the material [395]. Indeed adopting different process parameters combinations, and consequently different energy densities, specimens density did not vary significantly.

In the case of copper powder beds the mean absorptance to 1 μm wavelength laser beam is about 0.59 %. As a consequence most part of the radiation is reflected by the material and small quantities of energy are absorbed and transformed in thermal energy. At greater radiation wavelengths material absorptance further decreases and at 10 μm wavelength the average absorptance is just 0.26 % [114,197]. The powder bed laser absorption and reflectivity were investigated by Diffuse Reflectance Spectroscopy (DRS) analysis (Appendix A.7) and the results are reported in Figure 126. In order to evaluate the mean laser absorption the measured reflectance spectrum was converted to Kubelka-Munk (K-M) absorption factor by adopting the following equation [398]

$$f(R) = \frac{(1-R)^2}{2R}$$

with R the measured laser reflectivity of the powders. The DRS analysis confirmed the low laser absorption by copper powder bed during LPBF. The red line in Figure 126 highlights the LPBF processing conditions adopted and indicates how the powder bed absorbed less than 1 % laser radiation and reflected most part of the incident radiation. In these conditions the risk of laser beam back-reflection is relatively high: such phenomenon happens when the laser beam is reflected from the powder bed to the mirrors system of the LPBF machine. The back-reflected beam can provoke serious damages to the laser system and even compromise the LPBF machine.

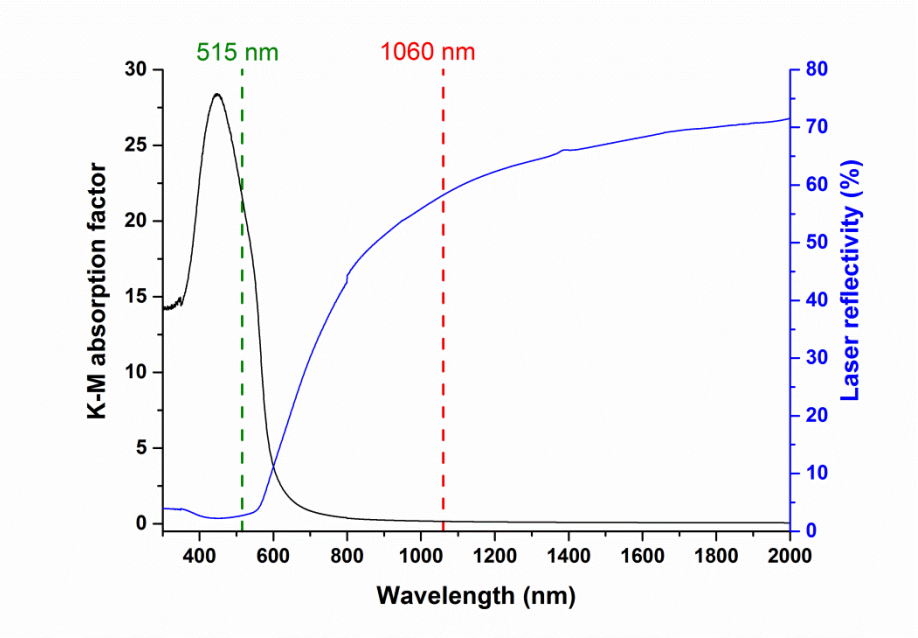


**Figure 126.** Diffuse reflectance spectroscopy of copper powder bed: The black and blue curves represent the variation of Kubella-Munk absorption factor and laser reflectivity, respectively, at different wavelength values.

Differently, adopting radiation wavelengths smaller than 1 μm, copper absorptance considerably increase, as in the case of 0.5 μm laser wavelength when copper powder absorptance rises up to 40% [113]. Similar conclusions were obtained by DRS analysis at low wavelength values (Figure 126). Indeed the K-M absorption factor drastically increased when the incident laser wavelength was lowered under 700 nm, reaching a peak at almost 500 nm.

Various studies on the laser welding of copper investigated the adoption of 515 nm laser systems (green line in Figure 126) generally named as "*green lasers*" [113,399,400]. The weld depth and stability on copper substrate was improved combing the use of green and infrared lasers. First the green laser pre-heated and pre-melted the substrate increasing the relative absorptance of the material. Then the infrared laser scanned the melt material increasing the weld penetration and stabilising it [399]. In the case of processing copper by LPBF, some studies are being carried out on the use of green lasers and on the realisation of commercial machines equipped with such systems [401].

### 5.2.3 X-ray diffraction analysis

XRD analysis of the HCP Cu powder and LPBF specimen (Appendix A.6) are presented in Figure 127. From the XRD pattern it can noted the presence of α *fcc* cubic phase of copper (according to [402]) and the oxide absence. During LPBF oxygen content is kept lower than 0.13 % in order to reduce material oxidation but the oxides can still form inside melt pool. Nevertheless the copper oxides (CuO and $Cu_2O$) are not thermodynamically stable at temperatures above 1400 °C so during laser scanning, when temperatures exceed such value [269], the thermal decomposition of copper oxides occured [153,245].

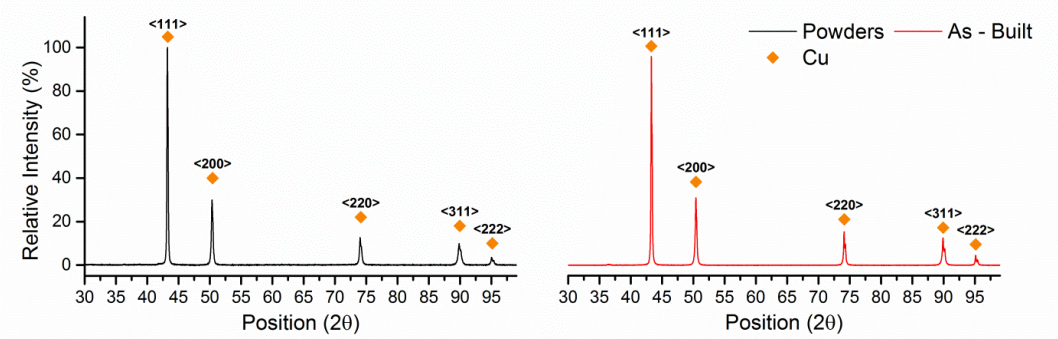


**Figure 127.** XRD analysis of the HCP Cu powder and of the as-built samples after the LPBF process.

### 5.2.4 Microstructural investigation

Figure 128 and Figure 129 show the micrographs of the fabricated samples acquired by optical microscopy while Figure 130 displays the investigation carried out by FESEM analysis (Appendix A.5). Microstructure appeared to be generally constituted by ultrafine grains of α copper cubic phase, pores and un-melted particles. The α grains were much finer than in the as-cast conditions, due to the different cooling conditions developed during the two processes. While during casting the material solidifies at low cooling rates, generating coarse and equiaxed grains [391], during LPBF process cooling rates are much more faster (up to $10^5$ K/s). During the LPBF process fast melting and ultra-rapid cooling of each layer induced the creation of ultrafine grained microstructure, very similar to the ones obtained by melt-spinning, another rapid solidification technique [403–405].

In Figure 128 the microstructures of the as-built LPBF specimens can be appreciated in the horizontal and vertical sections, respectively, at different magnifications. While the horizontal surface, parallel to building platform, was

mainly constituted by equiaxed grains and sporadic elongated grains (Figure 128c,e) the vertical section, parallel to building direction consisted of elongated grains, with repeated tilted growth direction (Figure 128d,f and Figure 129).

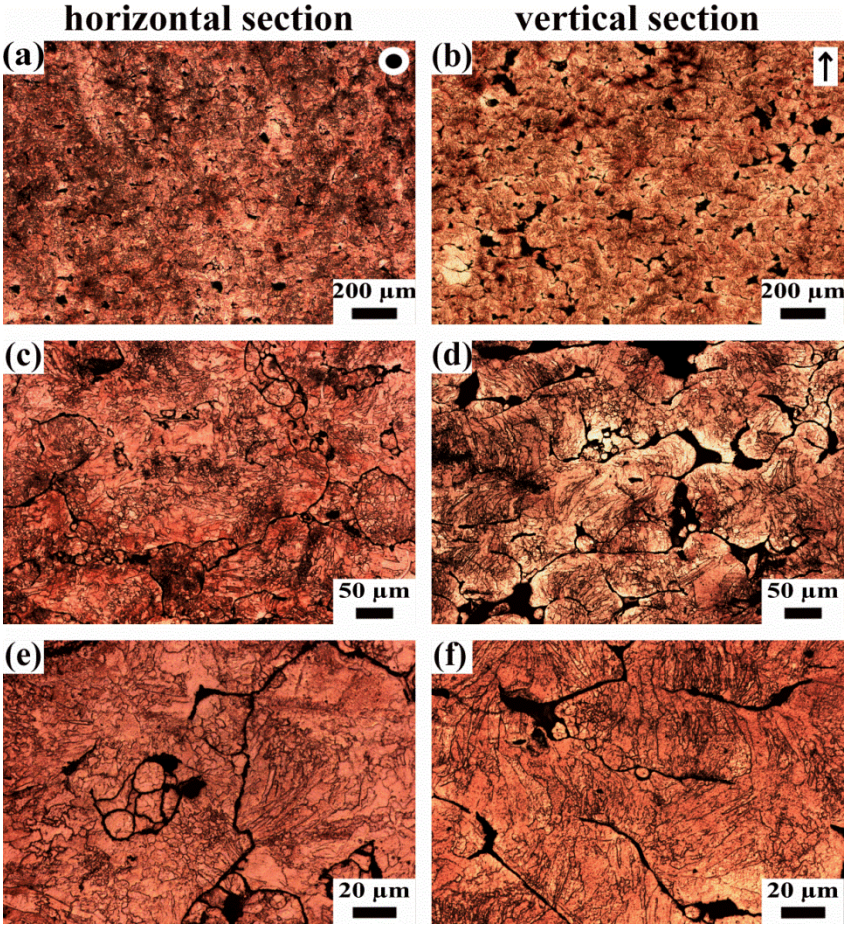


**Figure 128.** Optical micrographs of HCP Cu specimen made by LPBF after chemical etching: (a,c,e) horizontal section parallel to building platform and (b,d,f) vertical section parallel to building direction, at different magnification. The building direction is indicated by the circle in (a) and by the arrow in (b).

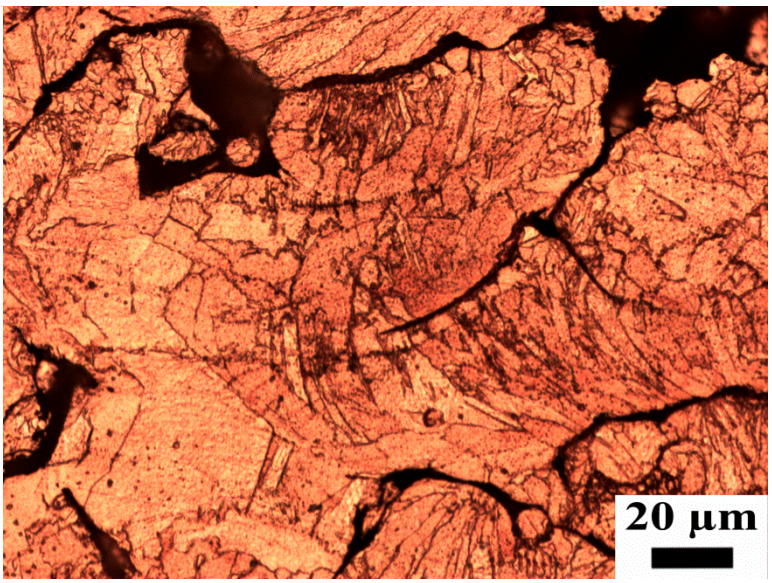


**Figure 129.** Optical micrograph of vertical cross section of copper specimen fabricated by LPBF after chemical etching.

As stated in previous chapters, the different grain growth depends on the thermal history and on the thermal fluxes developed inside the material. Indeed the main heat transfer inside the LPBF part occurs mainly along the vertical building direction rather than in the horizontal plane [116]. The average grain dimension was measured by image analysis. In the equiassic grained zones it varied between 1 µm and 4 µm, while in the elongated grained ones it considerably varied: the length of elongated grains varied from a minimum of 15 µm to a maximum of 75 µm while the average width was attested around 6 µm (Figure 130c,d). As shown in Figure 131 further EDS analysis (Appendix A.5) taken on as-built samples cross section confirmed the absence of Cu oxides as previously attested by XRD analysis (Figure 127).

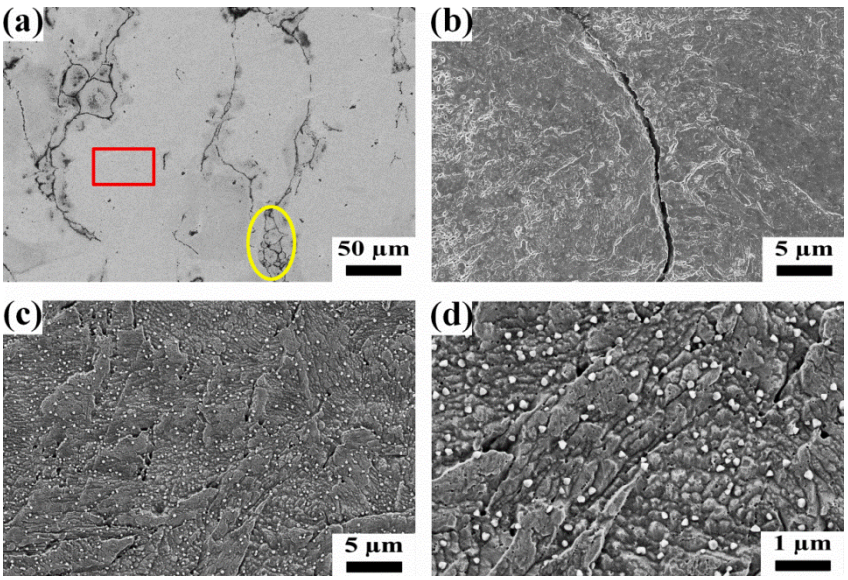


**Figure 130.** FESEM investigation of HCP Cu specimen after polishing and chemical etching: (a) overall microstructure, (b) microstructural anisotropy in correspondence of a crack, (c,d) elongated α Cu grains at different magnifications. The yellow ellipse in (a) highlights un-melted particles presence while the red rectangle is referred to EDS spectrum of Figure 131. The white spots present in the micrographs are $SiO_2$ nanoparticles derived by polishing treatment.

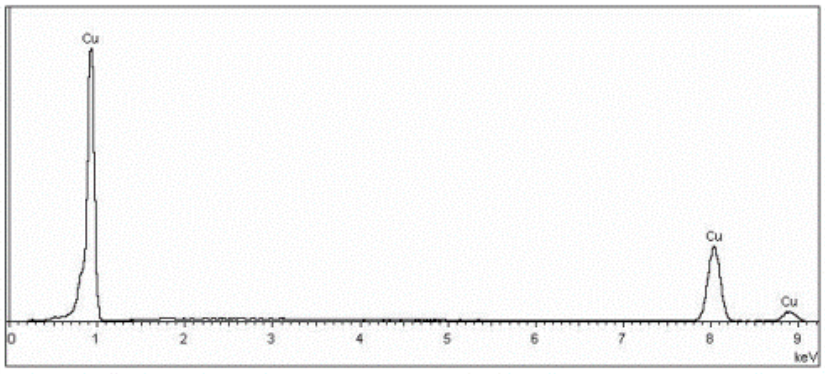


**Figure 131.** EDS spectrum of taken from a rectangular area (in red) of the micrograph in Figure 130. The total composition is measured as 100% Cu.

Also the tilted growth direction of the α grains in the vertical section (Figure 128f and Figure 129) was connected to the main heat flux direction: indeed the 67°C rotated strategy repeatedly altered the preferential heat flux direction between subsequent layers altering the growth direction of α grains [268]. Furthermore the elongated grains appeared delimited in correspondence of un-melted particles, cracks and pores (Figure 130a,b) which acted as heat flux interruptions. These

defects, created due to incomplete melting, material shrinkage and gas inclusions, blocked the heat exchange inside the consolidate material and consequently modified the microstructural growth (Figure 130b).

### 5.2.5 Conclusions

In this study HCP Cu powders were processed by LPBF process using a machine equipped with a 200 W infrared Yb fiber laser. Up to the author knowledge, few studies have been carried out on pure copper using such commercial LPBF machines. The main results obtained could be summarized as follows:

- With the above mentioned laser it was possible to obtain samples with 83% density; the low specimens densification was correlated to the low powder bed absorption of laser radiation, as confirmed by DRS analysis, and to the high thermal conductivity of the material.

- The XRD and EDS analysis confirmed the fabrication of pure copper samples with no detectable oxides traces in the fabricated parts.

- Optical microscopy and FESEM analyses showed that the fabricated samples are constituted by very fine α Cu phase with complex grains morphology depending on the additively nature of the process and on the presence of preferential heat fluxes in the material.

- Further studies should investigate the adoption of “green lasers” systems in LPBF process in order to improve the powder bed absorptance and consequently increase the part densification.

# Chapter 6

# Conclusions

## 6.1 Purpose of the work

Laser Powder Bed Fusion (LPBF) process is a relatively new and highly promising technique in the metallic components manufacturing. An increasing number of industries, from aerospace and medicine to automotive and jewellery, have been installing the latest LPBF machines and started to adopt such advance process to produce their final products with innovative designs and structures. In the past few years, together with the market expansion, the development of new alloys, post-processing treatments and standards has been remarkably encouraged and funded.

In recent decades numerous investigations showed how the parts processed by LPBF possess unprecedented microstructures, mechanical and physical properties disclosing new scientific and industrial researches even though the metallurgical knowledge of aluminium, titanium and other commercial alloys was already profoundly settled. The reasons are several and represent the key influencing characteristics of LPBF technology, such as the extremely high rates during melting and cooling in a very concentrated area, which mainly depend on the fiber laser spot size.

This thesis took under investigation the study and characterisation of three different metal systems of high interest in industry: A357 aluminium alloy, Ti-6Al-4V titanium alloy and pure copper. The researches carried out focused on the material properties of the parts fabricated using commercial LPBF machines and further studied the effect of post-processing treatments. The processed samples, as well the metal powders used, were characterised by microstructural investigations and by evaluation of the main mechanical properties, such as tensile strength, elongation at rupture and Young's Modulus. The main conclusions obtained in the different studies are described in the next sub-chapters.

## 6.2 Research projects

### 6.2.1 Laser Powder Bed Fusion of A357

The aim of this study was to define the process parameters to build components for industrial applications in A357 aluminium alloy by LPBF and to evaluate the effects of post-processing heat treatments on the microstructure and mechanical properties of machined parts. Several combinations of hatching distance and scanning speed values were adopted to define the process parameters combination to produce full dense components with highest productivity. Then, the obtained values were used to build samples for microstructural, hardness and tensile strength investigation. The samples were compared in different conditions: as-built, after a stress relieving treatment, and after a precipitation hardening treatment, known as T6. For this latest treatment, different conditions of solution and ageing were investigated to find the best conditions in terms of final hardness achievable. The obtained results showed that:

- Founding the correct combinations of hatching distance and scanning speed it was possible to produced 99 % full dense samples through LPBF, keeping a high productivity rate.

- Longer solution treatments enabled to obtain higher hardness values and to reduce the time required to reach peak hardening conditions. A maximum hardness value of 116 $HV_{0.1}$, comparable to as-built parts conditions, was obtained after 8 h solution treatment, water quenching and 3 h ageing treatment.

- The as-built parts fabricated by LPBF were characterised by a supersaturated α-Al phase surrounded by an ultrafine cellular network of eutectic phase structure, and micrometric melt pool structures. Post-processing stress relieving treatment favoured the diffusion of Si out of the supersaturated solid solution and promoted the disaggregation of sub-micrometric network maintaining the original melt pool structures. On the other hand, by the application of subsequent optimised T6 treatment, anisotropic features, such as laser tracks and melt pools disappeared leading to a more homogeneous microstructure composed by α-Al matrix, Si particles and $Mg_2Si$ precipitates.

- Regarding the tensile properties of machined samples, stress relieving treatment at 300 °C for 2 h increased the ductility of the as-built material to detriment of the tensile strength, due to the modification of the microstructure

and the reduced residual stresses. Applying a subsequent T6 treatment increased the material stiffness and yield strength, reaching values comparable to the as-built conditions. However T6 treatment did not increase the ductility of the material. From fracture surface investigation the presence of cracked Si particles was detected in the T6 treated specimens, while in the other conditions, a finely rough fracture surface was found.

### 6.2.2 Laser Powder Bed Fusion of Ti-6Al-4V

This study proposed the comparison of the mechanical and fatigue properties of components manufactured by commercial LPBF machine in Ti-6Al-4V titanium alloy with different post-processing heat treatments, building directions and oxygen contents. The adopted powders contained two different contents of oxygen in the chemical composition, a low and high oxygen amount, respectively, in order to simulate the processing of Ti-6Al-4V ELI and Ti-6Al-4V grade 5, respectively. The microstructural and mechanical analyses investigated the principal factors influencing the fatigue properties of the final parts. For such reason two different building orientation, vertical and horizontal, respectively, were chosen for the specimens fabrication and furthermore three different post-processing treatments were performed: stress relieving, stress relieving plus heat treatment and stress relieving plus Hot Isostatic Pressing (HIP). In order to avoid the influence of surface roughness on the mechanical behaviour of the material, all the specimens tested were machined before the tests. From the results the main conclusions were:

- Stress relieved samples possessed a fine α +β lamellar structure which was modified by further treatments at higher temperature into coarse lamellar structure. The heat treatment and HIP at 930 °C favoured the blurring of original β grains in the vertical sections of the material. The microstructure modification altered the tensile behaviour of the material, leading to lower strength and higher ductility. From fatigue results the anisotropy induced by specimens building orientation considerably decreased and disappeared leading to more homogeneous fatigue resistance.
- Pores and other defects were found as the principal responsible of the low ductility and fatigue resistance showed by the tested specimens. The application of high temperature heat treatment after stress relieving was found to be deleterious for the mechanical performances while on the contrary by applying a HIP treatment, the elongation at break and fatigue life were strongly increased. HIP process permitted to reduce the amount of porosities and defects

inside the material, thanks to the application of high temperature and pressure, which enabled the closure of these imperfections.

- Adopting different amount of oxygen inside the original powders slightly affected the microstructure of the material fabricated and investigated after post-processing heat treatment. The strongest effect of oxygen was observed for the tensile strength and hardness while for the fatigue resistance only a slight difference was measured in the stress relieving conditions. After further heat treatment or HIP the fatigue behaviour of the material appeared more homogeneous, with no appreciable differences between low and high oxygen contents.
- The most important factor affecting the mechanical response of the material was the porosity level present inside the parts. The variation of oxygen content and building orientation did not appeared much more influent on the fatigue behaviour of the parts. Only HIP treatment permitted to increase the fatigue life of the material over $10^7$ cycles for an applied stress higher than 450 MPa, thanks to the reduction of porosities.

### 6.2.3 Laser Powder Bed Fusion of pure copper

This study focused on the feasibility of producing chemical pure copper by LPBF process with a commercial machine equipped with 200 W Yb fibre laser. Furthermore the chemical composition and microstructure of the fabricated materials were investigated by XRD, optical and electron microscopy and EDS. The main results obtained are listed below:

- Using an infrared laser radiation permitted to produce cubic specimens with a maximum density of 83 %. The low level of densification was related to the low powder bed absorptivity, as proved by DRS analysis, and to the high thermal conductivity of copper.

- The XRD and EDS analyses did not detect oxides traces in the samples realised while microstructural investigations, carried out by optical and electron microscopy, revealed a very fine microstructure constituted of α Cu phase. The shape and size of the α grains appeared to vary between the vertical and horizontal cross section of the specimens showing equiassic and elongated grains, respectively. The anisotropic morphology of the α phase derived from the extreme rapid melting and cooling of the powder bed, which favoured the high fineness of the grains and altered the heat fluxes inside the material influencing the grain growth.

## 6.3 Future outlook

The improvement of materials properties of the LPBF processed parts represents a crucial interest in the industrial practise and the researches presented above can highlight some major topics for the future development of such technology.

First of all LPBF parts possess ultrafine and unprecedented microstructures which require a new set of optimised post-processing heat treatments. Secondly, inner porosity inside the parts represents the major influencing factor on the mechanical properties of the final parts, and should be consistently reduced by the optimisation of process parameters, the good quality of the raw materials and the improvement of post-processing treatments, such as Hot Isostatic Pressing. Finally, by the adoption of more powerful laser sources the processing of innovative and different metal alloys would be possible but at the same the investigation of different laser system, as in the case of green lasers, would facilitate the processing of high reflective materials, such as copper and precious alloys.

# Appendix
# Materials and characterisation techniques

This chapter illustrates the experimental methods used for the characterisation and study of the samples produced within this thesis.

## A.1 Powders microscopy

The morphology of the metal powders was observed by electron microscopy using a Zeiss SupraTM 40 Field Emission Scanning Electron Microscope (FESEM, SEM-FEG Assing SUPRA 25, Zeiss, Jena, Germany).

The cross-section of the powders was observed using a Leica DMI 5000 M optical microscope (Leica Microsystems, Wetzlar, Germany): the metallic powders were incorporated into epoxy cold mounting system (curing at room temperature) provided by Struers, then grinded and polished with silicon carbide abrasive papers up to 1 μm diamond paste and subsequently by sub-micrometric colloidal silica suspension up to 0.03 μm. In order to highline the fine microstructure of rapidly solidified powders, the samples were etched adopting proper metallographic etchant, as illustrated in Table 23.

**Table 23.** Chemical etchants used for metallographic investigations of LPBF specimens.

| Material | Etchant | Conditions |
|---|---|---|
| **A357** | Keller's reagent (95 ml $H_2O$, 2.5 ml $HNO_3$, 1.5 ml HCl, 1 ml HF) | Immersion for 12 s |
| **Ti-6Al-4V** | Kroll's reagent (92 ml $H_2O$, 6 ml $HNO_3$, 2 ml HF) | Immersion for 15 s |
| **Cu** | 100 ml $H_2O$, 50 ml HCl, 5 g $FeCl_3$ | Immersion for 13 s |

## A.2 Laser granulometry

The diameter distribution of metal powders were measured in as received conditions by laser granulometry method. To fulfil this aim, a Fritsch Analysette 22 Compact instrument, with a measuring range between 0.3 μm and 300 μm, was used. The data of mean size distribution and the frequency distribution of each powder were based on a volumetric assumption. Moreover, for each composition the $D_{10}$, $D_{50}$ and $D_{90}$ diameter points were found and reported. These specific data correspond to the diameters values of the 10, 50 and 90 % of the cumulative size distribution respectively.

## A.3 Density evaluation by Archimedes method

Porosity level inside the material was investigated adopting Archimedes method for each metal alloy studied within this thesis, testing 10 mm x 10 mm x 10 parallelepipeds fabricated by LPBF.

In order to measure the relative density by Archimedes method, according to ASTM B962-14, the mass of the samples was measured in the air and in the deionized water, adopting an ORMA BCA200S balance (accuracy ± 0,1 mg). Before testing all the specimen were grinded adopting SiC grinding papers, in order to remove the external skin and any contaminant present on the surface.

The calculation of the density $\rho_p$ of the part under investigation can be calculated by the following equation

$$\rho_p = \frac{m_a}{m_a - m_{fl}} \cdot \rho_{fl} \qquad \left[\frac{g}{cm^3}\right]$$

where $\rho_{fl}$ is the deionized water density at room temperature, $m_a$ is the mass of the specimen measured in air and $m_{fl}$ is the mass measured when the sample is immersed in the fluid [406]. Each specimen was measured independently five times. The relative density was calculated from the ratio between $\rho_p$ and $\rho_{th}$ representing the theoretical density of the material: the values of theoretical density adopted for A357, Ti-6Al-4V and pure copper were 2.68 g/cm$^3$, 4.42 g/cm$^3$ and 8.94 g/cm$^3$, respectively [281].

## A.4 Microhardness evaluation

To investigate the hardness, 10 mm x 10 mm x 10 mm specimens were fabricated and tested using a Leica VMHT micro-indenter: ten measurements were performed on each sample with a load of 100 g for 15 s. The following equation was used to calculate the micro hardness of the specimens

$$HV_{0.1} = \frac{1854.4\,P}{d^2}$$

where P is the load applied and d is the mean value of the diagonal of the indentation in μm.

A357 specimens were tested in the as-built conditions and after different heat treatments (stress relieving and optimized T6). Instead in the case of Ti-6Al-4V, all the specimens were tested after post-processing treatment, stress relieving, 930 °C heat treatment and HIP respectively.

## A.5 Optical and electronic microscopy

Top and lateral surfaces of the specimens were grinded using SiC abrasive papers of different grits (from 320 to 4000 grit) and later polished adopting diamond paste up to 1 μm. Finally, the surfaces were polished by sub-micrometric colloidal silica suspension up to 0.03 μm. In order to highline the fine microstructure of LPBF specimens the samples were etched adopting proper metallographic etchant (Table 23), and subsequently observed at Leica DMI 5000 M optical microscope (Leica Microsystems, Wetzlar, Germany).The same samples preparation was adopted for the electronic microscopy, by using a Zeiss SupraTM 40 Field Emission Scanning Electron Microscope (FESEM, SEM-FEG Assing SUPRA 25, Zeiss, Jena, Germany), equipped with energy-dispersive X-ray spectroscopy (EDS) probe, was used for the investigation.

## A.6 X-ray diffraction analysis

X-ray diffraction (XRD) analysis was adopted to investigate the phases constitution in the specimens fabricated. The samples tested were previously grinded using different SiC grinder papers up to 1200 grit. A Philips PW3040 diffractometer was used for the X-rays measurement, adopting CuKα radiation ($\lambda$=0.1504 nm) and 2θ range varying between 30 and 90°.

## A.7 Diffuse reflectance spectroscopy

Diffuse Reflectance Spectroscopy (DRS) analysis was adopted to study and measure the powder bed absorption and reflectivity of laser radiation in the case of chemical pure copper powders. A Varian Cary 5000 UV-Vis-NIR spectrophotometer was used to perform the test varying the incident laser radiation wavelength between 300 and 2000 nm. The instrument is equipped with a 150 mm diameter integrating sphere coated with Spectralon with 1 nm spectral resolution. A Spectralon reference was used to measure the 100 % reflectance and internal attenuators were used to determine zero reflectance in order to remove background and noise. The powders were placed in a quartz cuvette, sealed, and mounted on a Teflon sample holder for the DRS measurement [398]. The measured reflectance spectra were subsequently converted to Kubelka-Munk (K-M) absorption factors to evaluate the absorption spectra of the powders.

# References

[1] ASTM International, ASTM F2792-12a: Standard terminology for additive manufacturing technologies, (2012). doi:10.1520/F2792-12A.2.

[2] T. Economist, A third industrial revolution, (n.d.). http://www.economist.com/node/21552901 (accessed May 11, 2017).

[3] I. Gibson, D.W. Rosen, B. Stucker, Additive Manufacturing Technologies - Rapid Prototyping to Direct Digital Manufacturing, 2010.

[4] I. Gibson, Advanced Manufacturing Technology for medical applications, john Wiley & Sons, Ltd, 2005. doi:10.1017/CBO9781107415324.004.

[5] I. Popov, S.O. Onuh, Reverse engineering of pelvic bone for hip joint replacement., J. Med. Eng. Technol. 33 (2009) 454–459. doi:10.1080/03091900902952634.

[6] 3D Systems, 3D Systems : Our Story, (2013) 1–7. https://www.3dsystems.com/our-story (accessed May 8, 2017).

[7] Wohlers Associates, Wohlers Report 2015 - Additive Manufacturing and 3D Printing State on the industry, 2015.

[8] EOS e-Manufacturing Solutions, EOS Hystory, (2017). https://www.eos.info/about_eos/history (accessed May 8, 2017).

[9] A. Bandyopadhyay, T. Gualtieri, S. Bose, Global Engineering and Additive Manufacturing, in: Addit. Manuf., 2015: pp. 1–18. doi:doi:10.1201/b18893-2.

[10] R.P. Mudge, N.R. Wald, Laser engineered net shaping advances additive manufacturing and repair, Weld. Journal-New York-. 86 (2007) 44–48.

[11] Laboratories Sandia National, Creating a complex metal part in a day is goal of commercial consortium, (2017). http://www.sandia.gov/media/lens.htm (accessed May 8, 2017).

[12] Arcam AB, Arcam History, (2016). http://www.arcam.com/company/about-arcam/history/ (accessed May 8, 2017).

[13] ExOne, History of ExOne, (2017). http://www.exone.com/About-ExOne/History.

[14] W.J. Sames, F.A. List, S. Pannala, R.R. Dehoff, S.S. Babu, The metallurgy and processing science of metal additive manufacturing, Int. Mater. Rev. 6608 (2016) 1–46. doi:10.1080/09506608.2015.1116649.

[15] Fabrisonic, Fabrisonic LLC, (2017). http://fabrisonic.com/company/ (accessed May 8, 2017).

[16] W.W. Wits, S.J. Weitkamp, J. Van Es, Metal additive manufacturing of a high-pressure micro-pump, Procedia CIRP. 7 (2013) 252–257. doi:10.1016/j.procir.2013.05.043.

[17] Airbus Is Ready for Industrialization of 3D Printing in 2016, Peter Sander Reveals, 3Dprinting Ind. (2016). http://www.3ders.org/articles/20151202-airbus-a320-3d-printed-bionic-partition-made-from-high-strength-scalmalloy-metal-alloy.html (accessed May 16, 2017).

[18] Airbus Press, Printing the future: Airbus expands its applications of the revolutionary additive layer manufacturing process, Airbus Press Cent. (2014). doi:10.1017/CBO9781107415324.004.

[19] C. Dordlofva, A. Lindwall, P. Törlind, Opportunities and Challenges for Additive Manufacturing in Space Applications, in: Proc. Nord. 2016 Biannu. Conf. Des. Dev., NTNU – Norwegian University of Science and TechnologyTrondheim, Norway, 2016: pp. 404–410.

[20] L.J. Kumar, C.G.K. Nair, Current Trends of Additive Manufacturing in the Aerospace Industry, in: Adv. 3D Print. Addit. Manuf. Technol., 2017: pp. 39–53. doi:10.1007/978-981-10-0812-2.

[21] R. Huang, M. Riddle, D. Graziano, J. Warren, S. Das, S. Nimbalkar, J. Cresko, E. Masanet, Energy and emissions saving potential of additive manufacturing: the case of lightweight aircraft components, J. Clean. Prod. 135 (2015) 1–12. doi:10.1016/j.jclepro.2015.04.109.

[22] Www.3ders.org, AIRBUS A320 saves weight with 3D printed bionic partition, made from high strength scalmalloy metal alloy, (2015) 1–8. http://www.3ders.org/articles/20151202-airbus-a320-3d-printed-bionic-partition-made-from-high-strength-scalmalloy-metal-alloy.html.

[23] M. Seifi, A. Salem, J. Beuth, O.L.A. Harrysson, J.J. Lewandowski, Overview of Materials Qualification Needs for Metal Additive Manufacturing, JOM. 68 (2016). doi:10.1007/s11837-015-1810-0.

[24] G. Reports, The FAA Cleared the First 3D Printed Part to Fly in a Commercial Jet Engine from GE - GE Reports, (2015) 1–6. http://www.gereports.com/post/116402870270/the-faa-cleared-the-first-3d-printed-part-to-fly/.

[25] A.J. Pinkerton, Lasers in additive manufacturing, Opt. Laser Technol. 78 (2016) 25–32. doi:10.1016/j.optlastec.2015.09.025.

[26] R. Leal, F.M. Barreiros, L. Alves, F. Romeiro, J.C. Vasco, M. Santos, C. Marto, Additive manufacturing tooling for the automotive industry, Int. J. Adv. Manuf. Technol. (2017) 1–7. doi:10.1007/s00170-017-0239-8.

[27] EOS e-Manufacturing Solutions, Audi and EOS : Development partnership focuses on holistic approach for metal-based additive manufacturing, (2017) 3–5. https://www.eos.info/press/development-partnershi-between-audi-and-eos (accessed January 1, 2017).

[28] L.-C. Zhang, H. Attar, Selective Laser Melting of Titanium Alloys and Titanium Matrix Composites for Biomedical Applications: A Review, Adv. Eng. Mater. 18 (2015) 463–475. doi:10.1002/adem.201500419.

[29] J. Sun, Y. Yang, D. Wang, Parametric optimization of selective laser melting for forming Ti6Al4V samples by Taguchi method, Opt. Laser Technol. 49 (2013) 118–124. doi:10.1016/j.optlastec.2012.12.002.

[30] X. Wang, S. Xu, S. Zhou, W. Xu, M. Leary, P. Choong, M. Qian, M. Brandt, Y.M. Xie, Topological design and additive manufacturing of porous metals for bone scaffolds and orthopaedic implants: A review, Biomaterials. 83 (2016) 127–141. doi:10.1016/j.biomaterials.2016.01.012.

[31] A. Fukuda, M. Takemoto, T. Saito, S. Fujibayashi, M. Neo, D.K. Pattanayak, T. Matsushita, K. Sasaki, N. Nishida, T. Kokubo, T. Nakamura, Osteoinduction of porous Ti implants with a channel structure fabricated by selective laser melting, Acta Biomater. 7 (2011) 2327–2336. doi:10.1016/j.actbio.2011.01.037.

[32] G. Pyka, A. Burakowski, G. Kerckhofs, M. Moesen, S. Van Bael, J. Schrooten, M. Wevers, Surface modification of Ti6Al4V open porous structures produced by additive manufacturing, Adv. Eng. Mater. 14 (2012) 363–370. doi:10.1002/adem.201100344.

[33] Y. Yan, G.L. Nash, P. Nash, Effect of density and pore morphology on fatigue properties of sintered Ti-6Al-4V, Int. J. Fatigue. 55 (2013) 81–91. doi:10.1016/j.ijfatigue.2013.05.015.

[34] V. Weißmann, R. Bader, H. Hansmann, N. Laufer, Influence of the structural orientation on the mechanical properties of selective laser melted Ti6Al4V open-porous scaffolds, Mater. Des. 95 (2016) 188–197. doi:10.1016/j.matdes.2016.01.095.

[35] C. Emmelmann, P. Scheinemann, M. Munsch, V. Seyda, Laser additive manufacturing of modified implant surfaces with osseointegrative characteristics, Phys. Procedia. 12 (2011) 375–384. doi:10.1016/j.phpro.2011.03.048.

[36] D.K. Pattanayak, T. Matsushita, H. Takadama, a. Fukuda, M. Takemoto, S. Fujibayashi, K. Sasaki, N. Nishida, T. Nakamura, T. Kokubo, Fabrication of Bioactive Porous Ti Metal with Structure Similar to Human Cancellous Bone by Selective Laser Melting, Bioceram. Dev. Appl. 1 (2010) 1–3. doi:10.4303/bda/D101206.

[37] T. Traini, C. Mangano, R.L. Sammons, F. Mangano, A. Macchi, A. Piattelli, Direct laser metal sintering as a new approach to fabrication of an isoelastic functionally graded material for manufacture, 4 (2008) 1525–1533. doi:10.1016/j.dental.2008.03.029.

[38] C. Mangano, M. Raspanti, T. Traini, A. Piattelli, R. Sammons, Stereo imaging and cytocompatibility of a model dental implant surface formed by direct laser fabrication, (2008). doi:10.1002/jbm.a.32033.

[39] J. Wieding, A. Fritsche, P. Heinl, C. Körner, M. Cornelsen, H. Seitz, W. Mittelmeier, R. Bader, Biomechanical behavior of bone scaffolds made of additive manufactured tricalciumphosphate and titanium under different loading conditions., J. Appl. Biomater. Funct. Mater. 11 (2013) 159–166. doi:10.5301/JABFM.2013.10832.

[40] R. Hasan, R. Mines, P. Fox, Characterization of selectively laser melted Ti-6Al-4V microlattice struts, Procedia Eng. 10 (2011) 536–541. doi:10.1016/j.proeng.2011.04.090.

[41] J. Wieding, A. Jonitz, R. Bader, The effect of structural design on mechanical properties and cellular response of additive manufactured titanium scaffolds, Materials (Basel). 5 (2012) 1336–1347. doi:10.3390/ma5081336.

[42] K.C. Nune, R.D.K. Misra, S.M. Gaytan, L.E. Murr, Interplay between cellular activity and three-dimensional scaffold-cell constructs with different foam structure processed by electron beam melting, J. Biomed. Mater. Res. - Part A. 103 (2015) 1677–1692. doi:10.1002/jbm.a.35307.

[43] S. Ponader, C. Von Wilmowsky, M. Widenmayer, R. Lutz, P. Heinl, C.

Körner, R.F. Singer, E. Nkenke, F.W. Neukam, K.A. Schlegel, In vivo performance of selective electron beam-melted Ti-6Al-4V structures, J. Biomed. Mater. Res. - Part A. 92 (2010) 56–62. doi:10.1002/jbm.a.32337.

[44] C.M. Haslauer, J.C. Springer, O.L.A. Harrysson, E.G. Loboa, N.A. Monteiro-Riviere, D.J. Marcellin-Little, In vitro biocompatibility of titanium alloy discs made using direct metal fabrication, Med. Eng. Phys. 32 (2010) 645–652. doi:10.1016/j.medengphy.2010.04.003.

[45] F. Trevisan, F. Calignano, A. Aversa, G. Marchese, M. Lombardi, S. Biamino, D. Ugues, D. Manfredi, Additive manufacturing of titanium alloys in the biomedical field: processes, properties and applications, J. Appl. Biomater. Funct. Mater. (2017) 1–24. doi:10.5301/jabfm.5000371.

[46] J. Parthasarathy, Additive Manufacturing of Medical Devices, in: CRC Press T&FG (Ed.), Addit. Manuf. Innov. Adv. Appl., 2016: pp. 369–388.

[47] J. Parthasarathy, Medical Applications of Additive Manufacturing, in: Addit. Manuf. Innov. Adv. Appl., 2016: pp. 389–402.

[48] A.L. Jardini, M.A. Larosa, C.A.D.C. Zavaglia, L.F. Bernardes, C.S. Lambert, P. Kharmandayan, D. Calderoni, R. Maciel Filho, Customised titanium implant fabricated in additive manufacturing for craniomaxillofacial surgery, Virtual Phys. Prototyp. 9 (2014) 1–11. doi:10.1080/17452759.2014.900857.

[49] A.L. Jardini, M.A. Larosa, R.M. Filho, C.A.D.C. Zavaglia, L.F. Bernardes, C.S. Lambert, D.R. Calderoni, P. Kharmandayan, Cranial reconstruction: 3D biomodel and custom-built implant created using additive manufacturing, J. Cranio-Maxillofacial Surg. 42 (2014) 1877–1884. doi:10.1016/j.jcms.2014.07.006.

[50] L.S. Bertol, W.K. Jùnior, F.P. da Silva, C. Aumund-Kopp, Medical design: Direct metal laser sintering of Ti-6Al-4V, Mater. Des. 31 (2010) 3982–3988. doi:10.1016/j.matdes.2010.02.050.

[51] Medical Alphaform-Production of hip implant by using additive manufacturing, (n.d.). http://www.eos.info/press/case_study/additive_manufactured_hip_implant (accessed January 1, 2017).

[52] Industrial applications of Renishaw metal additive manufacturing technology, (n.d.). http://www.renishaw.com/en/industrial-applications-of-renishaw-metal-additive-manufacturing-technology--15256 (accessed September 15, 2016).

[53] Micro Cooler Formula 1 Roll Hoop Acetabular Cups Revised Trinity â€™ s Sole Heat Exchanger, (n.d.). http://www.withinlab.com/case-studies/new_index4.php (accessed January 1, 2017).

[54] Additive manufacturing in medical technology, (2017) 2–5. https://www.concept-laser.de/en/industry/medical.html (accessed January 1, 2017).

[55] M. Cronskär, M. Bäckström, L.-E. Rännar, Production of customized hip stem prostheses – a comparison between conventional machining and electron beam melting (EBM), Rapid Prototyp. J. 19 (2013) 365–372. doi:10.1108/RPJ-07-2011-0067.

[56] V.K. Balla, S. Banerjee, S. Bose, A. Bandyopadhyay, Direct Laser Processing of Tantalum Coating on Titanium for Bone Replacement Structures, Acta Biomater. 6 (2010) 2329–2334. doi:10.1016/j.actbio.2009.11.021.Direct.

[57] V.K. Balla, P.D. DeVasConCellos, W. Xue, S. Bose, A. Bandyopadhyay, Fabrication of compositionally and structurally graded Ti-TiO2 structures using laser engineered net shaping (LENS), Acta Biomater. 5 (2009) 1831–1837. doi:10.1016/j.actbio.2009.01.011.

[58] M. Roy, B. Vamsi Krishna, A. Bandyopadhyay, S. Bose, Laser processing of bioactive tricalcium phosphate coating on titanium for load-bearing implants, Acta Biomater. 4 (2008) 324–333. doi:10.1016/j.actbio.2007.09.008.

[59] S.L. Sing, J. An, W.Y. Yeong, F.E. Wiria, Laser and electron-beam powder-bed additive manufacturing of metallic implants: A review on processes, materials and designs, J. Orthop. Res. 34 (2016) 369–385. doi:10.1002/jor.23075.

[60] V. Petrovic, J. Vicente, H. Gonzalez, O.J. Ferrando, D. Gordillo, J. Ramón, B. Puchades, L.P. Griñan, V. Petrovic, J. Vicente, H. Gonzalez, O.J. Ferrando, Additive layered manufacturing : sectors of industrial application shown through case studies, Int. J. Prod. Res. 49 (2011) 1061–1079. doi:10.1080/00207540903479786.

[61] J. Gardan, Additive manufacturing technologies: state of the art and trends, Int. J. Prod. Res. 54 (2016) 3118–3132. doi:10.1080/00207543.2015.1115909.

[62] V. Petrovic, V.J. Haro, O. Jordà, J. Delgado, J.R. Blasco, L. Portolès, Additive Layer Manufacturing: State of the art in industrial applications

through case studies., Int. J. Prod. Res. 49 (2010) 1061–1079. doi:10.1080/09593330.2015.1134677.

[63] R.R. Technology, Wohlers 2017 Report on 3D Printing Industry Points to Softened Growth, (2017). http://www.rapidreadytech.com/2017/04/wohlers-2017-report-on-3d-printing-industry-points-to-softened-growth/ (accessed January 1, 2017).

[64] M.D. Monzón, Z. Ortega, A. Martínez, F. Ortega, Standardization in additive manufacturing : activities carried out by international organizations and projects, Int. J. Adv. Manuf. Technol. 76 (2015) 1111–1121. doi:10.1007/s00170-014-6334-1.

[65] ASTM International, ISO/ASTM 52921:2013 (E) . Standard Terminology for Additive Manufacturing — Coordinate Systems and Test, (2011) 1–13. doi:10.1520/F2921.

[66] I.S. Organisation, A. International, ISO/ASTM 52900 : 2015 Standard terminology for Additive Manufacturing - General Principles - Terminology, (2015). doi:10.1520/F2792-12A.2.

[67] ASTM International, ASTM F3122-14 : Standard Guide for Evaluating Mechanical Properties of Metal Materials Made via Additive Manufacturing Processes, (2015) 1–6. doi:10.1520/F3122-14.2.

[68] I.S. Organisation, A. International, ISO/ASTM 52915:2016 : Standard Specification for Additive Manufacturing File Format (AMF) Version 1.2, (2016).

[69] I.S. Organisation, A. International, ISO/ASTM 52901:2016 _Standard Guide for Additive Manufacturing – General Principles – Requirements for Purchased AM Parts, (2017).

[70] I.S. Organisation, A. International, ISO/ASTM 52910:2017 - Standard guidelines for design for additive manufacturing, (2017). doi:10.1520/ISO.

[71] ASTM International, ASTM F3049-14 : Standard Guide for Characterizing Properties of Metal Powders Used for Additive Manufacturing Processes, (2015) 13–15. doi:10.1520/F3049-14.

[72] ASTM International, ASTM F2924 - 14 : Standard Specification for Additive Manufacturing Titanium-6 Aluminum-4 Vanadium with Powder Bed Fusion, (2015). doi:10.1520/F2924-14.2.

[73] ASTM International, ASTM F3001-14 : Standard Specification for Additive

Manufacturing Titanium-6 Aluminum-4 Vanadium ELI (Extra Low Interstitial) with Powder Bed Fusion, (2012) 1–8. doi:10.1520/F2924-12A.2.

[74] ASTM International, ASTM F2971-13 : Standard practice for test specimens prepared by Addtive Manufacturing, (2014) 3–6. doi:10.1520/F2971-13.

[75] ASTM International, ASTM F3056 - 14 : Standard Specification for Additive Manufacturing Nickel Alloy ( UNS N06625 ) with Powder Bed Fusion, (2014). doi:10.1520/F3056-14.Copyright.

[76] A. International, ASTM F3055-14a : Standard Specification for Additive Manufacturing Nickel Alloy (UNS N07718 ) with Powder Bed Fusion, (2014) 1–8. doi:10.1520/F3055-14A.Copyright.

[77] ASTM International, ASTM F3184-16 : Standard Specification for Additive Manufacturing Stainless Steel Alloy ( UNS S31603 ) with Powder Bed Fusion, (2016) 1–9. doi:10.1520/F3184.

[78] ASTM International, ASTM F3187 - 16 : Standard Guide for Directed Energy Deposition of Metals, (2015). doi:10.1520/F3187.

[79] T. Himmer, T. Nakagawa, M. Anzai, Lamination of metal sheets, Comput. Ind. 39 (1999) 27–33. doi:10.1016/S0166-3615(98)00122-5.

[80] S. Yi, F. Liu, J. Zhang, S. Xiong, Study of the key technologies of LOM for functional metal parts, J. Mater. Process. Technol. 150 (2004) 175–181. doi:10.1016/j.jmatprotec.2004.01.035.

[81] T. Himmer, A. Techel, S. Nowotny, E. Beyer, Recent developments in metal laminated tooling by multiple laser processing, Rapid Prototyp. J. 9 (2003) 24–29. doi:Doi 10.1108/13552540310455629.

[82] B. Xu, X. Wu, J. Lei, F. Luo, F. Gong, C. Du, X. Sun, S. Ruan, Research on micro-electric resistance slip welding of copper electrode during the fabrication of 3D metal micro-mold, J. Mater. Process. Technol. 213 (2013) 2174–2183. doi:http://dx.doi.org/10.1016/j.jmatprotec.2013.06.009.

[83] H.T. Fujii, M.R. Sriraman, S.S. Babu, Quantitative evaluation of bulk and interface microstructures in Al-3003 alloy builds made by very high power ultrasonic additive manufacturing, Metall. Mater. Trans. A Phys. Metall. Mater. Sci. 42 (2011) 4045–4055. doi:10.1007/s11661-011-0805-x.

[84] G.D. Janaki Ram, Y. Yang, B.E. Stucker, Effect of process parameters on bond formation during ultrasonic consolidation of aluminum alloy 3003, J. Manuf. Syst. 25 (2006) 221–238. doi:10.1016/S0278-6125(07)80011-2.

[85] C.Y. Kong, R.C. Soar, P.M. Dickens, Optimum process parameters for ultrasonic consolidation of 3003 aluminium, J. Mater. Process. Technol. 146 (2004) 181–187. doi:10.1016/j.jmatprotec.2003.10.016.

[86] D. White, Ultrasonic object consolidation, Pat. No. US 6,519,500 B1. (2003).

[87] R.J. Friel, R.A. Harris, Ultrasonic additive manufacturing - A hybrid production process for novel functional products, Procedia CIRP. 6 (2013) 35–40. doi:10.1016/j.procir.2013.03.004.

[88] G.D.J. Ram, C. Robinson, Y. Yang, B.E. Stucker, Use of ultrasonic consolidation for fabrication of multi-material structures, Rapid Prototyp. J. 13 (2007) 226–235. doi:10.1108/13552540710776179.

[89] M.R. Sriraman, S.S. Babu, M. Short, Bonding characteristics during very high power ultrasonic additive manufacturing of copper, Scr. Mater. 62 (2010) 560–563. doi:10.1016/j.scriptamat.2009.12.040.

[90] S. Masurtschak, R.J. Friel, A. Gillner, J. Ryll, R.A. Harris, Fiber laser induced surface modification/manipulation of an ultrasonically consolidated metal matrix, J. Mater. Process. Technol. 213 (2013) 1792–1800. doi:10.1016/j.jmatprotec.2013.04.008.

[91] R. Hahnlen, M.J. Dapino, NiTi-Al interface strength in ultrasonic additive manufacturing composites, Compos. Part B Eng. 59 (2014) 101–108. doi:10.1016/j.compositesb.2013.10.024.

[92] S. Atre, J. Porter, T. Batchelor, K. Kate, M. Bulger, P. Gangopadhya, Process Parameter Optimization for Binder Jetting using 420 Stainless Steel, in: WorldPM 2016, Hamburg, Germany (GE), 2016.

[93] D.A. Snelling, C.B. Williams, C.T.A. Suchicital, A.P. Druschitz, Binder jetting advanced ceramics for metal-ceramic composite structures, Int. J. Adv. Manuf. Technol. (2017). doi:10.1007/s00170-017-0139-y.

[94] ExOne, 3D Printing Binders, (2017). http://www.exone.com/Resources/Binders (accessed May 22, 2017).

[95] M. Doyle, K. Agarwal, W. Sealy, K. Schull, Effect of Layer Thickness and Orientation on Mechanical Behavior of Binder Jet Stainless Steel 420 + Bronze Parts, Procedia Manuf. 1 (2015) 251–262. doi:10.1016/j.promfg.2015.09.016.

[96] H. Chen, Y.F. Zhao, Process parameters optimization for improving surface quality and manufacturing accuracy of binder jetting additive manufacturing

process, Rapid Prototyp. J. 22 (2016) 527–538. doi:10.1108/RPJ-11-2014-0149.

[97] S. Shrestha, G. Manogharan, Optimization of Binder Jetting Using Taguchi Method, Jom. 69 (2017) 491–497. doi:10.1007/s11837-016-2231-4.

[98] Y. Tang, Y. Zhou, T. Hoff, M. Garon, Y.F. Zhao, Elastic modulus of 316 stainless steel lattice structure fabricated via binder jetting process, Mater. Sci. Technol. 32 (2016) 648–656. doi:10.1179/1743284715Y.0000000084.

[99] M. Vaezi, C.K. Chua, Effects of layer thickness and binder saturation level parameters on 3D printing process, Int. J. Adv. Manuf. Technol. 53 (2011) 275–284. doi:10.1007/s00170-010-2821-1.

[100] H. Miyanaji, S. Zhang, A. Lassell, A.A. Zandinejad, L. Yang, Optimal Process Parameters for 3D Printing of Porcelain Structures, Procedia Manuf. 5 (2016) 870–887. doi:10.1016/j.promfg.2016.08.074.

[101] ExOne, Industry Grade Materials, (2017) 1–5. http://www.exone.com/Resources/Materials (accessed May 23, 2017).

[102] V.K. Balla, Deposition-Based and Solid-State Additive Manufacturing Technologies for Metals, in: Addit. Manuf., 2015: pp. 65–96. doi:doi:10.1201/b18893-4.

[103] L.D. Bobbio, R.A. Otis, J. Paul, R.P. Dillon, A.A. Shapiro, Z. Liu, A.M. Beese, Additive manufacturing of a functionally graded material from Ti-6Al-4V to Invar : Experimental characterization and thermodynamic calculations, Acta Mater. 127 (2017) 133–142.

[104] K. Shah, I. ul Haq, A. Khan, S.A. Shah, M. Khan, A.J. Pinkerton, Parametric study of development of Inconel-steel functionally graded materials by laser direct metal deposition, Mater. Des. 54 (2014) 531–538. doi:10.1016/j.matdes.2013.08.079.

[105] P. Muller, P. Mognol, J. Hascoet, Modeling and control of a direct laser powder deposition process for Functionally Graded Materials (FGM) parts manufacturing, J. Mater. Process. Technol. 213 (2013) 685–692.

[106] N. Guo, M.C. Leu, Additive manufacturing : technology, applications and research needs, Front. Mech. Eng. 8 (2013) 215–243. doi:10.1007/s11465-013-0248-8.

[107] Application of LENS 3D Metal Printing at Washington State University, (n.d.). http://www.optomec.com/category/webinars. 15 (accessed September

15, 2016).

[108] X. Wu, A review of laser fabrication of metallic engineering components and of materials, Mater. Sci. Technol. 23 (2007) 631–640. doi:10.1179/174328407X179593.

[109] D.D. Gu, W. Meiners, K. Wissenbach, R. Poprawe, Laser additive manufacturing of metallic components: materials, processes and mechanisms, Int. Mater. Rev. 57 (2012) 133–164. doi:10.1179/1743280411Y.0000000014.

[110] A. Segerstark, J. Andersson, L.-E. Svensson, Evaluation of a temperature measurement method developed for laser metal deposition, Sci. Technol. Weld. Join. 22 (2017) 1–6. doi:10.1080/13621718.2016.1169363.

[111] N.A. Kistler, A.R. Nassar, E.W. Reutzel, D.J. Corbin, A.M. Beese, Effect of directed energy deposition processing parameters on laser deposited Inconel® 718: Microstructure, fusion zone morphology, and hardness, J. Laser Appl. 29 (2017) 22005. doi:10.2351/1.4979702.

[112] P. Guo, B. Zou, C. Huang, H. Gao, Study on microstructure , mechanical properties and machinability of efficiently additive manufactured AISI 316L stainless steel by high-power direct laser deposition, J. Mater. Process. Technol. 240 (2017) 12–22. doi:10.1016/j.jmatprotec.2016.09.005.

[113] S. Engler, R. Ramsayer, R. Poprawe, Process studies on laser welding of copper with brilliant green and infrared lasers, Phys. Procedia. 12 (2011) 342–349. doi:10.1016/j.phpro.2011.03.142.

[114] N.K. Tolochko, Y. V. Khlopkov, S.E. Mozzharov, M.B. Ignatiev, T. Laoui, V.I. Titov, Absorptance of powder materials suitable for laser sintering, Rapid Prototyp. J. 6 (2000) 155–161. doi:10.1108/13552540010337029.

[115] P.A. Lykov, E. V. Safonov, A.M. Akhmedianov, Selective Laser Melting of Copper, Mater. Sci. Forum. 843 (2016) 284–288. doi:10.4028/www.scientific.net/MSF.843.284.

[116] A. Popovich, V. Su, I. Polozov, E. Borisov, D. Masaylo, A. Orlov, Microstructure and mechanical properties of additive manufactured copper alloy, Mater. Lett. 179 (2016) 38–41. doi:10.1016/j.matlet.2016.05.064.

[117] D. Ding, Z. Pan, D. Cuiuri, H. Li, Wire-feed additive manufacturing of metal components: technologies, developments and future interests, Int. J. Adv. Manuf. Technol. 81 (2015) 465–481. doi:10.1007/s00170-015-7077-3.

[118] A.N.D. Gasper, S. Catchpole-Smith, A.T. Clare, In-situ synthesis of titanium aluminides by direct metal deposition, J. Mater. Process. Technol. 239 (2017) 230–239. doi:10.1016/j.jmatprotec.2016.08.031.

[119] W.U.H. Syed, A.J. Pinkerton, L. Li, Combining wire and coaxial powder feeding in laser direct metal deposition for rapid prototyping, Appl. Surf. Sci. 252 (2006) 4803–4808. doi:10.1016/j.apsusc.2005.08.118.

[120] H.C. Chen, G. Bi, M.L.S. Nai, J. Wei, Enhanced welding efficiency in laser welding of highly reflective pure copper, J. Mater. Process. Technol. 216 (2015) 287–293. doi:10.1016/j.jmatprotec.2014.09.020.

[121] K.M.B. Taminger, R.A. Hafley, Electron beam freeform fabrication: a rapid metal deposition process, in: Proc. 3rd Annu. Automot. Compos. Conf., 2003: pp. 1–5. http://www.ntrs.nasa.gov/archive/nasa/casi.ntrs.nasa.gov/20040042496_2004036110.pdf.

[122] A. Robinson, The Power of 3D Printing in Manufacturing : An Illustrated Guide, Cerasis. (2014). http://cerasis.com/2014/12/10/3d-printing-in-manufacturing/.

[123] J. Gu, B. Cong, J. Ding, S.W. Williams, Y. Zhai, Wire+ arc additive manufacturing of aluminium, in: Solid Free. Fabr. Proc., 2014: pp. 451–458.

[124] F. Wang, S. Williams, P. Colegrove, A.A. Antonysamy, Microstructure and mechanical properties of wire and arc additive manufactured Ti-6Al-4V, Metall. Mater. Trans. A Phys. Metall. Mater. Sci. 44 (2013) 968–977. doi:10.1007/s11661-012-1444-6.

[125] J. Ding, P. Colegrove, J. Mehnen, S. Ganguly, P.M.S. Almeida, F. Wang, S. Williams, Thermo-mechanical analysis of Wire and Arc Additive Layer Manufacturing process on large multi-layer parts, Comput. Mater. Sci. 50 (2011) 3315–3322. doi:10.1016/j.commatsci.2011.06.023.

[126] D. Ding, Z. Pan, D. Cuiuri, H. Li, A tool-path generation strategy for wire and arc additive manufacturing, Int. J. Adv. Manuf. Technol. 73 (2014) 173–183. doi:10.1007/s00170-014-5808-5.

[127] S.W. Williams, F. Martina, A.C. Addison, J. Ding, G. Pardal, P. Colegrove, Wire + arc additive manufacturing, Mater. Sci. Technol. 836 (2015) 1743284715Y.000. doi:10.1179/1743284715Y.0000000073.

[128] K.P. Karunakaran, S. Suryakumar, V. Pushpa, S. Akula, Low cost integration of additive and subtractive processes for hybrid layered manufacturing,

Robot. Comput. Integr. Manuf. 26 (2010) 490–499. doi:10.1016/j.rcim.2010.03.008.

[129] S. Akula, K.P. Karunakaran, Hybrid adaptive layer manufacturing: An Intelligent art of direct metal rapid tooling process, Robot. Comput. Integr. Manuf. 22 (2006) 113–123. doi:10.1016/j.rcim.2005.02.006.

[130] K.P. Karunakaran, S. Suryakumar, V. Pushpa, S. Akula, Retrofitment of a CNC machine for hybrid layered manufacturing, Int. J. Adv. Manuf. Technol. 45 (2009) 690–703. doi:10.1007/s00170-009-2002-2.

[131] S. Suryakumar, K.P. Karunakaran, A. Bernard, U. Chandrasekhar, N. Raghavender, D. Sharma, Weld bead modeling and process optimization in Hybrid Layered Manufacturing, CAD Comput. Aided Des. 43 (2011) 331–344. doi:10.1016/j.cad.2011.01.006.

[132] T.S. Srivatsan, K. Manigandan, T.S. Sudarshan, Additive Manufacturing: Innovations, Advances, and Applications, in: Addit. Manuf. Innov. Adv. Appl., 2016: pp. 1–48.

[133] Fabbaloo, GE Dramatically Expanding Their Recent 3D Metal Acquisitions, (2017). http://www.fabbaloo.com/blog/2017/3/14/ge-dramatically-expanding-their-recent-3d-metal-acquisitions.

[134] B. Vayre, F. Vignat, F. Villeneuve, Identification on some design key parameters for additive manufacturing: Application on Electron Beam Melting, Procedia CIRP. 7 (2013) 264–269. doi:10.1016/j.procir.2013.05.045.

[135] M.A. Lodes, R. Guschlbauer, C. Körner, Process development for the manufacturing of 99.94% pure copper via selective electron beam melting, Mater. Lett. 143 (2015) 298–301. doi:10.1016/j.matlet.2014.12.105.

[136] C. Körner, Additive manufacturing of metallic components by selective electron beam melting — a review, Int. Mater. Rev. 61 (2016) 361–377. doi:10.1080/09506608.2016.1176289.

[137] A.A. Antonysamy, J. Meyer, P.B. Prangnell, Effect of build geometry on the β -grain structure and texture in additive manufacture of Ti-6Al-4V by selective electron beam melting, Mater. Charact. 84 (2013) 153–168.

[138] A. Klassen, A. Bauereiß, C. Körner, Modelling of electron beam absorption in complex geometries, J. Phys. D. Appl. Phys. 47 (2014) 1–11. doi:10.1088/0022-3727/47/6/065307.

[139] L. Yang, K. Hsu, B. Baughman, D. Godfrey, F. Medina, M. Menon, S. Wiener, Additive Manufacturing of Metals: The Technology, Materials, Design and Production, 2017. doi:10.1007/978-3-319-55128-9.

[140] S. Ponader, E. Vairaktaris, P. Heinl, C. V. Wilmowsky, A. Rottmair, C. Körner, R.F. Singer, S. Holst, K.A. Schlegel, F.W. Neukam, E. Nkenke, Effects of topographical surface modifications of electron beam melted Ti-6Al-4V titanium on human fetal osteoblasts, J. Biomed. Mater. Res. - Part A. 84 (2008) 1111–1119. doi:10.1002/jbm.a.31540.

[141] J.E. Biemond, G. Hannink, N. Verdonschot, P. Buma, Bone ingrowth potential of electron beam and selective laser melting produced trabecular-like implant surfaces with and without a biomimetic coating, J. Mater. Sci. Mater. Med. 24 (2013) 745–753. doi:10.1007/s10856-012-4836-7.

[142] E. Marin, M. Pressacco, S. Fusi, A. Lanzutti, S. Turchet, L. Fedrizzi, Characterization of grade 2 commercially pure Trabecular Titanium structures, Mater. Sci. Eng. C. 33 (2013) 2648–2656. doi:10.1016/j.msec.2013.02.034.

[143] L.E. Murr, S.M. Gaytan, E. Martinez, F. Medina, R.B. Wicker, Next Generation Orthopaedic Implants by Additive Manufacturing Using Electron Beam Melting, Int. J. Biomater. 2012 (2012) 1–14. doi:10.1155/2012/245727.

[144] A. Mazzoli, M. Germani, R. Raffaeli, Direct fabrication through electron beam melting technology of custom cranial implants designed in a PHANToM-based haptic environment, Mater. Des. 30 (2009) 3186–3192. doi:10.1016/j.matdes.2008.11.013.

[145] J. Wang, H. Tang, Review on metals additively manufactured by SEBM, Mater. Technol. 31 (2016) 86–89. doi:10.1179/1753555715Y.0000000081.

[146] Arcam - EBM hardware, (n.d.). http://www.arcam.com/technology/electron-beam-melting/hardware (accessed January 1, 2017).

[147] R. Dehoff, C. Duty, W. Peter, Y. Yamamoto, W. Chen, C. Blue, C. Tallman, Case study: Additive manufacturing of aerospace brackets, Adv. Mater. Process. 171 (2013) 19–22.

[148] S. Biamino, A. Penna, U. Ackelid, S. Sabbadini, O. Tassa, P. Fino, M. Pavese, P. Gennaro, C. Badini, Electron beam melting of Ti e 48Al e 2Cr e 2Nb alloy : Microstructure and mechanical properties investigation, Intermetallics. 19 (2011) 776–781. doi:10.1016/j.intermet.2010.11.017.

[149] G. Baudana, S. Biamino, B. Kloden, A. Kirchner, T. Weißgarber, B. Kieback, M. Pavese, D. Ugues, P. Fino, C. Badini, Intermetallics Electron Beam Melting of Ti-48Al-2Nb-0.7Cr-0.3Si: Feasibility investigation, Intermetallics. 73 (2016) 43–49. doi:10.1016/j.intermet.2016.03.001.

[150] J. Schwerdtfeger, C. Körner, Selective electron beam melting of Tie48Ale2Nbe2Cr: Microstructure and aluminium loss, Intermetallics. 49 (2014) 29–35. doi:10.1016/j.intermet.2014.01.004.

[151] H.P. Tang, G.Y. Yang, W.P. Jia, W.W. He, S.L. Lu, M. Qian, Additive manufacturing of a high niobium-containing titanium aluminide alloy by selective electron beam melting, Mater. Sci. Eng. A. 636 (2015) 103–107. doi:10.1016/j.msea.2015.03.079.

[152] L.E. Murr, S.M. Gaytan, A. Ceylan, E. Martinez, J.L. Martinez, D.H. Hernandez, B.I. Machado, D.A. Ramirez, F. Medina, S. Collins, R.B. Wicker, Characterization of titanium aluminide alloy components fabricated by additive manufacturing using electron beam melting, Acta Mater. 58 (2010) 1887–1894. doi:10.1016/j.actamat.2009.11.032.

[153] F. Trevisan, F. Calignano, M. Lorusso, J. Pakkanen, A. Aversa, E.P. Ambrosio, M. Lombardi, P. Fino, D. Manfredi, On the Selective Laser Melting (SLM) of the AlSi10Mg Alloy: Process, Microstructure, and Mechanical Properties, Materials (Basel). 10 (2017) 1–23. doi:10.3390/ma10010076.

[154] E. e-M. Solutions, Systems and Equipment for Metal Manufacturing, (2017). https://www.eos.info/systems_solutions/metal (accessed June 14, 2017).

[155] C. Laser, Metal 3D printers, (2017). https://www.concept-laser.de/en/products/machines.html (accessed June 14, 2017).

[156] Renishaw, Metal additive manufacturing (3D printing) systems, (2017). http://www.renishaw.com/en/metal-additive-manufacturing-3d-printing-systems--37011 (accessed June 14, 2017).

[157] Realizer, Realizer: The pioneer of 3-D printers, (2017). http://www.realizer.com/en/ (accessed June 14, 2017).

[158] Sisma Industry, Laser Metal Fusion, (2018). http://www.sisma.com/ita/industry/prodotti/additive-manufacturing/#famiglia_22 (accessed March 12, 2018).

[159] S. Solutions, SLM Solutions Machine, (2017). https://slm-solutions.com/machines (accessed June 14, 2017).

[160] Trumpf, 3D printing systems, (2017). https://www.trumpf.com/en_US/products/machines-systems/3d-printing-systems/?LS=1 (accessed June 14, 2017).

[161] 3DSystems, 3D Printers, (2017) 1–31. https://www.3dsystems.com/3d-printers (accessed June 15, 2017).

[162] S. and Market, 3D Printing of Metals: 2015-2025, (2016). https://www.researchandmarkets.com/research/xh9qsm/3d_printing_of (accessed June 26, 2017).

[163] Reuters, GE buys Germany's Concept Laser after SLM bid fails, (2016). https://www.reuters.com/article/us-ge-3dprinting-germany/ge-buys-germanys-concept-laser-after-slm-bid-fails-idUSKCN12R0JT (accessed March 12, 2018).

[164] tct Magazine, DMG MORI acquires majority share in additive manufacturing firm REALIZER, (2017). https://www.tctmagazine.com/3d-printing-news/dmg-mori-50-shares-additive-manufacturing-realizer/ (accessed March 12, 2018).

[165] 3D Printing Industry, SLM report 105% increase in 3D printing sales, "faster rate" than market, (2016). https://3dprintingindustry.com/news/slm-report-105-increase-3d-printing-sales-faster-rate-market-93830/ (accessed June 26, 2017).

[166] B.J. Dawes, R. Bowerman, Introduction to the Additive Manufacturing Powder Metallurgy Supply Chain, Johnson Matthey Technol. Rev. 59 (2015) 243–256. doi:http://dx.doi.org/10.1595/205651315X688686.

[167] W. Schatt, K.P. Wieters, Powder metallurgy: processing and materials, 1997.

[168] P. Sun, Z.Z. Fang, Y. Zhang, Y. Xia, Review of the Methods for Production of Spherical Ti and Ti Alloy Powder, Jom. 69 (2017) 1853–1860. doi:10.1007/s11837-017-2513-5.

[169] K. Traina, R. Cloots, S. Bontempi, G. Lumay, N. Vandewalle, F. Boschini, Flow abilities of powders and granular materials evidenced from dynamical tap density measurement, Powder Technol. 235 (2013) 842–852. doi:10.1016/j.powtec.2012.11.039.

[170] G. Lumay, F. Boschini, K. Traina, S. Bontempi, J.C. Remy, R. Cloots, N. Vandewalle, Measuring the flowing properties of powders and grains, Powder Technol. 224 (2012) 19–27. doi:10.1016/j.powtec.2012.02.015.

[171] A. Strondl, O. Lyckfeldt, H. Brodin, U. Ackelid, Characterization and Control of Powder Properties for Additive Manufacturing, Jom. 67 (2015) 549–554. doi:10.1007/s11837-015-1304-0.

[172] A.J. Pinkerton, L. Li, Direct additive laser manufacturing using gas- and water-atomised H13 tool steel powders, Int. J. Adv. Manuf. Technol. 25 (2005) 471–479. doi:10.1007/s00170-003-1844-2.

[173] A.B. Spierings, N. Herres, G. Levy, Influence of the particle size distribution on surface quality and mechanical properties in AM steel parts, Rapid Prototyp. J. 17 (2011) 195–202. doi:10.1108/13552541111124770.

[174] G. Spierings, A.B., Levy, Comparison of density of stainless steel 316L parts produced with selective laser melting using different powder grades, in: Annu. Int. Solid Free. Fabr. Symp., The University of Texas, Austin, Texas, USA, 2009: pp. 342–353.

[175] M. Lutter-Günther, F. Schwer, C. Seidel, G. Reinhart, Effects on Properties of Metal Powders for Laser Beam Melting Along the Powder Process Chain, in: Frauhofer Direct Digit. Manuf. Conf., Berlin, 2016: pp. 1–8.

[176] A. Jillavenkatesa, S.J. Dapkunas, L.-S.H. Lum, Particle Size Characterisation, Washinton D.C., 2001. http://www.horiba.com/fileadmin/uploads/Scientific/Documents/PSA/NIST_SP9601.pdf.

[177] D.M. Bauer, I. Ludwig, D. Greitemeier, F. Palm, G. Witt, Additive manufactured aluminum alloys based on different powder grades, in: Frauhofer Direct Digit. Manuf. Conf., Berlin, 2016: pp. 1–5.

[178] D. Manfredi, F. Calignano, M. Krishnan, R. Canali, E.P. Ambrosio, E. Atzeni, From powders to dense metal parts: Characterization of a commercial alsimg alloy processed through direct metal laser sintering, Materials (Basel). 6 (2013) 856–869. doi:10.3390/ma6030856.

[179] M. Averyanova, E. Cicala, P. Bertrand, D. Grevey, Experimental design approach to optimize selective laser melting of martensitic 17-4 PH powder: part I – single laser tracks and first layer, Rapid Prototyp. J. 18 (2012) 28–37. doi:10.1108/13552541211193476.

[180] C. Aumund-kopp, D. Zibelius, J. Isaza, M. Uhlirsch, Practical Powder Analysis for Metal Powder Bed Based AM, in: Frauhofer Direct Digit. Manuf. Conf., Berlin, 2016: pp. 1–6.

[181] A. International, ASTM Designation B213-17: Standard test methods for

flow rate of metal powders using the hall flowmeter, (2017). doi:10.1520/B0213-17.2.

[182] ASTM International, ASTM Designation B417-2013: Standard Test Method for Apparent Density of Non-Free-Flowing Metal Powders Using the Carney Funnel, (2013). doi:10.1520/B0417-13.2.

[183] A. Amado, M. Schmid, G. Levy, K. Wegener, Advances in SLS Powder Characterization, in: Int. Conf. Solid Free. Fabr., 2011: pp. 438–452.

[184] B. Moorhouse, Controlling the interstitial element concentration in Ti-6Al-4V using Calciothermic Reduction By, 2013.

[185] J. Oh, B. Lee, S. Cho, S. Lee, G. Choi, J. Lim, Oxygen Effects on the Mechanical Properties and Lattice Strain of Ti and Ti-6Al-4V, Met. Mater. Int. 17 (2011) 733–736. doi:10.1007/s12540-011-1006-2.

[186] K. Nagal, T. Yuri, T. Ogata, K. Ishikawa, Cryogenic Mechanical Properties of Ti-6AI Alloys with Three Levels of Oxygen Content, ISIJ Int. 31 (1991) 882–889.

[187] Y.T. Lee, G. Welsch, Young â€TM s Modulus and Damping of Ti-6AI-4V Alloy as a Function of Heat Treatment and Oxygen Concentration, Mater. Sci. Eng. A. 128 (1990) 77–89.

[188] J. Vaithilingam, R.D. Goodridge, R.J.M. Hague, S.D.R. Christie, S. Edmondson, The effect of laser remelting on the surface chemistry of Ti6al4V components fabricated by selective laser melting, J. Mater. Process. Technol. 232 (2016) 1–8. doi:10.1016/j.jmatprotec.2016.01.022.

[189] E.O. Olakanmi, R.F. Cochrane, K.W. Dalgarno, A review on selective laser sintering/melting (SLS/SLM) of aluminium alloy powders: Processing, microstructure, and properties, Prog. Mater. Sci. 74 (2015) 401–477. doi:10.1016/j.pmatsci.2015.03.002.

[190] E. Louvis, P. Fox, C.J. Sutcliffe, Selective laser melting of aluminium components, J. Mater. Process. Technol. 211 (2011) 275–284. doi:10.1016/j.jmatprotec.2010.09.019.

[191] C. Weingarten, D. Buchbinder, N. Pirch, W. Meiners, K. Wissenbach, R. Poprawe, Formation and reduction of hydrogen porosity during selective laser melting of AlSi10Mg, J. Mater. Process. Technol. 221 (2015) 112–120. doi:10.1016/j.jmatprotec.2015.02.013.

[192] X.P. Li, K.M.O. Donnell, T.B. Sercombe, Selective laser melting of Al-12Si

alloy : Enhanced densification via powder drying, Addit. Manuf. 10 (2016) 10–14. doi:10.1016/j.addma.2016.01.003.

[193] A. Simchi, Direct laser sintering of metal powders: Mechanism, kinetics and microstructural features, Mater. Sci. Eng. A. 428 (2006) 148–158. doi:10.1016/j.msea.2006.04.117.

[194] S. Das, Physical Aspects of Process Control in Selective Laser Sintering of Metals, Adv. Eng. Mater. 5 (2003) 701–711. doi:10.1002/adem.200310099.

[195] J.P. Kruth, X. Wang, T. Laoui, L. Froyen, Lasers and materials in selective laser sintering, Assem. Autom. 23 (2003) 357–371. doi:10.1108/01445150310698652.

[196] N.T. Aboulkhair, N.M. Everitt, I. Ashcroft, C. Tuck, Reducing porosity in AlSi10Mg parts processed by selective laser melting, Addit. Manuf. 1–4 (2014) 77–86. doi:10.1016/j.addma.2014.08.001.

[197] R.W. McVey, R.M. Melnychuk, J. a. Todd, R.P. Martukanitz, Absorption of laser irradiation in a porous powder layer, J. Laser Appl. 19 (2007) 214. doi:10.2351/1.2756854.

[198] S. Engler, R. Ramsayer, R. Poprawe, Process studies on laser welding of copper with brilliant green and infrared lasers, Phys. Procedia. 12 (2011) 342–349. doi:10.1016/j.phpro.2011.03.142.

[199] Y. Li, D. Gu, Parametric analysis of thermal behavior during selective laser melting additive manufacturing of aluminum alloy powder, Mater. Des. 63 (2014) 856–867. doi:10.1016/j.matdes.2014.07.006.

[200] I. Yadroitsev, I. Smurov, Selective laser melting technology: From the single laser melted track stability to 3D parts of complex shape, Phys. Procedia. 5 (2010) 551–560. doi:10.1016/j.phpro.2010.08.083.

[201] H. Rao, S. Giet, K. Yang, X. Wu, C.H.J. Davies, The influence of processing parameters on aluminium alloy A357 manufactured by Selective Laser Melting, Mater. Des. 109 (2016) 334–346. doi:10.1016/j.matdes.2016.07.009.

[202] L.E. Loh, Z.H. Liu, D.Q. Zhang, W.Y. Yeong, C.K. Chua, Effect of laser beam profile on melt track in Selective Laser Melting, High Value Manuf. Adv. Res. Virtual Rapid Prototyp. - Proc. 6th Int. Conf. Adv. Res. Rapid Prototyping, VR@P 2013. (2014) 83–87. http://www.scopus.com/inward/record.url?eid=2-s2.0-84892178146&partnerID=tZOtx3y1.

[203] I. Yadroitsev, a. Gusarov, I. Yadroitsava, I. Smurov, Single track formation in selective laser melting of metal powders, J. Mater. Process. Technol. 210 (2010) 1624–1631. doi:10.1016/j.jmatprotec.2010.05.010.

[204] M.J. Galba, T. Reischle, Additive Manufacturing of Metals Using Powder-Based Technology, in: A. Bandyopadhyay, S. Bose (Eds.), Addit. Manuf., CRC Press - Taylor & Francis Group, 2015: pp. 97–142.

[205] F. Calignano, D. Manfredi, E.P. Ambrosio, L. Iuliano, P. Fino, Influence of process parameters on surface roughness of aluminum parts produced by DMLS, Int. J. Adv. Manuf. Technol. 67 (2013) 2743–2751. doi:10.1007/s00170-012-4688-9.

[206] F. Calignano, G. Cattano, D. Manfredi, Manufacturing of thin wall structures in AlSi10Mg alloy by laser powder bed fusion through process parameters, J. Mater. Process. Technol. 255 (2018) 773–783. doi:10.1016/j.jmatprotec.2018.01.029.

[207] A. Simchi, H. Pohl, Effects of laser sintering processing parameters on the microstructure and densification of iron powder, Mater. Eng. A. 359 (2003) 119–128. doi:10.1016/S0921-5093(03)00341-1.

[208] F. Calignano, M. Lorusso, J. Pakkanen, F. Trevisan, E.P. Ambrosio, Investigation of accuracy and dimensional limits of part produced in aluminum alloy by selective laser melting, Int. J. Adv. Manuf. Technol. (2016). doi:10.1007/s00170-016-8788-9.

[209] T. Kimura, T. Nakamoto, Microstructures and mechanical properties of A356 ( AlSi7Mg0 . 3 ) aluminum alloy fabricated by selective laser melting, JMADE. 89 (2016) 1294–1301. doi:10.1016/j.matdes.2015.10.065.

[210] N. Read, W. Wang, K. Essa, M.M. Attallah, Selective laser melting of AlSi10Mg alloy: Process optimisation and mechanical properties development, Mater. Des. 65 (2015) 417–424. doi:10.1016/j.matdes.2014.09.044.

[211] H. Meier, C. Haberland, Experimental studies on selective laser melting of metallic parts, Materwiss. Werksttech. 39 (2008) 665–670. doi:10.1002/mawe.200800327.

[212] J.P. Kruth, P. Mercelis, J. Van Vaerenbergh, L. Froyen, M. Rombouts, Binding mechanisms in selective laser sintering and selective laser melting, Rapid Prototyp. J. 11 (2005) 26–36. doi:10.1108/13552540510573365.

[213] D. Gu, Y. Shen, Balling phenomena in direct laser sintering of stainless steel

powder : Metallurgical mechanisms and control methods, Mater. Des. 30 (2009) 2903–2910. doi:10.1016/j.matdes.2009.01.013.

[214] C.C. Ng, M.M. Savalani, H.C. Man, I. Gibson, Layer manufacturing of magnesium and its alloy structures for future applications, Virtual Phys. Prototyp. 5 (2010) 13–19. doi:10.1080/17452751003718629.

[215] E.O. Olakanmi, Selective laser sintering/melting (SLS/SLM) of pure Al, Al-Mg, and Al-Si powders: Effect of processing conditions and powder properties, J. Mater. Process. Technol. 213 (2013) 1387–1405. doi:10.1016/j.jmatprotec.2013.03.009.

[216] L. Wang, S. Wang, J. Wu, Experimental investigation on densification behavior and surface roughness of AlSi10Mg powders produced by selective laser melting, 96 (2017) 88–96.

[217] I. Yadroitsev, P. Bertrand, I. Smurov, Parametric analysis of the selective laser melting process, Appl. Surf. Sci. 253 (2007) 8064–8069. doi:10.1016/j.apsusc.2007.02.088.

[218] K.H. Low, K.F. Leong, Review of Selective Laser Melting process parameters for Commercially Pure Titanium and Ti6Al4V, in: Proc. 6th Int. Conf. Adv. Res. Virtual Rapid Prototyp., Leira, Portugal, 2014: pp. 71–76.

[219] H. Krauss, M.F. Zaeh, Investigations on manufacturability and process reliability of selective laser melting, Phys. Procedia. 41 (2013) 815–822. doi:10.1016/j.phpro.2013.03.153.

[220] B. Cheng, S. Shrestha, K. Chou, Stress and deformation evaluations of scanning strategy effect in selective laser melting, Addit. Manuf. 12 (2016) 240–251. doi:10.1016/j.envexpbot.2012.01.010.

[221] K.W. A.B. Spierings, T.L. Starr, Fatigue performance of additive manufactured metallic parts, Rapid Prototyp. J. 19 (2013) 88–94. doi:10.1108/13552541311302932.

[222] L.N. Carter, C. Martin, P.J. Withers, M.M. Attallah, The influence of the laser scan strategy on grain structure and cracking behaviour in SLM powder-bed fabricated nickel superalloy, J. Alloys Compd. 615 (2014) 338–347. doi:10.1016/j.jallcom.2014.06.172.

[223] X. Su, Y. Yang, Research on track overlapping during Selective Laser Melting of powders, J. Mater. Process. Tech. 212 (2012) 2074–2079. doi:10.1016/j.jmatprotec.2012.05.012.

[224] P. Mercelis, J.-P. Kruth, Residual stresses in selective laser sintering and selective laser melting, Rapid Prototyp. J. 12 (2006) 254–265. doi:10.1108/13552540610707013.

[225] J.P. Kruth, L. Froyen, J. Van Vaerenbergh, P. Mercelis, M. Rombouts, B. Lauwers, Selective laser melting of iron-based powder, J. Mater. Process. Technol. 149 (2004) 616–622. doi:10.1016/j.jmatprotec.2003.11.051.

[226] K. Guan, Z. Wang, M. Gao, X. Li, X. Zeng, Effects of processing parameters on tensile properties of selective laser melted 304 stainless steel, Mater. Des. 50 (2013) 581–586. doi:10.1016/j.matdes.2013.03.056.

[227] Y. Lu, S. Wu, Y. Gan, T. Huang, C. Yang, L. Junjie, J. Lin, Study on the microstructure , mechanical property and residual stress of SLM Inconel-718 alloy manufactured by differing island scanning strategy, Opt. Laser Technol. 75 (2015) 197–206. doi:10.1016/j.optlastec.2015.07.009.

[228] L. Thijs, F. Verhaeghe, T. Craeghs, J. Van Humbeeck, J.P. Kruth, A study of the microstructural evolution during selective laser melting of Ti-6Al-4V, Acta Mater. 58 (2010) 3303–3312. doi:10.1016/j.actamat.2010.02.004.

[229] I. Yadroitsev, L. Thivillon, P. Bertrand, I. Smurov, Strategy of manufacturing components with designed internal structure by selective laser melting of metallic powder, Appl. Surf. Sci. 254 (2007) 980–983. doi:10.1016/j.apsusc.2007.08.046.

[230] J. Pakkanen, F. Calignano, F. Trevisan, M. Lorusso, E.P. Ambrosio, D. Manfredi, P. Fino, Study of Internal Channel Surface Roughnesses Manufactured by Selective Laser Melting in Aluminum and Titanium Alloys, Metall. Mater. Trans. A. (2016). doi:10.1007/s11661-016-3478-7.

[231] B. Song, X. Zhao, S. Li, C. Han, Q. Wei, S. Wen, J. Liu, Y. Shi, Differences in microstructure and properties between selective laser melting and traditional manufacturing for fabrication of metal parts: A review, Front. Mech. Eng. 10 (2015) 111–125. doi:10.1007/s11465-015-0341-2.

[232] E. Chlebus, K. Gruber, B. Ku, J. Kurzac, T. Kurzynowski, Effect of heat treatment on the microstructure and mechanical properties of Inconel 718 processed by selective laser melting, Mater. Sci. Eng. A. 639 (2015) 647–655. doi:10.1016/j.msea.2015.05.035.

[233] W. Shifeng, L. Shuai, W. Qingsong, C. Yan, Z. Sheng, S. Yusheng, Effect of molten pool boundaries on the mechanical properties of selective laser melting parts, J. Mater. Process. Tech. 214 (2014) 2660–2667. doi:10.1016/j.jmatprotec.2014.06.002.

[234] X.J. Wang, L.C. Zhang, M.H. Fang, T.B. Sercombe, The effect of atmosphere on the structure and properties of a selective laser melted Al – 12Si alloy, Mater. Sci. Eng. A. 597 (2014) 370–375. doi:10.1016/j.msea.2014.01.012.

[235] G.B. Schaffer, B.J. Hall, S.J. Bonner, S.H. Huo, T.B. Sercombe, The effect of the atmosphere and the role of pore filling on the sintering of aluminium, Acta Mater. 54 (2006) 131–138. doi:10.1016/j.actamat.2005.08.032.

[236] C.J. Ferrar, B., Mullen, L., Jones, E., Stamp, R., Sutcliffe, Gas flow effects on selective laser melting ( SLM ) manufacturing performance, J. Mater. Process. Technol. 212 (2012) 355–364. doi:10.1016/j.jmatprotec.2011.09.020.

[237] D. Dai, D. Gu, Effect of metal vaporization behavior on keyhole-mode surface morphology of selective laser melted composites using different protective atmospheres, Appl. Surf. Sci. 355 (2015) 310–319. doi:10.1016/j.apsusc.2015.07.044.

[238] B. Zhang, L. Dembinski, C. Coddet, The study of the laser parameters and environment variables effect on mechanical properties of high compact parts elaborated by selective laser melting 316L powder, Mater. Sci. Eng. A. 584 (2013) 21–31. doi:10.1016/j.msea.2013.06.055.

[239] A. Masmoudi, R. Bolot, C. Coddet, Investigation of the laser – powder – atmosphere interaction zone during the selective laser melting process, J. Mater. Process. Tech. 225 (2015) 122–132. doi:10.1016/j.jmatprotec.2015.05.008.

[240] A. Aversa, M. Lorusso, F. Trevisan, E. Ambrosio, F. Calignano, D. Manfredi, S. Biamino, P. Fino, M. Lombardi, M. Pavese, Effect of Process and Post-Process Conditions on the Mechanical Properties of an A357 Alloy Produced via Laser Powder Bed Fusion, Metals (Basel). 7 (2017) 1–9. doi:10.3390/met7020068.

[241] I. Yadroitsev, P. Krakhmalev, I. Yadroitsava, S. Johansson, I. Smurov, Energy input effect on morphology and microstructure of selective laser melting single track from metallic powder, J. Mater. Process. Technol. 213 (2013) 606–613. doi:10.1016/j.jmatprotec.2012.11.014.

[242] D. Buchbinder, W. Meiners, K. Wissenbach, R. Poprawe, Selective laser melting of aluminum die-cast alloy—Correlations between process parameters, solidification conditions, and resulting mechanical properties, J. Laser Appl. 27 (2015) S29205. doi:10.2351/1.4906389.

[243] N. Kaufamann, M. Imran, T.M. Wischeropp, C. Emmelmann, S. Siddique, F. Walther, Influence of process parameters on the quality of aluminium alloy EN AW 7075 using selective laser melting (SLM), Physic Procedia. 83 (2016) 918–926. doi:10.1016/j.phpro.2016.08.096.

[244] M.F. Zaeh, G. Branner, Investigations on residual stresses and deformations in selective laser melting, Prod. Eng. 4 (2010) 35–45. doi:10.1007/s11740-009-0192-y.

[245] C.Y. Yap, C.K. Chua, Z.L. Dong, Z.H. Liu, D.Q. Zhang, L.E. Loh, S.L. Sing, C.Y. Yap, C.K. Chua, Z.L. Dong, Z.H. Liu, D.Q. Zhang, L.E. Loh, Review of selective laser melting : Materials and applications, Appl. Phys. Rev. 2 (2015) 1–21. doi:10.1063/1.4935926.

[246] G. Casalino, S.L. Campanelli, N. Contuzzi, a.D. Ludovico, Experimental investigation and statistical optimisation of the selective laser melting process of a maraging steel, Opt. Laser Technol. 65 (2015) 151–158. doi:10.1016/j.optlastec.2014.07.021.

[247] E.A. Jägle, P. Choi, J. Van Humbeeck, D. Raabe, Precipitation and austenite reversion behavior of a maraging steel produced by selective laser melting, J. Mater. Res. 29 (2014) 2072. doi:10.1557/jmr.2014.204.

[248] H. Attar, M. Calin, L.C. Zhang, S. Scudino, J. Eckert, Manufacture by selective laser melting and mechanical behavior of commercially pure titanium, Mater. Sci. Eng. A. 593 (2014) 170–177. doi:10.1016/j.msea.2013.11.038.

[249] D. Gu, Y. Hagedorn, W. Meiners, G. Meng, R.J.S. Batista, K. Wissenbach, R. Propawe, Densification behavior , microstructure evolution , and wear performance of selective laser melting processed commercially pure titanium, Acta Mater. 60 (2012) 3849–3860. doi:10.1016/j.actamat.2012.04.006.

[250] N. Dai, L.-C. Zhang, J. Zhang, Q. Chen, M. Wu, Corrosion Behaviour of Selective Laser Melted Ti-6Al-4V Alloy in NaCl Solution, Corros. Sci. 102 (2016) 484–489. doi:10.1016/j.corsci.2015.10.041.

[251] B. Dutta, F.H.S. Froes, The additive manufacturing (AM) of titanium alloys, Elsevier Inc., 2015. doi:10.1016/B978-0-12-800054-0/00024-1.

[252] R. Wauthle, B. Vrancken, B. Beynaerts, K. Jorissen, J. Schrooten, J.-P. Kruth, J. Van Humbeeck, Effects of build orientation and heat treatment on the microstructure and mechanical properties of selective laser melted Ti6Al4V lattice structures, Addit. Manuf. 5 (2015) 77–84.

doi:10.1016/j.addma.2014.12.008.

[253] D.K. Do, P. Li, The effect of laser energy input on the microstructure , physical and mechanical properties of Ti-6Al-4V alloys by selective laser melting, Virtual Phys. Prototyp. 11 (2016) 41–47. doi:10.1080/17452759.2016.1142215.

[254] M. Koike, P. Greer, K. Owen, G. Lilly, L.E. Murr, S.M. Gaytan, E. Martinez, T. Okabe, Evaluation of Titanium Alloys Fabricated Using Rapid Prototyping Technologies—Electron Beam Melting and Laser Beam Melting, Materials (Basel). 4 (2011) 1776–1792. doi:10.3390/ma4101776.

[255] M. Simonelli, Y.Y. Tse, C. Tuck, On the Texture Formation of Selective Laser Melted Ti-6Al-4V, JOM. 45 (2014) 2863–2872. doi:10.1007/s11661-014-2218-0.

[256] E. Chlebus, T. Kurzynowski, B. Dyba, Microstructure and mechanical behaviour of Ti-6Al-7Nb alloy produced by selective laser melting, Mater. Charact. 62 (2011) 488–495. doi:10.1016/j.matchar.2011.03.006.

[257] P. Szymczyk, A. Junka, G. Ziolkowski, D. Smutnicka, M. Bartoszewicz, E. Chlebus, The ability of S.aureus to form biofilm on the TI-6Al-7Nb scaffolds produced by Selective Laser Melting and subjected to the different types of surface modifications, Acta Bioeng. Biomech. 15 (2013) 69–76. doi:10.5277/abb130109.

[258] T. Marcu, M. Todea, I. Gligor, P. Berce, C. Popa, Effect of surface conditioning on the flowability of Ti6Al7Nb powder for selective laser melting applications, Appl. Surf. Sci. 258 (2012) 3276–3282. doi:10.1016/j.apsusc.2011.11.081.

[259] L.C. Zhang, D. Klemm, J. Eckert, Y.L. Hao, T.B. Sercombe, Manufacture by selective laser melting and mechanical behavior of a biomedical Ti – 24Nb – 4Zr – 8Sn alloy, Scr. Mater. 65 (2011) 21–24. doi:10.1016/j.scriptamat.2011.03.024.

[260] K.N. Amato, S.M. Gaytan, L.E. Murr, E. Martinez, P.W. Shindo, Microstructures and mechanical behavior of Inconel 718 fabricated by selective laser melting, Acta Mater. 60 (2012) 2229–2239. doi:10.1016/j.actamat.2011.12.032.

[261] Q. Jia, D. Gu, Selective laser melting additive manufacturing of Inconel 718 superalloy parts : Densification , microstructure and properties, J. Alloys Compd. 585 (2014) 713–721. doi:10.1016/j.jallcom.2013.09.171.

[262] Y. Wang, J. Shi, S. Lu, Y. Wang, Selective Laser Melting of Graphene-Reinforced Inconel 718 Superalloy: Evaluation of Microstructure and Tensile Performance, J. Manuf. Sci. Eng. 139 (2016) 41005. doi:10.1115/1.4034712.

[263] G. Marchese, E. Bassini, M. Calandri, E.P. Ambrosio, F. Calignano, M. Lorusso, D. Manfredi, M. Pavese, S. Biamino, P. Fino, Microstructural investigation of as-fabricated and heat-treated Inconel 625 and Inconel 718 fabricated by direct metal laser sintering: contribution of Politecnico di Torino and Istituto Italiano di Tecnologia (IIT) di Torino, Met. Powder Rep. 71 (2016) 273–278. doi:10.1016/j.mprp.2016.06.002.

[264] G. Marchese, X. Garmendia Colera, F. Calignano, M. Lorusso, S. Biamino, P. Minetola, D. Manfredi, Characterization and Comparison of Inconel 625 Processed by Selective Laser Melting and Laser Metal Deposition, Adv. Eng. Mater. 19 (2017) 1–9. doi:10.1002/adem.201600635.

[265] G. Marchese, S. Biamino, M. Pavese, D. Ugues, M. Lombardi, Heat treatment optimization of Hastelloy X superalloy produced by Direct Metal Laser Sintering, Proc. Euro PM 2015 Int. Power Metall. Congr. Exhib. (2015) 1–6. https://www.epma.com/publications/euro-pm-abstracts-proceedings/cd-and-usb-proceedings/product/euro-pm2015-proceedings-usb.

[266] S. Scudino, C. Unterdörfer, K.G. Prashanth, H. Attar, N. Ellendt, V. Uhlenwinkel, Additive manufacturing of Cu – 10Sn bronze, Mater. Lett. 156 (2015) 202–204. doi:10.1016/j.matlet.2015.05.076.

[267] Z. Mao, D. Zhang, P. Wei, K. Zhang, Manufacturing Feasibility and Forming Properties of Cu-4Sn in Selective Laser Melting, Materials (Basel). 10 (2017) 1–12. doi:10.3390/ma10040333.

[268] A.P. Ventura, C.A. Wade, G. Pawlikowski, M. Bayes, M. Watanabe, W.Z. Misiolek, Mechanical Properties and Microstructural Characterization of Cu-4.3 Pct Sn Fabricated by Selective Laser Melting, Metall. Mater. Trans. A Phys. Metall. Mater. Sci. 48 (2017) 178–187. doi:10.1007/s11661-016-3779-x.

[269] D.Q. Zhang, Z.H. Liu, C.K. Chua, Investigation on forming process of copper alloys via Selective Laser Melting, High Value Manuf. Adv. Res. Virtual Rapid Prototyp. Proc. 6th Int. Conf. Adv. Res. Virtual Rapid Prototyping, Leir. Port. 1-5 October, 2013. (2013) 285.

[270] Z.H. Liu, D.Q. Zhang, S.L. Sing, C.K. Chua, L.E. Loh, Interfacial

characterization of SLM parts in multi-material processing: Metallurgical diffusion between 316L stainless steel and C18400 copper alloy, Mater. Charact. 94 (2014) 116–125. doi:10.1016/j.matchar.2014.05.001.

[271] M. Khan, P. Dickens, Selective laser melting (SLM) of pure gold for manufacturing dental crowns, Rapid Prototyp. J. 20 (2014) 471–479. doi:10.1108/RPJ-03-2013-0034.

[272] D. Herzog, V. Seyda, E. Wycisk, C. Emmelmann, Additive manufacturing of metals, Acta Mater. 117 (2016) 371–392. doi:10.1016/j.actamat.2016.07.019.

[273] N.T. Aboulkhair, I. Maskery, C. Tuck, I. Ashcroft, N.M. Everitt, The microstructure and mechanical properties of selectively laser melted AlSi10Mg : The effect of a conventional T6-like heat treatment, Mater. Sci. Eng. A. 667 (2016) 139–146. doi:10.1016/j.msea.2016.04.092.

[274] E.O. Olakanmi, R.F. Cochrane, K.W. Dalgarno, Densification mechanism and microstructural evolution in selective laser sintering of Al-12Si powders, J. Mater. Process. Technol. 211 (2011) 113–121. doi:10.1016/j.jmatprotec.2010.09.003.

[275] B.A. Fulcher, D.K. Leigh, T.J. Watt, Comparison Of AlSi10Mg and Al 6061 Processed Through DMLS, (n.d.) 404–419.

[276] A.J.H. Rao, Y. Zhang, X. Fang, Y. Chen, The origins for tensile properties of selective laser melted aluminium alloy A357, Addit. Manuf. 17 (2017) 113–122. doi:10.1016/j.addma.2017.08.007.

[277] F. Trevisan, F. Calignano, M. Lorusso, J. Pakkanen, E.P. Ambrosio, M. Lombardi, M. Pavese, D. Manfredi, P. Fino, Effects of Heat Treatments on A357 Alloy Produced by Selective Laser Melting, in: World PM2016, 2016: pp. 1–6.

[278] P.& M.S. GPI, EOSINT M 270, (2017). http://gpiprototype.com/services/eosintm270.html (accessed September 23, 2017).

[279] H. Zhao, D.. White, T. DebRoy, Current issues and problems in laser welding of automotive aluminium alloys, Int. Mater. Rev. 44 (1999) 238–266.

[280] I.J. Polmear, Light Alloys: From Traditional Alloys to Nanocrystals, Fourth Edi, Oxford, UK, 2006.

[281] ASM International, ASM Handbook : Properties and selection: non ferrous

alloys and special-purpose materials, ASM International, 1992.

[282] J. Suryawanshi, K.G. Prashanth, S. Scudino, J. Eckert, O. Prakash, U. Ramamurty, Simultaneous enhancements of strength and toughness in an Al-12Si alloy synthesized using selective laser melting, Acta Mater. 115 (2016) 285–294. doi:10.1016/j.actamat.2016.06.009.

[283] R. González, A. González, J. Talamantes-silva, S. Valtierra, R.D. Mercado-solís, N.F. Garza-montes-de-oca, R. Colás, Fatigue of an aluminium cast alloy used in the manufacture of automotive engine blocks, Int. J. Fatigue. 54 (2013) 118–126.

[284] J. Mertens, A., Dedry, O., Reuter, D., Rigo O. and Lecomte-Beckers, Thermal Treatments of AlSi10Mg Processed By Laser Beam Melting, Solid Free. Fabr. Symp. 1 (2015) 1007–1016. doi:10.1017/CBO9781107415324.004.

[285] L. Ventola, F. Robotti, M. Dialameh, F. Calignano, D. Manfredi, E. Chiavazzo, P. Asinari, International Journal of Heat and Mass Transfer Rough surfaces with enhanced heat transfer for electronics cooling by direct metal laser sintering, Int. J. Heat Mass Transf. 75 (2014) 58–74. doi:10.1016/j.ijheatmasstransfer.2014.03.037.

[286] M. Cabrini, S. Lorenzi, T. Pastore, S. Pellegrini, M. Pavese, P. Fino, E.P. Ambrosio, F. Calignano, D. Manfredi, Corrosion resistance of direct metal laser sintering AlSiMg alloy, (2016). doi:10.1002/sia.5981.

[287] K. Kempen, L. Thijs, J. Van Humbeeck, J.-P. Kruth, Mechanical Properties of AlSi10Mg Produced by Selective Laser Melting, Phys. Procedia. 39 (2012) 439–446. doi:10.1016/j.phpro.2012.10.059.

[288] M. Cabrini, S. Lorenzi, T. Pastore, S. Pellegrini, D. Manfredi, P. Fino, S. Biamino, C. Badini, Evaluation of corrosion resistance of Al-10Si-Mg alloy obtained by means of Direct Metal Laser Sintering, J. Mater. Process. Tech. 231 (2016) 326–335. doi:10.1016/j.jmatprotec.2015.12.033.

[289] M. Cabrini, S. Lorenzi, T. Pastore, S. Pellegrini, E.P. Ambrosio, F. Calignano, D. Manfredi, M. Pavese, P. Fino, Effect of heat treatment on corrosion resistance of DMLS AlSi10Mg alloy, Electrochim. Acta. 206 (2016) 346–355. doi:10.1016/j.electacta.2016.04.157.

[290] E. Brandl, U. Heckenberger, V. Holzinger, D. Buchbinder, Additive manufactured AlSi10Mg samples using Selective Laser Melting (SLM): Microstructure, high cycle fatigue, and fracture behavior, Mater. Des. 34 (2012) 159–169. doi:10.1016/j.matdes.2011.07.067.

[291] I. Maskery, N.T. Aboulkhair, M.R. Cor, C. Tuck, A.T. Clare, R.K. Leach, R.D. Wildman, I.A. Ashcroft, R.J.M. Hague, Quantification and characterisation of porosity in selectively laser melted Al–Si10–Mg using X-ray computed tomography, Mater. Charact. 111 (2016) 193–204. doi:10.1016/j.matchar.2015.12.001.

[292] W. Li, S. Li, J. Liu, A. Zhang, Y. Zhou, Q. Wei, C. Yan, Y. Shi, Effect of heat treatment on AlSi10Mg alloy fabricated by selective laser melting: Microstructure evolution, mechanical properties and fracture mechanism, Mater. Sci. Eng. A. 663 (2016) 116–125. doi:10.1016/j.msea.2016.03.088.

[293] I. Rosenthal, A. Stern, N. Frage, Microstructure and Mechanical Properties of AlSi10Mg Parts Produced by the Laser Beam Additive Manufacturing (AM) Technology, Metallogr. Microstruct. Anal. 3 (2014) 448–453. doi:10.1007/s13632-014-0168-y.

[294] N.T. Aboulkhair, C. Tuck, I. Ashcroft, I. Maskery, N.M. Everitt, On the Precipitation Hardening of Selective Laser Melted AlSi10Mg, Metall. Mater. Trans. A. 46 (2015) 3337–3341. doi:10.1007/s11661-015-2980-7.

[295] L.P. Lam, D.Q. Zhang, Z.H. Liu, C.K. Chua, Phase analysis and microstructure characterisation of AlSi10Mg parts produced by Selective Laser Melting, Virtual Phys. Prototyp. 10 (2015) 207–215. doi:10.1080/17452759.2015.1110868.

[296] L. Thijs, K. Kempen, J.P. Kruth, J. Van Humbeeck, Fine-structured aluminium products with controllable texture by selective laser melting of pre-alloyed AlSi10Mg powder, Acta Mater. 61 (2013) 1809–1819. doi:10.1016/j.actamat.2012.11.052.

[297] D. Manfredi, F. Calignano, M. Krishnan, R. Canali, E.P. Ambrosio, S. Biamino, D. Ugues, M. Pavese, P. Fino, Additive Manufacturing of Al Alloys and Aluminium Matrix Composites ( AMCs ), in: Waldemar A. Monteiro (Ed.), Light Met. Alloy. Appl., InTech, 2014: pp. 3–34. doi:10.5772/58534.

[298] Y. Birol, Response to artificial ageing of dendritic and globular Al-7Si-Mg alloys, J. Alloys Compd. 484 (2009) 164–167. doi:10.1016/j.jallcom.2009.05.043.

[299] K.G. Prashanth, S. Scudino, H.J. Klauss, K.B. Surreddi, L. Löber, Z. Wang, A.K. Chaubey, U. Kühn, J. Eckert, Microstructure and mechanical properties of Al-12Si produced by selective laser melting: Effect of heat treatment, Mater. Sci. Eng. A. 590 (2014) 153–160. doi:10.1016/j.msea.2013.10.023.

[300] M. Simonelli, C. Tuck, N.T. Aboulkhair, I. Maskery, I. Ashcroft, R.D. Wildman, R. Hague, A Study on the Laser Spatter and the Oxidation Reactions During Selective Laser Melting of 316L Stainless Steel, Al-Si10-Mg, and Ti-6Al-4V, Metall. Mater. Trans. A Phys. Metall. Mater. Sci. (2015). doi:10.1007/s11661-015-2882-8.

[301] K. Kempen, L. Thijs, J. Van Humbeeck, J.-P. Kruth, Processing AlSi10Mg by selective laser melting: parameter optimisation and material characterisation, Mater. Sci. Technol. 31 (2015) 917–923. doi:10.1179/1743284714Y.0000000702.

[302] X.P. Li, X.J. Wang, M. Saunders, A. Suvorova, L.C. Zhang, Y.J. Liu, M.H. Fang, Z.H. Huang, T.B. Sercombe, A selective laser melting and solution heat treatment refined Al – 12Si alloy with a controllable ultrafine eutectic microstructure and 25 % tensile ductility, Acta Mater. 95 (2015) 74–82. doi:10.1016/j.actamat.2015.05.017.

[303] D. Buchbinder, W. Meiners, K. Wissenbach, R. Poprawe, Selective laser melting of aluminum die-cast alloy—Correlations between process parameters, solidification conditions, and resulting mechanical properties, J. Laser Appl. 27 (2015) 1–6. doi:10.2351/1.4906389.

[304] T.M. Mower, M.J. Long, Mechanical Behavior of Additive Manufactured, Powder-bed Laser-Fused Materials, Mater. Sci. Eng. A. 651 (2015) 198–213. doi:10.1016/j.msea.2015.10.068.

[305] J. Guo, H. Zhu, J. Jia, Mechanical properties of Al-7Si-Mg casting alloy under various aging conditions, Mater. Sci. Technol. 14 (1998) 476–478.

[306] P. a. Rometsch, G.B. Schaffer, An age hardening model for Al-7Si-Mg casting alloys, Mater. Sci. Eng. A. 325 (2002) 424–434. doi:10.1016/S0921-5093(01)01479-4.

[307] R.X. Li, R.D. Li, Y.H. Zhao, L.Z. He, C.X. Li, H.R. Guan, Z.Q. Hu, Age-hardening behavior of cast Al-Si base alloy, Mater. Lett. 58 (2004) 2096–2101. doi:10.1016/j.matlet.2003.12.027.

[308] N.D. Alexopoulos, S.G. Pantelakis, Quality evaluation of A357 cast aluminum alloy specimens subjected to different artificial aging treatment, Mater. Des. 25 (2004) 419–430. doi:10.1016/j.matdes.2003.11.007.

[309] Y.X. Gan, R. a. Overfelt, Fatigue property of semisolid A357 aluminum alloy under different heat treatment conditions, J. Mater. Sci. 41 (2006) 7537–7544. doi:10.1007/s10853-006-0838-5.

[310] Z. Chen, Y. Lei, H. Zhang, Structure and properties of nanostructured A357 alloy produced by melt spinning compared with direct chill ingot, J. Alloys Compd. 509 (2011) 7473–7477. doi:10.1016/j.jallcom.2011.04.082.

[311] ASTM International, ASTM E8/E8M : Standard Test Methods for Tension Testing of Metallic Materials, (2010). doi:10.1520/E0008.

[312] S. Bremen, W. Meiners, A. Diatlov, Selective Laser Melting. A manufacturing technology for the future?, Rapid Manuf. 2 (2012) 33–38. doi:10.1002/latj.201290018.

[313] S. Leuders, M. Thöne, a. Riemer, T. Niendorf, T. Tröster, H. a. Richard, H.J. Maier, On the mechanical behaviour of titanium alloy TiAl6V4 manufactured by selective laser melting: Fatigue resistance and crack growth performance, Int. J. Fatigue. 48 (2013) 300–307. doi:10.1016/j.ijfatigue.2012.11.011.

[314] W. Xu, M. Brandt, S. Sun, J. Elambasseril, Q. Liu, K. Latham, K. Xia, M. Qian, Additive manufacturing of strong and ductile Ti–6Al–4V by selective laser melting via in situ martensite decomposition, Acta Mater. 85 (2015) 74–84. doi:10.1016/j.actamat.2014.11.028.

[315] X. Dong, L. He, G. Mi, P. Li, Two directional microstructure and effects of nanoscale dispersed Si particles on microhardness and tensile properties of AlSi7Mg melt-spun alloy, J. Alloys Compd. 618 (2015) 609–614.

[316] A. Uriondo, M. Esperon-Miguez, S. Perinpanayagam, The present and future of additive manufacturing in the aerospace sector: A review of important aspects, J. Aerosp. Eng. 229 (2015) 2132–2147. doi:10.1177/0954410014568797.

[317] S. Menargues, E. Martín, M.T. Baile, J. a. Picas, New short T6 heat treatments for aluminium silicon alloys obtained by semisolid forming, Mater. Sci. Eng. A. 621 (2015) 236–242. doi:10.1016/j.msea.2014.10.078.

[318] T.B. Sercombe, X. Li, Selective laser melting of aluminium and aluminium metal matrix composites : review, Mater. Technol. 31 (2016) 77–85. doi:10.1179/1753555715Y.0000000078.

[319] ASM International, ASM handbook 3, Alloy phase diagrams, Materials Park, OH, 1992. doi:10.1007/BF02869318.

[320] I. Rosenthal, A. Stern, N. Frage, Strain rate sensitivity and fracture mechanism of AlSi10Mg parts produced by Selective Laser Melting, Mater. Sci. Eng. A. 682 (2017) 509–517.

[321] U. Tradowsky, J. White, R.M. Ward, N. Read, W. Reimers, M.M. Attallah, Selective laser melting of AlSi10Mg : Influence of post-processing on the microstructural and tensile properties development, Mater. Des. 105 (2016) 212–222.

[322] R. Singh, Titanium foams for biomedical applications: a review, Mater. Technol. 25 (2010) 127–136. doi:10.1179/175355510X12744412709403.

[323] H. Matsumoto, S. Watanabe, S. Hanada, Beta TiNbSn alloys with low young's modulus and high strength, Mater. Trans. 46 (2005) 1070–1078. doi:10.2320/matertrans.46.1070.

[324] F.C. Campbell, Superalloys, in: Manuf. Technol. Aerosp. Struct. Mater., 1st editio, Elsevier Ltd., 2006: pp. 212–272.

[325] Y. Okazaki, E. Gotoh, T. Manabe, K. Kobayashi, Comparison of metal concentrations in rat tibia tissues with various metallic implants, Biomaterials. 25 (2004) 5913–5920. doi:10.1016/j.biomaterials.2004.01.064.

[326] M. Niinomi, Mechanical biocompatibilities of titanium alloys for biomedical applications, J. Mech. Behav. Biomed. Mater. 1 (2008) 30–42. doi:10.1016/j.jmbbm.2007.07.001.

[327] H. Hermawan, D. Ramdan, J.R.P. Djuansjah, Metals for Biomedical Applications, in: Biomed. Eng. Theory to Appl., 2011: pp. 411–430.

[328] S.M. Thompson, Z.S. Aspin, N. Shamsaei, A. Elwany, Additive manufacturing of heat exchangers : A case study on a multi-layered Ti – 6Al – 4V oscillating heat pipe, Addit. Manuf. 8 (2015) 163–174. doi:10.1016/j.addma.2015.09.003.

[329] I. Ullah, J. Elambasseril, M. Brandt, S. Feih, Performance of bio-inspired Kagome truss core structures under compression and shear loading, Compos. Struct. 118 (2014) 294–302. doi:10.1016/j.compstruct.2014.07.036.

[330] J. Kranz, D. Herzog, C. Emmelmann, J. Kranz, D. Herzog, Design guidelines for laser additive manufacturing of lightweight structures in TiAl6V4, J. Laser Appl. 27 (2015) 16. doi:10.2351/1.4885235.

[331] L.T. Jurg Marten, Dean Mosseveld, Martin Leary, Innovative new options in liquid fuelled rocket motor manufacturing methods - Additive manufacturing in high stress applications, in: Int. Astronaut. Congr., Toronto, Canada, 2014: pp. 1–13.

[332] D.E. Cooper, M. Stanford, K.A. Kibble, G.J. Gibbons, Additive Manufacturing for product improvement at Red Bull Technology, Mater. Des. 41 (2012) 226–230. doi:10.1016/j.matdes.2012.05.017.

[333] D. Rugg, Materials for future gas turbine applications, Mater. Sci. Technol. 30 (2014) 1848–1852. doi:10.1179/1743284714Y.0000000609.

[334] W. Sha, S. Malinov, Introduction to titanium alloys, in: Titan. Alloy. Model. Microstruct. Prop. Appl., Woodhead Publishing Limited, Abington Hall, Granta Park, Great Abington, Cambridge CB21 6AH, UK, 2009: pp. 1–8. doi:10.1533/9781845695866.1.

[335] H.M. Flower, High Performance Materials in Aerospace, First Edit, Springer-Science+Business Media, 1995.

[336] D. Banerjee, J.C. Williams, Perspectives on Titanium Science and Technology, Acta Mater. 61 (2013) 844–879. doi:10.1016/j.actamat.2012.10.043.

[337] Dabrowski, R., The kinetics of phase transformations during continous cooling of Ti-6Al-4V alloy from the diphase alpha + beta range, Arch. Metall. Mater. 56 (2011) 4–8. doi:10.2478/v10172-011-0025-9.

[338] 2006 - Montanari - Lattice expansion of Ti–6Al–4V by nitrogen and oxygen absorption.pdf, (n.d.).

[339] B. Babu, Physically Based Model for Plasticity and Creep Physically of Ti-6Al-4V, Lulea University of Technology, 2008.

[340] T. Vilaro, C. Colin, J.D. Bartout, As-Fabricated and Heat-Treated Microstructures of the Ti-6Al-4V Alloy Processed by Selective Laser Melting, Metall. Mater. Trans. A. 42A (2011) 3190–3199. doi:10.1007/s11661-011-0731-y.

[341] H. Search, C. Journals, A. Contact, M. Iopscience, I.P. Address, Microstructure of Ti-6Al-4V produced by selective laser melting, J. Phys. Conf. Ser. 371 (2012) 0–4. doi:10.1088/1742-6596/371/1/012084.

[342] X. Zhao, S. Li, M. Zhang, Y. Liu, T.B. Sercombe, S. Wang, Y. Hao, R. Yang, L.E. Murr, Comparison of the microstructures and mechanical properties of Ti-6Al-4V fabricated by selective laser melting and electron beam melting, Mater. Des. 95 (2016) 21–31. doi:10.1016/j.matdes.2015.12.135.

[343] S. Palanivel, A.K. Dutt, E.J. Faierson, R.S. Mishra, Spatially dependent properties in a laser additive manufactured Ti-6Al-4V component, Mater.

Sci. Eng. A. 654 (2016) 39–52. doi:10.1016/j.msea.2015.12.021.

[344] M. Simonelli, Y.Y. Tse, C. Tuck, Effect of the build orientation on the mechanical properties and fracture modes of SLM Ti-6Al-4V, Mater. Sci. Eng. A. 616 (2014) 1–11. doi:10.1016/j.msea.2014.07.086.

[345] C. Qiu, N.J.E. Adkins, M.M. Attallah, Microstructure and tensile properties of selectively laser-melted and of HIPed laser-melted Ti-6Al-4V, Mater. Sci. Eng. A. 578 (2013) 230–239. doi:10.1016/j.msea.2013.04.099.

[346] M. Simonelli, Y.Y. Tse, C. Tuck, The formation of alpha + beta microstructure in as-fabricated selective laser melting of Ti – 6Al – 4V, J. Mater. Res. 29 (2014) 2028–2035. doi:10.1557/jmr.2014.166.

[347] B. Vrancken, L. Thijs, J.-P. Kruth, J. Van Humbeeck, Heat treatment of Ti6Al4V produced by Selective Laser Melting: Microstructure and mechanical properties, J. Alloys Compd. 541 (2012) 177–185. doi:10.1016/j.jallcom.2012.07.022.

[348] W. Xu, S. Sun, J. Elambasseril, Q. Liu, M. Brandt, Ti-6Al-4V Additively Manufactured by Selective Laser Melting with Superior Mechanical Properties, Miner. Met. Mater. Soc. 67 (2015) 668–673. doi:10.1007/s11837-015-1297-8.

[349] B. Song, S. Dong, B. Zhang, H. Liao, C. Coddet, Effects of processing parameters on microstructure and mechanical property of selective laser melted Ti6Al4V, Mater. Des. 35 (2012) 120–125. doi:10.1016/j.matdes.2011.09.051.

[350] H. Gong, K. Rafi, H. Gu, T. Starr, B. Stucker, Analysis of Defect Generation in Ti-6Al-4V Parts Made using Powder Bed Fusion Additive Manufacturing Processes, Addit. Manuf. 1–4 (2014) 87–98. doi:10.1016/j.addma.2014.08.002.

[351] C. Qiu, C. Panwisawas, M. Ward, H.C. Basoalto, J.W. Brooks, M.M. Attallah, On the role of melt flow into the surface structure and porosity development during selective laser melting, Acta Mater. 96 (2015) 72–79. doi:10.1016/j.actamat.2015.06.004.

[352] A.M. Khorasani, I. Gibson, M. Goldberg, G. Littlefair, A survey on mechanisms and critical parameters on solidification of selective laser melting during fabrication of Ti-6Al-4V prosthetic acetabular cup, Mater. Des. 103 (2016) 348–355. doi:10.1016/j.matdes.2016.04.074.

[353] P. Edwards, M. Ramulu, Fatigue performance evaluation of selective laser

melted Ti – 6Al – 4V, Mater. Sci. Eng. A. 598 (2014) 327–337. doi:10.1016/j.msea.2014.01.041.

[354] H.K. Rafi, N. V Karthik, H. Gong, T. Starr, B. Stucker, Defect Morphology in Ti-6Al-4V Parts Fabricated by Selective Laser Melting and Electron Beam Melting, J. Mater. Eng. Perform. 22 (2013) 3872–3883. doi:10.1007/s11665-013-0658-0.

[355] L. Facchini, E. Magalini, P. Robotti, A. Molinari, S. Höges, K. Wissenbach, Ductility of a Ti-6Al-4V alloy produced by selective laser melting of prealloyed powders, Rapid Prototyp. J. 16 (2010) 450–459. doi:10.1108/13552541011083371.

[356] H.K. Rafi, N. V. Karthik, H. Gong, T.L. Starr, B.E. Stucker, Microstructures and mechanical properties of Ti6Al4V parts fabricated by selective laser melting and electron beam melting, J. Mater. Eng. Perform. 22 (2013) 3872–3883. doi:10.1007/s11665-013-0658-0.

[357] F.W. Eric Wycisk, Claus Emmelmann, Shafaqat Siddique, High Cycle Fatigue HCF Performance of Ti-6Al-4V Alloy Processed by SLM, Adv. Mater. Res. 816–817 (2013) 134–139.

[358] H.K. Rafi, T.L. Starr, B.E. Stucker, A comparison of the tensile, fatigue, and fracture behavior of Ti-6Al-4V and 15-5 PH stainless steel parts made by selective laser melting, Int. J. Adv. Manuf. Technol. 69 (2013) 1299–1309. doi:10.1007/s00170-013-5106-7.

[359] B. Van Hooreweder, R. Boonen, D. Moens, J.P. Kruth, P. Sas, On the determination of fatigue properties of Ti6Al4V produced by selective laser melting, in: 53rd AIAA Struct. Struct. Dyn. Mater. Conf., 2012: pp. 1–9. doi:10.2514/6.2012-1733.

[360] S. Leuders, M. Vollmer, F. Brenne, T. Tro, T. Niendorf, Fatigue Strength Prediction for Titanium Alloy TiAl6V4 Manufactured by Selective Laser Melting, Metall. Mater. Trans. A. 46 (2015) 3816–3823. doi:10.1007/s11661-015-2864-x.

[361] G. Kasperovich, J. Hausmann, Improvement of fatigue resistance and ductility of TiAl6V4 processed by selective laser melting, J. Mater. Process. Technol. 220 (2015) 202–214. doi:10.1016/j.jmatprotec.2015.01.025.

[362] E. Wycisk, A. Solbach, S. Siddique, D. Herzog, F. Walther, Effects of Defects in Laser Additive Manufactured Ti-6Al-4V on Fatigue Properties, Phys. Procedia. 56 (2014) 371–378. doi:10.1016/j.phpro.2014.08.120.

[363] T. Leuders, S., Lieneke, T. and Lammers, S., Troster, T., Niendorf, On the fatigue properties of metals manufactured by selective laser melting-The role of ductility, J. Mater. Res. 29 (2014) 1911–1919. doi:10.1557/jmr.2014.157.

[364] R.K. Nalla, B.L. Boyce, J.P. Campbell, J.O. Peters, R.O. Ritchie, Influence of Microstructure on High-Cycle Fatigue of Ti-6Al-4V : Bimodal vs . Lamellar Structures, Metall. Mater. Trans. A. 33A (2002) 899–918.

[365] Y. Cao, F. Zeng, B. Liu, Y. Liu, J. Lu, Z. Gan, Characterization of fatigue properties of powder metallurgy titanium alloy, Mater. Sci. Eng. A. 654 (2016) 418–425. doi:10.1016/j.msea.2015.12.058.

[366] B. Gong, H., Rafi, K., Starr, T., Stucker, Effect of defects on fatigue tests of as-built Ti-6Al-4V parts fabricated by selective laser melting, in: 2012 Annu. Int. Solid Free. Fabr. Symp., 2012: pp. 499–506.

[367] G. Nicoletto, Anisotropic high cycle fatigue behavior of Ti-6Al-4V obtained by powder bed laser fusion, Int. J. Fatigue. 94 (2017) 255–262. doi:10.1016/j.ijfatigue.2016.04.032.

[368] E. Wycisk, S. Siddique, D. Herzog, F. Walther, C. Emmelmann, Fatigue Performance of Laser Additive Manufactured Ti–6Al–4V in Very High Cycle Fatigue Regime up to 10^9 Cycles, Front. Mater. 2 (2015) 2–9. doi:10.3389/fmats.2015.00072.

[369] E. Sallica-leva, R. Caram, A.L. Jardini, J.B. Fogagnolo, Ductility improvement due to martensite α' decomposition in porous Ti-6Al-4V parts produced by selective laser melting for orthopedic implants, J. Mech. Behav. Biomed. Mater. 54 (2016) 149–158. doi:10.1016/j.jmbbm.2015.09.020.

[370] E. Brandl, D. Greitemeier, Microstructure of additive layer manufactured Ti–6Al–4V after exceptional post heat treatments, Mater. Lett. 81 (2012) 84–87. doi:10.1016/j.matlet.2012.04.116.

[371] P. Li, D.H. Warner, A. Fatemi, N. Phan, Critical assessment of the fatigue performance of additively manufactured Ti-6Al-4V and perspective for future research, Int. J. Fatigue. 85 (2016) 130–143. doi:10.1016/j.ijfatigue.2015.12.003.

[372] I. Yadroitsev, P. Krakhmalev, I. Yadroitsava, Selective laser melting of Ti6Al4V alloy for biomedical applications : Temperature monitoring and microstructural evolution, J. Alloys Compd. 583 (2014) 404–409. doi:10.1016/j.jallcom.2013.08.183.

[373] M.W. Wu, P.H. Lai, The positive effect of hot isostatic pressing on

improving the anisotropies of bending and impact properties in selective laser melted Ti-6Al-4V alloy, Mater. Sci. Eng. A. 658 (2016) 429–438. doi:10.1016/j.msea.2016.02.023.

[374] Y.V.R.K. Prasad, T. Seshacharyulu, S.C. Medeiros, W.G. Frazier, Influence of oxygen content on the forging response of equiaxed (alpha + beta) preform of Ti ± 6Al ± 4V : commercial vs. ELI grade, J. Mater. Process. Technol. 108 (2001) 320–327.

[375] M. Yan, W. Xu, M.S. Dargusch, H.P. Tang, M. Brandt, M. Qian, Review of effect of oxygen on room temperature ductility of titanium and titanium alloys, Powder Metall. 57 (2014) 251–257. doi:10.1179/1743290114Y.0000000108.

[376] A.I. Kahveci, G.E. Welsch, Effect of oxygen on the hardness and Alpha/beta phase ratio of Ti6Al4V, Scr. Metall. 20 (1986) 1287–1290.

[377] A. Mertens, S. Reginster, H. Paydas, Q. Contrepois, T. Dormal, O. Lemaire, J.L. Beckers, Mechanical properties of alloy Ti-6Al-4V and of stainless steel 316L processed by selective laser melting: influence of out-of-equilibrium microstructures, Powder Metall. 57 (2014) 184–189. doi:10.1179/1743290114Y.0000000092.

[378] A.M. Beese, B.E. Carroll, Review of Mechanical Properties of Ti-6Al-4V Made by Laser-Based Additive Manufacturing Using Powder Feedstock, Jom. 68 (2016) 724–734. doi:10.1007/s11837-015-1759-z.

[379] D.A. Hollander, M. Von Walter, T. Wirtz, R. Sellei, B. Schmidt-Rohlfing, O. Paar, H.J. Erli, Structural, mechanical and in vitro characterization of individually structured Ti-6Al-4V produced by direct laser forming, Biomaterials. 27 (2006) 955–963. doi:10.1016/j.biomaterials.2005.07.041.

[380] N. Dai, L.-C. Zhang, J. Zhang, X. Zhang, Q. Ni, Y. Chen, M. Wu, C. Yang, Distinction in corrosion resistance of selective laser melted Ti-6Al-4V alloy on different planes, Corros. Sci. 111 (2016) 703–710. doi:10.1016/j.corsci.2016.06.009.

[381] F. Cardaropoli, V. Alfieri, F. Caiazzo, V. Sergi, Dimensional analysis for the definition of the influence of process parameters in selective laser melting of Ti-6Al-4V alloy, Proc. Inst. Mech. Eng. Part B J. Eng. Manuf. 226 (2012) 1136–1142. doi:10.1177/0954405412441885.

[382] ASTM International, ASTM E466-15: Standard practice for conducting force controlled constant amplitude axial fatigue tests of metallic materials, (2015). doi:10.1520/E0466-15.2.

[383] ASTM International, ASTM E29-13 : Standard Practice for Using Significant Digits in Test Data to Determine Conformance with Specifications, (2013). doi:10.1520/E0029-13.2.

[384] A. Saboori, D. Gallo, S. Biamino, P. Fino, M. Lombardi, An Overview of Additive Manufacturing of Titanium Components by Directed Energy Deposition: Microstructure and Mechanical Properties, Appl. Sci. 7 (2017) 1–23. doi:10.3390/app7090883.

[385] S. Tammas-Williams, P.J. Withers, I. Todd, P.B. Prangnell, Porosity regrowth during heat treatment of hot isostatically pressed additively manufactured titanium components, Scr. Mater. 122 (2016) 72–76. doi:10.1016/j.scriptamat.2016.05.002.

[386] H.A.R. M. Thöne, S. Leuders, A. Riemer, T. Tröster, Influence of heat-treatment on Selective Laser Melting products – e.g. Ti6Al4V, in: 2012 Annu. Int. Solid Free. Fabr. Symp., 2012: pp. 492–498.

[387] R. Montanari, G. Costanza, M.E. Tata, C. Testani, I. Meccanica, U.R. Vergata, V. Politecnico, C.S. Materiali, C. Romano, C. Romano, Lattice expansion of Ti – 6Al – 4V by nitrogen and oxygen absorption, Mater. Charact. 59 (2008) 334–337. doi:10.1016/j.matchar.2006.12.014.

[388] J. Günther, D. Krewerth, T. Lippmann, S. Leuders, T. Tröster, A. Weidner, H. Biermann, T. Niendorf, Fatigue life of additively manufactured Ti-6Al-4V in the very high cycle fatigue regime, Int. J. Fatigue. 94 (2017) 236–245. doi:10.1016/j.ijfatigue.2016.05.018.

[389] G. Ivanova, Svetlana, R. Biederman, Ronald, J. Sisson, Richad, D., Investigation of Fatigue Crack Initiation in Ti-6Al-4V During Tensile-Tensile Fatigue, J. Mater. Eng. Perform. 11 (2002) 226–231.

[390] M. Li, S.J. Zinkle, Physical and mechanical properties of copper and copper alloys, Compr. Nucl. Mater. 4 (2012) 667–690. doi:10.1016/B978-0-08-056033-5.00122-1.

[391] S.D. Henry, B.R. Sanders, N. Hrivnak, J.A. Kinson, W.W. Scott, ASM Specialty Handbook: Copper and copper alloys, 2001. doi:10.1097/00000433-198206000-00020.

[392] H.H. Zhu, L. Lu, J.Y.H. Fuh, Development and characterisation of direct laser sintering Cu-based metal powder, J. Mater. Process. Technol. 140 (2003) 314–317. doi:10.1016/S0924-0136(03)00755-6.

[393] D. Gu, Y. Shen, Effects of dispersion technique and component ratio on

densification and microstructure of multi-component Cu-based metal powder in direct laser sintering, J. Mater. Process. Technol. 182 (2007) 564–573. doi:10.1016/j.jmatprotec.2006.09.026.

[394] C. Song, Y. Yang, Y. Liu, Z. Luo, Study on manufacturing of W-Cu alloy thin wall parts by selective laser melting, Int. J. Adv. Manuf. Technol. 78 (2015) 885–893. doi:10.1007/s00170-014-6689-3.

[395] J. Stašić, M. Trtica, V. Rajković, J. Ružić, D. Božić, Laser sintering of Cu–Zr–ZrB2 composite, Appl. Surf. Sci. 321 (2014) 353–357. doi:10.1016/j.apsusc.2014.10.021.

[396] D. Becker, Additive Manufacturing of copper components, Fraunhofer Inst. Laser Technol. ILT, Www.ilt.fraunhofer.de. (2013) 69572.

[397] J. Ma, B. Wang, Z. liang Yang, G. xin Wu, J. yu Zhang, S. li Zhao, Microstructure simulation of rapidly solidified ASP30 high-speed steel particles by gas atomization, Int. J. Miner. Metall. Mater. 23 (2016) 294–302. doi:10.1007/s12613-016-1238-8.

[398] X.P. Li, G. Ji, Z. Chen, A. Addad, Y. Wu, H.W. Wang, J. Vleugels, J. Van Humbeeck, J.P. Kruth, Selective laser melting of nano-TiB 2 decorated AlSi10Mg alloy with high fracture strength and ductility, Acta Mater. 129 (2017) 183–193. doi:10.1016/j.actamat.2017.02.062.

[399] A. Hess, R. Schuster, A. Heider, R. Weber, T. Graf, Continuous wave laser welding of copper with combined beams at wavelengths of 1030 nm and of 515 nm, Phys. Procedia. 12 (2011) 88–94. doi:10.1016/j.phpro.2011.03.012.

[400] A. Blom, P. Dunias, P. van Engen, W. Hoving, J. Kramer, Process spread reduction of laser micro-spot welding of thin copper parts using real-time control, in: Phot. Process. Microelectron. Photonics II, 2003: pp. 493–507. doi:10.1117/12.478612.

[401] S. Sauders, Fraunhofer ILT Researching Green Lasers for 3D Printing, 3DPrint.com. (n.d.). https://3dprint.com/186009/fraunhofer-ilt-3d-print-copper/ (accessed September 6, 2017).

[402] Y. Wan, X. Wang, H. Sun, Y. Li, K. Zhang, Y. Wu, Corrosion Behavior of Copper at Elevated Temperature, Electrochem. Sci. 7 (2012) 7902–7914.

[403] M. Suler, L. Kosec, A.. Kneissl, M. Bizjak, K. Raic, M. Bruncko, B. Kosec, I. Anzel, Rapidly solidified copper alloys ribbons, Metal. - J. Metall. (2014) 67–74.

[404] Z. Sun, Y. Wang, J. Guo, Y. Zhu, X. Song, R. Zhu, Liquid and solid phase separation during melt spinning and annealing in melt-spun Cu-Cr ribbons, Mater. Sci. Eng. A. 452–453 (2007) 411–416. doi:10.1016/j.msea.2006.10.112.

[405] F. Lopez, J. Reyes, B. Campillo, Rapid Solidification of Copper Alloys with High Strength and High Conductivity, J. Mater. Eng. Perform. 6 (1997) 611–614.

[406] A.B. Spierings, M. Schneider, R. Eggenberger, Comparison of density measurement techniques for additive manufactured metallic parts, Rapid Prototyp. J. 17 (2011) 380–386. doi:10.1108/13552541111156504.